MECHANOCHEMISTRY FOR SUSTAINABLE SYNTHESIS OF FRAMEWORK MATERIALS

Daniel Nikolaus Rainer

A Thesis Submitted for the Degree of PhD
at the
University of St Andrews

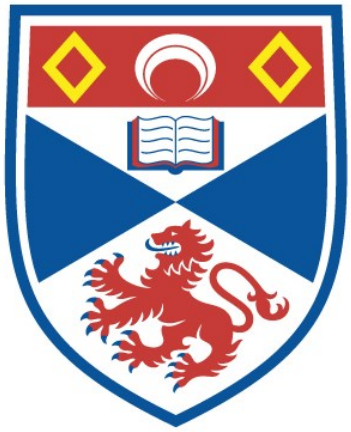

2022

Mechanochemistry for sustainable synthesis of framework materials

Daniel Nikolaus Rainer

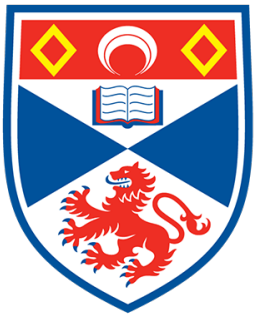

University of
St Andrews

This thesis is submitted in partial fulfilment for the degree of

Doctor of Philosophy (PhD)

at the University of St Andrews

October 2021

Declarations

Candidates's declaration

I, Daniel Nikolaus Rainer, do hereby certify that this thesis, submitted for the degree of PhD, which is approximately 43,000 words in length, has been written by me, and that it is the record of work carried out by me, or principally by myself in collaboration with others as acknowledged, and that it has not been submitted in any previous application for any degree. I confirm that any appendices included in my thesis contain only material permitted by the 'Assessment of Postgraduate Research Students' policy.

I was admitted as a research student at the University of St Andrews in January 2018.

I received funding from an organisation or institution and have acknowledged the funder(s) in the full text of my thesis.

Date 14th February 2022 Signature of candidate

Supervisor's declaration

I hereby certify that the candidate has fulfilled the conditions of the Resolution and Regulations appropriate for the degree of PhD in the University of St Andrews and that the candidate is qualified to submit this thesis in application for that degree. I confirm that any appendices included in the thesis contain only material permitted by the 'Assessment of Postgraduate Research Students' policy.

Date 14th February 2022 Signature of supervisor

Permission for publication

In submitting this thesis to the University of St Andrews we understand that we are giving permission for it to be made available for use in accordance with the regulations of the University Library for the time being in force, subject to any copyright vested in the work not being affected thereby. We also understand, unless exempt by an award of an embargo as requested below, that the title and the abstract will be published, and that a copy of the work may be made and supplied to any bona fide library or research

worker, that this thesis will be electronically accessible for personal or research use and that the library has the right to migrate this thesis into new electronic forms as required to ensure continued access to the thesis.

I, Daniel Nikolaus Rainer, have obtained, or am in the process of obtaining, third-party copyright permissions that are required or have requested the appropriate embargo below.

The following is an agreed request by candidate and supervisor regarding the publication of this thesis:

Printed copy

Embargo on all of print copy for a period of 2 years on the following ground(s):

- Publication would preclude future publication

Supporting statement for printed embargo request

Work contained within this thesis will be part of a manuscript we are preparing to submit to a peer-reviewed journal.

Electronic copy

Embargo on all of electronic copy for a period of 2 years on the following ground(s):

- Publication would preclude future publication

Supporting statement for electronic embargo request

Work contained within this thesis will be part of a manuscript we are preparing to submit to a peer-reviewed journal.

Title and abstract

- I agree to the title and abstract being published

Date 14th February 2022 Signature of candidate

Date 14th February 2022 Signature of supervisor

Underpinning Research Data or Digital Outputs

Candidate's declaration

I, Daniel Nikolaus Rainer, understand that by declaring that I have original research data or digital outputs, I should make every effort in meeting the University's and research funders' requirements on the deposit and sharing of research data or research digital outputs.

Date 14th February 2022 Signature of candidate

Permission for publication of underpinning research data or digital outputs

We understand that for any original research data or digital outputs which are deposited, we are giving permission for them to be made available for use in accordance with the requirements of the University and research funders, for the time being in force.

We also understand that the title and the description will be published, and that the underpinning research data or digital outputs will be electronically accessible for use in accordance with the license specified at the point of deposit, unless exempt by award of an embargo as requested below.

The following is an agreed request by candidate and supervisor regarding the publication of underpinning research data or digital outputs:

Embargo on all of electronic files for a period of 2 years on the following ground(s):

- Publication would preclude future publication

Supporting statement for electronic embargo request

Work contained within this thesis will be part of a manuscript we are preparing to submit to a peer-reviewed journal.

Date 14th February 2022 Signature of candidate

Date 14th February 2022 Signature of supervisor

Acknowledgements

I would like to thank Russell Morris for his supervision throughout the years and for giving me the opportunity to carry out my research in his group.

I want to thank my funding institution EPSRC (grant number EP/N509759/1), and the RSC for a Researcher Mobility Grant (M19-7166) supporting my three month stay at Charles University (CUNI) in Prague, Czech Republic.

I want to thank the University of St Andrews School of Chemistry admin and technical staff for all their help with matters scientific and beyond. Special thanks go to the staff of the electron microscopy facilities Ross, David, and Aaron, PXRD scientist Yuri, and solid-state analysis technician Gavin.

Many thanks to all past and present members of the Russell E. Morris (REM) research group and lab mates from other groups for their help and friendliness in the lab and office, company at conferences and enjoyable past times. Simon, thanks for all your encouragement, the help with work, the relaxed evenings with a dram or two, and our tennis matches. Thank you Aamod, for being a tremendous office and lab mate, inspiring me with new ideas, helping wherever possible, and joining me for interesting discussions about essentially everything.

Special thanks go to Michał, for introducing me to zeolite science in St Andrews, then electron microscopy in Prague, and overall mentoring me throughout the years. I'm more than excited for our upcoming time as colleagues in Prague, producing good science, playing some football, and enjoying more whiskies.

I'm thankful to my colleagues and friends at CUNI for their hospitality and friendliness during my stay. Without them my time in Prague would not have been nearly as pleasant.

I also want to thank the lunchtime footy group, the chemistry football league teams, and our six-a-side team Fluorescent FC, which were all great fun to be part of, getting my mind off of science for a bit.

I'm grateful to my family and friends for their continued support throughout the years, even despite me rarely getting the chance to visit.

Finally, and most importantly I will ever be grateful to my girlfriend Jaci. None of this would've even been remotely possible without you. Thank you for keeping me honest, enjoying the good times, building me up when I'm down, going with me through thick and thin and emerging on the other, brighter side; simply making my life better.

Publications and courses attended

Publications within the scope of the thesis

Daniel N. Rainer, Cameron M. Rice, Stewart J. Warrender, Sharon E. Ashbrook and Russell E. Morris, Mechanochemically assisted hydrolysis in the ADOR process, *Chem. Sci.*, 2020, **11**, 7060–7069.
DOI: 10.1039/D0SC02547J

Daniel N. Rainer and Russell E. Morris, New avenues for mechanochemistry in zeolite science, *Dalton Trans.*, 2021, **50**, 8995–9009.
DOI: 10.1039/D1DT01440D

Daniel N. Rainer, Aamod V. Desai, A. Robert Armstrong, and Russell E. Morris, Mechanochemical synthesis of sodium carboxylates as anode materials in sodium ion batteries, *J. Mater. Chem. A*, 2021, **9**, 27 361–27 369.
DOI: 10.1039/D1TA07897F

Publications outside the scope of the thesis

Daniel N. Rainer and Michal Mazur, Electron microscopy methods for characterisation of zeolite catalysts, in Catalysis, Royal Society of Chemistry, 2020, vol. 32, pp. 151–187.
DOI: 10.1039/9781788019477-00151

Qiudi Yue, Jakub Halamek, Daniel N. Rainer, Jin Zhang, Roman Bulánek, Russell E. Morris, Jiří Čejka, and Maksym Opanasenko, Tuning the CHA framework composition by isomorphous substitution for CO_2/CH_4 separation, *Chem. Eng. J.*, 2022, **429**, 131277.
DOI: 10.1016/j.cej.2021.131277

Simon M. Vornholt, Caroline G. Elliott, Cameron M. Rice, Samantha E. Russell, Peter J. Kerr, Daniel N. Rainer, Michal Mazur, Mark R. Warren, Paul S. Wheatley, and Russell E. Morris, Controlled Synthesis of Large Single Crystals of Metal-Organic Framework CPO-27-Ni Prepared by a Modulation Approach: In situ Single Crystal X-ray Diffraction Studies, *Chem. – A Eur. J.*, 2021, **27**, 8537–8546.
DOI: 10.1002/chem.202100528

Samantha E. Russell, Susan E. Henkelis, Simon V. Vornholt, Daniel N. Rainer, Karena W. Chapman, and Russell E. Morris, In Situ Flow Pair Distribution Function Analysis to Probe the Assembly-Disassembly-Organisation-Reassembly (ADOR) Mechanism of Zeolite IPC-2 Synthesis, *Mater. Adv.*, 2021, **2**, 7949–7955.
DOI: 10.1039/D1MA00335F

Aamod V. Desai, Daniel N. Rainer, Atin Pramanik, Joel M. Cabañero Jr., Russell E. Morris, and A. Robert Armstrong, Rapid microwave-assisted synthesis and electrode optimization of organic anode in sodium-ion batteries, *Small Methods*, 2021, **5**, 2101016.
DOI: 10.1002/smtd.202101016

Courses attended

- Powder diffraction for materials chemists (Yuri Andreev) – November 2018
- Zeolites and MOFs – Blockbuster solids (Russell E. Morris) – May 2018
- Practical electron microscopy (Wuzong Zhou) – May 2018

Abstract

The following work presents the successful application of mechanochemical methods in the synthesis of framework materials, namely zeolites and sodium carboxylate coordination polymers. Common benefits of employing mechanical forces to aid and cause chemical reactions are typically decreased reaction times, lower amounts or avoidance of solvents, and highly efficient reactions, leading to overall more sustainable processes.

A mechanochemically aided hydrolysis protocol for the second step of the ADOR (Assembly-Disassembly-Organisation-Reassembly) process was devised using zeolites with **UTL** framework as parent material. In contrast to conventional disassembly, which relies on the reaction occurring in solution at elevated temperatures, the use of a rotary ball mill allows for significant reduction of employed liquids (water or hydrochloric acid) and completion can be achieved on much shorter time scales. This reaction setup minimises waste production and requires lower energy input. Obtained intermediate zeolite phases can be reassembled into known daughter zeolites with ***PCS**, **OKO**, and **PCR** frameworks. The developed protocol and its low volumetric requirements for the hydrolytic reagent are not only beneficial from a purely synthetic point of view but could be applied successfully in the enrichment of product zeolite phases with the NMR active isotope ^{17}O. Such enrichment procedures are typically time and energy consuming as well as carrying a high financial burden due to the low natural abundance of this isotope, which necessitates enrichment procedures in the first place.

Several of the more complex zeolite frameworks are only obtainable as germanosilicate variant, suffering from the comparatively high cost of germanium reagents compared to silicon or aluminium analogues. In an attempt to extend the scope of the solvent-free route for zeolite synthesis, mechanochemical treatment of starting materials prior to the crystallisation reaction was performed, targeting four different frameworks. Reproducing literature reports, zeolites with **ITH** structure could be obtained. Further, materials with **UOV** structure were targeted, but instead yielding structurally related **BEC** zeolites. Synthesis of **UTL** was so far unsuccessful, but experiments additionally using seed crystals of the desired phase showed some preliminary success. Finally, pure silica and germanosilicate materials with **ISV** framework were synthesised for the first time using a solvent-free approach.

Sodium carboxylates, members of the class of framework materials called coordination polymers, are promising candidates for organic-based anodes of sodium ion batteries,

but face difficulties in large scale production. A mechanochemical synthesis route for sodium carboxylates using several, chemically varied organic carboxylic acids and the environmentally benign sodium acetate as source for the alkali metal, has been developed to alleviate most of these concerns. Produced materials show electrochemical performance on par with compounds obtained through conventional solution-based synthesis, with improved reaction conditions, avoidance of solvent and thus reduced waste.

Table of contents

Chapter 1

Introduction

Parts of this chapter have been published in:

Daniel N. Rainer and Russell E. Morris, *Dalton Transactions*, 2021, **50**, 8995–9009.
DOI: 10.1039/D1DT01440D

1.1 Mechanochemistry – the green chemistry solution

A big challenge in modern chemistry is the economical and ecological impact of current chemical technologies and processes, especially in an industrial setting. This concerns efficiency of synthesis techniques as well as waste management and sustainability of processes as a whole.

Today's chemistry is overwhelmingly conducted in the solution state, where chemical reagents are dissolved in an appropriate solvent and reacted with each other, often employing a heating source to increase reaction rates. The product of such a transformation is typically washed with more solvent to remove unreacted starting materials or by-products and obtain a purified material. This is a proven and tremendously successful way to produce almost all types of useful compounds and is thus utilised in all branches of chemistry, be it organic or inorganic, biochemistry, or materials science. However, when looking at this approach from an efficiency point of view it often performs rather poorly. Large amounts of solvent are required which are often difficult to recycle and need to be disposed of appropriately. In order to drive reactions towards the desired product, one of the reagents may also be used in excess, thus eventually becoming waste too. Additionally, many reactions are performed in solvents which are considered hazardous and harmful, especially chlorinated chemicals like dichloromethane or chloroform, but also diethyl ether, which is unsafe due to its high volatility.

In an effort to improve standard reaction conditions and induce a change of thinking towards increased awareness about above described issues, the idea of "green chemistry" was born. Early proponents are P.T. Anastas and J.C. Warner, who can be credited with laying out the fundamental *12 principles of green chemistry* in their book published in the year 2000.[1] They describe good practices and important areas for improvement to further current technologies and processes. Each of the twelve points targets a different topic, some of which can be easily implemented, whereas others may necessitate a more radical paradigm shift in how to conduct chemical reactions.[2] A recent overview of progress on green chemistry is given by Anastas' group.[3]

One of the technologies that has emerged as a potent solution to take on the challenges set out by the green chemistry principles is *mechanochemistry*. Mechanochemical procedures are typically solid-state reactions only requiring a minute amount of liquid if any at all. They are mostly stoichiometric reactions, where no or only a small amount of the starting materials remains after the reaction has concluded. Often, these reactions

are also faster compared to a solution-based counterpart. The relevance of mechanochemistry as "green" alternative in synthetic chemistry has been highlighted in recent literature[3,4] and a dedicated assessment has been conducted by Ardila-Fierro et al. They concluded that this general methodology is well suited to complement existing sustainable technologies and is thought to be able to help make the chemical industry more economical.[5]

Utilising mechanical forces to induce chemical transformations can be dated back to the 1800s, where M. Faraday reported on the chemical reaction involving silver halides and zinc and M. Carey Lea investigated the difference between thermal and mechanical energy input in the reaction of silver and mercury chloride.[6,7] The first occurrence of the term "mechanochemistry" was published soon after, being used by Ostwald in the early 20th century.[8] Dedicated use of mechanical forces seemingly disappeared for the following decades from the academic literature in chemistry. In contrast, the effects of mechanical treatments were widely used and studied in metallurgy and ore processing. Further investigations of underlying principles in chemistry were continued from research groups in Russia and Germany in the 1950s. Slowly, mechanochemical methods were employed in other areas of chemistry, producing metal alloys and oxides, but also probing the possibilities in organic chemistry. Finally, in the 21st century mechanochemistry has spread into many different areas and continues to grow, evidenced by a large number of publications throughout chemistry. A comprehensive account of the historical progress of mechanochemistry is given by Takacs in recent reviews.[9,10]

Mechanochemistry can be performed using mortar and pestle but is more often conducted in mills, more specifically ball mills. Using such dedicated instruments enables comparison between different laboratories. Synthesis parameters such as frequency, rotation speed, and employed milling media can be unequivocally established and allow for greater reproducibility. One of the most important implications is that the general design of ball mills is usually scalable and as such, novel procedures developed on a small scale are translatable to plant scale in a rather straight forward way. In addition to mills, larger scale mechanochemical reactions can also be realised using extrusion techniques which are well established in fields like polymer chemistry and food chemistry. Especially twin screw extrusion is a commonly used technique[11] which is now also applied in pharmaceutical and material processing on an industrial scale.[12–14]

The seemingly universal applicability of mechanochemistry as a synthetic tool is evidenced by a great number of publications in a variety of different areas of chemistry. The

last years have seen comprehensive reviews of these studies in organic[15] and main group chemistry,[16] medicinal chemistry,[17] and materials chemistry.[18–23] Despite the possibly intuitive assumption that a reaction under the influence of strong mechanical forces may inevitably lead only to dense products, even porous materials are obtainable.[24,25] This has seen particular success in the field of coordination polymers,[26] specifically metal-organic frameworks (MOFs),[27–30] the related zeolitic imidazolate frameworks (ZIFs)[31] and covalent organic frameworks (COFs).[32] Likewise, application of mechanochemical methods in zeolite science has been shown to enable interesting new pathways towards a desired material.[33,34]

1.2 Zeolites

One of the most important types of materials in the current chemical industry are zeolites. These microporous, silicate-based materials are built from tetrahedral TO_4 units (T = Si, Al, Ge, ...), which are connected by corner sharing oxygen atoms. Using only this small primary building unit gives a lot of freedom for combination in 3D space, leading to a large number of possible structures. Some of these are found in nature, whereas most of the currently known structures have been made synthetically in laboratories. In today's chemical industry, zeolites play a vital role due to their beneficial properties of high available surface area and porosity, thermal stability and variety in chemical composition. They are used as catalysts in petrochemistry as well as fine chemical production, gas storage and separation, and ion-exchange materials, to name but a few applications.[35–41]

1.2.1 Historical overview

The following section gives a brief summary of key steps in the history of zeolite science. Further details on this topic can be found in various excellent papers such as the review by Cundy and Cox,[42] or the account by Masters and Maschmeyer.[43]

Zeolites were originally described by Axel F. Cronstedt, a Swedish mineralogist of the 18th century.[44] He had found a mineral known as stilbite, which released water steam upon heating, leading to their name which derives from the Greek words for heating or boiling (ζειν, zein) and stone (λιθοσ, lithos). The phenomenon occurs due to the internal porosity of zeolites, which can store a substantial amount of water. This available void space inside the otherwise robust solid and the concomitant available high surface are the main factors for the success of zeolites in chemical applications.

In the 19th century, the first deliberate synthesis of a zeolite was reported by Saint-

Claire Deville[45] and reports emerged about gas storage and ion exchange capabilities of natural zeolites, providing further clues for their structure, composition, and properties. Finally, a combination of characterisation techniques and crystal structure solutions of several zeolite frameworks in the first half of the 20th century,[46–48] allowed a preliminary description of zeolites as three-dimensional, porous aluminosilicates comprised of corner-sharing TO_4 (T = Si, Al) units. Zeolite structures show pore channels and/or cages in at least one direction, which are typically filled with water, removable by thermal treatment, enabling subsequent uptake of other gases or liquids. The trivalent aluminium ions in the framework are charge balanced with an alkali or earth alkali cation (Na^+, K^+, Ca^{2+}, ...). This knowledge was soon exploited industrially as zeolites were used as water softeners owing to their function as ion exchange materials, effectively removing the divalent Ca^{2+} and Mg^{2+} from water by exchange for monovalent Na^+ or K^+ initially present in the material.

The pioneering work by Barrer in the 1940s can be seen as the birth of modern zeolite science, owing to his discovery of the first zeolite materials with no natural counterpart, which he synthesised by dissolving and recrystallising minerals in basic solutions and at high temperatures.[49] These works were complemented in the 1950s by researchers Milton, Breck, Flanigen, and Rabo working at Union Carbide who contributed to the field with the synthesis of several new zeolite materials as well as using a gel-based preparation method using aqueous sodium silicate and aluminate solutions allowing for lower synthesis temperatures.[50] Barrer with his colleague Denny can also be credited with the first report of a successful synthesis employing tetramethylammonium hydroxide (TMA-OH) as an organic structure-directing agent (OSDA) in the synthesis composition.[51] This was a revolutionary change in the synthesis methodology, since now different elemental compositions with higher silicon content as well as previously unseen pore sizes were available. This is possible due to the larger size of the organic molecule compared to inorganic cations such as sodium. The increased size per charge allows for a higher Si/Al ratio in the final zeolite material, ultimately leading to greater thermal stability of the framework. Using this OSDA approach, Flanigen et al. were later on able to produce the first pure silica zeolite "silicalite".[52]

During this time, zeolite materials beta and ZSM-5 were discovered, which are among the most heavily used in industrial processes to this day.[53,54] Their application as catalysts was made possible by introduction of Brønsted acid sites at the aluminium locations. After the successful synthesis, the negative charge in the framework due to the presence

of aluminium is charge balanced by a cation, for example sodium. Exchanging Na^+ with ammonium NH_4^+ and subsequently heat treating the zeolite material to remove ammonia (NH_3) results in a proton as the counterion, thus creating an active site for Brønsted acid catalysis. This tuning of catalytic properties together with designed composition and high achievable thermal stability led to zeolites becoming the state-of-the-art heterogeneous catalysts.

Expanding the pool of zeolitic materials, the preparation of the closely related AlPOs (aluminophosphates) and SAPOs (silicoaluminophosphates) was achieved in the 1980s, both with frameworks known as aluminosilicates as well as novel types.[55,56] Similarly, incorporation of other heteroelements such as the trivalent boron and gallium,[57,58] or the tetravalent germanium was accomplished by post-synthetic isomorphous substitution into pre-existing T atom site as well as by using corresponding reagents directly in the synthesis.[59] Especially the usage of germanium is noteworthy, as it has an additional structure directing effect, facilitating the formation of small building blocks, which in turn can lead to novel frameworks with larger pore openings.[60]

Another important discovery was made around 1990 with the two-dimensional, layered zeolite phases EU-19[61] and perhaps more importantly MCM-22P and the entire MCM-22 family of zeolites.[62–65] The layers of these zeolite precursor materials can be connected to each other by simple heat treatment, forming a conventional 3D framework. However, for some applications delaminated, individual layers may be preferable due to the higher available surface area.[66,67] Additionally, it is possible to intercalate reagents in between these layers, granting access to pillared and interlayer expanded zeolite materials (IEZ) with specific properties such as a designed interlayer space with a desirable pore size.[68–70]

1.2.2 Zeolite structures

Zeolites can be defined as open, three-dimensional framework materials built from tetrahedral, corner sharing [TO_4] units (T = Si, Al, Ge, B, ...). Negatively charged frameworks are balanced by inorganic or organic cations, which are exchangeable and the void space is filled with an organic compound or water, which is reversibly removable.[71]

Zeolite materials are typically described using their framework types, so that several materials which may have different elemental composition, but share the same, underlying structural characteristics and topology can be combined into one group. These frameworks are idealised versions of an experimentally determined crystal structure of a

certain type material, typically the first described zeolite exhibiting this specific, unique framework type. For example, the framework **UTL** is obtained from the crystal structure of the material IM-12, reported by Paillaud et al. in 2004.[72] The three letters of this framework type code (FTC) are typeset in boldface and are loosely derived from the names of their respective type materials. Unfortunately, the connection is mostly rather obscure, as in this case from "Institut Français du Pétrole and University of M**u**lhouse-**t**we**l**ve" for IM-12 (**UTL**). Two symbols augment the FTCs, a minus symbols indicating interrupted frameworks such as in **−ITV**, and an asterisk declaring a disordered framework such as ***CTH**.

1.2.2.1 Building units

Currently, there are 253 unique framework types acknowledged by the IZA and their crystal structures and other important information are collated in the Database of Zeolite Structures by the IZA.[71] In order to be able to easily but still accurately describe these structures, the concept of building units can be employed. The primary, smallest building units are the [TO_4] tetrahedra, which can be connected in various ways. Secondary building units (SBU) are a convenient way of classifying such combinations, consisting of at least three T atoms. They are used to describe the different zeolite frameworks, where only one type of SBU is employed to make up the whole structure. This approach was abandoned more than a decade ago due to the fast growing complexity of new framework types and the resulting inapplicability of the SBU system. It was superseded by the composite building unit (CBU) description, essentially a more practical version of the SBU method, where now no restriction on the number of different units per framework is imposed. Although this abandons the uniqueness of the definition by SBUs, it gives more freedom to the researcher to choose the most appropriate way of highlighting structural features of a material. This makes it also easier to compare different frameworks with each other. Figure 1.1 shows some common CBUs, which can be a small, distinct unit such as *d4r* or *d6r*, or a unit with importance for practical aspects such as the *sod* or the even larger *lta* cage, which can contain guest molecules.

Another way of describing zeolite frameworks is by using natural tiles, also called natural building units (NBUs). This approach is unambiguous in the description of a given framework and is well suited for porous materials. A tile is the space within a polyhedron and every tile shares each of its faces with one other tile. This means that the entire space of the framework is filled using this tiling method, without overlap of

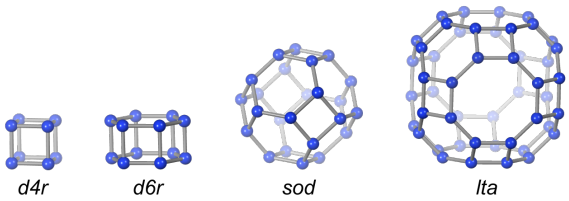

Figure 1.1. Some of the most common CBUs (composite building units) for the description of zeolite frameworks. T atoms are shown in blue, oxygen atoms are omitted for clarity.

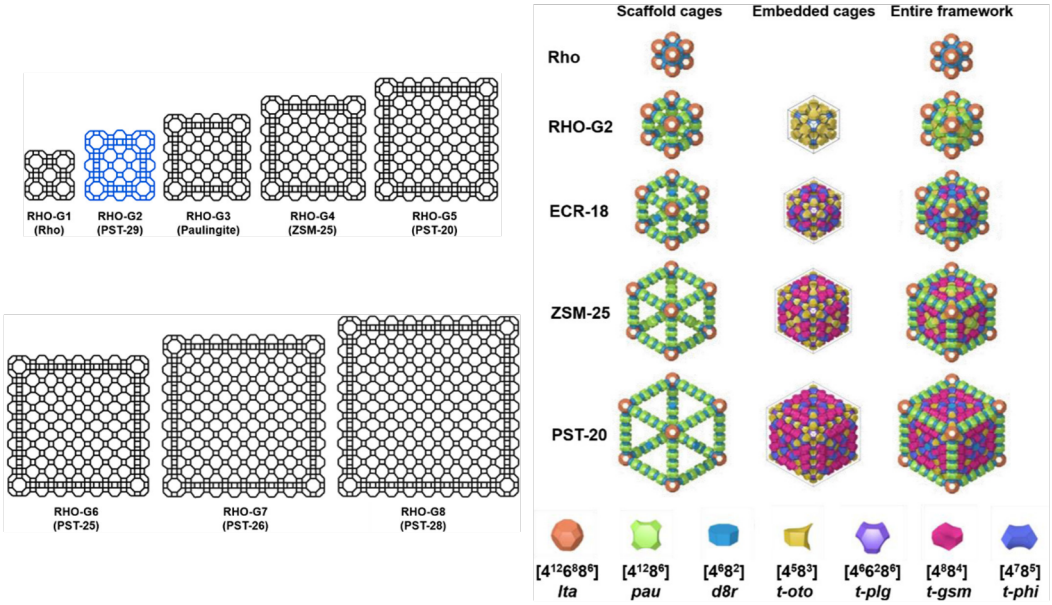

Figure 1.2. Frameworks of the **RHO** family of zeolites and tilings of some of its members. Reprinted with permission from references [73, 74]. Copyright 2017 and 2018 American Chemical Society.

building units. A good example for the applicability of the tiling method is the **RHO** family of zeolites, shown in Figure 1.2.

Zeolite ZSM-25 had first been reported at the beginning of the 1980s, although no structure could be determined at that time. Only with modern electron diffraction techniques and realising the structural similarity between this material and the known zeolites Rho (**RHO**) and paulingite (**PAU**), could its structure be determined.[75] With this knowledge and looking at the tiles present in these frameworks, further extension of this family to larger constructs as well as the synthesis of the missing intermediate between Rho and paulingite could be realised.[74,76]

1.2.2.2 Pore systems

Another important way to describe zeolites is using their pore channel system. The pore size is usually given by its ring size, i.e., how many T atoms are outlining it. The smallest ring size to be considered a pore is an 8-ring or 8MR (8-membered ring), referred to as

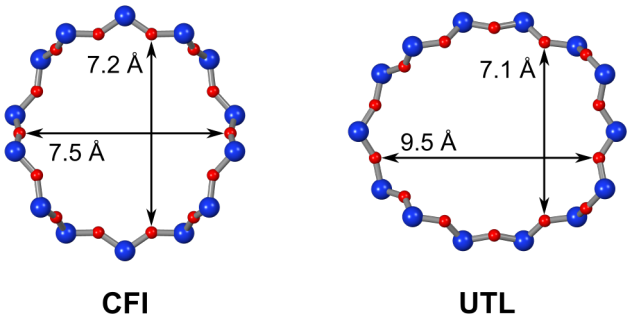

Figure 1.3. 14MR pores of zeolite frameworks **CFI** and **UTL** demonstrating the different possible dimensions for a pore of the same ring size. Silicon atoms are shown in blue, oxygen atoms in red. The distances are calculated using a van-der-Waals radius for oxygen of 1.35 Å.

small pore. 10MR are considered medium sized pores, 12MR large and every size above as extra-large. The shape of these pores is also important, giving an indication not only for the size of molecule to enter the zeolite but also their three-dimensional shape. For example the 14MR pore in zeolite IM-12 (**UTL**) has dimensions of 7.1×9.5 Å, whereas the 14MR in the **CFI** framework is almost circular with 7.2×7.5 Å, shown in Figure 1.3. These values are calculated using the van-der-Waals radius of oxygen (1.35 Å) to obtain values representative of available free space for diffusion of molecules.

These pore channels can occur in different directions in a zeolite framework and may or may not be interconnected. Depending on the desired application, a certain pore-system is preferable over another. For example, some processes benefit from a 1D pore system with only one specific type of pore with its size chosen so that only one type of molecule may pass through at a time. Several catalytic applications on the other hand favour multidimensional systems, where the diffusion and access to active sites within the pores is facilitated much more easily. Exemplarily, Figure 1.4 displays zeolite **CHA**, which has a three-dimensional pore system. **MOR** on the other hand, has two separate 1D pore channels, both along the *c* direction. Such knowledge about dimension and direction of pore channels is also of importance when designing materials for applications such as membranes, where it may be crucial to direct crystal growth in the appropriate direction.

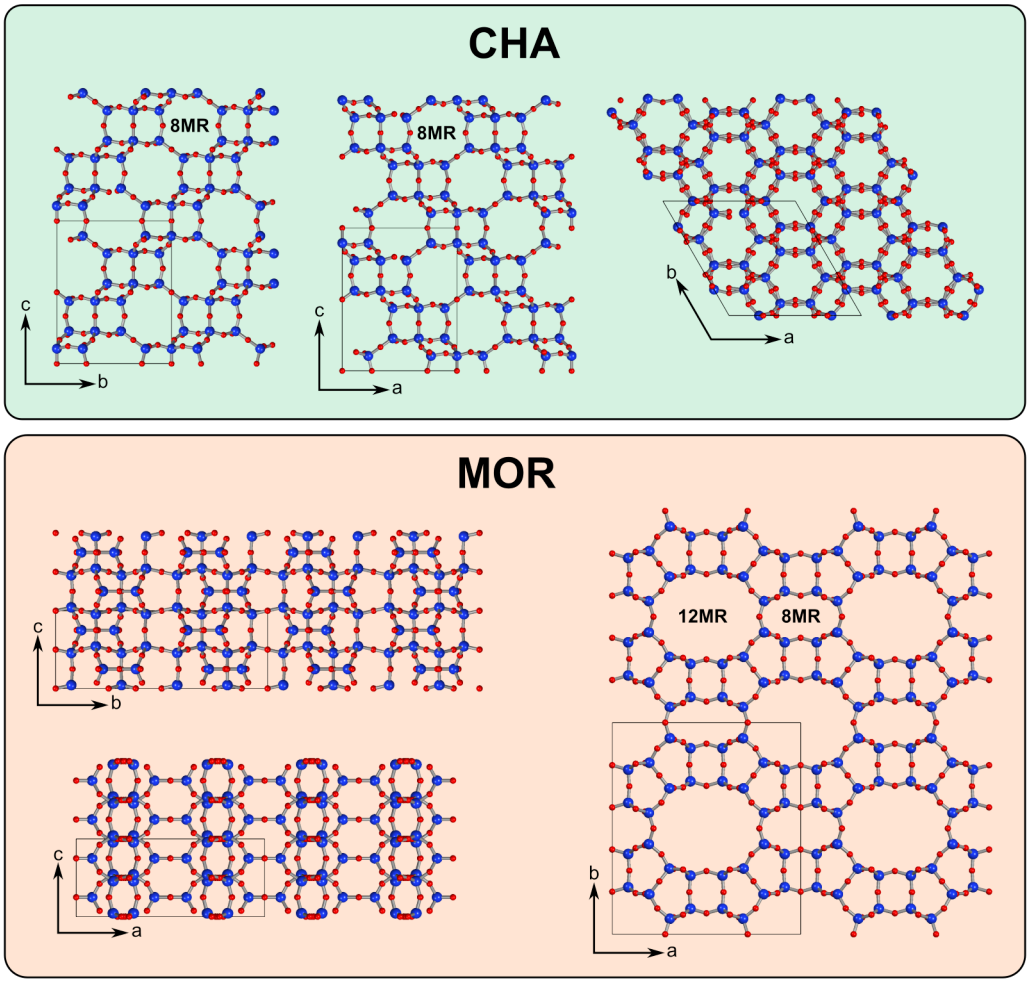

Figure 1.4. Framework of zeolites **CHA** and **MOR** shown along each of the three crystallographic axes. Drawings are produced from the corresponding CIF from the IZA database.[71]

1.2.2.3 Zeolite framework examples

Of the many possible frameworks, only the most relevant to this thesis are described in more detail below. A complete and comprehensive definition of these and all other frameworks can be found at the IZA (International Zeolite Association) database website.[71]

1.2.2.3.1 Framework UTL

The framework **UTL** was determined as structure for germanosilicate zeolites IM-12, discovered by Paillaud et al.[72] and ITQ-15 reported by Corma et al.,[77] both in 2004. Projections of the structure along each of the unit cell axes are displayed in Figure 1.5. The zeolite can be described by layers stacked along the *a* axis, connected by cubic *d4r* units. The layers themselves are built from *non* CBUs, forming chains along the *b* axis and connected to each other by their oxygen atoms and one more T atom to form

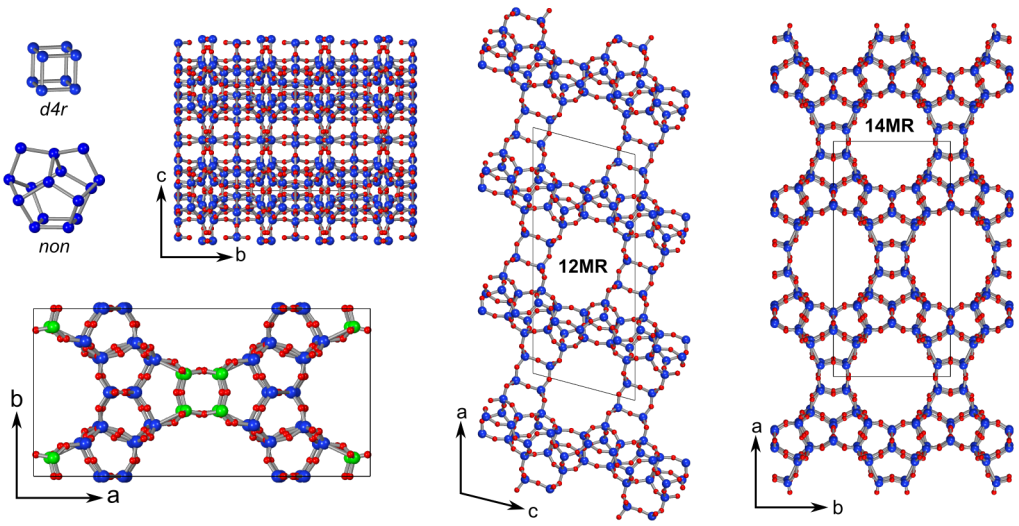

Figure 1.5. UTL framework shown along the three unit cell axes and a separate figure depicting the unit cell contents. Also shown are the two composite building units *d4r* and *non*, that make up the framework (only T atoms shown in blue). T atoms are shown in blue, oxygen atoms in red and T atoms in the *d4r* CBU highlighted in green in the single unit cell display. Drawings are produced from the corresponding CIF from the IZA database.[71]

the dense layers. The full set of possible CBUs is *mor*, *cas*, *fer*, *non*, *ton*, and *d4r*. The framework has a 2D pore system, with a 12MR channel along the *b* axis linked to a 14MR channel along the *c* axis. As can be seen in Figure 1.5, the two pore channels connect in the interlayer space and the layers themselves do not contain pores (compare projection along the *a* axis). As mentioned, IM-12 is obtained as germanosilicate and the germanium atoms are preferentially located in T positions in the *d4r* unit, highlighted in green in the unit cell depiction.[78] This feature has been exploited in the ADOR process (see section 1.2.3.8) to produce related the frameworks shown below.

1.2.2.3.2 Framework OKO

So far, no zeolite material with **OKO** framework has been made using traditional solvothermal synthesis, but exploiting the hydrolytic instability of the Ge−O bond, Verheyen et al. (material COK-14) and Roth et al. (material IPC-2) were able to chemically alter the layer-connecting species resulting in an overall more condensed zeolite (see section 1.2.3.8 below for details).[79–81] The difference between this framework and **UTL** is the unit connecting the dense layers with each other. Instead of the *d4r* seen in **UTL**, now only a square *s4r* (single-4-ring) unit (SBU) remains, whereas the layers themselves are unaltered. This is also reflected in the possible combination of CBUs describing the **OKO** framework: *mor*, *cas*, *fer*, *non*, and *ton*. Due to the decreased layer distance, the pore sizes are correspondingly decreased and **OKO** possesses a 12MR and a 10MR pore channel.

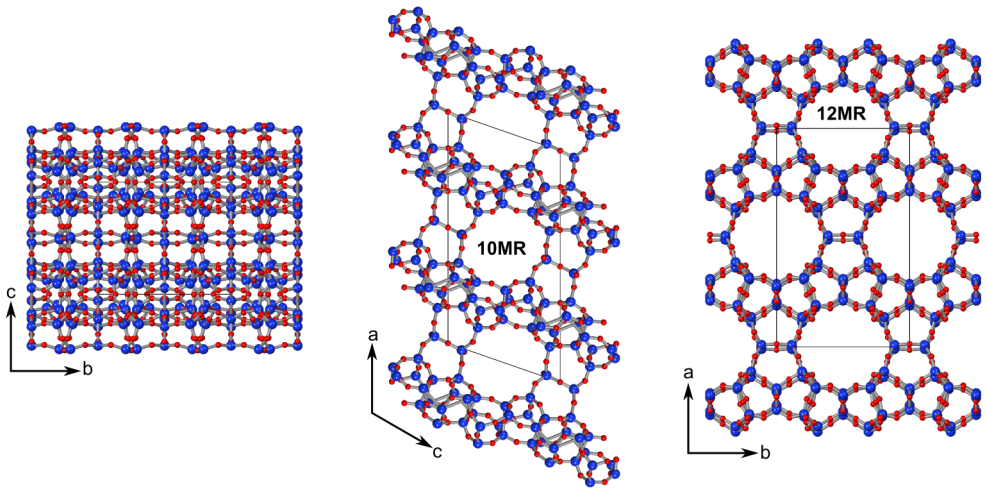

Figure 1.6. OKO framework shown along the three unit cell axes. T atoms are shown in blue, oxygen atoms in red. Drawings are produced from the corresponding CIF from the IZA database.[71]

1.2.2.3.3 Framework PCR

Similarly to the description for **OKO**, the framework **PCR** (material IPC-4[81]) shows the the same dense layers as **UTL**. In this case, however, they are only connected by single oxygen bridges as shown in Figure 1.7. This results in even smaller 10MR and 8MR pores parallel to the [001] and the [010] planes, respectively. Due to the absence of the quadratic faces of *s4r* or *d4r* units, the possible CBUs to describe the framework change slightly. Both *mor* and *ton*, consisting only of pentagonal faces, are still available, now complemented by *mtt*, *mso*, and the new CBU *pcr*.

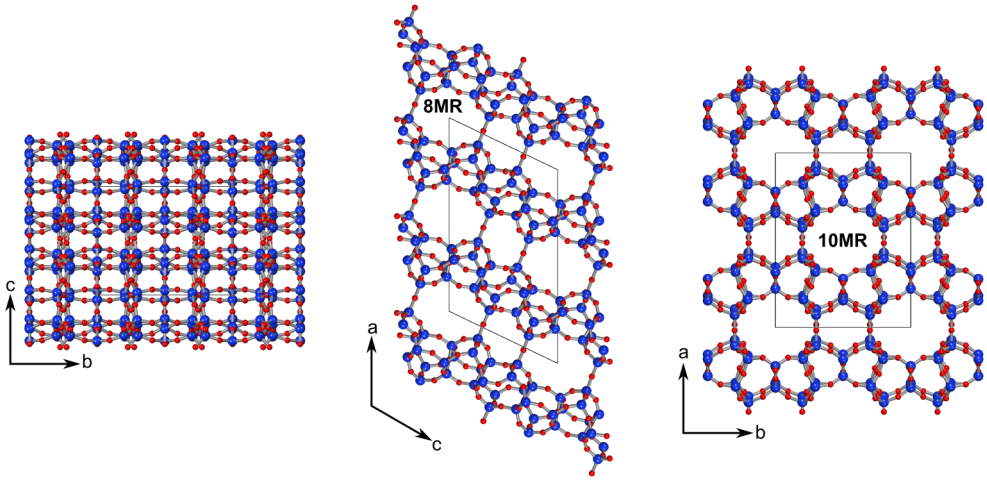

Figure 1.7. PCR framework shown along the three unit cell axes. T atoms are shown in blue, oxygen atoms in red. Drawings are produced from the corresponding CIF from the IZA database.[71]

1.2.2.3.4 Framework *PCS

The last member of the **UTL** derived frameworks to date is ***PCS**. It shows two different

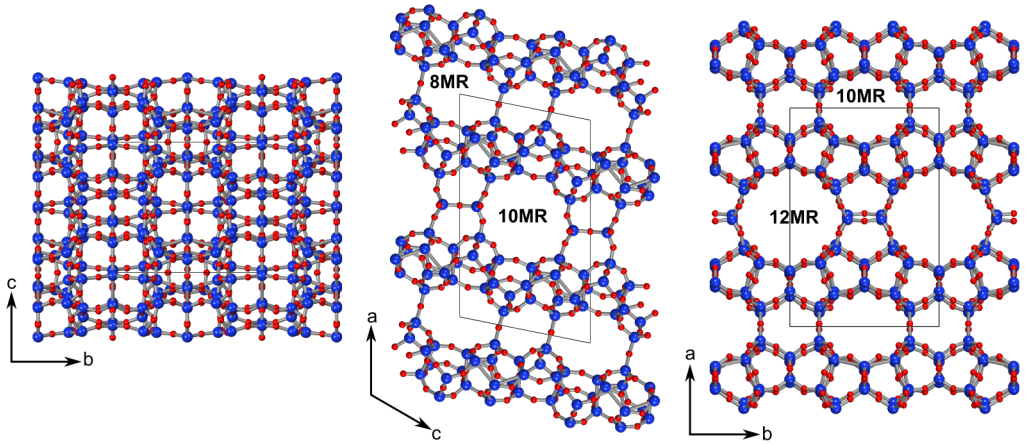

Figure 1.8. PCS framework shown along the three unit cell axes. T atoms are shown in blue, oxygen atoms in red. Drawings are produced from the corresponding CIF from the IZA database.[71]

connections of the layers, one with *s4r* units as in **OKO** and the second one with direct oxygen linkages as in **PCR**. As indicated with the prefixed asterisk, ***PCS** has intrinsic disorder in its layer stacking. The structural description is performed using an idealised stacking order, however, no material has been made with this exact layer sequence and the type material for this framework is the disordered zeolite IPC-6.[82] The strictly alternating layer connectivity between **OKO** and **PCR** linkages shown in Figure 1.8 serves as an example to show the possible pore channels. As can be assumed from comparison with the related frameworks above, two types of separated 2D pore systems exist in this framework. *d4r* linkages results in 12MR and 10MR pores, whereas oxygen connected layers show 10MR and 8MR pore channels. Due to the lack of intralayer porosity no passage is possible from one system into the other.

1.2.2.3.5 Framework ITH

The framework **ITH** is an example where several known materials exhibit this framework type. The type material is ITQ-13, a pure silica zeolite discovered by Corma's group.[83] The same structure can be obtained using a different synthesis route yielding IM-7,[84] as germanosilicate,[85] or aluminogermanosilicate,[86] amongst others. This structure has three pores along each of the unit cell axes (9MR, 10MR, and 10MR along *a*, *b*, and *c*, respectively), which are linked to form a 3D pore system. Once more, *d4r* units are present in this framework as well, but in this case they are located in all three dimensions.

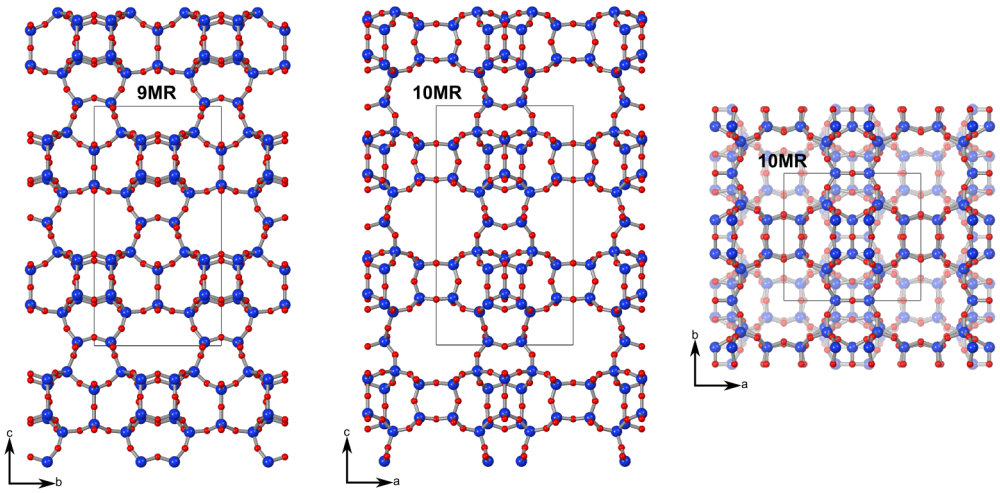

Figure 1.9. ITH framework shown along the three unit cell axes. T atoms are shown in blue, oxygen atoms in red. Drawings are produced from the corresponding CIF from the IZA database.[71]

1.2.3 Zeolite synthesis

Since zeolites occur naturally, the development of synthetic methods to reproduce these crystalline materials started with understanding the geological formation of the porous minerals.[87] Deposits rich in zeolite phases are mostly found in volcanic areas and in basins of former alkaline lakes. As such, it is by now accepted that these phases form in alkaline environments with typical pH values around 9–10. The basic conditions allow for dissolution of silicon and aluminium containing rock, enabling recrystallisation into a zeolite phase. Important factors for these reactions are also the temperature and pressure exerted onto the system. As described in section 1.2.2, zeolites are porous materials, thus, pressure has a profound impact on the structure of resulting phases. The nature and concentration of present alkali and earth alkali metal ions is also crucial and may favour one zeolite phases over another. This also hints at one of the biggest issues with zeolite formation, whether it being natural or synthetic, which is phase purity. Only rarely are samples found or made which contain only one single phase. One of the reasons is that during zeolite formation, one phase may act as precursor for another one and so several different zeolites may be present in a given sample. They are also often accompanied by impurity phases of dense crystalline solids like quartz or cristobalite as well as amorphous (alumino-)silicate glasses.

As described in section 1.2.1, the first synthetic zeolites were obtained by mimicking conditions in nature, using high temperatures and pressures to transform minerals into porous zeolites. Improvement was achieved by using prepared aqueous solutions of dissolved aluminosilicates, enabling employment of milder conditions around 100 °C

and requiring only autogenous pressure. This general synthesis method is referred to as hydrothermal synthesis. Knowledge obtained from these initial studies was complemented and adapted over the years and a general mechanism for the crystallisation of zeolite phases can be discerned.[88,89] A typical zeolite synthesis requires silica and alumina sources, as well as water, and organic and inorganic structure directing agents. The following sections provide a general introduction for the mechanism and influential parameters for hydrothermal synthesis of zeolites, by far the most widely used technique. Most of these topics are also applicable to alternative synthesis methods, the intricacies of which will be highlighted below. Practical aspects of hydrothermal synthesis and other synthetic methods are outlined in chapter 3.

1.2.3.1 Hydrothermal synthesis mechanism

Hydrothermal synthesis of zeolites is based on sol-gel chemistry, where reagents are dissolved in water and initially form a meta-stable, typically amorphous, loosely connected network of small building blocks which can eventually be transformed into a zeolite phase.[89,90] The smallest unit is the previously mentioned [TO_4] unit (T = Si, Ge, Al, ...). In order for the employed T atom containing chemicals (section 1.2.3.2) to react, they require dissolution by hydrolysis which is facilitated using mineralising agents (section 1.2.3.3). Typically, this is achieved under basic conditions, in the presence of hydroxyl ions (Equation 1). The formation of reactive intermediates in Equation 2 is followed by a condensation to produce the desired connectivity between monomeric species, shown in Equation 3 and Equation 4.[91,92]

$$O_3T{-}O{-}TO_3 + 2\,OH^- \rightleftharpoons 2\,O_3T{-}O^- + H_2O \quad [1]$$

$$O_3T{-}OH + OH^- \rightleftharpoons O_3T{-}O^- + H_2O \quad [2]$$

$$O_3T{-}O^- + HO{-}TO_3 \rightleftharpoons O_3T{-}O{-}TO_3 + OH^- \quad [3]$$

$$O_3T{-}OH + HO{-}TO_3 \rightleftharpoons O_3T{-}O{-}TO_3 + H_2O \quad [4]$$

The primary building blocks (monomeric unit) connect to form small oligomeric units, whose size and shape depend on parameters like nature of the T atom (Si, Al, Ge, ...), time, temperature, pH, and the presence of inorganic or organic additives in the mixture, all of which also dictate the rate of the above mentioned reactions. It is crucial to ensure homogeneity in the reaction system until all reagents have been added. This is especially true for reactions containing comparatively low amounts of water where the

mixture quickly transforms into a rigid gel. After the addition of chemicals has been completed, an ageing period may be required where now the formation of a stable gel may even be intended. This step can occur at room temperature but may also take place at elevated temperatures, depending on the targeted zeolite phase and is conducted to facilitate phase purity in most cases. The crystallisation of the zeolite then requires heating of the mixture at temperatures between 100–200 °C and typically autogenous pressure which is facilitated by using sealed autoclaves. The reaction times can vary a lot, taking only hours for some of the more stable and kinetically favoured phases but may also take up to weeks or even months. The important factors are the time it takes for nucleation to start, which is then followed by the crystal growth stage. During the induction period, the initially amorphous sol or gel transforms into a secondary amorphous phase, which shows some degree of ordering, albeit not yet a crystalline phase. From this point onwards, as soon as distinct nucleation commences, the amorphous material is gradually used up and a zeolite crystal grows. It is important to keep in mind that most zeolite phases are not the overall favoured thermodynamic product of these reactions and are considered meta-stable phases. This means that often very specific combinations of reaction mixture, time, and temperature are necessary to obtain the desired, pure material.

1.2.3.2 Choice of reagents

For a successful synthesis, suitable reagents containing the desired T atoms are required. Typical silicon sources include fumed, precipitated, and colloidal silica as SiO_2 or alkoxysilanes, most notably TEOS (tetraethoxysilane or tetraethyl orthosilicate). Depending on the targeted zeolite phase one reagent may be preferable over another. TEOS is considered free of contamination by other, potentially interfering T atom elements, however, requires breakdown of the alkoxy groups into silica intermediates and ethanol. The produced ethanol should also be removed entirely, sometimes requiring prolonged periods of stirring or even slightly elevated temperatures. Both treatments, however, may already have an influence on the mechanism by ageing processes and formation of specific oligomeric species or even beginning crystallisation of kinetically favoured phases (see section 1.2.3.1). Precipitated silica is probably the easiest reagent in terms of practical handling, but typically suffers from poor solubility due to a broad particle size range including comparatively large particles which may resist complete dissolution and can remain an amorphous impurity. Fumed silica on the other hand consists of

appreciably small particles, which has a main drawback of posing a safety hazard and requiring appropriate PPE for the researchers such as dust masks. Finally, alkali silicate solutions (mostly sodium silicate) are also a convenient silicon source, however, potentially require lowering the pH value as too high concentration of OH^- can result in failure of zeolite synthesis due to enhanced solubility of the silica species or crystallisation of only dense phases. Aluminium sources must be considered similarly, but sometimes the additional reagent remedies a drawback of a silica source. For example lowering of the pH value of the synthesis mixture can be achieved by employing an acidic Al salt such as aluminium sulfate or nitrate. Similarly, using TEOS may be less of a hindrance if a synthesis protocol specifically requires the use of an aluminium alkoxide (e.g. aluminium propoxide), since evaporation of the alcohol by-product needs to take place irrespective of the chosen silicon source. Depending on the targeted zeolite phase, one reagent will be preferable over another and their careful selection can determine success or failure of a synthesis attempt.

1.2.3.3 Mineralising agents

As briefly touched upon in the previous section, the dissolution of T atom precursors is a crucial first reaction step in the synthesis of zeolites. The most commonly used mineralising agent is the hydroxyl ion, present in alkaline aqueous solutions and essentially acting as a catalyst for the hydrolysis of the reagents. The kinetics for hydrolysis under alkaline conditions is directly correlated with the pH value of the solution. These basic regimes can be easily generated by use of alkali or earth alkali hydroxide solutions or when employing an organic structure directing agent (OSDA) in its hydroxide form. The effect of the respective cations on zeolite formation will be discussed below. One of the crucial factors for the success of the synthesis is the concentration of these alkaline solutions. A balance must be found between sufficient solubility of the T atom precursors, while still ensuring it is low enough for the condensation reaction to be proceeding at appreciable rates. The general pH range for zeolite syntheses is about 9–13, and heavily depends on the desired phase. Due to the kinetics of the Si−O and Al−O bond formation reactions at different pH values, different oligomeric species are present, both with respect to the number of involved T atoms as well as with the Si/Al ratio of these intermediates. A general trend can be made out for higher Si/Al content in the final zeolite to be favoured when the mixture has pH values at the lower end of the mentioned range. On the other hand, zeolites with Si/Al ratios close to one are often

obtained around pH 12–13 or even higher.[90,93]

The second used mineraliser is fluoride, which shows great potential for highly or purely siliceous zeolite phases.[94–96] This follows the trend described above since such compositions can have pH values even in the acidic regime. Under these neutral or slightly acidic conditions the solubility of silica in water would reach a minimum, however, the presence of fluoride facilitates a different dissolution pathway through the formation of silicon hexafluoride anion complexes. Employing fluoride ions in the synthesis mixture is also beneficial for the stability of the final, silicon-rich zeolites. When using organic cations as OSDAs, their charge is balanced by aluminium T atoms, which impose a negative charge on the framework. In absence of these charge-balancing element and under basic synthesis conditions, the framework would accommodate this by framework defects in the form of bare $Si-O^-$ groups. These sites are prone to induce framework collapse upon heating of the material to remove the organic species, thus making the zeolite unusable for applications involving their precious porosity. In the presence of fluoride ions, however, pentacoordinated O_4Si-F^- species are formed, providing a suitable counterion for the OSDA. As such, pure silica zeolites prepared using the fluoride route tend to be robust materials.

Many siliceous materials exhibiting frameworks previously only known as aluminosilicates could be prepared using this method, as well as a range of new frameworks. Furthermore, the presence of fluoride ions in the synthesis has a strong structure directing effect. The size of this anion is a near perfect match for the space inside a *d4r* unit, leading to preferential formation of frameworks featuring this CBU when following this synthesis route.[97–99] Another beneficial outcome of fluoride-based syntheses is the increased size of obtained crystalline materials, especially compared to the hydroxy-route. This has a positive effect for structure determination of novel phases, as these single crystals are usually large enough for single-crystal X-ray diffraction analysis. The major drawback of this method is the toxicity of hydrofluoric acid which is generally used as reagent. Solid fluoride reagents such as ammonium or alkali metal fluorides can be used instead, but they are still classified as hazardous chemicals and are therefore often also not considered for large scale production due to the associated safety concerns.

1.2.3.4 Organic structure directing agents, OSDAs

One of the major milestones in zeolite science was the discovery of organic molecules as organic structure directing agents (OSDA) in the synthesis of zeolites. Prior to this

development, such an effect was only exerted by the present small, inorganic cations, typically as part of the T atom reagent such as Na^+ in sodium silicate. Although these cations can effectively direct the formation of certain framework types, restrictions on the framework composition (Si/Al ratio), other synthesis parameters, and the number and complexity of available frameworks limits this approach. This changed with the first usage of tetramethylammonium hydroxide (TMA-OH) to facilitate the formation of several zeolite frameworks with higher Si/Al ratios as previously seen. This is possible due to the increased size of the cation and can be illustrated by comparing the directing effect and crystallographic siting of sodium ions and TMA in the *sod* cage.[100] A single TMA molecule fits into this CBU, whereas three sodium ions can be located within the polyhedron. This means that only one aluminium atom is required for charge balancing the organic cation, leading to an overall Si/Al ratio of 5 for a zeolite with **SOD** framework. In an organic-free synthesis the necessary three Al atoms per cage result in a Si/Al ratio of 1.

Building on this concept further, several different frameworks could be synthesised using TMA as the OSDA. However, many of these were only obtainable if sodium was present too. For example, the **LTA** framework, in which *sod* cages are connected to each other by *d4r*, is only afforded using both of these components. This was ascribed to the inability of the organic molecule to favour the formation of small CBUs such as *d4r*.[51,101] The fact that just one single OSDA can be used to produce several different framework is the reason why researchers have changed from the initially used term templating to the more appropriate “structure directing”. There are some cases where a specific organic compound indeed only induces the formation of one singular framework type by templating a unique cage-type for example. Generally speaking though, these molecules function as space fillers and are therefore only able to facilitate the crystallisation of generic features such as pore channels or pore windows within a certain size range.

The essentially unrestricted possibilities for the synthesis of organic compounds that can act as an OSDA opened up pathways for the formation of many new frameworks.[102] This is especially interesting with respect to accessible pore sizes, which can be facilitated by larger organic molecules.[103] This goes as far as enabling the formation of mesopores in addition to the framework intrinsic microporosity. Materials featuring pores in two (or even more) different regimes are called “hierarchical”.[104–106] The addition of such larger pores enables faster diffusion in and out of the crystal. This is important for example for catalytic applications, where the active site is often located inside the microporous

channels of the framework. Shortening the diffusion path length enables faster kinetics for the catalysis overall.

1.2.3.5 Composition of the reaction mixtures

Another important parameter in the synthesis of zeolite phases is the composition of the reaction mixture. A typical synthesis recipe is given as ratios of T atoms (typically in their oxide form irrespective of the used regent), water, possible inorganic cations such as sodium, OSDA, and fluoride for syntheses following this alternative route. For example, the batch composition for the synthesis of SSZ-13 **CHA** listed in the Verified Syntheses of Zeolitic Materials (based on Zones and Van Nordstrand[107]) requires 10 Na_2O : 2.5 Al_2O_3 : 100 SiO_2 : 4400 H_2O : 20 OSDA−OH, with N,N,N-trimethyl-1-adamantyl-ammonium hydroxide as the OSDA.[108] Following these guidelines, the resulting zeolite phase exhibits the **CHA** framework and has a framework composition of $[Al_{2.4}Si_{33.6}O_{72}]$, which translates to a Si/Al ratio of 14. Noteworthy is the discrepancy between this value and the Si/Al ratio of 80 in the synthesis gel. This is only a simple example demonstrating that the amounts of T atoms in the gel do not necessarily translate to the framework composition of the final material. One of the reasons is the higher solubility of silica compared to alumina, so that a higher percentage of present aluminium is incorporated in the framework. Additionally, the interplay between cations, OSDA, and Si/Al ratio results in the preferential formation of certain CBUs, which may accommodate a higher or lower number of aluminium atoms. This means that seemingly small changes to the batch composition can have wide-ranging impact on composition or even the structure of the product itself. Formation of zeolite X **FAU** with a product composition of Si/Al $\approx$ 1 can be achieved from a gel with 5.5 Na_2O : 1.65 K_2O : Al_2O_3 : 2.2 SiO_2 : 122 H_2O.[108] When Si/Al in the mixture is 2 or higher, a competing phase with **LTA** topology is produced. On the other hand, lowering the amount of water can lead to contamination with a zeolite exhibiting the **SOD** framework. These three frameworks are closely related, all containing the *sod* CBU. In the dense **SOD** framework, these cage units are connected directly, whereas in **LTA** a *d4r* acts as a spacer between two *sod* cages. Instead of this cubic CBU, the **FAU** framework features *d6r* CBUs as linkages.

1.2.3.6 Influence of heteroatoms

Chemical variety in the zeolite framework can be introduced by incorporating other elements that are viable in terms of possible tetrahedral coordination. Typical candidates

are elements of Group 13 and 14. The trivalent gallium and boron play a similar role as aluminium, inducing a negative charge on the framework, stabilised by cations, and their locations can be turned into Brønsted acid sites. Employing these other trivalent elements has an effect on the possible structural units and CBUs, which is caused by the respective bond lengths for Ga−O and B−O. This effect is observable in the absence of a gallosilicate material with **LTA** framework due to the heavily disfavoured formation of the crucial *d4r* units. The situation is slightly different when the base structure of the framework changes from a silica-based material to a gallophosphate, where this obstacle can be overcome due to the different bond length of the P−O bond and the correspondingly slightly altered angles in the framework.[58,109]

Boron can also be substituted into T atom positions in zeolite frameworks.[57,110] In such synthesis compositions, the boron content is generally required to be much higher than in the target composition of the final product, necessitated by the high solubility of boron reagents such as boric acid. The resulting borosilicate zeolites, sometimes referred to as boralites, are thermally less stable than either aluminosilicate or pure silica zeolites. During conventional calcination treatments to remove occluded OSDA molecules, boron is often removed from the framework which can lead to collapse of the structure. Nonetheless, the slightly different nature of boron with a shorter B−O bond can result in the formation of novel framework types, such as the recently described EMM-25.[111]

Similarly to the mentioned trivalent elements, the tetravalent germanium can also be isomorphically substituted into T atom positions. In this case, the heteroelement does not change the charge state of the framework. As discussed above, the positive charge from used OSDA cations is balanced either by defect sites in the framework or when using fluoride as mineraliser in the synthesis. Due to the similarity of Ge and Si, many frameworks previously known only as (alumino-)silicates can be made as (alumino-)germanosilicates. Although such a germanosilicate zeolite has been made already by Barrer in 1959,[59] studies utilising this element in the synthesis have only been taken up in the late 1990s and 2000s. In synthesis gels with germanium, the formation of small CBUs such as *d4r* is heavily favoured due to the Ge−O bond length which allows for smaller, unconstrained T−O−T angles.[78,85,112–117] This is most obvious when synthesising pure germanate zeolites with frameworks such as **AST** or **ASV** which are built from this cubic CBU, connected by [GeO_4] bridges.[118] The structure directing effect is enhanced by combining it with fluoride ions, effectively guaranteeing the presence

of this CBU. The downside of germanates is their susceptibility to hydrolysis in the presence of water. After removal of employed OSDAs by calcination, moisture in air is often enough to induce structural decomposition. Several of these structures can also be obtained as germanosilicates, which then allows for careful post-synthetic isomorphic substitution of germanium for silicon or even introduction of catalytically active acid sites by replacing Ge with Al or other trivalent elements. Such a treatment also enables careful adjustment of the overall acidity due to more precise tunability of the aluminium content in the final material.[119,120]

Next to the many new germanate structures, several germanosilicates exhibiting novel frameworks have been discovered in the last 30 years. The presence of the small *d4r* (and to a lesser degree *d3r*) units results in many of these frameworks possessing large and extra-large pores. An example is given above in Figure 1.5, showing the **UTL** framework discovered in 2004.[72] Again, such materials require substitution of germanium with silicon to improve stability for potential applications.[121] However, this inherent structural weakness of Ge containing zeolites can be exploited. Under carefully selected conditions, the structural collapse can be initiated and continued in a controlled manner, leading to an isolatable, crystalline intermediate zeolitic product.[79,80,122] The so obtained compound can be used as a precursor for the formation of a new zeolite material, which is structurally related to the original germanosilicate phase. This synthesis method is referred to as “ADOR process” and will be discussed in detail in section 1.2.3.8.

1.2.3.7 Alternative synthesis methods

Besides the traditional hydrothermal synthesis method, several alternative routes have been developed to produce zeolites.[123] A short overview of these is given in this section, whereas the most important methods with respect to this thesis, the “ADOR process” and the “solvent-free synthesis” will be discussed in the dedicated sections below.

In light of economical aspects for industrial use of zeolites, there is a trend to avoid OSDAs, as these are often the most expensive of the used reagents. Unfortunately, many materials are typically only obtained by employing organic additives which can aid in the formation of specific pore shapes and connectivity. Overcoming this issue, seed-assisted synthesis has seen great success in facilitating the synthesis of the desired zeolite phase in absence of an OSDA.[124–127] Crystals of the targeted phases are added to the initial synthesis gel together with all other reagents. The seeds can act directly as particles to grow large crystals from, but more often are dissolved due to the highly alkaline

conditions. The dissolution, however, progresses not necessarily all the way to primary building units but may conclude at semi-stable CBUs. These units are then reconnected in the same manner as in regular hydrothermal synthesis, while favouring the formation of the seed crystal phase. Due to the similarity of some frameworks it is also possible to obtain materials of distinct, but closely related frameworks.[128] This is why the method is sometimes referred to as inter-zeolite conversion (IZC), since the reaction conditions can be tuned to change the nature of the product phase.

It is also possible to change the synthesis medium from water to different organic solvents, then called solvothermal synthesis.[129] Employed solvents include alcohols such as glycerol, and amines like pyridine. In most of these reaction systems, some residual amount of water aids the hydrolysis reactions and may be considered a catalyst. Helping the dissolution of the reagents most protocols also require the presence of fluoride ions, typically in the form of hydrofluoric acid. The different physical properties such as increased viscosity of these organic solvents and thus reduced mobility of the precursor species can be beneficial in terms of crystal size of the products leading to large single crystals, optimal for structure determination by single-crystal X-ray diffraction. Furthermore, these solvents can also act as structure directing agents instead of or in addition to a dedicated OSDA additive. This concept is employed intentionally in "ionothermal synthesis", where an ionic liquid (IL) is employed as both solvent and structure directing agent.[130–132] ILs are salts of organic cations and often inorganic anions, with low melting points typically below 100 °C and negligible vapour pressure. For reported ionothermal syntheses, imidazolium halides and hydroxides are typically used. Several zeolites of different elemental composition such as pure silica,[133,134] germanosilicates,[135] and AlPOs and other metallophosphates[109,136–139] can be obtained using this method.

Besides these changes to used reagents, adaptions to the synthesis procedures themselves and the employed instrumentation have also been investigated. Microwave assisted reactions employ radiation instead of heat from conventional convection ovens.[130,140,141] This leads to faster reaction times, and usually high uniformity in particle size and elemental composition. Improvement in synthesis rates were also achieved by Okubo's group using a tubular reactor which also enables a continuous flow setup.[142] Pure phasic zeolites can be made in mere minutes due to fast heating at much higher temperatures up to 300 °C and applying several of the above mentioned beneficial methods such as pre-crystallisation ageing and seed crystals.

1.2.3.8 The ADOR synthesis for zeolites

Employing germanium in the synthesis of zeolite materials has led to a great number of new framework structures. However, the resulting materials are prone to structural collapse as the Ge−O bond is susceptible to be attacked by water even in low concentrations such as air moisture. Looking closer at the framework **UTL** and keeping in mind that Ge preferentially occupies T positions in *d4r* units, the observation was made that it can be viewed as comprised siliceous layers, connected by Ge-rich *d4r* CBUs. When choosing the correct conditions, the Ge−O bonds can be cleaved selectively, while the Si−O bonds remain stable. This concept has been realised in the ADOR process, which stands for **A**ssembly, **D**isassembly, **O**rganisation, **R**esassembly. Generally speaking it is a 3D-2D-3D zeolite transformation and its steps and mechanism are explained below.

The *assembly* step is the (conventional) synthesis of a germanosilicate zeolite material, featuring the mentioned structural weakness in the form of hydrolytically labile Ge−O bonds. The frequency and distribution of the germanium containing *d4r* units is important. Similarly, the dimensionality of the pore system can be an important factor for the stability of of the entire framework. The choice of an appropriate framework as parent material is crucial for the success of the ADOR procedure.

Exploiting the intrinsic structural weakness of the Ge−O bond through selective removal of the *d4r* unit is possible by exposure of the material to acid or water in a controlled manner. The ideal products of such a hydrolysis reaction are the completely disassembled layers, hence the name of the second step in the ADOR process *disassembly*. The layers themselves are self-stabilised to a certain extent by hydrogen bonding between silanol groups which are left behind on the surface of the layers where previously a connection to a *d4r* unit existed.

The subsequent *organisation* stage involves rearrangement of the layers with respect to each other, typically by intercalation of inorganic or organic reagents. Instead of a dedicated synthetic step this can also occur during the hydrolysis reaction, depending on the chosen conditions. In the final *reassembly* stage, the aligned silanol groups undergo a condensation reaction to form a fully connected 3D zeolite structure.

The ADOR process was designed and developed by Roth et al. using a germanosilicate zeolite of the **UTL** framework as parent material (see also section 1.2.2.3.1).[80,81,122] Using this example, the whole process is shown schematically in Figure 1.10. After successfully synthesising the zeolite material with **UTL** framework, the germanosilicate is disassembled into the intermediate, lamellar zeolite phase IPC-1P. To ensure ideal

layer stacking, the linear octylamine is employed to facilitate proper organisation of the layers with respect to each other. The final reassembly is conducted under conventional conditions for calcination, removing the organic compound and more importantly inducing the condensation reaction between the silanol groups. Under these conditions, the layers are connected by oxygen atoms and the final zeolite is called IPC-4, which was assigned the framework type code **PCR**.

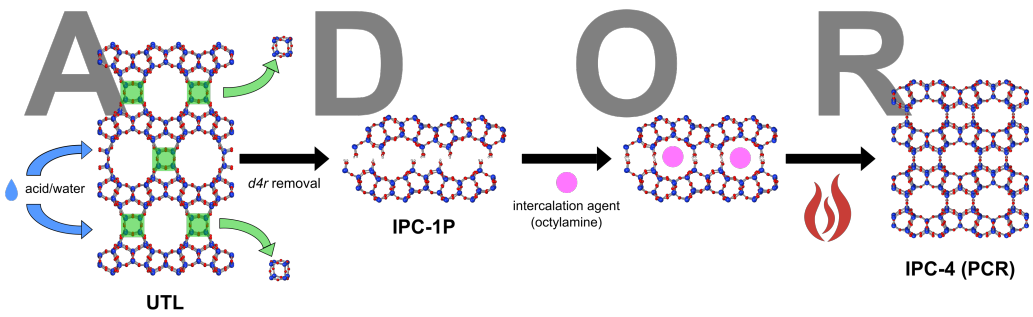

Figure 1.10. Schematic overview of the ADOR process using a zeolite with **UTL** framework as parent material.

All materials at the various stages of the ADOR process are structurally related to each other. They share the same *intra*-layer structure and differ in the *inter*-layer distance. This knowledge is used to track the progress by using powder X-ray diffraction (PXRD). The dominant peak in these PXRD patterns arises from diffraction corresponding to this interlayer spacing and its value can be calculated. The distance is largest for the parent material **UTL**, where the layers are separated by *d4r* units and shortest for **PCR**, where this linkage is reduced to single oxygen atoms.

Instead of a octylamine, which simply serves as a structure-directing agent, it is also possible to intercalate IPC-1P with the silicon containing reagent diethoxydimethoxysilane (DEDMS). The silylating agent interacts with the silanol groups in the interlayer space serving as a more rigid connection between adjacent layers. In the subsequent condensation, neighbouring methoxy groups of two former silane molecules condense, to form a square shaped *s4r* unit as linking unit between the layers. The obtained zeolite is called IPC-2 and exhibits the **OKO** framework.

As briefly alluded to earlier, it is also possible to combine the disassembly and organisation step in one synthetic procedure by increasing the concentration of hydrochloric acid[79,143] or prolonging the reaction time.[144] Both approaches aim to induce intercalation of silicon species from the parent zeolite itself. Although the Si−O bond is more stable than the Ge−O bond, it does break as well, given the right environment. Such acid catalysed bond cleavage is even intended when dissolving silica reagents using

the fluoride route in hydrothermal synthesis. Under highly acidic conditions the rate for re-condensation of the silicon-oxygen bond is also increased. When using water as hydrolysis reagent, the reconnection of layers commences given enough time. This is assumed to be thermodynamically and entropically favoured, reducing the number of species in the reaction system. The produced intermediate, which is structurally almost identical to the species obtained with DEDMS, is called IPC-2P to indicate the relation to its reassembled product IPC-2.

Investigating the effect of acidity, Wheatley et al. showed that adjusting the concentration of hydrochloric acid enables the formation of structures in between **PCR** and **OKO** as well as between **OKO** and **UTL**.[145] It was established that the re-intercalation of silicon is dependant on the employed acidity. As seen previously, high concentrations above 8 M lead to the formation of samples with **OKO** framework, whereas low acidity results in IPC-4 materials. Interestingly, the intermediate range showed a linear correlation between acid concentration and average interlayer spacing. Under such conditions, the bond making and breaking rates can settle at different equilibria, yielding interesting materials IPC-6 and IPC-7. These zeolites feature two types of layer connections, oxygen and *s4r* in IPC-6, and *s4r* and *d4r* in IPC-7, resulting in the combination of two pore systems. For IPC-6, a structural model was eventually developed and could be verified experimentally.[82] The two sets of layer connections are not strictly alternating, however, the same type of linkage is not found more than twice successively. Acknowledging the disorder in layer stacking of the synthesised materials, the assigned framework type code ***PCS** includes an asterisk indicating as much.

Expanding the possibilities of the ADOR method, Mazur et al. further experimented with intercalation chemistry on IPC-1P and successfully prepared two additional materials. Employing choline hydroxide as reagent in the organisation step induces a shift of the bare layers of IPC-1P with respect to each other.[146] In this configuration, the layers can be connected directly to produce IPC-9 (only oxygen bridges akin to **PCR**) or similarly to IPC-2 with *s4r* units leading to IPC-10. Due to the layer shift, the resulting pores are made from an odd number of T atoms, 7MR and 9MR for IPC-9 and IPC-10, respectively, which are rarely seen in zeolites. The framework energy in relation to the density of Si atoms is also higher than typically observed for zeolite materials and as such would be considered “unfeasible”. Being able to obtain materials of this nature with the ADOR method is an important step towards overcoming the possible barriers imposed by traditional hydrothermal synthesis of zeolites.

Besides using **UTL** as parent material, germanosilicates of several frameworks such as **IWW**, **UOV**, and ***CTH** have been used successfully in the ADOR process to produce new zeolite materials.[147–152] Recently, it was also shown that it is even possible to rebuild the **UTL** framework by adapting the hydrolysis conditions to employ alcoholic acid solutions, effectively decelerating this process so that the rate of re-intercalation becomes dominant.[153] Thus obtained materials still contain a considerable amount of germanium, which may be unfavourable depending on the application for such a material. This can be avoided by effectively reversing the ADOR process, demonstrated by Veselý et al., who employed tetrabutylammonium hydroxide (TBAOH) to expand the interlayer space of IPC-1P to the size of the *d4r* CBU. A subsequent treatment with silicon containing reagents allowed for a reconnection of the layers with the cubic CBU and the material with **UTL** framework can be considered germanium free.[154]

The ADOR process has great potential as a method to obtain and discover new materials and zeolite frameworks, especially since the products can be rationalised and designed prior to experiments. The possibility to tune and choose the pore size of the obtained daughter materials has great value for a range of applications. In view of such potential industrial use, however, there are still several drawbacks to be considered. The main concern is the requirement for a germanosilicate as the parent material. Germanium reagents are costly, thus typically not considered in industrially used zeolites. It is conceivable that the ADOR process may work with some other, cheaper zeolitic metallo-silicate, however, this has not been shown so far. Some relief for this situation comes from a study by Zhang et al., where it was shown that it is possible to recover the germanium species which are removed during the hydrolysis of parent germanosilicate.[155] This recovered solid can be used as reagent for successive synthesis of the parent material and so the contribute to an overall cost reduction of thus prepared zeolite materials. Nonetheless, there is still room for improvement in terms of sustainability with respect to the practical aspects of the treatment, especially the hydrolysis. These aspects are the focus of chapter 4.

1.2.4 Mechanochemistry in zeolite science

The renewed interest in mechanochemistry in recent years has also led to several research groups in the field of zeolites to adopt such methods. The success of employing mechanical forces for synthesis of porous MOFs and ZIFs can be seen as indicatory that it may be similarly applicable for zeolites. Initial studies of mechanochemistry in zeolite

science have been reviewed by Majano et al. in 2014.[33] The current possibilities and advances in this respect have been reviewed as part of this PhD project and have recently been published.[34] A somewhat briefer account of this perspective is given here.

In general, mechanochemistry can be employed prior to the crystallisation step to form a zeolite or post-synthetically. So far, true mechanosynthesis where a zeolite is obtained directly after treatment using mechanical forces still proves elusive. Only one report from the early 2000s exists where the PXRD pattern of the milled product shows peaks suggestive of zeolite NaA, however, of rather poor crystallinity and indicative of a highly defective structure.[156] The sample was also calcined, resulting in conversion of some residual starting reagents. The system was further studied to include inexpensive starting materials like metakaolin.[157–160]

1.2.4.1 Solvent-free synthesis of zeolites

The concept of mechanochemically treating raw materials prior to crystallisation has led to one of the most recent additions to the repertoire of synthetic methods for zeolite synthesis. The so-called solvent-free synthesis was developed by Xiao's group and is based on the idea that instead of dissolving the reagents in water, the solid raw materials are ground or milled together in order to transform them into an state from which crystallisation can commence.[161–164] The formation of a zeolite phase then occurs under similar conditions as in regular hydrothermal synthesis, using temperatures between 150–200 °C and employing autoclaves to facilitate autogenous pressure. As the name promises, no solvent is required for this type of synthesis, however, some water appears to be necessary to catalyse the reactions. This is similar to what has been reported for ionothermal synthesis. Also important to note is that the basic conditions typically seen in zeolite synthesis are established by the use of an additional ammonium halide reagent. Ammonium chloride or fluoride are used in the synthesis to obtain materials with common frameworks like **MFI** or **MOR**. A plausible reaction mechanism could be established by rationalising the effect of this salt additive.[161,165–168] The ammonium ion reacts with residual water present in the starting materials, forming ammonia which can result in localised areas with alkaline character. This enables easier Si−O bond breaking and making and so a zeolite can eventually form.

From the original publication by Ren et al. in 2012[169] until today, zeolites of many different frameworks and with varying elemental composition have been made. This ranges from traditional aluminosilicates to purely siliceous ones,[170–175] several heteroa-

tom zeolites,[176–179] and even includes AlPOs[180–182] and SAPOs.[183,184] A comprehensive review of the methodology and a collection of obtained materials is given in recent reviews.[161–164]

Besides conventional parameters in the synthesis of zeolites such as reagent ratios, the specifics of the mechanical treatment have a great influence on the product formation. Several studies have shown that insufficient energy, for example when using manual grinding, may not result in the formation of any zeolite phase, whereas the higher impact in ball mills is sufficient for the activation of the reagents to induce crystallisation upon heating.[166,185] Similarly to hydrothermal synthesis, the choice of appropriate reagents is also crucial in solvent-free synthesis. For example using aluminium sulfate as aluminium source requires significantly more milling time compared to aluminium hydroxide.[168]

The main advantages of this type of synthesis are the drastic reduction in waste since there is no solvent required for the reaction. Additionally, an increased yield per volume unit of reaction vessel can be achieved. In conventional hydrothermal syntheses most of the volume is taken up by the solvent, whereas in the solvent-free method, essentially all present reagents are transformed into the final zeolite framework, with possibly an OSDA present in the framework. This leads to another advantage of the used protocols. OSDAs do not need to be present in the hydroxide forms but can be used in their halide forms, which they are typically synthesised in. This, in turn, makes it possible to use higher temperatures than typically possible when using the less stable hydroxide OSDA compounds. The increased heat as well as the type of reaction result in decreased synthesis time for these zeolite phases, reducing it to only hours in many cases instead of days or even weeks.

1.2.4.2 Mechanochemical activation of seed crystals

As mentioned above, using seed crystals exhibiting the same (or a similar) framework as the target zeolite can be a useful way to steer the crystallisation in the desired direction. This adaption to the standard hydrothermal synthesis can also be augmented by mechanochemistry, treating these seed crystals in a mill prior to their use.

One of the earliest reports of a mechanochemical method for zeolites was contributed by Valtchev et al. The authors used the described protocol of milling seed crystals in the synthesis of zeolite Y (**FAU**), reducing the crystallisation time by a factor of almost 10.[186] The seeds were milled directly in the synthesis gel to ensure homogeneity for the subsequent hydrothermal synthesis. A shortened synthesis time was also observed for

ball milled seeds towards zeolite **DDR**, used in membranes for gas separation.[187,188] The benefits of using seed crystals in conventional hydrothermal zeolite syntheses also apply when the seeds are milled before adding them to a reaction mixture. Most importantly, this means that zeolites can be made OSDA-free, by using seeds to facilitate formation of the desired framework and avoid impurity phases.[189,190]

One of the studies involving seed crystals has shed some light on possible underlying causes for the improved reactivity of the milled seeds. Zhang et al. were able to show that such a treatment leads to the formation of oxygen radicals on these crystals, effectively serving as active sites for chemical reactions.[191,192] The concept of radical assisted crystallisation has been shown to accelerate the formation in solution-based syntheses just a few years prior, where radical starter reagents or UV light were necessary.[193]

1.2.4.3 Heteroatom zeolites from mechanochemistry

Zeolites not only serve as shape- and size-selectors due to their frameworks, but can also be tailored with respect to their chemical composition. Incorporating heteroatoms into the framework can alter acid strength of Brønsted acid sites, add Lewis acidity, or make particular catalytic processes possible. An example for the latter are titanosilicates which can be used to facilitate epoxidation reactions.[194] Producing titanium containing zeolites using hydrothermal methods is usually only possible using expensive titanium alkoxides. Several groups, however, where successful in using ball milling as pre-synthesis treatment to enable use of cheap TiO_2. The oxide is treated together with silica to form a mixed metal oxide precursor, which can then be used in regular hydrothermal synthesis. When titania is used directly, it is rarely incorporated into the zeolite framework and remains as a secondary, impurity phase. In contrast, employing the ball milled precursor results in the formation of an active titanosilicate zeolite catalyst with **MFI** and ***BEA** frameworks.[195–198] Utilising this approach, further potential cost reduction can be achieved using the bromide salt of the required tetrapropylammonium OSDA, which is otherwise used in its hydroxide form.[199,200]

Since these promising results for titanosilicates, using this mixed metal oxide approach, several other elements were incorporated into zeolite frameworks in a similar manner. Generation of Lewis acidity is possible in stannosilicates[201,202] and a zincosilicate has been prepared in this way showing improved ion exchange capacity.[203] Extension to **MFI** zeolites with gallium or iron has been reported as well, demonstrating the versatility of the approach.[204,205]

Instead of adding the desired heteroelement to the synthesis, it is also possible to perform the incorporation post-synthetically. This can be accomplished by selectively removing aluminium from the framework using an acid treatment. The created empty T sites in the structure can then be filled with an appropriate cation. Instead of performing this incorporation in solution, Hammond et al. demonstrated that this is also possible using tin acetate as solid reagent and performing the reaction in a ball mill.[206,207] Further investigation of the process was done by Schüth's group, who showed once more that the choice of reagent is crucial to the success of the reaction.[208]

These examples of heteroatom zeolites showcase the great potential of mechanochemistry for zeolites, overcoming bottlenecks in traditional, hydrothermal synthesis. Employing ball milling techniques enables fast and cost-efficient production of materials with properties on par or even better than conventionally synthesised ones. This has wide-reaching implications since the incorporation of heteroatoms is often what transforms a zeolite into a viable functional material.

1.2.4.4 Mechanochemically assisted recrystallisation

Adjusting zeolite synthesis parameters so that the product material exhibits appreciable size and uniform size distribution can prove rather difficult. This material property, however, can be vital for its performance, influencing diffusion and thus reaction rates in many typical zeolite applications like catalysis or separation.[209,210] Using mechanical forces to break down a material into particles of smaller size is one of the main applications of mills. The energy of such a milling process, however, often leads not only to the desired physical change but also induces chemical changes such as partial amorphisation, which is typically an unwanted side-effect. This amorphisation was investigated by Zielinski et al.,[211] as well as Kosanović and co-workers who published a series of papers investigating influential parameters of this process.[212–216] For example, the amorphisation is slowed down when OSDA molecules are still present in the framework of the zeolite, stabilising the structure. Other parameters are the nature of the framework itself, size of inorganic cations, and elemental composition of the material.

The crystallinity of such amorphised particles can be restored by a recrystallisation, however, if performed in an uncontrolled manner would lead to simultaneous crystal growth, reversing the effect of the milling. By carefully adjusting the conditions of this recrystallisation, Okubo's group was successful in retaining the desired small particle size by using dilute aluminosilicate solutions as reaction medium.[217–221] This milling

and subsequent recovery of crystallinity is also possible in one step. However, it requires adaption to the milling vessels to withstand the highly alkaline conditions of the employed aqueous solutions.[222] This recrystallisation procedure was further extended to the above mentioned ultrafast synthesis method using a tubular reactor.[223–226] Several industrially important zeolites such as **CHA** were successfully synthesised in much decreased synthesis times of only minutes using this specialised reaction system.

There are many applications for mechanochemical methods in zeolite science, several of which have already shown great potential for overcoming obstacles using traditionally used methods. Noteworthy are especially the solvent-free methodology as well as techniques to incorporate heteroatoms into zeolite frameworks. Improving synthesis conditions and enabling use of cheaper, more widely available reagents is a great advantage and further investigation into underlying mechanisms should enable further generalisation of the published methods.

1.3 Coordination polymers

Coordination polymers (CPs) are a class of materials featuring organic ligands which coordinate to metal centres. The structure of these materials can be chain-like (1D), two-dimensional sheets, or 3D frameworks. If the formed structure has accessible pores and voids, akin to above described zeolites, the term metal-organic framework (MOF) is used.[227] Most of the current literature in this general field is focused on MOFs, which are typically based on transition metals. Alkali metal coordination polymers are often non-porous and thus can seldom be classified as MOFs.[228,229] The framework connectivity, however, is essentially identical in both CPs and MOFs. The metal cation, or more rarely the metal in its zero-valence state, serves as a node, connected to another metal by the organic molecule. Instead of a single metal ion (or atom) this can also be a metal-oxide cluster. The number of linkers per node depends on the coordination number of the metal or cluster. Likewise, the number of coordinating groups within each of the organic molecules can vary, but must be at least two, else no extended framework would be possible.

Two exemplary frameworks are shown in Figure 1.11, both built with benzenedicarboxylic acid (terephthalic acid, BDC) as linker. If the metal is the monovalent sodium, metal oxide chains are formed, which are connected to each other by the BDC molecule (Figure 1.11a). In contrast, divalent zinc forms distinct octahedral oxide clusters, so that

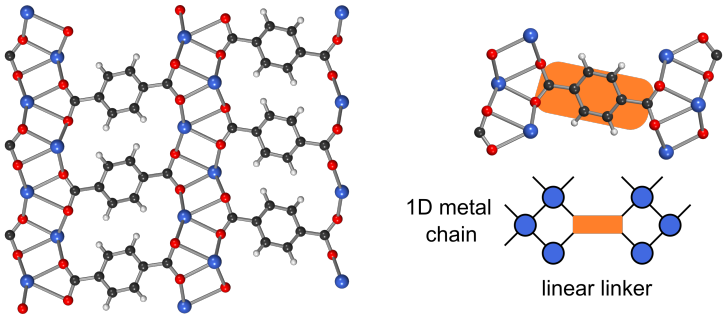

a) Structure and connection of metal and organic linker for the coordination polymer sodium terephthalate (CCDC code QQQDHD01)[230]

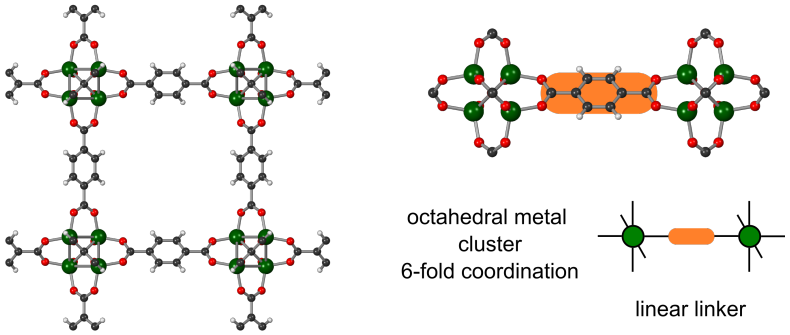

b) Structure and connection of metal cluster and organic linker for the metal-organic framework MOF-5 (CCDC code MIBQAR).[231]

Figure 1.11. Representative structures for a coordination polymer and a metal-organic framework. Oxygen atoms are shown in red, carbon in black, hydrogen in white, sodium in blue, and zinc in green. Drawings are produced from the corresponding CIF from the CCDC (Cambridge Crystallographic Data Centre) database and respective deposition codes are stated.

each cluster connects to six other clusters through bridging dicarboxylates (Figure 1.11b). This leads to the aforementioned porosity seen in MOFs. The most commonly used organic linkers are carboxylic acids, but in principle any functional group that can coordinate to a metal centre can be used. Imidazoles, for example, even make up their own subgroup called zeolitic imidazolate frameworks (ZIFs), due to their structural resemblance to zeolite frameworks, owing to the metal-imidazole-metal angle of 145°.

Coordination compounds are being explored in a diverse range of applications.[232] The mentioned available surface area and tunable pore size of MOFs can be utilised for catalysis and separation applications.[233–235] The accessible void space can also be used to store molecules long term but also host them as guest molecules which can be released on demand useful for example as drug delivery system in the biomedical sector.[37,236] A very promising application of the property to host guest molecules is harvesting of water from air, a possible solution for looming issues regarding supply of clean water in several regions around the globe.[237] Utilisation of MOFs and also more generally CPs has been expanded into the important field of electrical energy storage, more specifically as active

materials in rechargeable alkali metal ion batteries.[238–243]

1.3.1 Synthesis of coordination polymers

CPs are typically synthesised using solution-based syntheses either under ambient pressure conditions or employing autogenous pressures in solvothermal syntheses. The metal salt and the organic linker are dissolved in an appropriate solvent and reacted typically for several hours up to a few days, often at elevated temperatures. Depending on the specific system, modulating agents and additives to adjust parameters such as the pH of the solution can be added. Although these synthesis methods are widely used and are robust techniques for the synthesis of a myriad of new materials, several concerns about the economical and ecological feasibility of this approach have been raised. The main issues are the nature of the used reagents as well as the large amounts of solvent, which are often even toxic like DMF (N,N′-dimethylformamide) or DMAc (N,N′-dimethylacetamide).

Several alternative ways for the synthesis of CPs and MOFs have been developed over the last decades.[244] Microwave based syntheses are an acknowledged way to improve reaction rates, leading to higher efficiency and thus lower impact in terms of resource and cost.[245–247] Arguably even more promising are mechanochemical methods, which require no solvent at all. This re-emerging technology relies on energy input through mechanical forces showing great promise to overcome many issues encountered with modern CP and MOF synthesis both from a sustainability point of view, but also in view of potential industrial scale production.[29,248–253]

In the mechanochemical synthesis approach on a laboratory scale, the solid reagents are typically reacted using ball mills, facilitating energy sufficiently high to induce the chemical reaction.[249,254] In many cases it is beneficial to add a small amount of a salt to improve reactivity or minute volumes of liquid to increase mobility of the particles and potentially catalysing the transformation. These adaptions are referred to as ion- and liquid-assisted grinding (ILAG and LAG), respectively.[255] A very important additional benefit of these mechanochemical reactions is the possibility to employ cheap metal precursors, which are unsuitable for conventional syntheses due to their low solubility. These include metal oxides such as ZnO for the synthesis of Zn-MOF-74,[256] or $Cu(OH)_2$ in the case of HKUST-1.[257]

Investigation into the mechanism behind this synthesis technique to produce coordination compounds have been conducted employing a series of *in situ* techniques,

especially powder X-ray diffraction (PXRD). Utilising the high resolution available at synchrotrons, the teams around Friščić and Užarević were able to demonstrate the rapid transformation of solid starting materials into the respective MOF phases on several examples.[256,258–262] These studies also provided further insight into the effects of liquid additives where for example the MOF material HKUST-1 was formed either directly or by way of crystalline intermediates.[257] An intermediate phase was also revealed in the mechanochemical reaction towards MOF-74 (also known as CPO-27).[256] The starting materials ZnO and 2,5-dhtp (2,5-dihydroxyterephthalic acid) form initially a coordination polymer with one equivalent of zinc. Employing a second equivalent of the metal source, the reaction proceeds further to form the porous MOF compound. This knowledge about the mechanism could be utilised to produce a range of different mixed metal MOFs exhibiting the MOF-74 framework.[263]

1.3.2 Coordination polymers for sodium ion batteries

Rechargeable batteries are one of the most important technologies in today's energy industry. They are the core piece of mobile electronic devices which modern society is heavily reliant on. Dependent on the specific application, different battery types are more suited than others. Influential factors for which battery technology is most appropriate for a given application are the required electrical energy as well as aspects such as safety and cost of the device. One of the most common types of battery is the lead/acid battery used in cars. Both electrodes contain lead as the active material, making use of the three possible valence states Pb^0, Pb^{II}, and Pb^{IV}. An aqueous sulfuric acid solution is used as electrolyte so that the electrochemical reactions are:

$$PbO_2 + 2\,e^- + SO_4^{2-} + 4\,H^+ \rightleftharpoons 2\,PbSO_4 + 2\,H_2O \qquad \text{anode} \qquad [5]$$

$$Pb + SO_4^{2-} \rightleftharpoons PbSO_4 + 2\,e^- \qquad \text{cathode} \qquad [6]$$

$$Pb + PbO_2 + 2\,H_2SO_4 \rightleftharpoons 2\,PbSO_4 + 2\,H_2O \qquad \text{overall} \qquad [7]$$

Important is that these reactions need to be reversible for a functioning rechargeable battery. The forward reactions occur during discharge, when electrical energy needs to be supplied, for example when starting a car. During driving the car, the battery is (re-)charged and the backward reactions take place. However, using chemicals like sulfuric acid is not always practical and represents a potential safety hazard, thus alternatives have been developed. One of these are nickel based, which are the heart of current

hybrid vehicles in the form of Ni/metal hydride batteries.

Using a different approach, alkali metal ion batteries (AMIB) have been established over the last decades as one of the most important types of batteries, mainly in the form of the lithium ion battery (LIB).[264] Although LIBs are today by far the most common type of AMIB, drawbacks like long term availability of raw materials call for viable alternatives. The closely related sodium ion batteries (NIBs) may be able to replace lithium analogues at least in some applications.[265,266] The basic principle behind these ion batteries is the same for all alkali metals. The technology revolves around the reversible exchange of alkali metal ions and electrons using redox reactions. A schematic representation of a single cell in an AMIB is shown in Figure 1.12. Electrical energy is stored in the battery during the charging process, which later on can be used to power a device during the discharge phase. In rechargeable batteries, these processes need to be reversible to a high degree for a long time and many charge-discharge cycles.

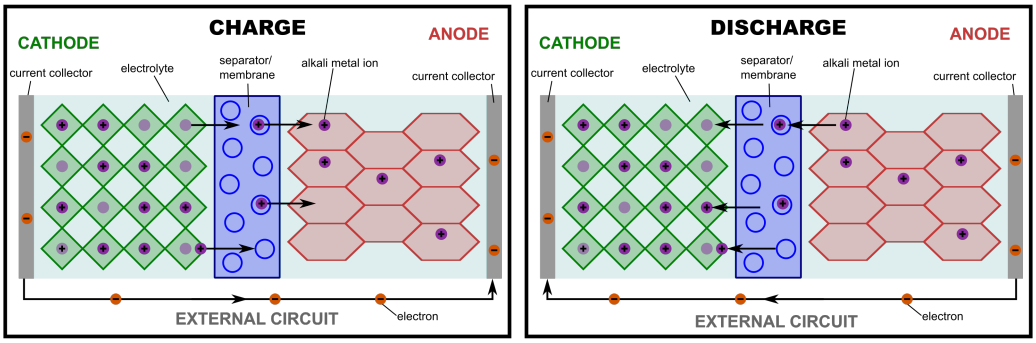

Figure 1.12. Schematic representation of the charge and discharge process in an alkali metal ion battery.

During charging, the electrons move from cathode to anode through the external circuit, facilitated by an oxidation in the active material on the cathode side. The resulting positive charge is balanced by moving alkali metal ions through a separator to the active material on the anode. There, they are intercalated into the active material and once more serve as charge balance for the surplus of electrons on this electrode. When electricity is to be supplied, this entire process is reversed and the cations diffuse back to the cathode material. Exemplarily, the redox reactions for a cell using a graphite anode and $LiCoO_2$ as cathode are shown below:

$$LiC_6 \rightleftharpoons C_6 + Li^+ + e^- \qquad \text{anode} \qquad [8]$$

$$CoO_2 + e^- + Li^+ \rightleftharpoons LiCoO_2 \qquad \text{cathode} \qquad [9]$$

$$LiC_6 + CoO_2 \rightleftharpoons C_6 + LiCoO_2 \qquad \text{overall} \qquad [10]$$

Although switching from electrode materials for LIBs to SIBs may seem like a straight forward process, several issues are encountered. For LIB anodes, graphite is the common standard, but this material is inapplicable for sodium due to disfavoured insertion of Na^+ ions, caused by the ion's size. Employed cathode materials are often transition metal oxides such as $LiCoO_2$ which come with similar concerns as lithium regarding abundance of metal deposits as well as safety issues, especially true for cobalt.

Finding alternative active electrode materials is one of the key challenges in current NIB research. Coordination polymers can be an attractive option for both cathodes and anodes, depending on the functional groups on the organic linkers. In either case they can accommodate insertion of ions very well and don't suffer from structural expansion upon ion insertion like many oxide materials. The redox reactions occur on the functional groups of the organic molecule such as carbonyl, azo, or imide groups. Depending on the nature of these groups, they can be capable of taking up electrons and are therefore called *n-type*. If the functional group can carry a positive charge, it is referred to as *p-type*. When both types of functional groups are present in a compound, it is considered bipolar or *b-type*, potentially applicable as both anode and cathode material.

Recent years have seen promising applications of sodium coordination compounds as electrode materials in NIBs.[242,267–269] Mostly, these are sodium carboxylates employing a variety of organic compounds. Although such organic materials have typically lower raw electrochemical performance compared to inorganics, their advantages have the potential to outweigh these drawbacks. The production of organic materials is usually more economical compared to traditional electrode materials such as oxides. The organic component can also be sourced from biomass, beneficial in view of sustainable fabrication of such materials.[270–272]

1.4 References

(1) P. T. Anastas and J. C. Warner, *Green Chemistry: Theory and Practice*, Oxford University Press, 2000, p. 135.

(2) C. Espro and D. Rodríguez-Padrón, *Curr. Opin. Green Sustain. Chem.*, 2021, **30**, 100478.

(3) H. C. Erythropel, J. B. Zimmerman, T. M. de Winter, L. Petitjean, F. Melnikov, C. H. Lam, A. W. Lounsbury, K. E. Mellor, N. Z. Janković, Q. Tu, L. N. Pincus, M. M. Falinski, W. Shi, P. Coish, D. L. Plata and P. T. Anastas, *Green Chem.*, 2018, **20**, 1929–1961.

(4) S. L. James, C. J. Adams, C. Bolm, D. Braga, P. Collier, T. Friščić, F. Grepioni, K. D. M. Harris, G. Hyett, W. Jones, A. Krebs, J. Mack, L. Maini, A. G. Orpen, I. P. Parkin, W. C. Shearouse, J. W. Steed and D. C. Waddell, *Chem. Soc. Rev.*, 2012, **41**, 413–447.

(5) K. J. Ardila-Fierro and J. G. Hernández, *ChemSusChem*, 2021, **14**, 2145–2162.

(6) M. Faraday, *Q. J. Sci., Lit., Arts*, 1820, **8**, 374–376.

(7) M. C. Lea, *London, Edinburgh, Dublin Philos. Mag. J. Sci.*, 1893, **34**, 46–50.

(8) W. Ostwald and C. Drucker, *Die chemische Literatur und die Organisation der Wissenschaft*, Akad. Verlag. Gesel., Leipzig, 1919.

(9) L. Takacs, *Chem. Soc. Rev.*, 2013, **42**, 7649.

(10) L. Takacs, *J. Mater. Sci.*, 2018, **53**, 13324–13330.

(11) F. Lechner, in *Reactive Extrusion*, Wiley-VCH Verlag GmbH & Co. KGaA, Weinheim, Germany, 2017, pp. 11–35.

(12) D. E. Crawford and J. Casaban, *Adv. Mater.*, 2016, **28**, 5747–5754.

(13) D. E. Crawford, C. K. G. Miskimmin, A. B. Albadarin, G. Walker and S. L. James, *Green Chem.*, 2017, **19**, 1507–1518.

(14) E. Colacino, V. Isoni, D. Crawford and F. García, *Trends Chem.*, 2021, **3**, 335–339.

(15) D. Tan and T. Friščić, *European J. Org. Chem.*, 2018, **2018**, 18–33.

(16) D. Tan and F. García, *Chem. Soc. Rev.*, 2019, **48**, 2274–2292.

(17) D. Tan, L. Loots and T. Friščić, *Chem. Commun.*, 2016, **52**, 7760–7781.

(18) T. Friščić, *J. Mater. Chem.*, 2010, **20**, 7599.

(19) T. Friščić, *Chem. Soc. Rev.*, 2012, **41**, 3493.

(20) Q. Zhang and F. Saito, *Adv. Powder Technol.*, 2012, **23**, 523–531.

(21) K. Ralphs, C. Hardacre and S. L. James, *Chem. Soc. Rev.*, 2013, **42**, 7701–7718.

(22) V. Šepelák, A. Düvel, M. Wilkening, K.-D. Becker and P. Heitjans, *Chem. Soc. Rev.*, 2013, **42**, 7507.

(23) M. J. Muñoz-Batista, D. Rodriguez-Padron, A. R. Puente-Santiago and R. Luque, *ACS Sustain. Chem. Eng.*, 2018, **6**, 9530–9544.

(24) S. B. Peh, Y. Wang and D. Zhao, *ACS Sustain. Chem. Eng.*, 2019, **7**, 3647–3670.

(25) B. Szczęśniak, S. Borysiuk, J. Choma and M. Jaroniec, *Mater. Horizons*, 2020, **7**, 1457–1473.

(26) E. R. Engel and J. L. Scott, *Green Chem.*, 2020, **22**, 3693–3715.

(27) M. Rubio-Martinez, C. Avci-Camur, A. W. Thornton, I. Imaz, D. Maspoch and M. R. Hill, *Chem. Soc. Rev.*, 2017, **46**, 3453–3480.

(28) Y. Li, H. Cao and J. Yu, *ACS Nano*, 2018, **12**, 4096–4104.

(29) S. Tanaka, in *Metal-Organic Frameworks for Biomedical Applications*, Elsevier, 2020, pp. 197–222.

(30) T. Stolar, A. Prašnikar, V. Martinez, B. Karadeniz, A. Bjelić, G. Mali, T. Friščić, B. Likozar and K. Užarević, *ACS Appl. Mater. Interfaces*, 2021, **13**, 3070–3077.

(31) B. Chen, Z. Yang, Y. Zhu and Y. Xia, *J. Mater. Chem. A*, 2014, **2**, 16811–16831.

(32) P. Zhang and S. Dai, *J. Mater. Chem. A*, 2017, **5**, 16118–16127.

(33) G. Majano, L. Borchardt, S. Mitchell, V. Valtchev and J. Pérez-Ramírez, *Microporous Mesoporous Mater.*, 2014, **194**, 106–114.

(34) D. N. Rainer and R. E. Morris, *Dalton Trans.*, 2021, **50**, 8995–9009.

(35) A. Corma, *Chem. Rev.*, 1997, **97**, 2373–2420.

(36) L. Ćurković, Š. Cerjan-Stefanović and T. Filipan, *Water Res.*, 1997, **31**, 1379–1382.

(37) R. E. Morris and P. S. Wheatley, *Angew. Chemie Int. Ed.*, 2008, **47**, 4966–4981.

(38) J. Čejka, G. Centi, J. Perez-Pariente and W. J. Roth, *Catal. Today*, 2012, **179**, 2–15.

(39) *Zeolites in Catalysis*, ed. J. Cejka, R. E. Morris and P. Nachtigall, Royal Society of Chemistry, Cambridge, 2017.

(40) M. Shamzhy, M. Opanasenko, P. Concepción and A. Martínez, *Chem. Soc. Rev.*, 2019, **48**, 1095–1149.

(41) J. Čejka, R. Millini, M. Opanasenko, D. P. Serrano and W. J. Roth, *Catal. Today*, 2020, **345**, 2–13.

(42) C. S. Cundy and P. A. Cox, *Chem. Rev.*, 2003, **103**, 663–702.

(43) A. F. Masters and T. Maschmeyer, *Microporous Mesoporous Mater.*, 2011, **142**, 423–438.

(44) A. F. Cronstedt, *Kongl Vetenskaps Acad. Handl. Stock.*, 1756, **17**, 120–123.

(45) H. E. Saint-Claire Deville, *Comptes rendus l'Académie des Sci.*, 1862, **54**, 324.

(46) W. H. Taylor, *Zeitschrift für Krist. - Cryst. Mater.*, 1930, **74**, 1–19.

(47) L. Pauling, *Proc. Natl. Acad. Sci.*, 1930, **16**, 453–459.

(48) L. Pauling, *Zeitschrift für Krist. - Cryst. Mater.*, 1930, **74**, 213–225.

(49) R. M. Barrer, *J. Chem. Soc.*, 1948, 127.

(50) R. M. Milton, *Molecular sieve adsorbents*, 1959.

(51) R. M. Barrer and P. J. Denny, *J. Chem. Soc.*, 1961, 971.

(52) E. M. Flanigen, J. M. Bennett, R. W. Grose, J. P. Cohen, R. L. Patton, R. M. Kirchner and J. V. Smith, *Nature*, 1978, **271**, 512–516.

(53) R. L. Wadlinger, G. T. Kerr and E. J. Rosinski, *Catalytic composition of crystalline zeolite*, 1967.

(54) R. J. Argauer and G. R. Landoldt, *Crystalline zeolite ZSM-5 and method of preparing the same*, 1972.

(55) S. T. Wilson, B. M. Lok, C. A. Messina, T. R. Cannan and E. M. Flanigen, *J. Am. Chem. Soc.*, 1982, **104**, 1146–1147.

(56) B. M. Lok, C. A. Messina, R. L. Patton, R. T. Gajek, T. R. Cannan and E. M. Flanigen, *J. Am. Chem. Soc.*, 1984, **106**, 6092–6093.

(57) N. A. Kutz, in *ACS Symp. Ser.* 1988, pp. 532–541.

(58) R. Fricke, H. Kosslick, G. Lischke and M. Richter, *Chem. Rev.*, 2000, **100**, 2303–2406.

(59) R. M. Barrer, J. W. Baynham, F. W. Bultitude and W. M. Meier, *J. Chem. Soc.*, 1959, 195.

(60) M. Opanasenko, M. Shamzhy, Y. Wang, W. Yan, P. Nachtigall and J. Čejka, *Angew. Chemie Int. Ed.*, 2020, **59**, 19380–19389.

(61) S. J. Andrews, M. Z. Papiz, R. McMeeking, A. J. Blake, B. M. Lowe, K. R. Franklin, J. R. Helliwell and M. M. Harding, *Acta Crystallogr. Sect. B Struct. Sci.*, 1988, **44**, 73–77.

(62) S. L. Lawton, A. S. Fung, G. J. Kennedy, L. B. Alemany, C. D. Chang, G. H. Hatzikos, D. N. Lissy, M. K. Rubin, H.-K. C. Timken, S. Steuernagel and D. E. Woessner, *J. Phys. Chem.*, 1996, **100**, 3788–3798.

(63) W. J. Roth, in *Stud. Surf. Sci. Catal.* Elsevier, 2005, vol. 158, pp. 19–26.

(64) M. E. Leonowicz, J. A. Lawton, S. L. Lawton and M. K. Rubin, *Science*, 1994, **264**, 1910–1913.

(65) M. Shamzhy, B. Gil, M. Opanasenko, W. J. Roth and J. Čejka, *ACS Catal.*, 2021, **11**, 2366–2396.

(66) W. J. Roth and J. Čejka, *Catal. Sci. Technol.*, 2011, **1**, 43.

(67) M. V. Opanasenko, W. J. Roth and J. Čejka, *Catal. Sci. Technol.*, 2016, **6**, 2467–2484.

(68) U. Díaz, *ISRN Chem. Eng.*, 2012, **2012**, 1–35.

(69) U. Díaz and A. Corma, *Dalton Trans.*, 2014, **43**, 10292–10316.

(70) W. J. Roth, P. Nachtigall, R. E. Morris and J. Čejka, *Chem. Rev.*, 2014, **114**, 4807–4837.

(71) C. Baerlocher and L. B. McCusker, *Database of Zeolite Structures*.

(72) J. L. Paillaud, B. Harbuzaru, J. Patarin and N. Bats, *Science*, 2004, **304**, 990–992.

(73) J. G. Min, H. J. Choi, J. Shin and S. B. Hong, *J. Phys. Chem. C*, 2017, **121**, 16342–16350.

(74) H. Lee, J. Shin, W. Choi, H. J. Choi, T. Yang, X. Zou and S. B. Hong, *Chem. Mater.*, 2018, **30**, 6619–6623.

(75) P. Guo, J. Shin, A. G. Greenaway, J. G. Min, J. Su, H. J. Choi, L. Liu, P. A. Cox, S. B. Hong, P. A. Wright and X. Zou, *Nature*, 2015, **524**, 74–78.

(76) J. Shin, H. Xu, S. Seo, P. Guo, J. G. Min, J. Cho, P. A. Wright, X. Zou and S. B. Hong, *Angew. Chemie Int. Ed.*, 2016, **55**, 4928–4932.

(77) A. Corma, M. J. Díaz-Cabañas, F. Rey, S. Nicolopoulus and K. Boulahya, *Chem. Commun.*, 2004, **4**, 1356–1357.

(78) N. Kasian, A. Tuel, E. Verheyen, C. E. Kirschhock, F. Taulelle and J. A. Martens, *Chem. Mater.*, 2014, **26**, 5556–5565.

(79) E. Verheyen, L. Joos, K. Van Havenbergh, E. Breynaert, N. Kasian, E. Gobechiya, K. Houthoofd, C. Martineau, M. Hinterstein, F. Taulelle, V. Van Speybroeck, M. Waroquier, S. Bals, G. Van Tendeloo, C. E. Kirschhock and J. A. Martens, *Nat. Mater.*, 2012, **11**, 1059–1064.

(80) W. J. Roth, O. V. Shvets, M. Shamzhy, P. Chlubná, M. Kubů, P. Nachtigall and J. Ĉejka, *J. Am. Chem. Soc.*, 2011, **133**, 6130–6133.

(81) W. J. Roth, P. Nachtigall, R. E. Morris, P. S. Wheatley, V. R. Seymour, S. E. Ashbrook, P. Chlubná, L. Grajciar, M. Položij, A. Zukal, O. Shvets and J. Čejka, *Nat. Chem.*, 2013, **5**, 628–633.

(82) S. A. Morris, G. P. M. Bignami, Y. Tian, M. Navarro, D. S. Firth, J. Čejka, P. S. Wheatley, D. M. Dawson, W. A. Slawinski, D. S. Wragg, R. E. Morris and S. E. Ashbrook, *Nat. Chem.*, 2017, **9**, 1012–1018.

(83) A. Corma, M. Puche, F. Rey, G. Sankar and S. J. Teat, *Angew. Chemie Int. Ed.*, 2003, **42**, 1156–1159.

(84) N. Bats, L. Rouleau, J.-L. Paillaud, P. Caullet, Y. Mathieu and S. Lacombe, in *Stud. Surf. Sci. Catal.* Elsevier, 2004, vol. 154, pp. 283–288.

(85) G. Sastre, A. Pulido, R. Castañeda and A. Corma, *J. Phys. Chem. B*, 2004, **108**, 8830–8835.

(86) R. Castañeda, A. Corma, V. Fornés, J. Martínez-Triguero and S. Valencia, *J. Catal.*, 2006, **238**, 79–87.

(87) R. L. Hay and R. A. Sheppard, *Rev. Mineral. Geochemistry*, 2001, **45**, 217–234.

(88) R. Barrer, *Stud. Surf. Sci. Catal.*, 1985, **24**, 1–26.

(89) C. S. Cundy and P. A. Cox, *Microporous Mesoporous Mater.*, 2005, **82**, 1–78.

(90) K. G. Strohmaier, in *Zeolites in Catalysis: Properties and Applications*, ed. J. Čejka, R. E. Morris and P. Nachtigall, RSC, 2017, pp. 73–102.

(91) R. K. Iler, in *The Chemistry of Silica*, Wiley, 1979, ch. 1, pp. 3–115.

(92) U. Schubert, in *The Sol-Gel Handbook*, ed. D. Levy and M. Zayat, Wiley-VCH Verlag GmbH & Co. KGaA, Weinheim, Germany, 2015, ch. 1, pp. 1–28.

(93) H. Lechert, in *Verified Synthesis of Zeolitic Materials*, Elsevier, 2001, ch. 5, pp. 33–38.

(94) S. I. Zones, S. J. Hwang, S. Elomari, I. Ogino, M. E. Davis and A. W. Burton, *Comptes Rendus Chim.*, 2005, **8**, 267–282.

(95) P. Caullet, J.-L. Paillaud, A. Simon-Masseron, M. Soulard and J. Patarin, *Comptes Rendus Chim.*, 2005, **8**, 245–266.

(96) J.-L. Paillaud, P. Caullet, J. Brendlé, A. Simon-Masseron and J. Patarin, in *Functionalized Inorganic Fluorides*, John Wiley & Sons, Ltd, Chichester, UK, 2010, pp. 489–518.

(97) J. A. Vidal-Moya, T. Blasco, F. Rey, A. Corma and M. Puche, *Chem. Mater.*, 2003, **15**, 3961–3963.

(98) R. M. Shayib, N. C. George, R. Seshadri, A. W. Burton, S. I. Zones and B. F. Chmelka, *J. Am. Chem. Soc.*, 2011, **133**, 18728–18741.

(99) X. Liu, U. Ravon and A. Tuel, *Microporous Mesoporous Mater.*, 2013, **170**, 194–199.

(100) M. E. Davis and R. F. Lobo, *Chem. Mater.*, 1992, **4**, 756–768.

(101) B. M. Lok, T. R. Cannan and C. A. Messina, *Zeolites*, 1983, **3**, 282–291.

(102) *Insights into the Chemistry of Organic Structure-Directing Agents in the Synthesis of Zeolitic Materials*, ed. L. Gómez-Hortigüela, Springer International Publishing, Cham, 2018, vol. 175.

(103) J. Jiang, J. Yu and A. Corma, *Angew. Chemie Int. Ed.*, 2010, **49**, 3120–3145.

(104) L.-H. Chen, X.-Y. Li, J. C. Rooke, Y.-H. Zhang, X.-Y. Yang, Y. Tang, F.-S. Xiao and B.-L. Su, *J. Mater. Chem.*, 2012, **22**, 17381.

(105) Y. Wei, T. E. Parmentier, K. P. de Jong and J. Zečević, *Chem. Soc. Rev.*, 2015, **44**, 7234–7261.

(106) A. Feliczak-Guzik, *Microporous Mesoporous Mater.*, 2018, **259**, 33–45.

(107) S. Zones and R. Van Nordstrand, *Zeolites*, 1988, **8**, 166–174.

(108) *Verified Syntheses of Zeolitic Materials*, ed. S. Mintova, 3rd edn., 2016.

(109) L. Han, Y. Wang, S. Zhang and X. Lu, *J. Cryst. Growth*, 2008, **311**, 167–171.

(110) R. Millini, G. Perego and G. Bellussi, *Top. Catal.*, 1999, **9**, 13–34.

(111) J. Cho, Y. Yun, H. Xu, J. Sun, A. W. Burton, K. G. Strohmaier, G. Terefenko, H. Vroman, M. Afeworki, G. Cao, H. Wang, X. Zou and T. Willhammar, *Chem. Mater.*, 2021, **33**, 4146–4153.

(112) G. Sastre, J. A. Vidal-Moya, T. Blasco, J. Rius, J. L. Jordá, M. T. Navarro, F. Rey and A. Corma, *Angew. Chemie Int. Ed.*, 2002, **41**, 4722–4726.

(113) T. Blasco, A. Corma, M. J. Díaz-Cabañas, F. Rey, J. A. Vidal-Moya and C. M. Zicovich-Wilson, *J. Phys. Chem. B*, 2002, **106**, 2634–2642.

(114) Y. Wang, J. Song and H. Gies, *Solid State Sci.*, 2003, **5**, 1421–1433.

(115) M. A. Zwijnenburg, S. T. Bromley, J. C. Jansen and T. Maschmeyer, *Microporous Mesoporous Mater.*, 2004, **73**, 171–174.

(116) J.-L. Paillaud, Y. Lorgouilloux, B. Harbuzaru, P. Caullet, J. Patarin and N. Bats, in *Stud. Surf. Sci. Catal.* 2007, pp. 389–396.

(117) P. Kamakoti and T. A. Barckholtz, *J. Phys. Chem. C*, 2007, **111**, 3575–3583.

(118) H. Li and O. M. Yaghi, *J. Am. Chem. Soc.*, 1998, **120**, 10569–10570.

(119) L. G. Van De Water, M. A. Zwijnenburg, W. G. Sloof, J. C. Van Der Waal, J. C. Jansen and T. Maschmeyer, *ChemPhysChem*, 2004, **5**, 1328–1335.

(120) M. V. Shamzhy, M. V. Opanasenko, F. S. d. O. Ramos, L. Brabec, M. Horáček, M. Navarro-Rojas, R. E. Morris, H. d. O. Pastore and J. Čejka, *Catal. Sci. Technol.*, 2015, **5**, 2973–2984.

(121) A. Rodríguez-Fernández, F. J. Llopis, C. Martínez, M. Moliner and A. Corma, *Microporous Mesoporous Mater.*, 2018, **267**, 35–42.

(122) P. Eliášová, M. Opanasenko, P. S. Wheatley, M. Shamzhy, M. Mazur, P. Nachtigall, W. J. Roth, R. E. Morris and J. Čejka, *Chem. Soc. Rev.*, 2015, **44**, 7177–7206.

(123) A. Deneyer, Q. Ke, J. Devos and M. Dusselier, *Chem. Mater.*, 2020, **32**, 4884–4919.

(124) Y. Kamimura, W. Chaikittisilp, K. Itabashi, A. Shimojima and T. Okubo, *Chem. - An Asian J.*, 2010, **5**, 2182–2191.

(125) Y. Kamimura, S. Tanahashi, K. Itabashi, A. Sugawara, T. Wakihara, A. Shimojima and T. Okubo, *J. Phys. Chem. C*, 2011, **115**, 744–750.

(126) Y. Kamimura, K. Iyoki, S. P. Elangovan, K. Itabashi, A. Shimojima and T. Okubo, *Microporous Mesoporous Mater.*, 2012, **163**, 282–290.

(127) M. H. Nada and S. C. Larsen, *Microporous Mesoporous Mater.*, 2017, **239**, 444–452.

(128) R. Jain and J. D. Rimer, *Microporous Mesoporous Mater.*, 2020, **300**, 110174.

(129) R. E. Morris and S. J. Weigel, *Chem. Soc. Rev.*, 1997, **26**, 309.

(130) R. E. Morris, *Angew. Chemie Int. Ed.*, 2008, **47**, 442–444.

(131) R. E. Morris, *Chem. Commun.*, 2009, 2990.

(132) R. E. Morris, in *Zeolites and Catalysis*, Wiley-VCH Verlag GmbH & Co. KGaA, Weinheim, Germany, 2010, ch. 3, pp. 87–105.

(133) P. S. Wheatley, P. K. Allan, S. J. Teat, S. E. Ashbrook and R. E. Morris, *Chem. Sci.*, 2010, **1**, 483.

(134) Q. Wu, X. Hong, L. Zhu, X. Meng, S. Han, J. Zhang, X. Liu, C. Jin and F.-S. Xiao, *Microporous Mesoporous Mater.*, 2019, **286**, 163–168.

(135) M. Wang, L. Zhang, K. Guo, Y. Lin, X. Meng, P. Huang, Y. Wei and R. Zhang, *Chem. - An Asian J.*, 2019, **14**, 621–626.

(136) E. R. Parnham and R. E. Morris, *Chem. Mater.*, 2006, **18**, 4882–4887.

(137) E. R. Parnham, P. S. Wheatley and R. E. Morris, *Chem. Commun.*, 2006, 380–382.

(138) E. R. Parnham and R. E. Morris, *J. Am. Chem. Soc.*, 2006, **128**, 2204–2205.

(139) X. Meng, K. Guo, Y. Lin, H. Wang, H. Chen, P. Huang, S. Tao, L. Zhang, Y. Wei and R. Zhang, *J. Porous Mater.*, 2021, **1**, 3.

(140) G. A. Tompsett, W. C. Conner and K. S. Yngvesson, *ChemPhysChem*, 2006, **7**, 296–319.

(141) I. Bilecka and M. Niederberger, *Nanoscale*, 2010, **2**, 1358.

(142) Z. Liu, J. Zhu, T. Wakihara and T. Okubo, *Inorg. Chem. Front.*, 2019, **6**, 14–31.

(143) M. Mazur, M. Kubů, P. S. Wheatley and P. Eliášová, *Catal. Today*, 2015, **243**, 23–31.

(144) S. E. Henkelis, M. Mazur, C. M. Rice, P. S. Wheatley, S. E. Ashbrook and R. E. Morris, *J. Am. Chem. Soc.*, 2019, **141**, 4453–4459.

(145) P. S. Wheatley, P. Chlubná-Eliášová, H. Greer, W. Zhou, V. R. Seymour, D. M. Dawson, S. E. Ashbrook, A. B. Pinar, L. B. McCusker, M. Opanasenko, J. Čejka and R. E. Morris, *Angew. Chemie Int. Ed.*, 2014, **53**, 13210–13214.

(146) M. Mazur, P. S. Wheatley, M. Navarro, W. J. Roth, M. Položij, A. Mayoral, P. Eliášová, P. Nachtigall, J. Čejka and R. E. Morris, *Nat. Chem.*, 2016, **8**, 58–62.

(147) P. Chlubná-Eliášová, Y. Tian, A. B. Pinar, M. Kubů, J. Čejka and R. E. Morris, *Angew. Chemie Int. Ed.*, 2014, **53**, 7048–7052.

(148) V. Kasneryk, M. Shamzhy, M. Opanasenko, P. S. Wheatley, S. A. Morris, S. E. Russell, A. Mayoral, M. Trachta, J. Čejka and R. E. Morris, *Angew. Chemie Int. Ed.*, 2017, **56**, 4324–4327.

(149) V. Kasneryk, M. Opanasenko, M. Shamzhy, Z. Musilová, Y. S. Avadhut, M. Hartmann and J. Čejka, *J. Mater. Chem. A*, 2017, **5**, 22576–22587.

(150) V. Kasneryk, M. Shamzhy, M. Opanasenko, P. S. Wheatley, R. E. Morris and J. Čejka, *Dalton Trans.*, 2018, **47**, 3084–3092.

(151) V. Kasneryk, M. Shamzhy, J. Zhou, Q. Yue, M. Mazur, A. Mayoral, Z. Luo, R. E. Morris, J. Čejka and M. Opanasenko, *Nat. Commun.*, 2019, **10**, 5129.

(152) D. S. Firth, S. A. Morris, P. S. Wheatley, S. E. Russell, A. M. Z. Slawin, D. M. Dawson, A. Mayoral, M. Opanasenko, M. Položij, J. Čejka, P. Nachtigall and R. E. Morris, *Chem. Mater.*, 2017, **29**, 5605–5611.

(153) J. Zhang, O. Veselý, Z. Tošner, M. Mazur, M. Opanasenko, J. Čejka and M. Shamzhy, *Chem. Mater.*, 2021, **33**, 1228–1237.

(154) O. Veselý, P. Eliášová, R. E. Morris and J. Čejka, *Mater. Adv.*, 2021, **2**, 3862–3870.

(155) J. Zhang, Q. Yue, M. Mazur, M. Opanasenko, M. V. Shamzhy and J. Čejka, *ACS Sustain. Chem. Eng.*, 2020, **8**, 8235–8246.

(156) N. E. Gordina, V. Y. Prokof'ev and A. P. Il'in, *Russ. J. Appl. Chem.*, 2003, **76**, 661–662.

(157) V. Y. Prokofév, N. E. Gordina, A. B. Zhidkova and A. M. Efremov, *J. Mater. Sci.*, 2012, **47**, 5385–5392.

(158) V. Y. Prokof'ev, N. E. Gordina and A. B. Zhidkova, *Russ. J. Appl. Chem.*, 2012, **85**, 1077–1082.

(159) V. Y. Prokof'ev and N. E. Gordina, *Russ. J. Appl. Chem.*, 2013, **86**, 332–338.

(160) N. E. Gordina, V. Y. Prokof'ev and S. P. Kochetkov, *Russ. J. Gen. Chem.*, 2018, **88**, 1981–1989.

(161) Q. Wu, X. Meng, X. Gao and F.-S. Xiao, *Acc. Chem. Res.*, 2018, **51**, 1396–1403.

(162) Y. Wang, H. Duan, Z. Tan, X. Meng and F.-S. Xiao, *Dalton Trans.*, 2020, **49**, 6939–6944.

(163) A. Kornas, J. E. Olszówka, P. Klein and V. Pashkova, *Catalysts*, 2021, **11**, 246.

(164) J. Mei, A. Duan and X. Wang, *Materials*, 2021, **14**, 788.

(165) Y. Xiao, N. Sheng, Y. Chu, Y. Wang, Q. Wu, X. Liu, F. Deng, X. Meng and Z. Feng, *Microporous Mesoporous Mater.*, 2017, **237**, 201–209.

(166) M. H. Nada, E. G. Gillan and S. C. Larsen, *Microporous Mesoporous Mater.*, 2019, **276**, 23–28.

(167) M. H. Nada, S. C. Larsen and E. G. Gillan, *Solid State Sci.*, 2019, **94**, 15–22.

(168) M. H. Nada, S. C. Larsen and E. G. Gillan, *Nanoscale Adv.*, 2019, **1**, 3918–3928.

(169) L. Ren, Q. Wu, C. Yang, L. Zhu, C. Li, P. Zhang, H. Zhang, X. Meng and F.-S. Xiao, *J. Am. Chem. Soc.*, 2012, **134**, 15173–15176.

(170) Q. Wu, X. Wang, G. Qi, Q. Guo, S. Pan, X. Meng, J. Xu, F. Deng, F. Fan, Z. Feng, C. Li, S. Maurer, U. Müller and F.-S. Xiao, *J. Am. Chem. Soc.*, 2014, **136**, 4019–4025.

(171) Q. Wu, X. Liu, L. Zhu, L. Ding, P. Gao, X. Wang, S. Pan, C. Bian, X. Meng, J. Xu, F. Deng, S. Maurer, U. Müller and F.-S. Xiao, *J. Am. Chem. Soc.*, 2015, **137**, 1052–1055.

(172) X. Wang, Q. Wu, C. Chen, S. Pan, W. Zhang, X. Meng, S. Maurer, M. Feyen, U. Müller and F.-S. Xiao, *Chem. Commun.*, 2015, **51**, 16920–16923.

(173) X. Meng and F. S. Xiao, *Chem. Rev.*, 2014, **114**, 1521–1543.

(174) X. Meng, Q. Wu, F. Chen and F.-S. Xiao, *Sci. China Chem.*, 2015, **58**, 6–13.

(175) Q. Wu, X. Liu, L. Zhu, X. Meng, F. Deng, F. Fan, Z. Feng, C. Li, S. Maurer, M. Feyen, U. Müller and F.-S. Xiao, *Chinese J. Chem.*, 2017, **35**, 572–576.

(176) L. Zhu, J. Zhang, L. Wang, Q. Wu, C. Bian, S. Pan, X. Meng and F. S. Xiao, *J. Mater. Chem. A*, 2015, **3**, 14093–14095.

(177) J. H. Zhang, M. B. Yue, X. N. Wang and D. Qin, *Microporous Mesoporous Mater.*, 2015, **217**, 96–101.

(178) X. Liu, Y. Chu, Q. Wang, W. Wang, C. Wang, J. Xu and F. Deng, *Solid State Nucl. Magn. Reson.*, 2017, **87**, 1–9.

(179) M. Shakeri, *ChemistrySelect*, 2019, **4**, 7566–7571.

(180) Y. Jin, X. Chen, Q. Sun, N. Sheng, Y. Liu, C. Bian, F. Chen, X. Meng and F.-S. Xiao, *Chem. - A Eur. J.*, 2014, **20**, 17616–17623.

(181) X. Zhao, X. Gao, X. Zhang and Z. Hao, *Microporous Mesoporous Mater.*, 2017, **242**, 160–165.

(182) X. Zhao, W. Duan, X. Zhang, D. Ji, Y. Zhao and G. Li, *React. Kinet. Mech. Catal.*, 2018, **125**, 1055–1070.

(183) Y. Jin, Q. Sun, G. Qi, C. Yang, J. Xu, F. Chen, X. Meng, F. Deng and F.-S. Xiao, *Angew. Chemie Int. Ed.*, 2013, **52**, 9172–9175.

(184) Y. Du, B. Feng, Y. Jiang, L. Yuan, K. Huang and J. Li, *Eur. J. Inorg. Chem.*, 2018, **2018**, 2599–2606.

(185) A. Kornas, J. E. Olszówka, M. Urbanova, K. Mlekodaj, L. Brabec, J. Rathousky, J. Dedecek and V. Pashkova, *Eur. J. Inorg. Chem.*, 2020, **2020**, 2791–2797.

(186) V. Valtchev, S. Mintova, V. Dimov, A. Toneva and D. Radev, *Zeolites*, 1995, **15**, 193–197.

(187) F. Zheng, W. Jing, X. Gu, N. Xu and J. Dong, *J. Mater. Sci.*, 2013, **48**, 6286–6292.

(188) N. Xu, D. Meng, X. Tang, X. Kong, L. Kong, Y. Zhang, H. Qiu, M. Wang and Y. Zhang, *Sep. Purif. Technol.*, 2020, **253**, 117505.

(189) K. Miyake, K. Ono, M. Nakai, Y. Hirota, Y. Uchida, S. Tanaka, M. Miyamoto and N. Nishiyama, *ChemistrySelect*, 2017, **2**, 7651–7653.

(190) J. Jiang, X. Wang, Y. Zhang, D. Liu and X. Gu, *Microporous Mesoporous Mater.*, 2015, **215**, 98–108.

(191) P. Cheng, M. Song, H. Zhang, Y. Xuan and C. Wu, *J. Mater. Sci.*, 2019, **54**, 4573–4578.

(192) H. Zhang, C. Wu, M. Song, T. Lu, W. Wang, Z. Wang, W. Yan, P. Cheng and Z. Zhao, *Microporous Mesoporous Mater.*, 2021, **310**, 110633.

(193) G. Feng, P. Cheng, W. Yan, M. Boronat, X. Li, J.-H. Su, J. Wang, Y. Li, A. Corma, R. Xu and J. Yu, *Science*, 2016, **351**, 1188–1191.

(194) J. Přech, *Catal. Rev.*, 2018, **60**, 71–131.

(195) K. Yamamoto, S. E. B. Garcia, F. Saito and A. Muramatsu, *Chem. Lett.*, 2006, **35**, 570–571.

(196) K. Yamamoto, S. E. Borjas García and A. Muramatsu, *Microporous Mesoporous Mater.*, 2007, **101**, 90–96.

(197) S. E. Borjas García, K. Yamamoto, F. Saito and A. Muramatsu, *J. Japan Pet. Inst.*, 2007, **50**, 53–60.

(198) S. E. Borjas Garcia, K. Yamamoto and A. Muramatsu, *J. Mater. Sci.*, 2008, **43**, 2367–2371.

(199) T. Iwasaki, M. Isaka, H. Nakamura, M. Yasuda and S. Watano, *Microporous Mesoporous Mater.*, 2012, **150**, 1–6.

(200) J. Zhang and S. R. Qiao, *Adv. Mater. Res.*, 2013, **652-654**, 693–697.

(201) T. Iida, A. Takagaki, S. Kohara, T. Okubo and T. Wakihara, *ChemNanoMat*, 2015, **1**, 155–158.

(202) K. Kanie, M. Sakaguchi, F. Muto, M. Horie, M. Nakaya, T. Yokoi and A. Muramatsu, *Sci. Technol. Adv. Mater.*, 2018, **19**, 545–553.

(203) P. Hu, K. Iyoki, H. Yamada, Y. Yanaba, K. Ohara, N. Katada and T. Wakihara, *Microporous Mesoporous Mater.*, 2019, **288**, 109594.

(204) M. Yabushita, M. Yoshida, F. Muto, M. Horie, Y. Kunitake, T. Nishitoba, S. Maki, K. Kanie, T. Yokoi and A. Muramatsu, *Mol. Catal.*, 2019, **478**, 110579.

(205) M. Yabushita, H. Kobayashi, R. Osuga, M. Nakaya, M. Matsubara, S. Maki, K. Kanie and A. Muramatsu, *Ind. Eng. Chem. Res.*, 2021, **60**, 2079–2088.

(206) C. Hammond, S. Conrad and I. Hermans, *Angew. Chemie Int. Ed.*, 2012, **51**, 11736–11739.

(207) C. Hammond, D. Padovan, A. Al-Nayili, P. P. Wells, E. K. Gibson and N. Dimitratos, *ChemCatChem*, 2015, **7**, 3322–3331.

(208) H. Joshi, C. Ochoa-Hernández, E. Nürenberg, L. Kang, F. R. Wang, C. Weidenthaler, W. Schmidt and F. Schüth, *Microporous Mesoporous Mater.*, 2020, **309**, 110566.

(209) S. Mintova, J. P. Gilson and V. Valtchev, *Nanoscale*, 2013, **5**, 6693–6703.

(210) V. Valtchev, G. Majano, S. Mintova and J. Pérez-Ramírez, *Chem. Soc. Rev.*, 2013, **42**, 263–290.

(211) P. Zielinski, A. Van Neste, D. Akolekar and S. Kaliaguine, *Microporous Mater.*, 1995, **5**, 123–133.

(212) C. Kosanović, J. Bronić, B. Subotić, I. Šmit, M. Stubičar, A. Tonejc and T. Yamamoto, *Zeolites*, 1993, **13**, 261–268.

(213) C. Kosanović, J. Bronić, A. Čižmek, B. Subotić, I. Šmit, M. Stubičar and A. Tonejc, *Zeolites*, 1995, **15**, 247–252.

(214) C. Kosanović, A. Čižmek, B. Subotić, I. Šmit, M. Stubičar, A. Tonejc, A. C̆iz̆mek, B. Subotić, I. S̆mit, M. Stubic̆ar and A. Tonejc, *Zeolites*, 1995, **15**, 632–636.

(215) C. Kosanović, B. Subotić, I. Šmit, A. Čižmek, M. Stubičar and A. Tonejc, *J. Mater. Sci.*, 1997, **32**, 73–78.

(216) C. Kosanović, B. Subotić and I. Šmit, *Thermochim. Acta*, 1998, **317**, 25–37.

(217) T. Wakihara, A. Ihara, S. Inagaki, J. Tatami, K. Sato, K. Komeya, T. Meguro, Y. Kubota and A. Nakahira, *Cryst. Growth Des.*, 2011, **11**, 5153–5158.

(218) T. Wakihara, R. Ichikawa, J. Tatami, A. Endo, K. Yoshida, Y. Sasaki, K. Komeya and T. Meguro, *Cryst. Growth Des.*, 2011, **11**, 955–958.

(219) T. Wakihara, K. Sato, K. Sato, J. Tatami, S. Kohara, K. Komeya and T. Meguro, *J. Ceram. Soc. Japan*, 2012, **120**, 341–343.

(220) S. Inagaki, K. Sato, S. Hayashi, J. Tatami, Y. Kubota and T. Wakihara, *ACS Appl. Mater. Interfaces*, 2015, **7**, 4488–4493.

(221) S. Inagaki, S. Shinoda, S. Hayashi, T. Wakihara, H. Yamazaki, J. N. Kondo and Y. Kubota, *Catal. Sci. Technol.*, 2016, **6**, 2598–2604.

(222) C. Anand, Y. Yamaguchi, Z. Liu, S. Ibe, S. P. Elangovan, T. Ishii, T. Ishikawa, A. Endo, T. Okubo and T. Wakihara, *Sci. Rep.*, 2016, **6**, 29210.

(223) Z. Liu, N. Nomura, D. Nishioka, Y. Hotta, T. Matsuo, K. Oshima, Y. Yanaba, T. Yoshikawa, K. Ohara, S. Kohara, T. Takewaki, T. Okubo and T. Wakihara, *Chem. Commun.*, 2015, **51**, 12567–12570.

(224) J. Zhu, Z. Liu, A. Endo, Y. Yanaba, T. Yoshikawa, T. Wakihara and T. Okubo, *CrystEngComm*, 2017, **19**, 632–640.

(225) A. Chokkalingam, K. Iyoki, N. Hoshikawa, H. Onozuka, W. Chaikittisilp, S. Tsutsuminai, T. Takewaki, T. Wakihara and T. Okubo, *React. Chem. Eng.*, 2020, **5**, 2260–2266.

(226) T. Yoshioka, Z. Liu, K. Iyoki, A. Chokkalingam, Y. Yonezawa, Y. Hotta, R. Ohnishi, T. Matsuo, Y. Yanaba, K. Ohara, T. Takewaki, T. Sano, T. Okubo and T. Wakihara, *React. Chem. Eng.*, 2021, **6**, 74–81.

(227) S. R. Batten, N. R. Champness, X.-M. Chen, J. Garcia-Martinez, S. Kitagawa, L. Öhrström, M. O'Keeffe, M. Paik Suh and J. Reedijk, *Pure Appl. Chem.*, 2013, **85**, 1715–1724.

(228) K. M. Fromm, *Coord. Chem. Rev.*, 2008, **252**, 856–885.

(229) D. Banerjee and J. B. Parise, *Cryst. Growth Des.*, 2011, **11**, 4704–4720.

(230) J. A. Kaduk, *Acta Crystallogr. Sect. B Struct. Sci.*, 2000, **56**, 474–485.

(231) N. Lock, Y. Wu, M. Christensen, L. J. Cameron, V. K. Peterson, A. J. Bridgeman, C. J. Kepert and B. B. Iversen, *J. Phys. Chem. C*, 2010, **114**, 16181–16186.

(232) R. Freund, O. Zaremba, G. Arnauts, R. Ameloot, G. Skorupskii, M. Dincă, A. Bavykina, J. Gascon, A. Ejsmont, J. Goscianska, M. Kalmutzki, U. Lächelt, E. Ploetz, C. S. Diercks and S. Wuttke, *Angew. Chemie Int. Ed.*, 2021, **60**, 23975–24001.

(233) V. Pascanu, G. González Miera, A. K. Inge and B. Martín-Matute, *J. Am. Chem. Soc.*, 2019, **141**, 7223–7234.

(234) H. Li, K. Wang, Y. Sun, C. T. Lollar, J. Li and H.-C. Zhou, *Mater. Today*, 2018, **21**, 108–121.

(235) D. Yang and B. C. Gates, *ACS Catal.*, 2019, **9**, 1779–1798.

(236) A. C. McKinlay, B. Xiao, D. S. Wragg, P. S. Wheatley, I. L. Megson and R. E. Morris, *J. Am. Chem. Soc.*, 2008, **130**, 10440–10444.

(237) N. Hanikel, M. S. Prévot and O. M. Yaghi, *Nat. Nanotechnol.*, 2020, **15**, 348–355.

(238) L. Wang, Y. Han, X. Feng, J. Zhou, P. Qi and B. Wang, *Coord. Chem. Rev.*, 2016, **307**, 361–381.

(239) Z. Wang, H. Tao and Y. Yue, *ChemElectroChem*, 2019, **6**, 5358–5374.

(240) C. Li, L. Liu, J. Kang, Y. Xiao, Y. Feng, F.-F. Cao and H. Zhang, *Energy Storage Mater.*, 2020, **31**, 115–134.

(241) Y. Bai, C. Liu, Y. Shan, T. Chen, Y. Zhao, C. Yu and H. Pang, *Adv. Energy Mater.*, 2022, **12**, 2100346.

(242) A. V. Desai, R. E. Morris and A. R. Armstrong, *ChemSusChem*, 2020, **13**, 4866–4884.

(243) W. Zhu, A. Li, Z. Wang, J. Yang and Y. Xu, *Small*, 2021, **17**, 2006424.

(244) S. Kumar, S. Jain, M. Nehra, N. Dilbaghi, G. Marrazza and K.-H. Kim, *Coord. Chem. Rev.*, 2020, **420**, 213407.

(245) N. A. Khan and S. H. Jhung, *Coord. Chem. Rev.*, 2015, **285**, 11–23.

(246) A. Laybourn, J. Katrib, R. S. Ferrari-John, C. G. Morris, S. Yang, O. Udoudo, T. L. Easun, C. Dodds, N. R. Champness, S. W. Kingman and M. Schröder, *J. Mater. Chem. A*, 2017, **5**, 7333–7338.

(247) I. Thomas-Hillman, A. Laybourn, C. Dodds and S. W. Kingman, *J. Mater. Chem. A*, 2018, **6**, 11564–11581.

(248) A. Pichon and S. L. James, *CrystEngComm*, 2008, **10**, 1839.

(249) T. Friščić, in *Encyclopedia of Inorganic and Bioinorganic Chemistry*, John Wiley & Sons, Ltd, Chichester, UK, 2014, pp. 1–19.

(250) P. A. Julien, C. Mottillo and T. Friščić, *Green Chem.*, 2017, **19**, 2729–2747.

(251) T. Stolar and K. Užarević, *CrystEngComm*, 2020, **22**, 4511–4525.

(252) C.-A. Tao and J.-F. Wang, *Crystals*, 2020, **11**, 15.

(253) J. Casaban, Y. Zhang, R. Pacheco, C. Coney, C. Holmes, E. Sutherland, C. Hamill, J. Breen, S. L. James, D. Tufano, D. Wong, E. Stavrakakis, H. Annath and A. Moore, *Faraday Discuss.*, 2021, **231**, 312–325.

(254) S. Głowniak, B. Szczęśniak, J. Choma and M. Jaroniec, *Mater. Today*, 2021, **46**, 109–124.

(255) T. Friščić, D. G. Reid, I. Halasz, R. S. Stein, R. E. Dinnebier and M. J. Duer, *Angew. Chemie Int. Ed.*, 2010, **49**, 712–715.

(256) P. A. Julien, K. Užarević, A. D. Katsenis, S. A. J. Kimber, T. Wang, O. K. Farha, Y. Zhang, J. Casaban, L. S. Germann, M. Etter, R. E. Dinnebier, S. L. James, I. Halasz and T. Friščić, *J. Am. Chem. Soc.*, 2016, **138**, 2929–2932.

(257) T. Stolar, L. Batzdorf, S. Lukin, D. Žilić, C. Motillo, T. Friščić, F. Emmerling, I. Halasz and K. Užarević, *Inorg. Chem.*, 2017, **56**, 6599–6608.

(258) T. Friščić, I. Halasz, P. J. Beldon, A. M. Belenguer, F. Adams, S. A. J. Kimber, V. Honkimäki and R. E. Dinnebier, *Nat. Chem.*, 2013, **5**, 66–73.

(259) I. Halasz, S. A. J. Kimber, P. J. Beldon, A. M. Belenguer, F. Adams, V. Honkimäki, R. C. Nightingale, R. E. Dinnebier and T. Friščić, *Nat. Protoc.*, 2013, **8**, 1718–1729.

(260) K. Užarević, I. Halasz and T. Friščić, *J. Phys. Chem. Lett.*, 2015, **6**, 4129–4140.

(261) A. D. Katsenis, A. Puškarić, V. Štrukil, C. Mottillo, P. A. Julien, K. Užarević, M.-H. Pham, T.-O. Do, S. A. J. Kimber, P. Lazić, O. Magdysyuk, R. E. Dinnebier, I. Halasz and T. Friščić, *Nat. Commun.*, 2015, **6**, 6662.

(262) L. S. Germann, A. D. Katsenis, I. Huskić, P. A. Julien, K. Užarević, M. Etter, O. K. Farha, T. Friščić and R. E. Dinnebier, *Cryst. Growth Des.*, 2020, **20**, 49–54.

(263) G. Ayoub, B. Karadeniz, A. J. Howarth, O. K. Farha, I. Đilović, L. S. Germann, R. E. Dinnebier, K. Užarević and T. Friščić, *Chem. Mater.*, 2019, **31**, 5494–5501.

(264) J. B. Goodenough and K.-S. Park, *J. Am. Chem. Soc.*, 2013, **135**, 1167–1176.

(265) M. D. Slater, D. Kim, E. Lee and C. S. Johnson, *Adv. Funct. Mater.*, 2013, **23**, 947–958.

(266) J.-Y. Hwang, S.-T. Myung and Y.-K. Sun, *Chem. Soc. Rev.*, 2017, **46**, 3529–3614.

(267) P. Poizot, J. Gaubicher, S. Renault, L. Dubois, Y. Liang and Y. Yao, *Chem. Rev.*, 2020, **120**, 6490–6557.

(268) B. Esser, F. Dolhem, M. Becuwe, P. Poizot, A. Vlad and D. Brandell, *J. Power Sources*, 2021, **482**, 228814.

(269) C. N. Gannett, L. Melecio-Zambrano, M. J. Theibault, B. M. Peterson, B. P. Fors and H. D. Abruña, *Mater. Reports Energy*, 2021, **1**, 100008.

(270) R. A. Sheldon, *Green Chem.*, 2014, **16**, 950–963.

(271) L. Wu, T. Moteki, A. A. Gokhale, D. W. Flaherty and F. D. Toste, *Chem*, 2016, **1**, 32–58.

(272) C. Liedel, *ChemSusChem*, 2020, **13**, 2110–2141.

Chapter 2

Aims

This PhD thesis aims to investigate possibilities of mechanochemical methods for the synthesis of framework materials, in particular zeolites and sodium coordination polymers. The intention is to find suitable opportunities for this methodology rendering existing processes more sustainable or creating alternative approaches for the production of desirable compounds.

One of the targets is an assessment of the applicability of ball milling in the hydrolytic transformation of germanosilicate zeolite **UTL** into daughter zeolites within the scope of the ADOR process. The goal is a more efficient and less wasteful process to increase the feasibility of this synthesis method for otherwise inaccessible zeolite frameworks. Reduction of required amounts of the hydrolysis agents water and hydrochloric acid would be beneficial with respect to produced waste and potential for shortening of reaction times are additional possible advantages for a more efficient synthesis.

The recently developed solvent-free synthesis of zeolites promises to be a great method for cost-efficient production of the most common zeolite types. Probing the extendability of the method, a further project within this thesis attempts to synthesise germanosilicate zeolites in this more sustainable fashion. Monetary cost of germanium precursors are one of the main hurdles for widespread use of these structurally complex zeolite types. Solvent-free protocols promise to be an atom-efficient alternative to conventional hydrothermal synthesis and may present means for a more feasible approach for these heteroatom zeolites.

The development of a mechanosynthesis protocol for the formation of sodium coordination polymers is the topic of the final chapter of the work carried out. This class of framework material shows great promise as environmentally benign active component in sodium ion batteries, but is fighting obstacles in large scale production. Mechanochemistry can provide means of overcoming such drawbacks and lab-scale experiments may be translatable more easily to large scale fabrication. Several carboxylic acids are used as reagents to probe the generalisability of the method and test its limitations with respect to chemical variation.

Chapter 3

Experimental methods

3.1 Hydrothermal synthesis of zeolites

The most common synthesis techniques to produce zeolites is through the so-called hydrothermal route.[1] It is based on mimicking the conditions present during the natural formation of zeolitic minerals, namely temperatures roughly between 100–200 °C and pressures above ambient conditions. Reproducing these is possible by utilising autoclaves, sometimes referred to as “steel bombs”, which are built to not only withstand such conditions but also do so in a relatively safe manner. In these sealed reaction vessels, autogenous pressure is generated due to heating the aqueous solution containing all reagents to a temperature beyond its boiling point. The safety features of the autoclave include a spring, allowing for some deviation in pressure, as well as pressure plates. Additionally, the chemicals are not placed directly into the stainless steel autoclave, but are rather added to a liner usually made of PTFE (polytetrafluoroethylene, Teflon). This material is inert to most chemical reactions and thermally robust under the typical conditions for zeolite synthesis. Example photos of an autoclave and its parts are shown in Figure 3.1.

Prior to the heat treatment, the starting materials need to be dissolved, at least partially, in water. This is performed using polymer-based labware, mostly PTFE beakers and stirring equipment. The low solubility of the reagents, such as fumed silica, require mineralising agents, either strong bases or fluoride, as found in hydrofluoric acid, HF or ammonium fluoride, NH_4F. The silicon (or other T atom) sources are only appreciably soluble under these conditions. However, in order to avoid dissolving parts of commonly used glassware, especially in the presence of fluoride, a change to inert materials such as the mentioned PTFE is necessary. This also helps to avoid contaminating the reaction media with alkali and earth alkali metal ions present in glassware, which often have an adverse effect on the desired structure-direction towards a specific zeolite framework.

Figure 3.1. Photos of a fully assembled autoclave and its individual parts, including spring, pressure plates and a PTFE liner.

This dissolution does not necessarily need to be complete, since conducting reactions under hydrothermal conditions enables higher solubilities of the reagents. This high temperature and pressure environment also allows structural complexity in the product phases. Only the simplest zeolite framework types, such as **LTA**, **SOD**, or **FAU** can be prepared under ambient pressure conditions, whereas more challenging structures require the described harsher environments.

3.2 Mechanochemical synthesis

Mechanochemical reactions in this thesis were conducted in three different ways: 1) manually, using mortar and pestle, 2) using a shaker ball mill, and 3) using a rotary ball mill.

The main advantage of a manual grinding setup is the availability of the equipment, which every or at least most labs will own, especially ones focused on solid materials. Likewise, the progression of unknown reactions is easy to follow for cases where distinct (by-)products are formed or obvious changes to the reaction mixtures occur. This could be the liberation of occluded solvent such as water, which can result in the transformation of a solid mix of powder into a paste. This is not necessarily unequivocal evidence that a reaction has taken place, but may still indicate changes in the structure of some of the reagents which may be beneficial for the desired outcome. Similarly, formation of an intermediate such as the release of ammonia when using an ammonium salt as reagent can be detected by its distinct smell, or by using wet pH paper, providing evidence for the reaction of the starting material. Finally, the products may exhibit a different colour compared to reagents. This is especially the case for transition metal complexes or other coordination compounds.

Despite these benefits, manual grinding suffers from drawbacks regarding reproducibility or also insight into reaction mechanisms. It is rather difficult to assess the energy put into a mixture by using manual labour. There may be some merit to attempting comparative reactions if only one person conducts them, but even so it will be quite difficult to exert the exact same amount of force onto the chemicals, especially for longer periods of grinding. Likewise, it is rare that published work considers the dimensions of the used equipment, other than that the grinding bowl is wide enough to accommodate the amount of used reagents. As a result, researchers have gone over to using ball mills for a more robust reaction setup, which allows parametrisation of the mechanochemical process and results have higher reproducibility.

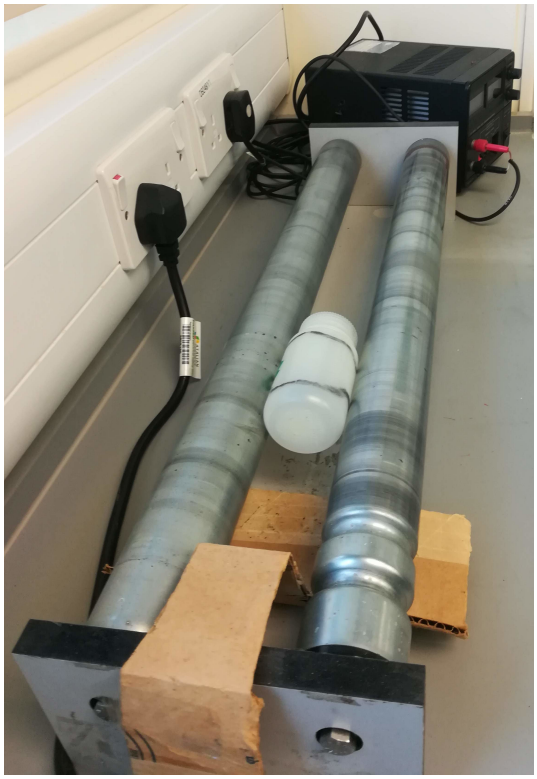

Figure 3.2. Photo of the bespoke rotary ball mill used in this work.

Ball mills are well suited for automating mechanochemical processing by keeping the complexity of instrumentation low, while adding discrete options to adjust reaction conditions.[2] Two kinds of ball mills were used in this work, a rotary mill which is typically used for particle diminution, and a shaker mill which is often operated when using small reaction scales but can induce greater forces. Another commonly used mill in a laboratory setting are planetary ball mills, in which the milling vessel and the plate it stands on are rotated along their vertical axes but in opposite directions.

The used rotary ball mill is a simple construction and was built previously by other members of the research group. A photograph is shown in Figure 3.2, showing one freely rotating rod, and the second rod, connected to a small electrical motor. In principle, any flask that is large enough to not fall through the gap between the rods can be used. In practice, conventional 125 mL polypropylene bottles, regularly used in labs, have proven to be a reliable choice. By adjusting the applied voltage of the motor, the rotation speed (frequency) can be altered.

The second type of ball mill used in this work is the commercial laboratory shaker mill Retsch Mixer Mill MM 400, displayed in Figure 3.3. Milling vessels are moved along horizontally (as indicated in Figure 3.3 with arrows), leading to the milling media inside to collide with the milling flask walls or if multiple balls are used also with each other. The

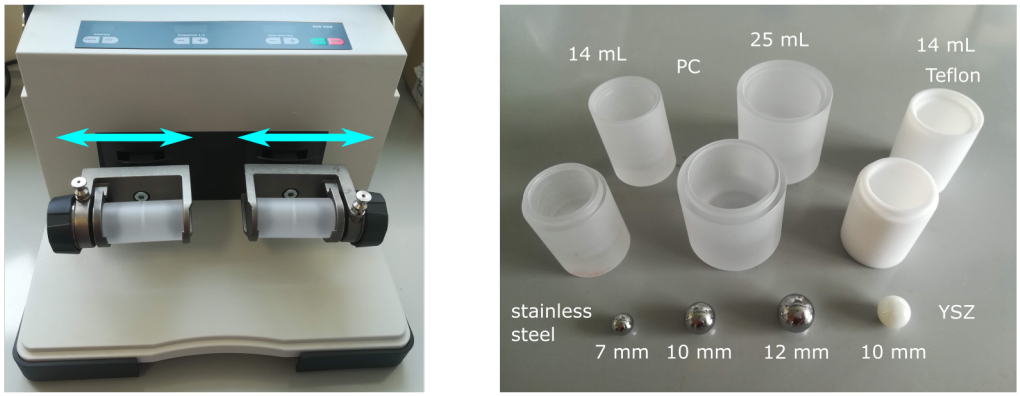

Figure 3.3. Photo of the commerical shaker ball mill used in this thesis and used equipment. Bespoke milling vessels made of polycarbonate (PC) or Teflon (PTFE) in two sizes and milling balls of stainless steel or yttrium stabilised zirconia (YSZ) are shown.

frequency of this back and forth motion can be adjusted, effectively altering the energy input into the reaction system. Both milling vessels and their content need to be of equal mass to ensure smooth operation and an evenly balanced instrument. For this work, milling vessels of polycarbonate (PC) and PTFE were used. These materials are readily available and flasks of different sizes were produced at the university's workshop. PTFE is a good choice due to its chemical robustness. Polycarbonate is less durable, but allows for visible observation of the reaction during milling due to its transparency. Chosen materials for milling media were stainless steel and YSZ (yttrium stabilised zirconia). Steel is a commonly used material as it is rather hard and most of the mechanical energy can be transferred into the chemicals of the desired reaction. However, abrasion of the material occurs, especially at high frequencies, potentially contaminating the sample with iron, nickel, or chromium impurities. Likewise, the material may undergo undesirable side-reactions with the chemicals used. Where these issues may be of concern, YSZ milling media are a suitable alternative. Despite the lower density of the material (roughly a quarter of steel), it is chemically much more inert and is also typically less prone to abrasion.

3.3 X-ray diffraction, XRD

The physical basis for diffraction techniques is the diffraction of an incoming X-ray beam by the electrons surrounding atoms in the investigated sample.[3,4] This is possible, if the wavelength (i.e. the energy of the particles) is on the same order of magnitude as the interatomic distances. This is true for X-rays, electromagnetic waves with a wavelength on the scale of 1×10^{-11}–1×10^{-8} m, coinciding with the distance between individual

atoms in solids, which is typically around 1 Å or 1×10^{-10} nm.

3.3.1 Crystal lattice and symmetry

In principle, every compound does scatter X-rays, however, crystalline materials can be distinguished from amorphous, glassy materials due to their distinct diffraction patterns. These patterns are caused by the specific, periodically repeating nature of the atomic arrangement in the structure, thus crystals can be described by a lattice. Due to the high and long-range ordering in crystals, it is convenient to choose a *unit cell*, which contains all information needed to reproduce the whole lattice. The unit cell is a parallelepiped, a polyhedron of six, pair-wise identical and parallel parallelograms; the most symmetric of it is a cube, both shown in Figure 3.4. The unit cell is chosen so that it encompasses the smallest volume of space, that by translation along the three dimensions of space (shifting) reproduces the entirety of the lattice. It is defined by six lattice parameters: three lengths of the unit cell edges a, b, and c and the three angles between each pair of cell edges α (between b and c), β (between a and c), and γ (between a and b).

In order to classify the different crystal structures, crystal lattices are combined, depending on the basic geometric shape of the unit cell. Table 3.1 shows a comparison of all seven crystal lattice systems, the 14 lattice types (also called Bravais lattices) and the imposed restrictions on the corresponding unit cells. A primitive lattice is possible for all systems, where lattice points are at the corners of the unit cell. For the monoclinic, orthorhombic, and cubic systems face centrings on one (A, B, or C) or all (F, from German "flächenzentriert") of the faces are possible. A body-centred unit cell (I, from German "innenzentriert") can be found for three of the crystal systems. In the trigonal system, a primitive or a rhombohedral unit cell can be chosen.

Next to the knowledge about the dimensions of the unit cell, information about the

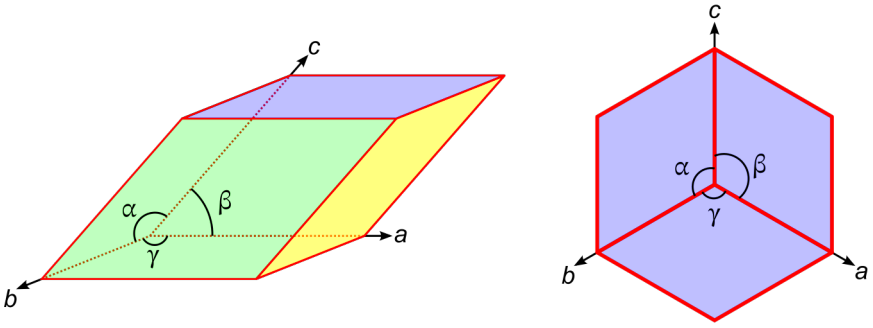

Figure 3.4. Unit cell for arbitrary lattice parameters and the more specific case of a cubic unit cell with all lengths equal and all angles equal to 90°.

Table 3.1. Crystal lattices systems, possible lattice types, and restrictions on lattice (unit cell) parameters.

lattice system	lattice types	unit cell restrictions
triclinic	P	–
monoclinic	P, C (I)	$\alpha = \gamma = 90°$
orthorhombic	P, C (A), I, F	$\alpha = \beta = \gamma = 90°$
tetragonal	P, I	$a = b$ $\alpha = \beta = \gamma = 90°$
trigonal	P	$a = b$ $\alpha = \beta = 90°, \gamma = 120°$
hexagonal	P	$a = b$ $\alpha = \beta = 90°, \gamma = 120°$
cubic	P, I, F	$a = b = c$ $\alpha = \beta = \gamma = 90°$

position of atoms within it is crucial. Typically, a unit cell contains several molecules or ensembles of atoms which are related to each other by symmetry. The most simple entity is called *asymmetric unit* and applying all except purely translational symmetry operations on it generates all other atom positions in the unit cell. These symmetry operations are rotation about a 2-, 3-, 4-, or 6-fold axes, reflection through a mirror plane, and inversion through a point. Additionally, there are combinations of these with translations resulting in screw axes (rotation plus translation) and glide planes (reflection plus translation). Finally, a rotation can also be combined with inversion.

Looking at a single entity such as a molecule and keeping one point in it fixed, all possible, unique symmetry operations are combined to form its point group. In total, there are 32 crystallographic point groups, ranging from 1 (Hermann-Maugin notation, C_1 in Schönflies notation) with only a "1-fold" rotation axis, up to groups with a high order of symmetry such as m$\bar{3}$m (O_h) present in octahedral objects and cubes. In order to describe a full crystal system, the point group symmetry needs to be extended to space group symmetry, which also includes considerations of translations, i.e. the crystal systems. Space groups are usually stated in the Hermann-Maugin notation. As an example, the space group C2/m (or more explicitly C 1 2/m 1, space group number 12) describes a monoclinic, C-centred unit cell, with a 2-fold rotation axis along the *b*-axis and a mirror plane perpendicular to it, in the *ac*-plane.

Another important part used in describing crystal systems are Miller planes. These are two-dimensional sections through space, which are chosen with respect to the unit

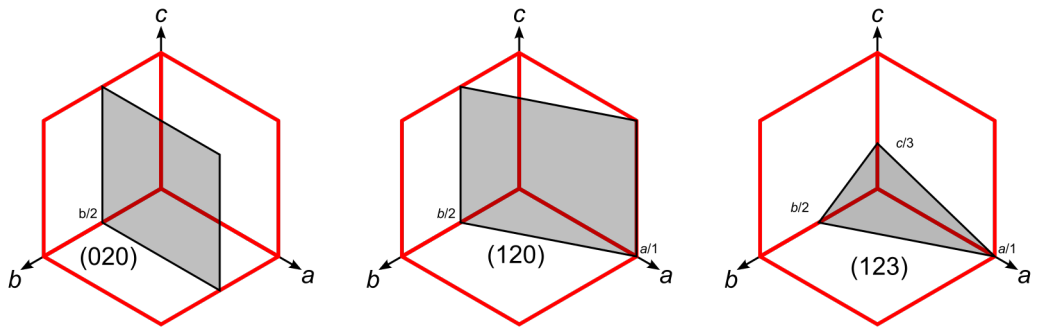

Figure 3.5. Intersections of (020), (120), and (123) Miller planes with the unit cell edges (red).

cell. They are stated using three integers (in the hexagonal system a fourth integer is added in some descriptions) indicating how often the plane intersects the respective unit cell edge. As an example, the (123) plane crosses the unit cell once in the a direction, twice in the b direction, and thrice in the c direction. These integers are referred to as h, k, and l (Miller) indices.

3.3.2 Diffraction in a crystal

Due to the ordered arrangement of atoms in a crystal, incoming X-ray beams are diffracted, and can be described as inelastic, coherent scattering of photons. For X-ray diffraction experiments, the approximation of kinematical diffraction is typically sufficient, which means that it is assumed that only one diffraction event occurs. Dynamical diffraction, which accounts for multiple events, is more relevant in electron diffraction, where the high energy of electrons warrants this more complex theory. In an approximation, the electrons surrounding each atom can be thought of as a point off of which the X-rays are scattered spherically. If the scattered waves are in phase with each other, they interfere constructively and their amplitude is doubled, whereas if they are completely out of phase, they cancel each other out. Since a crystal lattice can be viewed as a large, three-dimensional diffraction grating due to its repeating, periodical nature, the secondary, diffracted X-ray beams that leave the sample have heavily increased amplitudes depending on the geometrical orientation and can be detected using dedicated instruments.

The geometrical dependence means that complete constructive interference only occurs at specific incident angles for a given spacing between planes in the lattice, the aforementioned Miller planes. A schematic visualisation is shown in Figure 3.6. The Bragg equation (Equation 3.1) is a mathematical representation of this principle and is

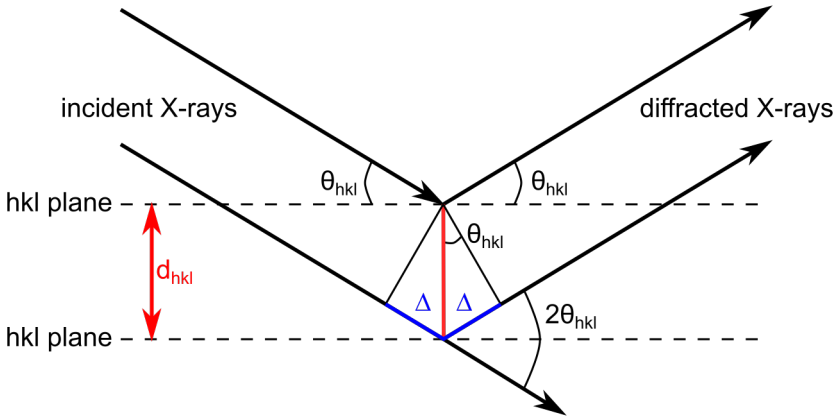

Figure 3.6. Geometrical visualisation of Bragg's law.

used in all interpretations of X-ray diffraction experiments.

$$2d_{hkl} \sin \theta_{hkl} = n\lambda \tag{3.1}$$

For a specific wavelength λ, the required angle θ depends on the distance (d-spacing) between two consecutive Miller planes of the same hkl indices. The path difference 2Δ of two parallel X-rays is an integer multiple of the wavelength (nλ) and can also be expressed through the trigonometrical considerations with the sine of the enclosed angle θ. This means that by measuring the angle of the diffracted beam with respect to the incident X-rays, information about the crystal structure can be obtained.

3.3.3 Diffraction experiments

X-rays for diffraction experiments are usually produced using an X-ray tube which contains a metal filament (typically tungsten) which is heated to a temperature where it emits electrons. These are then accelerated and focused onto a target metal. The energy of the electrons is sufficient to knock out inner shell electrons of the target metal atoms. When higher shell electrons transition into the energetically lower and thus favoured inner shells, the energy difference is emitted as X-ray radiation. Since electron energy levels are unique for each element, the produced X-rays are characteristic for the used metal. This means that the target metal can be chosen so that the produced X-rays are of a wavelength appropriate for the desired experiment. For an optimal experiment, a monochromator is employed to select only one specific wavelength out of the generated X-ray spectrum. The most intense line is $K\alpha_1$, originating from an L-K shell transition. The two most used elements are copper ($\lambda(K\alpha_1) = 1.5406$ Å) and molybdenum ($\lambda(K\alpha_1)$

= 0.7093 Å). The longer wavelength of Cu means that a smaller angular range can be covered, however, the diffraction pattern is more spread out, and intensities are more easily distinguished from another. Further benefits of using copper are its low cost and the ease of handling with respect to cooling to prevent melting of the target.

3.3.3.1 Single crystal X-ray diffraction, SCXRD

When shining X-rays on a single crystal, the beams diffracted by the crystal lattice produce a spot pattern, shown in Figure 3.7. This diffraction pattern is in itself a lattice. It is referred to as *reciprocal lattice* since spacings in the real space (or direct space) crystal lattice are inversely correlated to the corresponding distances in the diffraction pattern. From this information, the unit cell parameters can be determined. A diffraction pattern also exhibits symmetry which corresponds to the symmetry of the crystal lattice it originates from. The difference is that since a pattern is only a two-dimensional projection of the reciprocal lattice it has point group symmetry, in contrast to the space group of a three-dimensional lattice. Thus, only by analysing a combination of several patterns the correct space group can be assigned. Further to these geometry and symmetry considerations, the intensities of the diffraction spots correlate with the amount of electrons the incident X-ray has interacted with, which means that they can be used to calculate the position of atoms within a crystal structure.

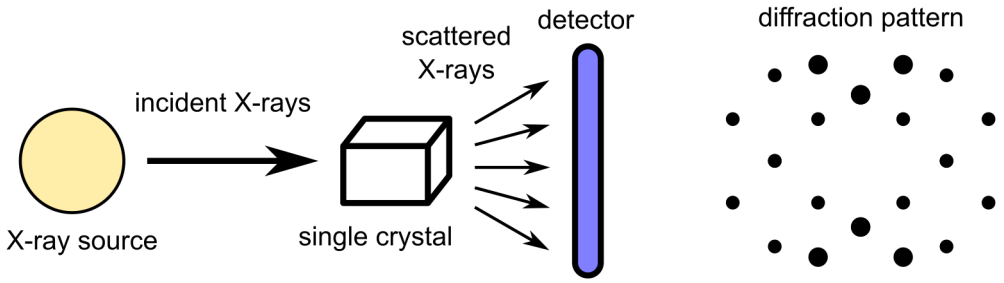

Figure 3.7. Schematic representation of a single crystal X-ray diffraction experiment and an exemplary diffraction pattern.

A practical necessity for successful determination of a crystal structure is the quality of the single crystals. For common SCXRD diffraction experiments, the crystal should be roughly 5 µm in each direction to ensure a sufficiently large diffraction volume. Dedicated instrumentation at large-scale synchrotron facilities is more lenient in this respect, due to higher brightness of the X-ray beam. Nonetheless, such restrictions are sometimes difficult to overcome in the synthesis of materials, especially zeolites. Often only dedicated studies on synthesis conditions find ways to produce samples suitable

for SCXRD. The size limitation but also the often seen polycrystalline nature of zeolite samples as well as common intergrowths of several crystals makes crystal structure determination of new zeolite phases challenging.

3.3.3.2 Powder X-ray diffraction, PXRD

X-ray diffraction from a polycrystalline powder follows the same principles as SCXRD, but instead of discrete diffraction spots, the detected pattern has the form of rings, schematically depicted in Figure 3.8. This is caused by the large number of crystals present in the sample, which are randomly aligned with respect to the incident beam so that scattering in different orientations is observed. Interpretation of the collected diffraction pattern is performed using only a slice of the circular pattern and the intensity of the reflection is plotted against the incident angle. Although a PXRD experiment can be performed much more rapidly than SCXRD, more information is lost and a full structure solution without prior knowledge about the crystal structure is often difficult. However, PXRD is a bulk characterisation technique and all present crystalline phases in a sample contribute to the observed pattern. Although a crystal structure may be obtained by SCXRD the selected crystal may only be a minor phase of the entire sample. Thus, PXRD can be used for quick phase identification of materials with a known structure. PXRD patterns may be viewed as a fingerprint of a given crystal structure and measured patterns can be compared to simulated ones rather easily. Further to this purely structural information, the peaks in the powder pattern also provide insight into the crystal shape and size by analysis of the peak intensities and the peak shape, respectively.

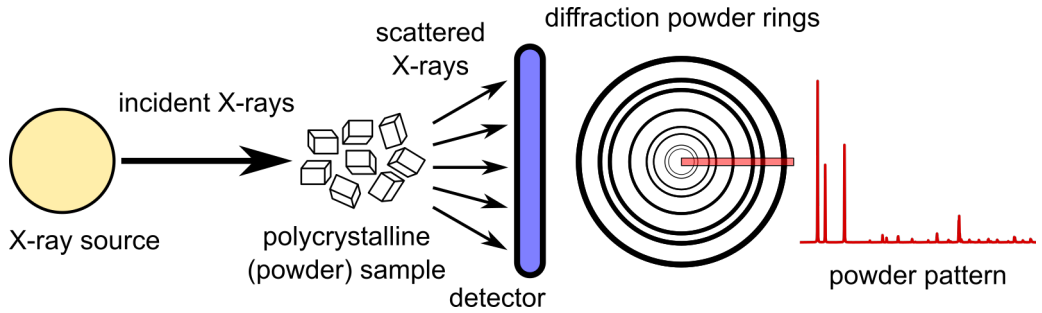

Figure 3.8. Schematic representation of a powder X-ray diffraction experiment and exemplary ring pattern and a powder pattern obtained by selecting a thin slice of the ring pattern.

PXRD measurements are conducted using either in reflectance or in transmission geometry. Reflection PXRD experiments are easy to set up due to horizontal alignment of the sample and show high peak intensities and good signal-to-noise ratios. It is also advantageous for samples which strongly absorb X-rays. However, this method is

prone to show preferred orientation effects, especially for flat crystals. Performing the experiment in transmission geometry often has the benefit of requiring lower amounts of sample is less affected by non-random orientation of crystals in the sample. In both cases, either X-ray source, or detector, or both can be moved with respect to the sample in order to cover the desired angular range. The step size of this movement and dwell time can be adjusted to the needs of each measurement and high quality data is obtainable for both cases.

Due to the polycrystalline nature of all samples produced in this thesis, only PXRD was used for analysis by X-ray diffraction. Both reflection and transmission geometry diffractometers were used, the choice mainly depending on sample amount as no particular limitations due to elemental composition or other factors needed to be considered.

3.4 Electron microscopy

Electron microscopy follows the similar principles as conventional light microscopy, but the sample is irradiated using a beam of electrons. As these particles have much higher energy than photons of visible light, the achievable resolution is much higher and features on nanometre scale can be investigated. Several techniques have been developed over the years and different types of data can be obtained depending on the specifics of the instrument and the employed conditions. In all cases a beam of electrons is generated in an electron gun (source) and focused onto a sample. Since electrons are charged particles their trajectories can be altered using electromagnetic lenses. There are two main types of guns that are used: thermionic and field emission. In thermionic sources, a tungsten filament or LaB_6 (lanthanum hexaboride) crystal is heated to temperatures high enough so that the thermal energy overcomes the work function of the material and electrons are emitted. Due to the high temperatures the filament burns out regularly and needs to be exchanged frequently. The produced electron beam is of suitable quality, but does not reach resolutions achievable with field emission sources. LaB_6 is more robust than tungsten and produces brighter electrons, however, is also more expensive.

Field emission guns (FEG) also use tungsten as electron emitter but require a thin, single crystalline wire. An electrical field is applied to the sharp tip of the wire, causing an oversaturation of electrons in this region and increasing the likelihood of electrons escaping from the metal. This drastically reduces the required temperatures for emission and prolongs both lifetime of the material and brilliance of the electron beam. In extreme cases the emission of electrons may even occur at room temperature (cold FEG).

Primary electrons from the electron beam interact with the sample in various ways, some of which can be exploited to characterise the sample, whereas others can lead to degradation of the material. There are two main electron microscopy methods: scanning electron microscopy (SEM) and transmission electron microscopy (TEM). Broadly speaking, investigations using an SEM focus on interactions where detectors are on the same side of the sample as the electron gun, whereas TEM has (most of) its related detecting devices on the opposite side of the sample. Desired electron-matter interactions are discussed below in sections about the corresponding microscope dedicated to their investigation. Although not a microscopy technique per se, energy-dispersive X-ray spectroscopy (EDS) is a common supplementary technique that is available for all types of electron microscopes and is used for qualitative and quantitative analysis of the elemental composition of the sample.

Besides the advantageous effects of irradiating a sample with a beam of electrons, their high energy can also have severe side-effects. Injecting electrons into a material leads to accumulation of negative charges. For metals or other conductive samples, the surplus of electrons can be directed out of the sample by grounding the sample stage and holder. However, for specimen which are electrically insulating this is not possible and leads to so-called *charging* of the material and obtained images are oversaturated. This is especially true when using secondary electrons (see below). Usually, the charged part of the sample is irreversibly damaged and cannot be investigated any further. Procedures to avoid charging of samples can be done during sample preparation as well as by adjusting imaging conditions. Lower acceleration voltages and short dwell times can be useful for samples where the build up of charging only progresses slowly. For SEM investigations and in more severe cases, the sample can be coated with a thin layer of an electrically conductive material. Typically metals such as gold or platinum, or also carbon, are used since a nanometre thin film of these materials can be deposited on the sample by sputtering, without altering the surface and morphology of the materials.

Additional to charging phenomena, structural degradation of the sample may be encountered. This is often the case for organic matter and organic based materials such as polymers, or metal-organic frameworks. Although such structural collapse is more severe in high energies used in TEM, even SEM analysis can lead to a breakdown. As mentioned for charging effects, lowering the dose of the electron beam (i.e. number of electrons per unit area) may prolong the integrity of the sample long enough for the desired analysis. Further, adjusting the beam energy to both lower but often higher

voltages may decrease radiation damage. Increasing the acceleration voltage can reduce the number of interaction on the surface of the sample, thus leaving the sample intact for longer time periods. Finally, cooling the sample is an expensive but tremendously successful way of preventing beam damage. Cryo-electron microscopy, especially during TEM operation, even enables investigation of biological matter.[5]

3.4.1 Scanning electron microscopy, SEM

In scanning electron microscopy,[6] the electrons are accelerated to an energy typically in a range of 1–30 keV. A schematic setup of an SEM is shown in Figure 3.9. Prior to reaching the sample, the beam passes through the optics of the instrument. The first of two sets of lenses is the condenser lens which is used to adjust the spot size of the beam, i.e. its spread. Scanning coils are used to scan the beam across the sample surface. The following objective lens is responsible for focusing the beam onto the sample. In order for the scanning to run smoothly, deflector coils are additionally present. The lens system must be aligned regularly to ensure high quality imaging conditions. Further, imperfections in the optical system can lead to astigmatism, which means that a circular object would appear elliptically distorted. This can be corrected using electromagnets referred to as stigmators.

An initial, important consideration is the penetration depth of impacting electrons and the resulting interaction volume. This is influenced by the energy of the incident beam but also by the elemental composition of the sample. Higher energy and lower atomic mass (thus lower number of electron in the sample) result in an enlarged interaction volume. Depending on the characteristic to be analysed, this may be advantageous but can also have an adverse effect. It is important to be aware of this phenomenon and consider the underlying interactions when interpreting SEM images. Elastic scattering of electrons in a given material can be simulated, providing a visual representation of the interaction volume in a material. For example, the volumes for incident beams with acceleration voltages of 5, and 20 kV in metallic copper and silica are shown in Figure 3.10.

Elastic scattering of primary electrons is the main propagation mechanism in the sample leading to large interaction volumes. If the statistics of these events are high enough, electrons can be scattered out of the sample, back towards the beam itself. These electrons are referred to as backscattered electrons (BSE). The probability for this overall process is heavily dependent on the mass of the atoms, as a higher number

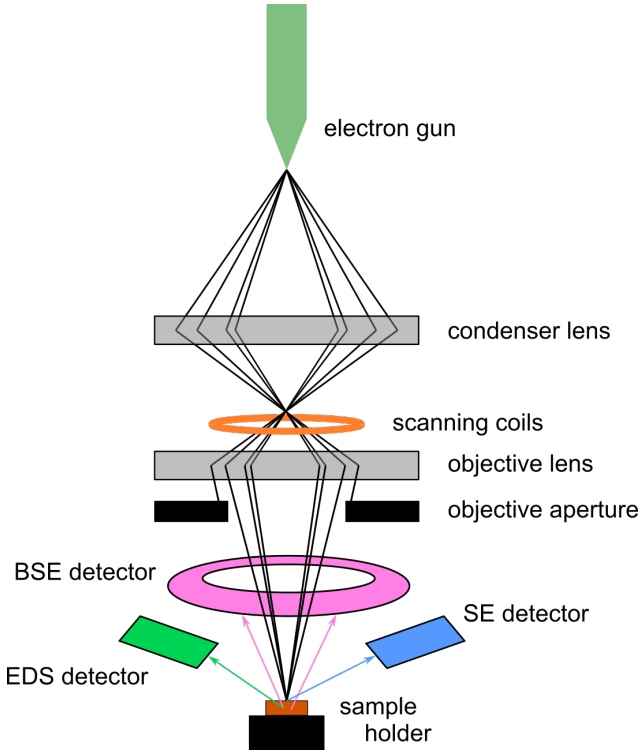

Figure 3.9. Simplified schematic of a scanning electron microscope, showing the optics of the column including lenses and three common detectors to collect backscattered electrons (BSE), secondary electrons (SE), and emitted X-rays with an energy-dispersive X-ray spectrometer (EDS).

of electrons increases the likelihood for elastic scattering events. The contrast in the produced image is generated due to the probabilistic difference for the different elements present in the sample, thus referred to as atomic number contrast. The corresponding BSE detector is torus-shaped and placed above the sample, around the incident beam (compare Figure 3.9).

Beam electrons are also able to knock out loosely bound electrons in the outer shells of atoms in the sample by inelastic scattering. The produced free electrons, called secondary electrons (SE) have comparatively low energy, which means that their mean free path is rather short. Thus, only a low percentage of all generated SEs are able to escape the sample and are detectable. Despite this low yield, the number of incident electrons ensure a sufficient amount of SE for analysis. Since detected SEs only originate from the surface of the sample, this technique is well suited to investigate the texture and morphology of the specimen. Areas that are closer to the detector appear brighter in the obtained image, whereas regions in valleys are darker. Thus, objects in an SE image appear three-dimensional as a result of their topographical features.

a) Electron trajectories in copper using an acceleration voltage of 5 kV.

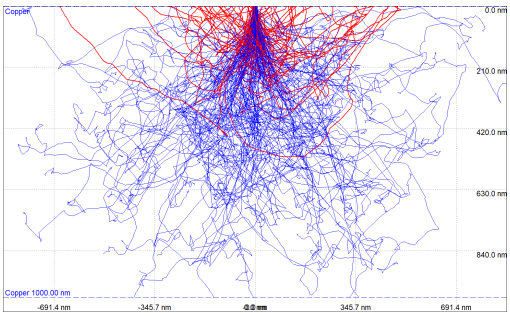

b) Electron trajectories in copper using an acceleration voltage of 20 kV.

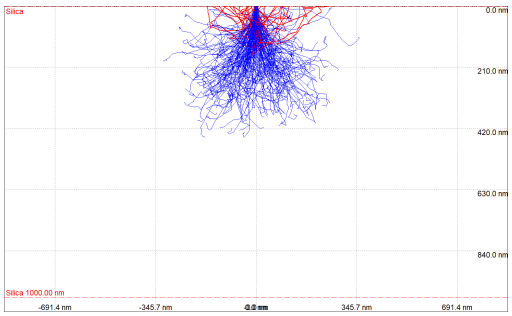

c) Electron trajectories in silica (SiO_2) using an acceleration voltage of 5 kV.

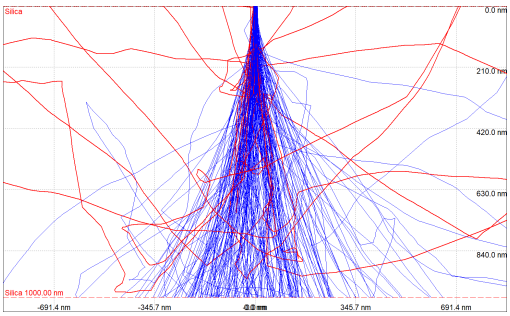

d) Electron trajectories in silica (SiO_2) using an acceleration voltage of 20 kV.

Figure 3.10. Monte Carlo simulations using the software CASINO,[7] showing the penetrations depth of electrons and the resulting interaction volume in the first 1000 nm using 500 trajectories. Red paths indicate electrons that are able to escape the material as backscattered electrons (BSE) and blue lines represent electrons that stay in the sample.

3.4.2 Transmission electron microscopy, TEM

As the name suggests, transmission electron microscopy relies on beam electrons being able to pass through the sample.[8] This is facilitated on the one hand by higher acceleration of the electrons to typically 100–300 keV and on the other hand by ensuring thin samples of a few hundred nanometres in thickness along the beam axis. The electron–matter interaction in a TEM results in diffraction of the beam (electron diffraction) yielding a diffraction pattern below the sample that can be recorded. In contrast to X-rays, an electron beam can be bent easily and focused using electromagnetic lenses, making a projection of the object that caused the scattering possible, leading to TEM images.

A schematic overview of the optics in a TEM are shown in Figure 3.11. Similar to the column in an SEM, the electron beam passes through a set of lenses before it reaches the sample. However, in a TEM the objective lens is placed below the sample, where the diffracted beam is passed through a second set of optics forming the image and focusing it onto the image plane, where a camera is placed for recording.

TEM is a valuable technique which can give a lot of information about a sample. It does provide some insight into the shape of individual particles, but since it is only a

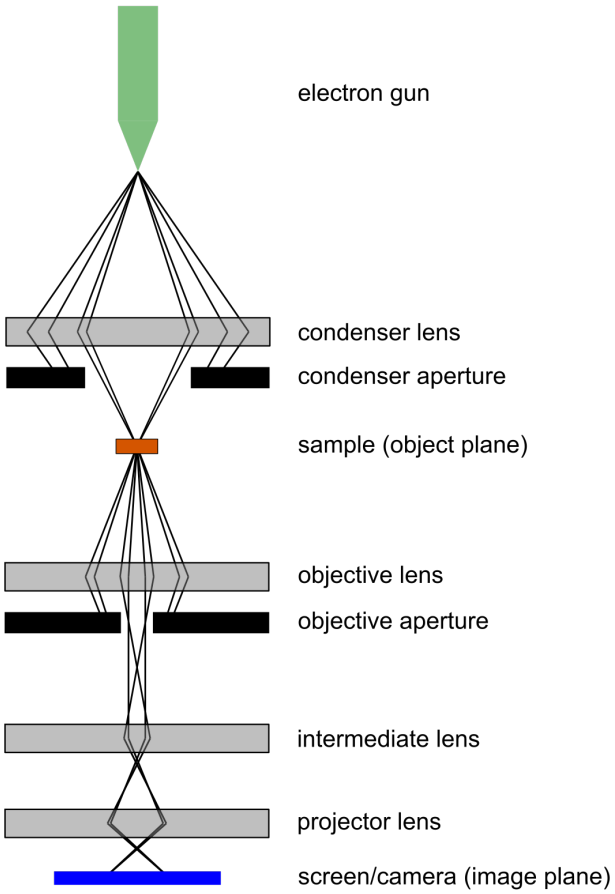

Figure 3.11. Simplified schematic of a transmission electron microscope (TEM) showing the optics of the column and image formation parts within a TEM.

projection, SEM is usually preferred. However, for materials with particle sizes below 100 nm, often only the resolution of a TEM is sufficient to distinguish individual particles. More importantly, since the technique is based on diffraction, information about the crystal structure can be obtained. If the observed crystal is aligned correctly with respect to the incident beam, lattice fringes corresponding to Miller planes (see also section 3.3.1) are visible in the image and allow determination of their d-spacing. This can help to identify different phases in the sample as well as aid in the structure determination process.

Further to conventional imaging methods in TEMs, electron diffraction patterns can be obtained readily.[9] Due to operational restrictions, often only individual frames are acquired, once perfect alignment of the crystal has been achieved. This is a slow and tedious process, especially compared to X-ray diffraction. However, due to the much stronger interaction of the high energy electrons with the sample, the size of a crystal can be much smaller compared to single crystal XRD and only 100 nm may be sufficient. In recent years, a lot of research has gone into the development of electron diffraction

techniques, specifically so-called 3DED (three dimensional electron diffraction).[10–12] It combines the advantages of electron diffraction with the collective knowledge from SCXRD and has been shown to be a powerful complementary technique for structure solution of novel materials. As mentioned above, especially framework materials such as zeolites and also MOFs and coordination polymers are often only obtained as polycrystalline powder, impeding determination of their structure by XRD methods. With the advent of the 3DED techniques such as cRED (continuous rotation electron diffraction), precession ED, ADT (automated electron diffraction tomography), and microED, crystal structures of many materials could be solved and refined.[13–15]

3.4.3 Energy-dispersive X-ray spectroscopy, EDS

X-rays are a side product of one of the possible interactions of the primary electron beam with the sample. Electrons of high energy are able to knock out inner shell electrons in atoms of the material, resulting in an electron hole. These are rapidly filled with an electron from a higher shell, which relaxes into the lower energy state. The energy difference is emitted as X-ray radiation which can be detected. Since the energy levels and their differences are characteristic for each element, the detected X-rays can be assigned to elements, thus providing means for qualitative but also quantitative determination of the elemental composition of the investigated sample. Keeping in mind the interaction volume description presented above (see Figure 3.10), the field of view or the area selected for EDS analysis may or may not be entirely representative of the volume from which X-rays are produced. This is important to keep in mind when analysing samples and only appropriate regions should be selected, if possible. Furthermore, elemental compositions determined from an individual EDS spectrum should not be considered representative of the entire sample. It is preferred to acquire multiple spectra of different particles to ensure unbiased and reproducible results. EDS detectors are often part of standard instrumentation of both SEM and TEM microscopes and the spectroscopic analysis can be performed routinely alongside microscopic investigations.

3.5 References

(1) C. S. Cundy and P. A. Cox, *Microporous Mesoporous Mater.*, 2005, **82**, 1–78.

(2) P. Balaz, *Mechanochemistry in Nanoscience and Minerals Engineering*, Springer Berlin Heidelberg, Berlin, Heidelberg, 2008.

(3) C. Hammond, *The Basics of Crystallography and Diffraction*, ed. C. Hammond, Oxford University Press, 4th edn., 2015.

(4) V. K. Pecharsky and P. Y. Zavalij, *Fundamentals of Powder Diffraction and Structural Characterization of Materials*, Springer US, Boston, MA, 2009.

(5) R. Henderson, *Angew. Chemie Int. Ed.*, 2018, **57**, 10804–10825.

(6) J. I. Goldstein, D. E. Newbury, J. R. Michael, N. W. Ritchie, J. H. J. Scott and D. C. Joy, *Scanning Electron Microscopy and X-Ray Microanalysis*, Springer New York, New York, NY, 2018.

(7) H. Demers, N. Poirier-Demers, A. R. Couture, D. Joly, M. Guilmain, N. de Jonge and D. Drouin, *Scanning*, 2011, **33**, 135–146.

(8) D. B. Williams and C. B. Carter, *Transmission Electron Microscopy*, Springer US, Boston, MA, 2009.

(9) X. Zou, S. Hovmöller and P. Oleynikov, *Electron Crystallography Electron Microscopy and Electron Diffraction*, Oxford University Press, 2011.

(10) M. Gemmi, E. Mugnaioli, T. E. Gorelik, U. Kolb, L. Palatinus, P. Boullay, S. Hovmöller and J. P. Abrahams, *ACS Cent. Sci.*, 2019, **5**, 1315–1329.

(11) M. Gemmi and A. E. Lanza, *Acta Crystallogr. Sect. B Struct. Sci. Cryst. Eng. Mater.*, 2019, **75**, 495–504.

(12) T. Gruene and E. Mugnaioli, *Chem. Rev.*, 2021, **121**, 11823–11834.

(13) M. O. Cichocka, J. Ångström, B. Wang, X. Zou and S. Smeets, *J. Appl. Crystallogr.*, 2018, **51**, 1652–1661.

(14) E. Mugnaioli, T. Gorelik and U. Kolb, *Ultramicroscopy*, 2009, **109**, 758–765.

(15) B. L. Nannenga, D. Shi, A. G. W. Leslie and T. Gonen, *Nat. Methods*, 2014, **11**, 927–930.

Chapter 4

Making ADORable zeolites sustainable

The contents of this chapter are based on data published in:

Daniel N. Rainer, Cameron M. Rice, Stewart J. Warrender, Sharon E. Ashbrook, and Russell E. Morris, *Chemical Science*, 2020, **11**, 7060–7069.
DOI: 10.1039/d0sc02547j

Solid-state NMR experiments, data processing and analyses were performed by Cameron M. Rice and Prof Sharon E. Ashbrook. The help by Dr Stewart J. Warrender with the rotary ball mill setup is acknowledged. Dr Michal Mazur is thanked for his help in teaching me how to operate TEMs.

4.1 Introduction

4.1.1 The ADOR process

The ADOR (assembly-disassembly-organisation-reassembly) process is a zeolite synthesis method which can be viewed as a 3D-2D-3D transformation from a parent zeolite phase structurally related, but still distinct daughter zeolite as described above in section 1.2.3.8.[1] The crucial property of the parent zeolite phase is the intrinsic structural weakness in the form of germanium rich, cubic *d4r* units which connect siliceous layers in frameworks such as **UTL**. The hydrolytically labile Ge−O bond can be cleaved selectively using acidic conditions or water, resulting in the disassembled layers. Depending on the conditions of this hydrolysis, different intermediate zeolitic precursors can be obtained and are subsequently reassembled into fully connected 3D zeolite materials. Using this unique synthesis approach, several new zeolite materials with novel frameworks have been discovered.

A schematic overview of ADOR daughter materials based on the parental **UTL** framework is shown in Figure 4.1. The fully disassembled, layered zeolite phase is called IPC-1P, which is self-stabilised by hydrogen bonding of surface silanol groups, formerly the anchors of the *d4r* units. The suffix "P" indicates the precursor nature of the material, which can be reassembled to the 3D zeolite IPC-4 which exhibits **PCR** framework. If the hydrolysis reaction is conducted under strongly acidic conditions the precursor IPC-2P is obtained. Silicon from the zeolite layers is self-intercalated and the basis for square *s4r* units are formed in the interlayer space. However, the material is not yet fully connected and requires the typical heat treatment to form the final IPC-2 (**OKO**). The concentration of the used hydrochloric acid has a profound effect on the formed zeolite intermediate and enables control over extent of this re-intercalation. Adjusting the concentration to 1.5 M results in the ratio of layers connected by single oxygens (as in **PCR**) and by *s4r* (like in **OKO**) as exactly 1 (i.e. 50 % **PCR** and 50 % **OKO**). The precursor has been named IPC-6P and its reassembled product correspondingly IPC-6. It is a highly crystalline single phase material, but due to the inherent disorder in the stacking sequence of the two linker types, the assigned framework type code ***PCS** is affixed with an asterisk. In a single hydrolysis reaction, the transition from IPC-1P over IPC-6P to IPC-2P is gradual and dependent on the rates of bond making and breaking, which in turn hinges on the acidic concentration.[2]

Indicated in Figure 4.1 are also the interlayer distances of intermediates and final

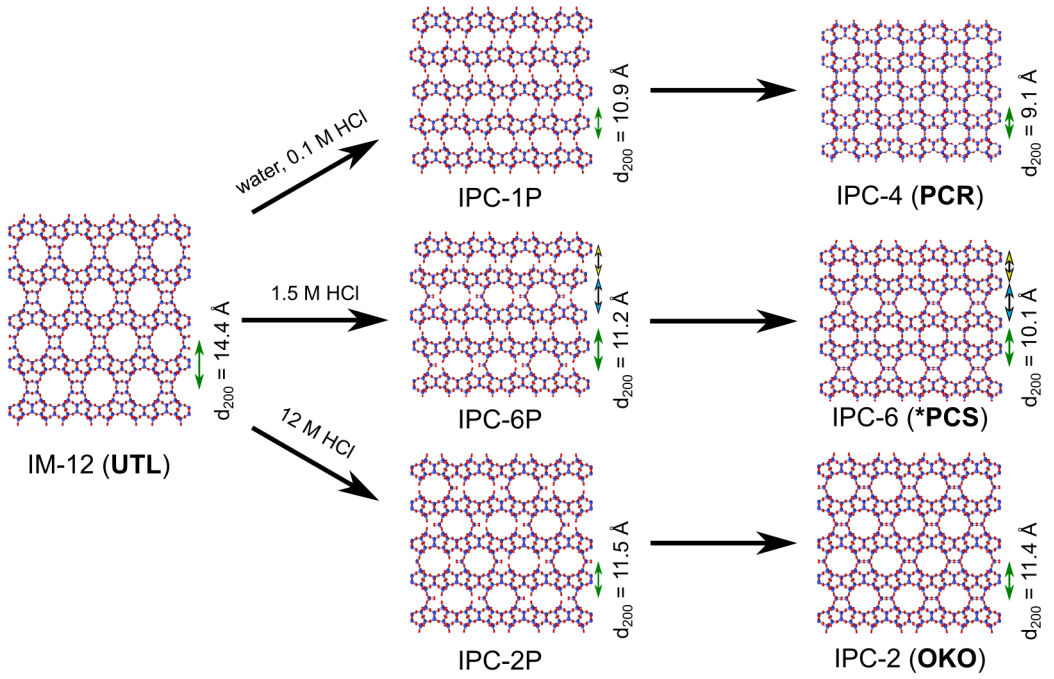

Figure 4.1. Structures of ADOR daughter zeolites derived from a zeolite with **UTL** framework. Reproduced from Ref. [3] with permission from the Royal Society of Chemistry.

zeolites. This information is crucial for fast and easy initial determination of the nature of a material obtained from a synthesis by using powder X-ray diffraction.[4] The distance between the layers is equivalent to the crystallographic d-spacing corresponding to the 200 plane in the lattice of these frameworks. This means that the PXRD peak position of the 200 reflection can be used to calculate this interlayer distance. In the case of IPC-1P this value is quite distinct, but the peak positions of IPC-6P and IPC-2P are almost indistinguishable. In this case only reassembly to the final material allows unequivocal assignment by this characterisation method.

4.1.2 Industrial viability of the ADOR process

Although the ADOR process has already been shown to yield several new materials and framework types otherwise unattainable, there are still some drawbacks which cause concern when thinking about potential applications of the method on a larger scale. A big problem is the cost of germanium precursors, which are substantially more expensive than reagents for other elements typically used for zeolite synthesis. This has mainly to do with its lower natural abundance, with only 1.5 mg kg^{-1} in the earth's crust, compared to 2.82×10^5 mg kg^{-1} for silicon and 8.23×10^4 mg kg^{-1} for aluminium.[5] Unfortunately, the necessity for a germanosilicate as parent zeolite appears to be unavoidable, at least at this point in time.

Common zeolites which also contain elements other than silicon such as aluminium and boron are not usually found in specific sites but are typically distributed throughout the framework. This means that even if chemical conditions which would lead to selective removal of these atoms can be devised, the resulting material would most likely not retain any structural integrity. Most other heteroelement zeolites are generally unsuitable due to the low incorporation of the element into the framework. In this case, removal of the element with the more labile oxygen bonding would not lead to a structural change at all and only create defect sites. There is certainly a possibility for specific combinations of elements where the ADOR strategy may prove to be applicable, but for silicate-based zeolites this has not been found yet. Some promising work comes from the area of AlPOs, where Huang et al. showed a closely related type of 3D-3D transformation,[6] as well as Maeda et al. who transformed an AlPO phase to a zinc-AlPO daughter material using a derived lamellar intermediate.[7]

Besides the restriction on the elemental composition of the parent material, the expensive germanium is of course also removed during the hydrolysis and would be treated as waste. This would mean that the most expensive component of the synthesis process overall does not even end up in the final material and is only disposed of. Zhang et al. took on the challenge of salvaging these germanium species from the hydrolysis reaction solution.[8] Solid GeO_2 can be filtered off using microfilters and a subsequent drying step. This way up to 94 % of the germanium removed during the hydrolysis can be recovered. The material can be used directly as a germanium source for further syntheses of germanosilicates, establishing an efficient recycling protocol.

A different approach to improve the viability of the ADOR process would be to optimise the synthesis conditions of the hydrolysis reaction. The commonly used protocol asks for large amounts of liquid, and the reaction is conducted under reflux conditions, typically overnight, for example for 16 h. These three reaction parameters are where mechanochemical synthesis methods can be of great value.[9–12] Energy input through mechanical forces enables avoidance of bulk solvents, based on the intimate contact of the reagents. This is often also accompanied by faster reaction rates compared to solution-based reactions. Additionally, the exerted energy can also result in increased local temperature due to friction and shear forces, which often makes an external heating source unnecessary. On a laboratory scale these reactions are usually carried out in small benchtop ball mills, but these instruments are available in sizes up to industrial scale. Depending on the type of mill, a translation of laboratory reactions to industrially

relevant capacities is in principle possible.

Employing mechanical forces to induce reactions has been reported in several branches of synthetic chemistry,[13] ranging from organic synthesis[14] to main group chemistry[15] and more importantly in the context of this chapter on materials chemistry,[10,16,17] especially zeolites.[18,19] In most of these reactions, high impact milling is used to exert the energies, required to induce the chemical reactions. However, such a treatment can also lead to severe amorphisation, which would need to be recovered by a subsequent recrystallisation (see also section 1.2.4.4). Liquids are excellent heat conductors, which can also be utilised in milling processes. Employing wet grinding methods, or even performing a mechanochemically assisted reaction within a solvent, lessens the stress on the material and can help mediate appropriate reaction conditions.[20]

4.2 Mechanochemically assisted hydrolysis in the ADOR process

The synthesis of the parent zeolite IM-12 (**UTL**) was performed following literature protocols using DMASD-OH (6,10-dimethyl-5-azoniaspiro[4.5]decane hydroxide) as structure directing agent and a Si/Ge ratio in the synthesis gel of 2.[2,21,22] The product of the hydrothermal synthesis is a white, polycrystalline powder consisting of stacks of plate-like crystals with rough dimensions of 35 µm × 45 µm × 1 µm (see Figure 4.2). The exhibited PXRD pattern of the material agrees well with a simulated pattern for the **UTL** framework.[23] The Si/Ge ratio of the samples is within 3.5–4.0 as determined by EDS. This value ensures the number of Ge atoms in the *d4r* units is sufficiently high for the ensuing disassembly by hydrolysis.

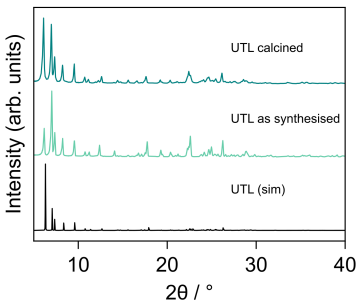

a) PXRD pattern of synthesised zeolite **UTL** and comparison with a pattern simulated for an ideal **UTL** framework.[23]

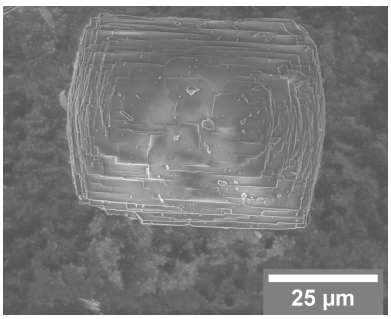

b) SEM image of synthesised zeolite **UTL** sample.

Figure 4.2. PXRD pattern and SEM image of synthesised zeolite **UTL**.

4.2.1 Hydrolysis of UTL in solution

Conventional solution-based experiments were conducted using water, hydrochloric acid, and acetic acid as hydrolysing agents to demonstrate that different ADOR daughter zeolites can be obtained from the parent **UTL** samples.[4,22,24,25] PXRD patterns of the products of these reactions, as well as the result of calcination thereof, are shown in Figure 4.3. As expected, using concentrated hydrochloric acid leads to the formation of IPC-2P and IPC-2 with **OKO** framework after calcination. The highly acidic conditions enable not only the removal of the germanium-rich *d4r* units but also lead to dissolution of silica from within the layers, followed by rapid re-intercalation of these species into the interlayer space. There, they form the foundation of what will finally become *s4r* units in the fully connected zeolite after reassembly through heat treatment. This is evidenced by the similarity in PXRD patterns of the precursor form and the fully connected zeolite and the position of the main peak at 7.58° and 7.70° 2θ for as made and calcined product, respectively.

The significantly lower acidity in the reaction using 1 M acetic acid, on the other hand, leads to the IPC-1P, where only the germanium containing parts are removed, leaving the bare siliceous layers. With no connection between the layers besides hydrogen bonding, the interlayer spacing is decreased, seen in the dominant peak shifting to 8.48°. The sample was then stirred in octylamine to enable proper orientation of the individual layers with respect to each other.[26] The linear amine intercalates in-between the layers and separates them slightly more. This gives the layers some additional freedom to organise themselves uniformly. In the subsequent calcination of this material the silanol groups on either side of the layers reconnect directly, employing only an oxygen atom as connection. This results in even smaller interlayer distances and correspondingly, the main peak in the PXRD pattern shifts to the even higher 2θ value of 9.64°.

Looking at water-based hydrolysis reactions, the importance of the duration of the reaction is evident as shown in Figure 4.3. Disassembling zeolite **UTL** under reflux conditions for 5 h results in precursor IPC-2P, which reconnects to form IPC-2 after calcination. Noteworthy is that for a material with no structural defects, the use of concentrated hydrochloric acid is still preferable. In contrast to a hydrolysis for several hours, stopping the reaction after only 1 h yields IPC-1P as product. The underlying kinetics for this temperature dependency have been described in detail by Henkelis et al.[25] Calcining this sample directly does lead to a material which exhibits a similar PXRD pattern as the one simulated for IPC-4 (**PCR**), however, the main is peak observed at a

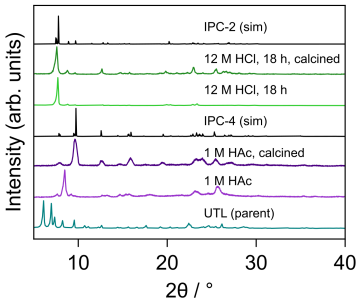

a) PXRD patterns of solution-based hydrolyses using 1 M acetic acid (HAc) or 12 M hydrochloric acid (HCl) and their reassembled products. Comparison with the parent zeolite with **UTL** framework and simulated patterns for IPC-2 (**OKO**) and ICP-4 (**PCR**.).

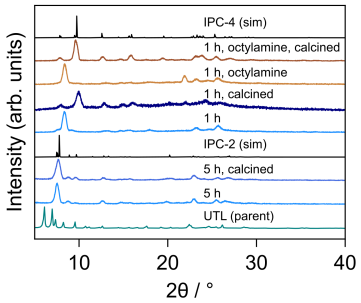

b) PXRD patterns of solution-based hydrolyses using water and their reassembled products. Comparison with the parent zeolite with **UTL** framework and simulated patterns for IPC-2 (**OKO**) and ICP-4 (**PCR**.).

Figure 4.3. PXRD patterns of products of solution-based hydrolysis of zeolite **UTL**.

slightly higher angle (9.98° compared to 9.74° for **PCR**). This indicates some disorder in the layer connectivity, where not every connection is the ideal straight oxygen bridge connecting two silanol groups opposite each each. When immersing this sample in octylamine prior to reassembly, the peak position would suggest a better and more well-ordered product. These results also agree well with what has been described in the literature.[22,26]

4.2.2 Hydrolysis of UTL in a ball mill

The described conventional solution-based hydrolysis conditions are very well suited to obtain ADOR daughter materials of high quality and purity as shown in the previous section. In light of economic and ecological sustainability of this entire process, however, there are several possibilities for improvement. Firstly, the amount of liquid used for the hydrolysis reaction is significant. Reduction of the required volumes of both solvent and washing liquid would help decrease cost and environmental impact. Additionally, these reactions are typically carried out under reflux conditions of water (i.e. 100 °C) and for at least several hours. With the aim of optimising reaction conditions for the disassembly step of the ADOR process, a mechanochemical methodology was targeted. Anticipated benefits of using a ball mill as the instrument of choice would include shorter reaction times, heavily reduced amounts of liquid, and no necessity for additional heating.

Using a bespoke rotary ball mill, initial test experiments were carried out using water, ethanol, and hydrochloric acid as hydrolysing agents, as well as a reaction with no additional liquid as a control experiment. A 125 mL polypropylene flask was used as milling vessel and filled with 250 g of YSZ (yttrium stabilised zirconia) milling balls (3 mm diameter), occupying roughly a third of the internal volume. A liquid volume of

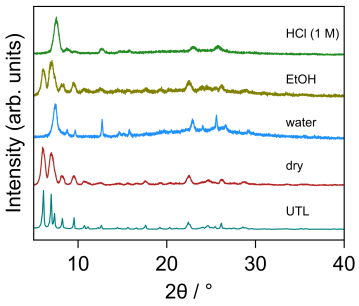

a) PXRD patterns of ball milled zeolite **UTL** using 25 mL of several liquids or no added liquid at all (dry).

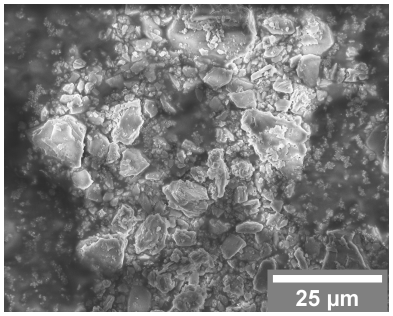

b) SEM images of ball milled zeolite **UTL** without using liquid.

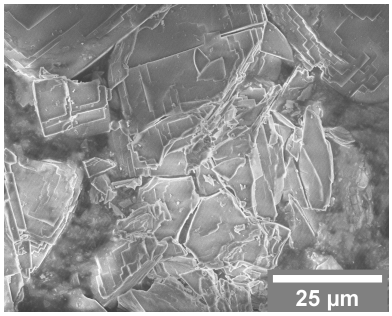

c) PXRD patterns of ball milled zeolite **UTL** using 25 mL of ethanol.

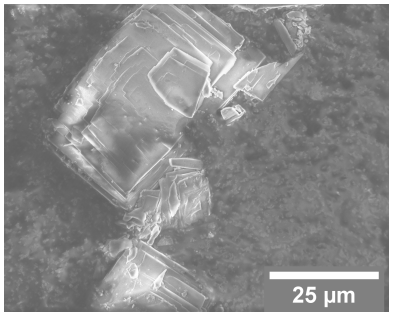

d) SEM images of ball milled zeolite **UTL** using 25 mL of 6 M HCl.

Figure 4.4. PXRD patterns and SEM images of initial experiments towards mechanochemically assisted hydrolysis of zeolite **UTL**.

25 mL was chosen to ensure complete coverage of the milling media. 500 mg of zeolite were employed in a typical synthesis. The reactions were carried out for 30 min at room temperature with no external heating source. Further synthesis details can be found in section 4.4.

The products were characterised using PXRD, shown in Figure 4.4, which clearly shows the expected result for the dry reaction, with no hydrolysed product discernible when comparing its PXRD pattern to the parent **UTL**. Likewise, the reaction containing ethanol did not appear to have induced disassembly either. A recent report by Zhang et al. showed that adding alcohols to water or using hydrochloric acid dissolved in ethanol instead of water effectively slows down the disassembly process.[27] Using pure alcohols, no disassembly was observed at all, in line with the outcome of the mechanochemical reaction.

In contrast, disassembly of the **UTL** sample is facilitated when switching to water or hydrochloric acid as the liquid additive. The is a significant result considering the differences in reaction conditions compared to conventional protocols. The volume of liquid used per gram of zeolite is halved from 100–200 $\mu L\,mg^{-1}$ to 50 $\mu L\,mg^{-1}$ (parameter η as introduced by Friščić and co-workers[10,28]) and no heating source is employed. These factors promise an overall more sustainable procedure for the ADOR disassembly step.

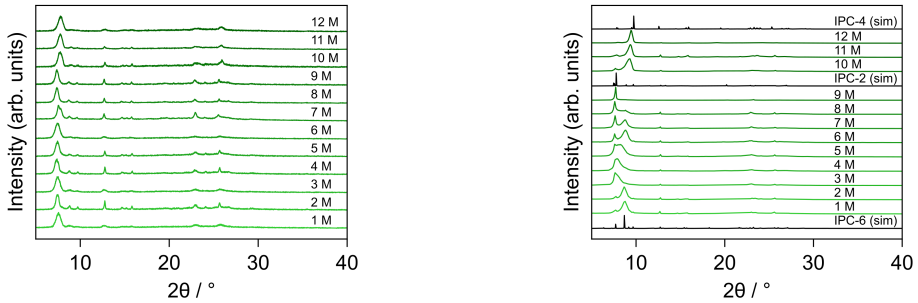

a) PXRD patterns of hydrolysis products using HCl in concentrations ranging from 1–12 M.

b) PXRD patterns of *calcined* hydrolysis products using HCl in concentrations ranging from 1–12 M.

Figure 4.5. PXRD patterns of products of mechanochemically assisted hydrolysis of zeolite **UTL** with hydrochloric acid (HCl) in varying concentrations.

4.2.2.1 Hydrolysis under acidic conditions

Since the disassembly step is much more favoured using acidic conditions, further studies using hydrochloric acid were conducted. By carefully adjusting the acid concentration in solution-based reactions, Wheatley et al. have shown that it is possible to target specific ADOR daughter zeolites IPC-4, -6, -2, and -7.[2] Probing the applicability of this concept in the mechanochemically assisted hydrolysis, the range of concentrations from 0.1–12 M HCl was tested. Comparison of PXRD patterns for these reaction products shows successful hydrolysis in all cases (Figure 4.5a). A slight difference of the main peak position, which is assigned the 200 reflection, is observed for higher concentrations > 9 M. This suggests IPC-6P as the structure for these samples, whereas others are more likely to be IPC-2P. The two precursor materials for their fully connected analogues IPC-2 and IPC-6 are very difficult to distinguish and certainty about the structural nature of the samples can only be reached by characterisation after reassembly by heat treatment (calcination).

Figure 4.5b shows clear differences depending on the used acid concentration. Low concentrations of 1 and 2 M produce sample with a pattern akin to IPC-6 (***PCS**). Liquids of intermediate acidity up to 5 M result in disordered IPC-2 products, with the possibility of a physical mixture with IPC-6. Increasing the concentration further, the share of crystals with IPC-2 structure increases gradually. This behaviour culminates at 9 M HCl, where a sample with a pattern matching the **OKO** framework is obtained. Surprisingly, very high concentrations of HCl favour denser frameworks, where the sample treated with concentrated HCl reassembles to a material whose structure is rather similar to IPC-4 (**PCR**). The sample at 12 M HCl shows a layer distance (d-spacing corresponding to the main peak position) which does not exactly match with the ideal structure, showing a lower peak position by about 0.2°. One cause for this may be that some of the linking

units between layers are not only oxygen atoms, but rather *s4r* units as seen in IPC-6 and IPC-2. As reported earlier, the disassembly step is a gradual process, where the germanium containing units are removed consecutively.[25,29] Given that there is no evidence for formation of the fully disassembled product IPC-1P, it is even rather likely that some *s4r* linkages may still remain in the structure. Given the idealised structures of IPC-2 (only *s4r*), IPC-6 (50 % *s4r*, 50 % -*O*-), and IPC-4 (only -*O*-) and the respective d_{200} peak positions, the ball milled product would have 14 % of *s4r* units linking the layers. Keeping in mind that an additional consideration is that the layer distance is expanded by virtue of residual reaction by-products, such as GeO_2, this number is most likely inaccurate, but gives some indication of the possible structure of this material.

These findings are quite surprising when compared to previous studies, where a positive, linear correlation was found for acid concentration and the d_{200} spacing of the resulting zeolite material.[2] A plausible cause for the discrepancy in the mechanochemically assisted hydrolyses lies in the formation of the by-product of the reaction. Germanium in the *d4r* units is attacked by chloride ions, forming soluble chlorinated germanium species, which are eventually transformed into GeO_2.[30] A recent study even exploits this by-product formation for successful recovery of germanium, to be re-used in subsequent germanosilicate zeolite syntheses.[8] The dissolution process is facilitated by both the presence of chloride ions and a low pH, the latter being advantageous for Ge−O (and also Si−O) bond breaking. In solution-based reactions, enough solvent is present to ensure complete removal of these dissolved germanium species from the interlayer space where they originate. This may, however, not be the case in the ball milling reactions, where the decreased amount of solvent is possibly not sufficient anymore. Additionally, the solubility of GeO_2 in hydrochloric acid reaches its minimum at a concentration of 5 M.[31] This coincides with the observed maximum for the d_{200} spacing of the sample obtained at this HCl concentration. This interlayer spacing is thought to not only be caused by the structure of the samples, but some additional contribution from residual hydrolysis by-products, artificially expanding this space and potentially causing disruption and disorder. If this hypothesis was to be true, some evidence of residual GeO_2 should be evident in the collected diffractograms. Indeed, closer inspection of the PXRD patterns show an additional peak at 26° 2θ, indicating an impurity with α-quartz structure such as germanium dioxide. Further evidence comes from EDS analysis of obtained materials, where the measured Si/Ge ratios range from 10–30, with higher values obtained for samples treated with HCl in greater concentrations. These values

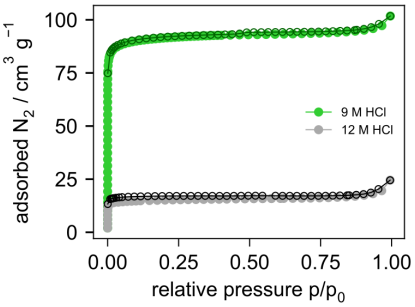

Figure 4.6. Nitrogen adsorption isotherms for samples obtained with 9 M HCl (green) and 12 M HCl (grey/black).

are in stark contrast to solution-based hydrolysis products, especially IPC-2, which is commonly essentially germanium-free.[24]

Of the obtained materials, the most intriguing samples are the ones produced using 9 M HCl which resulted in an IPC-2 material, and 12 M HCl yielding an IPC-4-type material. Thus, some further investigations were conducted using these two materials. One question that arises is how the mechanochemical treatment would effect the porosity as well as the available surface area. Consequently, nitrogen adsorption measurements were conducted. The isotherms show a typical type I behaviour with some very small indication of mesoporosity, most likely due to voids between particles.[32] For the sample obtained from 9 M HCl a BET surface area of 368 $m^2 g^{-1}$ was calculated. This value is in good agreement with literature data, further supporting the assignment of IPC-2 and validating the developed mechanochemical methodology as an alternative approach to obtain this material.[24] The amount of adsorbed nitrogen in the 12 M HCl sample, however, is very low and correspondingly the calculated BET area only amounts to 60 $m^2 g^{-1}$. The surface area of an IPC-4 material is expected to be lower than for IPC-2, due to the smaller pores (10 × 8 in IPC-4 compared 12 × 10 in ICP-2), however, it is still typically in the range of 200–300 $m^2 g^{-1}$. The much lower measured value for available surface area for this IPC-4-type sample may be caused by the aforementioned disorder and residual germanium species in the interlayer space which could not be removed. These species would effectively clog the pores by blocking the pore windows, thus reducing the nitrogen uptake during the adsorption measurement.

With hopes of shedding more light onto the situation, further structural characterisation was carried out by employing transmission electron microscopy (TEM). Looking at both samples in their reassembled forms, high resolution TEM images were acquired. From the sample obtained using 9 M HCl, crystals were found in different orientations and the d-spacings derived from Fast Fourier Transformation (FFT) match well with

what is expected for the **OKO** framework (Figure 4.7). For example, the d-spacing of 1.12 nm was found for several investigated crystals, which corresponds well with the interlayer spacing of IPC-2.

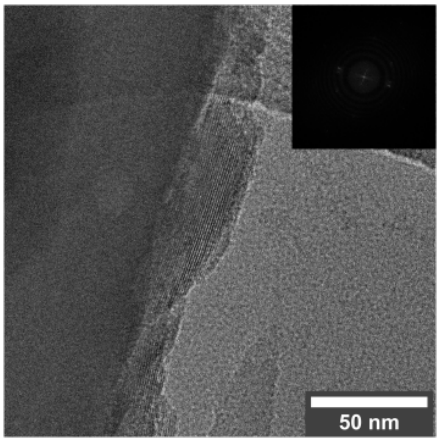

a) TEM image showing lattice fringes with a distance of roughly 1.12 nm which indicate a **OKO** framework. The corresponding FFT is shown as insert.

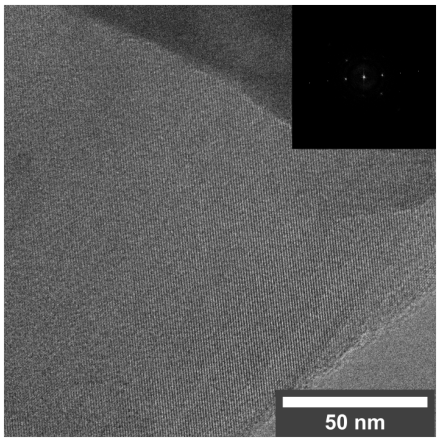

b) TEM image approximately along the [101] direction, with corresponding FFT as insert.

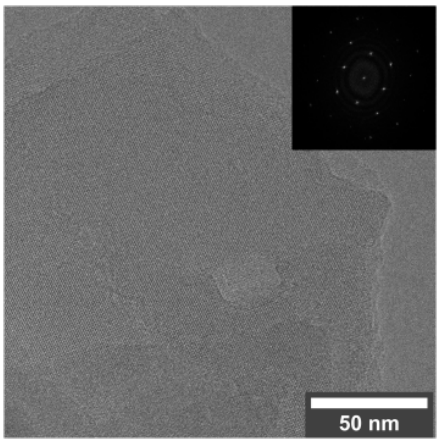

c) TEM image approximately along the [101] direction, with corresponding FFT as insert.

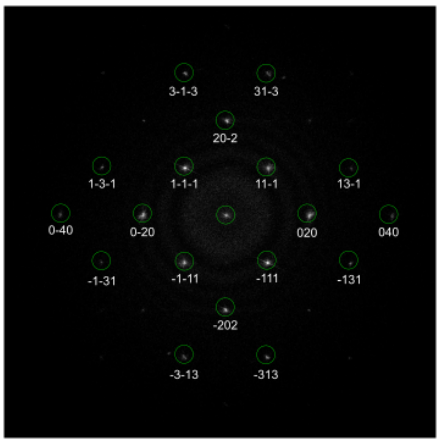

d) FFT of Figure 4.7c, and expected reflections for the **OKO** framework viewed along the [101] direction as overlay.

Figure 4.7. TEM images and corresponding FFTs of reassembled samples from mechanochemically assisted hydrolysis using 9 M HCl.

Similarly, the product of hydrolysis using 12 M HCl was investigated using TEM (Figure 4.8). Crystals with lattice fringe spacings of 0.93 nm on average were found, agreeing well with PXRD results and the ideal value for the **PCR** framework. In a few instances, however, a slightly larger distance of 1.06 nm was observed in some regions, which would correspond to the d_{200} spacing in IPC-6. Additionally, several regions showed interruptions in the lattice fringes, indicating partial collapse of the framework. This agrees well with the results of the gas adsorption experiments, which indicated

inaccessibility of the pore system, despite the average interlayer spacing matching with the porous **PCR** framework.

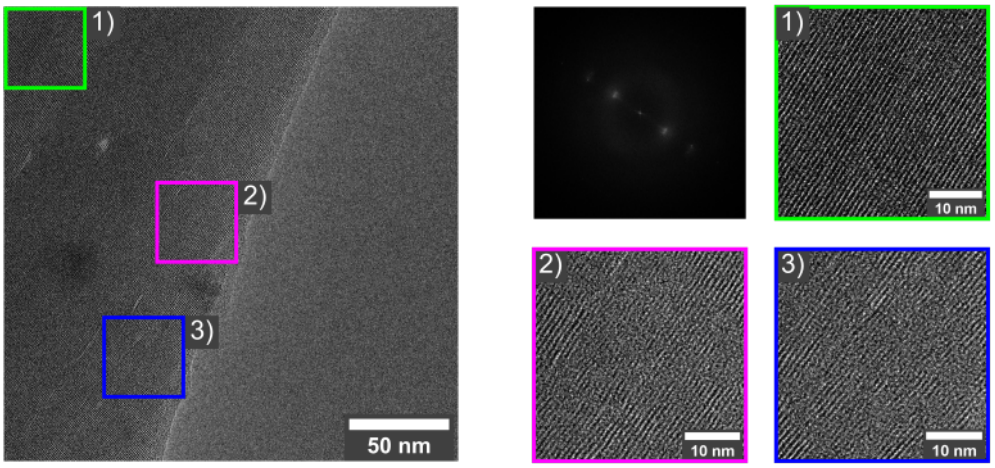

Figure 4.8. TEM image, corresponding FFTs and magnified parts of a reassembled sample from mechanochemically assisted hydrolysis using 12 M HCl. The magnified regions show highly crystalline (1) but also defective parts of the particle (2, 3).

In order to probe whether an increase in milling time would have an effect on the structure of obtained hydrolysis products, the two discussed synthesis conditions were adapted, varying the duration of the treatment. Figure 4.9 shows the PXRD patterns for each case, with both hydrolysis product and the corresponding final, reassembled material. The patterns indicate no change in obtained structures, even after the comparatively long time of 480 min. Only slight changes to the main peak position over the initial 2 h can be discerned. For the syntheses at 12 M HCl, this is in stark contrast to solution-based reactions, where especially at longer reaction times the formation of IPC-2 is essentially inevitable. In the here employed mechanochemical synthesis, the re-intercalation of silicon species must be inhibited.

The heavily reduced reaction time of 30 min, instead of several hours, producing either IPC-2 or IPC-4 materials is an important advantage of the here presented mechanochemical method compared to the conventional solution-based approach. This is thought to be caused by the occurring particle size reduction of the mechanochemical treatment, effectively decreasing the time required for the hydrolysing agent to access all layer-connecting units throughout the crystals. Furthermore, despite the lack of a dedicated heating source, milling reactions do produce heat, especially locally, which potentially may even exceed the 100 °C, typically employed for conventional, solution-based hydrolysis. Such high temperatures may contribute to faster reaction kinetics, resulting in lower reaction times.

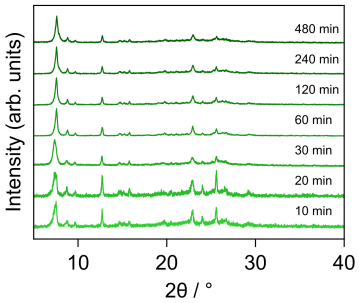

a) PXRD patterns of hydrolysis products using 9 M HCl, studied over a period of 480 min.

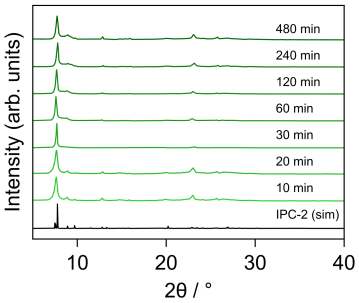

b) PXRD patterns of *calcined* hydrolysis products using 9 M HCl, studied over a period of 480 min.

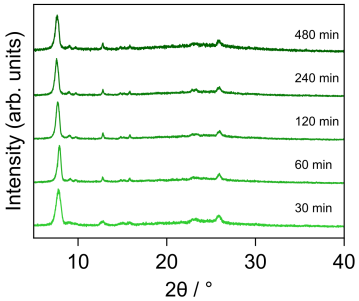

c) PXRD patterns of hydrolysis products using 12 M HCl, studied over a period of 480 min.

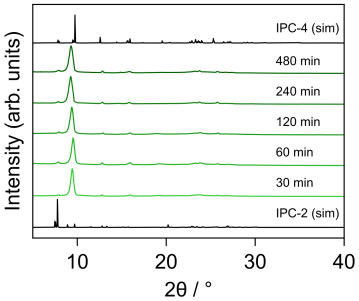

d) PXRD patterns of *calcined* hydrolysis products using 12 M HCl, studied over a period of 480 min.

Figure 4.9. PXRD patterns of products of mechanochemically assisted hydrolysis of zeolite **UTL** using 9 and 12 M HCl at varying reaction times.

4.2.2.2 Hydrolysis using water

Even though disassembly in the ADOR process is typically done using acids, water can also be used. As shown in preliminary experiments (compared Figure 4.4), this is also the case for the adapted mechanochemical protocol. The conditions employed using water as hydrolysis reagent yielded IPC-2P or IPC-6P type materials with a PXRD pattern similar to what has been observed for samples obtained with hydrochloric acid. The samples treated with low concentrations of acid (almost neutral conditions) reassembled to IPC-6, whereas using water in the hydrolysis, the resulting material exhibits a PXRD pattern much more like the framework **OKO**, shown in Figure 4.10.

Furthering the investigation into using only water as the hydrolysing agent, the effect of decreasing the volume of liquid was investigated. As Figure 4.10a unequivocally shows, disassembly occurs similarly well for volumes as low as 100 µL, translating to an η value of only 0.2. All of these hydrolysis products reassemble to an IPC-2 material, as seen for the initial test reaction using a volume of 25 mL. Such low values for η imply a true mechanochemical reaction, whereas the above described experiments should and have been referred to as *mechanochemically assisted*. The reason for this is that despite the experiment being conducted in a ball mill, the possibility of phenomena associated with conventional solution-based syntheses cannot be excluded as dominant

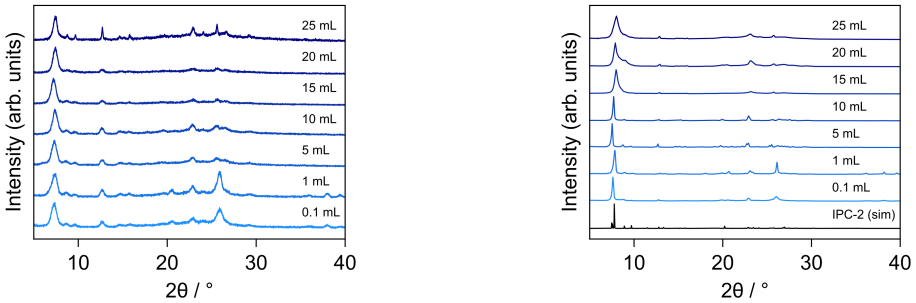

a) PXRD patterns of hydrolysis products using water, ball milled for varying volumes of liquid.

b) PXRD patterns of *calcined* hydrolysis products using water, ball milled for various time periods.

Figure 4.10. PXRD patterns of products of mechanochemically assisted hydrolysis of zeolite **UTL** using varying amounts of water.

factors. Reaching liquid to solid ratios below 2 μL mg^{-1}, however, strongly suggest that the impact of milling is at least part of the driving force for the observed transformation.[28] As shown previously (Figure 4.4a and 4.4b), complete absence of water does not induce this type of reaction, which is not surprising since a spontaneous, controlled breakdown of the parent **UTL** framework by a hydrolytic pathway can be excluded in such a solvent-free environment. Only particle size reduction and amorphisation were observed under such dry conditions.

TEM images shown in Figure 4.11 support the PXRD results with an observed interlayer spacing of 1.13 nm and thus the identification of the material as IPC-2. This analysis also revealed small particles of roughly 25 nm in diameter, which show a lattice fringe spacing of circa 0.43 nm This would correspond to the (010) plane of quartz-type GeO_2, an assumed impurity based on the PXRD results.

Intrigued by the low volume reaction using only 100 μL of water, ^{29}Si solid-state NMR was employed to investigate the as synthesised material. Using this spectroscopic characterisation technique, the environments of present silicon species can be determined. Fully connected $Si(OSi)_4$ environments (Q_4) can be compared to silicon environments including one silanol group $Si(OSi)_3(OH)$ (Q_3), giving an indication of the nature of the obtained hydrolysis product. From the obtained spectrum of this sample (see Figure 4.12), the ratio of Q_3/Q_4 sites was calculated to be 1/3.1. Comparing this value to previously published data for intermediate precursors suggests IPC-6P or a disordered IPC-2P as the most likely structures.[29,33,34]

This agrees well with the observed PXRD pattern, which is reminiscent of IPC-6P/IPC-2P as well. Important to note is this result cannot be taken as solid evidence for what the final material after calcination will become. The high potential for disorder in these intermediate structures makes a strong conclusion essentially impossible. Proof

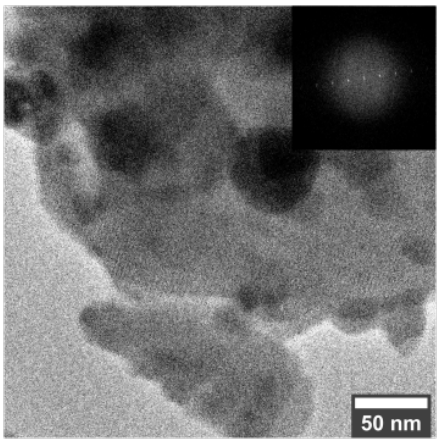

a) TEM image and corresponding FFT as insert showing both crystalline regions with lattice fringe spacings of 1.13 nm as well as dense particles, possibly GeO_2 impurities.

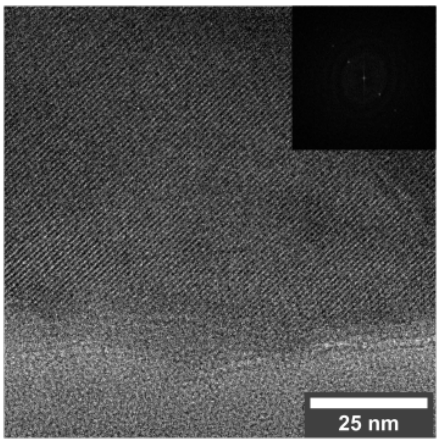

b) TEM image and corresponding FFT as insert showing a highly crystalline area.

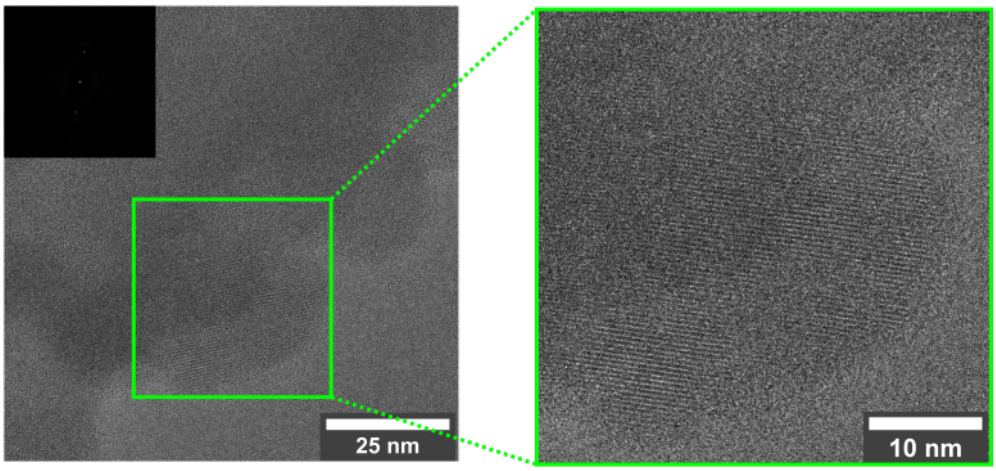

c) The highlighted region shows a particle assigned to an α-quartz type GeO_2 impurity based on the measured lattice fringe spacing of 0.43 nm.

Figure 4.11. TEM images and corresponding FFT of a reassembled sample from mechanochemically assisted hydrolysis using 100 μL water.

for a certain framework or structure has to be obtained from characterisation of the final material and can not be inferred with certainty from analysis of the as synthesised product. As such, the observed reassembly of this material to an IPC-2 structure does not disagree with given interpretation, despite the deviation of the Q_3/Q_4 ratio from the ideal value for IPC-2P of 1/7. It is also worth noting that the calculated amount for Q_3 sites may be inflated by surface defects, originating from the mechanical forces exerted on to the crystals. All instances of $Si(OSi)_3(OH)$ contribute to the feature observed in the NMR spectrum, whether they are located in the structurally important interlayer space or on the surface of crystallites.

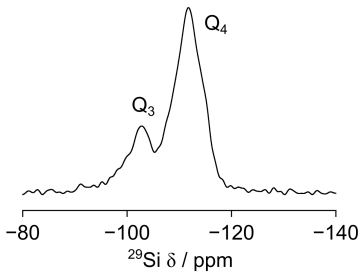

Figure 4.12. ^{29}Si (9.4 T, 14 kHz) MAS NMR spectrum of a sample hydrolysed during ball milling using water as hydrolysing reagent.

4.2.3 A mechanochemical methodology for ^{17}O enrichment

The fact that this hydrolysis reaction can occur with such minute amounts of water opens up a way for a potential application in the field of solid-state NMR spectroscopy, in particular with respect to the nucleus ^{17}O.[35] The issue regarding investigation of this element is that the NMR active isotope ^{17}O has a very low natural abundance of 0.037 %. Additionally, the moderate gyromagnetic ratio and its quadrupolar spin of 5/2 further complicate acquisition of such spectra. With current instrumentation, recording a spectrum of acceptable signal-to-noise ratios may take weeks or even longer.

One way to reconcile this situation is to enrich the material of interest with this heavier oxygen isotope, but one needs to keep in mind that due to its scarcity even the required reagents, such as $H_2{}^{17}O$, come with a substantial price tag. This is the reason why most enrichment procedures are performed post-synthetically, since synthesis itself typically involves large amounts of solvent and a washing step for purification. This can therefore endanger the levels of enrichment that may have been achieved during the synthesis. There are some relatively cost-efficient ways for post-synthetic enrichment using, for example, gaseous $^{17}O_2$; however, additional methods are sought after as alternatives for sensitive samples or as way to further reduce cost. With this in mind, the potential to use only 100 µL of a reagent containing the expensive oxygen isotope to enrich several hundred grams of zeolite promises to be a great opportunity. The fact that the enrichment can occur during a required synthetic step is an additional benefit.

Some similar studies on employing mechanochemical treatment for oxygen enrichment have recently been published by Laurencin's group. The authors showed successful incorporation of the NMR active isotope into metal hydroxides and oxides,[36–38] and fatty acids used in molecular chemistry and nanoscience.[39] Thanks to the described benefits of mechanochemistry, namely small amounts of liquid, fast reaction rates, and ambient reaction conditions, cost-efficient and rapid enrichment of the products was achieved.

This successful enrichment, without the need to alter the experimental setup, highlights the great potential for solid state NMR to be used to further probe the samples in this project.

The experiment using 100 µL water was adapted to employ 40 % $H_2{}^{17}O$ as hydrolysis agent. The obtained material was initially investigated using ^{17}O magic angle spinning (MAS) NMR employing spin echo,[40] shown in Figure 4.13a. The recorded spectrum is evidence of a successful enrichment procedure by virtue of showing features of high intensity despite the comparatively short acquisition time of 2 h. The broad signal, caused by quadrupolar interactions, ranges from −40–40 ppm. In order to gain insight into the nature of the observed oxygen environments, a 2D multiple-quantum (MQ) MAS spectrum was acquired over 18 h, which reveals three signals (see Figure 4.13b). Expected Si−^{17}O−Si environments of the zeolite material are assigned to the feature at δ_1, δ_2 = 30, 0–30 ppm.[34,41–43] The second prominent region at δ_1 = 45 ppm was identified as $Ge^{17}O_2$, the hydrolysis by-product. This interpretation was confirmed by comparison to a sample of α-quartz type $Ge^{17}O_2$, produced by following a protocol by Hussin et al.[44] The remaining, third region at δ_1, δ_2 = 28, −30–0 ppm can so far not be assigned unambiguously. A probable origin for this feature is a Ge−^{17}O−Si environment, which may stem from either the IPC-2 type material or a mixed silicon/germanium dioxide ($Si_xGe_{1-x}O_2$) or in fact both. The three present environments indicate that there is no explicit preferential enrichment of one type of material or site compared to others. This is important since despite the formation of an impurity phase (GeO_2), investigation of the material of interest is still possible.

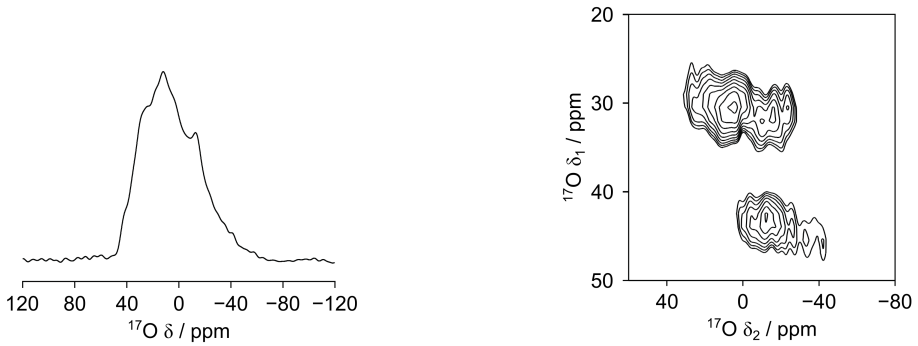

a) ^{17}O (14.1 T, 10 kHz) ^{1}H-decoupled MAS NMR spectrum.

b) ^{17}O (14.1 T, 10 kHz) ^{1}H-decoupled MQMAS NMR spectrum after a shearing transformation.

Figure 4.13. ^{17}O solid-state NMR spectra of a sample hydrolysed during ball milling, using 40 % enriched $H_2{}^{17}O$.

Assessing the viability of the presented ball milling approach for ^{17}O enrichment, an important aspect is resource efficiency. Direct and accurate measurement of enrichment

levels of the heavier oxygen isotope requires elaborate and expensive analysis, for example by SIMS (secondary ion mass spectrometry).[45] As such this is not a feasible option for routine characterisation. It is, however, possible to compare the NMR spectra and the required acquisition times with similar materials where such an analysis had been performed previously. Judging from earlier studies on other zeolites,[46,47] and the related materials MOFs (metal-organic frameworks)[45] and pyrochlores,[48] approximately 10 % of oxygen sites have been exchanged using this mechanochemical approach. This value compares excellently against the maximum level of enrichment of 11 % considering the ratio of $^{16}O/^{17}O$ in the compounds.

4.3 Conclusion and perspective

The goal of developing a methodology for a more economical ADOR process was successful. Employing a mechanochemically assisted route in the form of ball milling for the hydrolytic disassembly step, zeolites with the **UTL** framework can be transformed into known ADOR daughter zeolites. Improvements have been achieved with regard to synthesis time, required amounts of solvent, and energy input.

All reactions were conducted at room temperature, that is to say that no external heating source was employed. The fact that there is no need for additional instrumentation contrasts favourably to common protocols which are conducted under reflux conditions, i.e. at 100 °C. This does not mean, however, that the actual reaction temperature does not exceed 20 °C. The exerted mechanical energy typically results in increased local temperature, which can aid the reaction. The developed mechanochemical method is also advantageous in terms of reaction time, which was reduced to 30 min, after which no structural change to the formed product was observed. The combination of these two factors are attractive with respect to potential production at larger scales, where energy and resource efficiency are key factors in assessing the viability of a given process.

Similarly positive is the investigated reduction in reaction volume of the used hydrolytically active liquid. Using 12 M hydrochloric acid, the decreased volume in combination with the mechanical forces allowed the production of a material whose structure appears to have high similarity with IPC-4, without preceding complete disassembly into IPC-1P. Although there seems to be a lack of available porosity of the obtained material, the average crystal structure resembles that of the most dense of the ADOR daughter zeolites derived from **UTL**. Varying the acid concentration changes the formed product in a manner akin to conventional ADOR methodology, although no particular trend could

be established. Nonetheless, zeolites with IPC-2 (**OKO**) and IPC-6 (***PCS**) structures can also be targeted by adjusting the molarity of the used acid solution.

Zeolite IPC-2 is also obtained as product when changing the liquid from acid to pH neutral water. Additionally, it was shown that there is no change to the reaction when significantly decreasing the water volume, down to a liquid/zeolite ratio $\eta = 0.2$. This low amount of water to induce hydrolysis enables concomitant enrichment of the product with the NMR active isotope of oxygen, ^{17}O. This is an encouraging application of the mechanochemically assisted hydrolysis for ADOR zeolites, due to the severe limitations of ^{17}O NMR caused by its low natural abundance and the corresponding concerns with regard to its expense of isotope enrichment procedures.

All in all, this study is a further demonstration of the viability and applicability of mechanochemical methods in the field of zeolites. For this particular use case, expansion to include other germanosilicate zeolites as parent materials would be a next step in exploring the possibilities of the developed methodology. Candidate frameworks would be **UOV**, ***CTH**, and **IWW**, which have been shown to yield ADOR daughter zeolites. This is especially of interest for cases where a specific ADOR-derived zeolite has proven difficult to obtain or has even not been made yet. IPC-18, which is the analogue to IPC-2 but obtained from **IWW** (i.e. *s4r* instead of *d4r* linkages between layers), has only been obtained after developing a dedicated vapour-phase transport reaction system.[49] With the observed differences of the mechanochemically assisted hydrolysis compared to the conventional methods, it may be possible to target this and other, otherwise inaccessible zeolite materials.

Another possible future avenue for this methodology is what has been shown in a study by De Prins et al. using a similar type of experiment for an alumination reaction, producing a zeolite with Brønsted acid sites.[50] Taking this report as precedent, it may also be possible to include other heteroatoms which is disfavoured or cumbersome using conventional synthesis techniques. Possible candidates could be titanium or tin which have Lewis acidic properties and can be used as oxidation catalysts.

4.4 Experimental section

4.4.1 Reagents

All chemicals (see Table 4.1) were used without purification prior to synthesis.

Table 4.1. Chemicals and their suppliers.

Chemical	Abbreviation	Supplier
Fumed silica "Cab-O-Sil M5"	SiO_2	Acros Organics
Germanium dioxide	GeO_2	Sigma-Aldrich
cis-2,6-Dimethylpiperidine	DMP	Sigma-Aldrich
1,4-Dibromobutane	BDPC	Acros Organics
Potassium carbonate	K_2CO_3	Fisher Scientific
Acetonitrile	–	Fisher Scientific
Diethyl ether	DE	Honeywell
Ethanol	EtOH	VWR
Ambersep 900(OH) ion exchange resin	–	Alfa Aesar
Hydrochloric acid	HCl	Fisher Scientific
Octylamine	–	Sigma-Aldrich
^{17}O enriched water, 40 %	$H_2{}^{17}O$	CortecNet

4.4.2 Synthesis details

4.4.2.1 6,10-dimethyl-5-azoniaspiro[4.5]decane bromide (DMASD-Br)

Synthesis of 6,10-dimethyl-5-azoniaspiro[4.5]decane bromide (DMASD-Br) was conducted by an adapted procedure of Marino et al.[51] *cis*-2,6-Dimethylpiperidine (56.28 g, 0.5 mol, 1 eq) and potassium carbonate (82.93 g, 0.6 mol, 1.2 eq) were mixed in acetonitrile (500 mL). 1,4-Dibromobutane (108.48 g, 0.5 mol, 1 eq) was added dropwise over 30 min and the mixture subsequently refluxed for 18 h. Acetonitrile was removed under reduced pressure and the bromide salt dissolved in ethanol to be able to remove the remaining carbonate by filtration. Reprecipitation was performed using diethyl ether, the product recovered by filtration and dried *in vacuo*.

yield: 72.703 g white crystals (0.293 mol, 58 %)

^{1}H NMR (400 MHz, $CDCl_3$): δ (ppm) = 4.41 (s, 2 H), 4.04 (td, J = 7.6 Hz, 2 H), 4.04 (td, J = 7.6 Hz, 2 H), 3.36–3.30 (m, 2 H), 2.17–2.04 (m, 4 H), 1.95–1.79 (m, 3 H), 1.78–1.56 (m, 3 H), 1.40 (d, J = 6.4 Hz, 6 H).

^{13}C NMR (126 MHz, $CDCl_3$): δ (ppm) = 70.28, 63.53, 49.07, 30.43, 26.96, 25.78, 21.97, 17.54.

4.4.2.2 Zeolite IM-12 (UTL)

Synthesis of **UTL** was conducted in accordance with reported procedures in the literature.[2,3,21,22] In-house synthesised DMASD-Br was ion-exchanged using Ambersep 900(OH) resin in water. The composition of the zeolite gel prior to the heat treatment is aimed to be 1 SiO_2 : 0.5 GeO_2 : 0.5 DMASD : 35 H_2O. For a typical synthesis 18.69 g DMASD-Br were dissolved in 100 mL H_2O and 32 g of the resin were added. The mixture was stirred for 3.5 h and the resin filtered off subsequently. Thereafter, GeO_2 (7.75 g) and SiO_2 (8.90 g) were dissolved in the aqueous OSDA solution under stirring for 40 min using a mechanical stirrer performed in a PTFE beaker and using a PTFE stirrer blade and shaft. The obtained gel with pH = 10 was transferred into Teflon-lined stainless steel autoclaves of appropriate size and heated at 175 °C for 7 d under static conditions. The product was recovered by filtration, washed thoroughly with water until neutral and dried at 80 °C overnight. Eventual calcination to remove the occluded OSDA was conducted at 575 °C for 6 h using a ramp rate of 1 °C min^{-1}.

yield: 10.39 g white powder of polycrystalline plates (light microscopy)

4.4.2.3 Conventional hydrolysis of UTL in bulk solvent

Hydrolysis reactions were performed according to protocols in the published literature.[2,22,24] Calcined zeolite **UTL** was placed in a round bottom flask and and the various solvents added in the desired ratio (see Table 4.2). After the required reaction time, the remaining solid was filtered off and thoroughly washed with water and the solid dried at 80 °C overnight. Reassembly to form the final zeolite was accomplished by calcination at 575 °C for 6 h using a ramp rate of 1 °C min^{-1}.

Table 4.2. Experimental details of solution-based hydrolysis of zeolite **UTL**.

UTL [g]	solvent	volume [mL]	η [µL mg^{-1}]	temperature [°C]	time h	yield [g]
0.50	water	100	200	100	5	0.20
1.00	water	100	100	100	1	0.51
0.94	HAc (1 M)	160	160	100	18	0.34
1.00	HCl (12 M)	160	160	100	18	0.52

In order to obtain well ordered zeolite IPC-4, the precursor zeolite IPC-1P is intercalated with octylamine.[22] IPC-1P is added to octylamine in a ratio of 1/65 by mass and stirred at 80 °C for 5 h and then continued to stir at room temperature for a further 18 h (see

Table 4.3). The solid is filtered off and washed with ethanol, before drying at 80 °C overnight. The intercalated compound is then calcined as above at 575 °C for 6 h using a ramp rate of 1 °C min^{-1}.

Table 4.3. Experimental details of intercalation of zeolite precursor IPC-1P with octylamine.

IPC-1P [mg]	octylamine [g]	time @ 80 °C [h]	time @ r.t. [h]	hydrolysis solvent	yield [mg]
0.28	18.768	5	18	H_2O	0.23
0.31	20.176	5	18	HAc (1 M)	0.28

4.4.2.4 Hydrolysis of UTL in a ball mill

Hydrolysis reactions were performed using a bespoke rotary ball mill, employing polypropylene bottles (125 mL volume) as milling vessels and 250 g yttrium stabilised zirconia (YSZ) balls with a diameter of 3 mm as milling media. The amount of milling balls is chosen as it occupies roughly a third of the internal volume of the flask. Reactions were carried out at settings resulting in 155 rpm (2.6 Hz) which equates to roughly 75 % of the critical speed. These conditions ensure uniform impact throughout the milling process. After the milling operation the milling balls were sieved off and washed with 50 mL of ethanol. The mixture was then centrifuged and the recovered solid dried at 80 °C overnight. Reassembly to form the final zeolite was accomplished by calcination at 575 °C for 6 h using a ramp rate of 1 °C min^{-1}.

Table 4.4. Experimental details of mechanochemically assisted hydrolysis of zeolite **UTL**.

UTL [g]	liquid	volume [mL]	η [μL mg^{-1}]	time min	yield [g]
0.50	–		0	30	0.25
0.50	EtOH	25	50	30	0.21
0.50	H_2O	25	50	30	0.39
0.50	H_2O	20	40	30	0.37
0.50	H_2O	15	30	30	0.36
0.50	H_2O	10	20	30	0.38
0.50	H_2O	5	10	30	0.36
0.50	H_2O	1	2	30	0.38
0.50	H_2O	0.1	0.2	30	0.48

Table 4.5. Experimental details of mechanochemically assisted hydrolysis of zeolite **UTL** using hydrochloric acid in varying concentrations.

UTL [g]	liquid	concentration [M]	volume [mL]	η [μL mg^{-1}]	time min	yield [g]
0.50	HCl	1	25	50	30	0.36
0.50	HCl	2	25	50	30	0.34
0.50	HCl	3	25	50	30	0.34
0.50	HCl	4	25	50	30	0.36
0.50	HCl	5	25	50	30	0.36
0.50	HCl	6	25	50	30	0.16
0.50	HCl	7	25	50	30	0.35
0.50	HCl	8	25	50	30	0.35
0.50	HCl	9	25	50	30	0.38
0.50	HCl	10	25	50	30	0.36
0.50	HCl	11	25	50	30	0.33
0.50	HCl	12	25	50	30	0.35

Table 4.6. Experimental details of mechanochemically assisted hydrolysis of zeolite **UTL** using 9 and 12 M hydrochloric acid for various time periods.

UTL [g]	liquid	concentration [M]	volume [mL]	η [μL mg^{-1}]	time min	yield [g]
0.50	HCl	9	25	50	10	0.34
0.50	HCl	9	25	50	20	0.38
0.50	HCl	9	25	50	60	0.39
0.50	HCl	9	25	50	120	0.39
0.50	HCl	9	25	50	240	0.39
0.50	HCl	9	25	50	480	0.36
0.50	HCl	12	25	50	60	0.34
0.50	HCl	12	25	50	120	0.36
0.50	HCl	12	25	50	240	0.36
0.50	HCl	12	25	50	480	0.32

4.4.3 Physicochemical characterisation

Powder X-ray diffraction (PXRD) Experiments were carried out on a PANalytical Empyrean disc diffractometer, operated in Bragg Brentano geometry in θ–2θ mode or a STOE STADI/P capillary diffractometer, operated in Debye-Scherrer geometry. Both diffractometers are equipped with a primary beam monochromator resulting in Cu $K\alpha_1$ radiation. Patterns were typically collected from 3–40° 2θ.

Scanning electron microscopy (SEM) and energy dispersive X-ray spectroscopy (EDS) Images were acquired on a JEOL JSM-5600 (thermionic gun with tungsten filament) or a JEOL JSM-6700F (field emission gun, FEG). Both microscopes are equipped with an Oxford INCA EDS system, used to determine germanium and silicon content. Prior to investigation, samples were placed on sticky carbon tape and gold coated at 10 mA for 30 s using a Quorum Q150R ES sputter coater.

Transmission electron microscopy (TEM) Images were acquired on a JEOL JEM NEOARM-200F with a TVIPS CMOS XF416 camera, using an acceleration voltage of 200 kV. Samples were prepared by a conventional dropping method using acetone as dispersion medium and employing a holey carbon coated copper TEM-grid.

Solution-state nuclear magnetic resonance spectroscopy (NMR) Solution-state NMR spectra were obtained on a Bruker AV III 500, with a CryoProbe Prodigy BBO probe.

Solid-state NMR spectroscopy ^{17}O and ^{29}Si solid-state NMR spectra were collected on Bruker Avance III spectrometers, equipped with 14.1 T and 9.4 T wide-bore magnets, respectively, at Larmor frequencies of 81.4 MHz (^{17}O) and 79.5 MHz (^{29}Si) using a 4.0 mm low-γ HX probe. ^{17}O spectra were acquired at 10 kHz MAS with a recycle interval of 1 s and are referenced to water ($\delta_{iso} = 0$ ppm). A triple-quantum MAS NMR spectrum was acquired using a z-filtered pulse sequence[52] and is shown after shearing (referenced in the indirect dimension using the convention by Pike et al.[53]) ^{29}Si spectra were acquired at 14 kHz MAS with a recycle interval of 120 s and are referenced to Q8M8 (octakis-(trimethylsiloxy) silsesquioxane, $OSi(OMe)_3$; $\delta_{iso} = 11.5$ ppm).

4.5 References

(1) P. Eliášová, M. Opanasenko, P. S. Wheatley, M. Shamzhy, M. Mazur, P. Nachtigall, W. J. Roth, R. E. Morris and J. Čejka, *Chem. Soc. Rev.*, 2015, **44**, 7177–7206.

(2) P. S. Wheatley, P. Chlubná-Eliášová, H. Greer, W. Zhou, V. R. Seymour, D. M. Dawson, S. E. Ashbrook, A. B. Pinar, L. B. McCusker, M. Opanasenko, J. Čejka and R. E. Morris, *Angew. Chemie Int. Ed.*, 2014, **53**, 13210–13214.

(3) D. N. Rainer, C. M. Rice, S. J. Warrender, S. E. Ashbrook and R. E. Morris, *Chem. Sci.*, 2020, **11**, 7060–7069.

(4) S. E. Henkelis, M. Mazur, C. M. Rice, G. P. M. Bignami, P. S. Wheatley, S. E. Ashbrook, J. Čejka and R. E. Morris, *Nat. Protoc.*, 2019, **14**, 781–794.

(5) D. R. Lide, in *CRC Handb. Chem. Phys.* Ed. D. R. Lide, CRC Press, Boca Raton, 2005.

(6) Z. Huang, S. Seo, J. Shin, B. Wang, R. G. Bell, S. B. Hong and X. Zou, *Nat. Commun.*, 2020, **11**, 3762.

(7) K. Maeda, K. Wakui, K. Arakawa and A. Kondo, *CrystEngComm*, 2020, **22**, 3419–3423.

(8) J. Zhang, Q. Yue, M. Mazur, M. Opanasenko, M. V. Shamzhy and J. Čejka, *ACS Sustain. Chem. Eng.*, 2020, **8**, 8235–8246.

(9) V. V. Boldyrev and K. Tkáčová, *J. Mater. Synth. Process.*, 2000, **8**, 121–132.

(10) T. Friščić, *J. Mater. Chem.*, 2010, **20**, 7599.

(11) E. Boldyreva, *Chem. Soc. Rev.*, 2013, **42**, 7719–7738.

(12) T. Friščić, S. L. James, E. V. Boldyreva, C. Bolm, W. Jones, J. Mack, J. W. Steed and K. S. Suslick, *Chem. Commun.*, 2015, **51**, 6248–6256.

(13) T. Friščić, C. Mottillo and H. M. Titi, *Angew. Chemie Int. Ed.*, 2020, **59**, 1018–1029.

(14) D. Tan and T. Friščić, *European J. Org. Chem.*, 2018, **2018**, 18–33.

(15) D. Tan and F. García, *Chem. Soc. Rev.*, 2019, **48**, 2274–2292.

(16) V. Šepelák, A. Düvel, M. Wilkening, K.-D. Becker and P. Heitjans, *Chem. Soc. Rev.*, 2013, **42**, 7507.

(17) B. Szczęśniak, S. Borysiuk, J. Choma and M. Jaroniec, *Mater. Horizons*, 2020, **7**, 1457–1473.

(18) G. Majano, L. Borchardt, S. Mitchell, V. Valtchev and J. Pérez-Ramírez, *Microporous Mesoporous Mater.*, 2014, **194**, 106–114.

(19) D. N. Rainer and R. E. Morris, *Dalton Trans.*, 2021, **50**, 8995–9009.

(20) G. A. Bowmaker, *Chem. Commun.*, 2013, **49**, 334–348.

(21) J. L. Paillaud, B. Harbuzaru, J. Patarin and N. Bats, *Science*, 2004, **304**, 990–992.

(22) M. Mazur, P. Chlubná-Eliášová, W. J. Roth and J. Čejka, *Catal. Today*, 2014, **227**, 37–44.

(23) C. Baerlocher and L. B. McCusker, *Database of Zeolite Structures*.

(24) M. Mazur, M. Kubů, P. S. Wheatley and P. Eliášová, *Catal. Today*, 2015, **243**, 23–31.

(25) S. E. Henkelis, M. Mazur, C. M. Rice, P. S. Wheatley, S. E. Ashbrook and R. E. Morris, *J. Am. Chem. Soc.*, 2019, **141**, 4453–4459.

(26) W. J. Roth, P. Nachtigall, R. E. Morris, P. S. Wheatley, V. R. Seymour, S. E. Ashbrook, P. Chlubná, L. Grajciar, M. Položij, A. Zukal, O. Shvets and J. Čejka, *Nat. Chem.*, 2013, **5**, 628–633.

(27) J. Zhang, O. Veselý, Z. Tošner, M. Mazur, M. Opanasenko, J. Čejka and M. Shamzhy, *Chem. Mater.*, 2021, **33**, 1228–1237.

(28) T. Friščić, S. L. Childs, S. A. A. Rizvi and W. Jones, *CrystEngComm*, 2009, **11**, 418–426.

(29) S. A. Morris, G. P. M. Bignami, Y. Tian, M. Navarro, D. S. Firth, J. Čejka, P. S. Wheatley, D. M. Dawson, W. A. Slawinski, D. S. Wragg, R. E. Morris and S. E. Ashbrook, *Nat. Chem.*, 2017, **9**, 1012–1018.

(30) S. E. Henkelis, S. A. Morris, M. Mazur, P. S. Wheatley, L. N. McHugh and R. E. Morris, *J. Mater. Chem. A*, 2018, **6**, 17011–17018.

(31) W. Pugh, *J. Chem. Soc.*, 1929, 1537–1541.

(32) M. Thommes, K. Kaneko, A. V. Neimark, J. P. Olivier, F. Rodriguez-Reinoso, J. Rouquerol and K. S. Sing, *Pure Appl. Chem.*, 2015, **87**, 1051–1069.

(33) S. A. Morris, P. S. Wheatley, M. Položij, P. Nachtigall, P. Eliášová, J. Čejka, T. C. Lucas, J. A. Hriljac, A. B. Pinar and R. E. Morris, *Dalton Trans.*, 2016, **45**, 14124–14130.

(34) G. P. M. Bignami, D. M. Dawson, V. R. Seymour, P. S. Wheatley, R. E. Morris and S. E. Ashbrook, *J. Am. Chem. Soc.*, 2017, **139**, 5140–5148.

(35) S. E. Ashbrook, Z. H. Davis, R. E. Morris and C. M. Rice, *Chem. Sci.*, 2021, **12**, 5016–5036.

(36) T.-X. Métro, C. Gervais, A. Martinez, C. Bonhomme and D. Laurencin, *Angew. Chemie Int. Ed.*, 2017, **56**, 6803–6807.

(37) C.-H. Chen, E. Gaillard, F. Mentink-Vigier, K. Chen, Z. Gan, P. Gaveau, B. Rebière, R. Berthelot, P. Florian, C. Bonhomme, M. E. Smith, T.-X. Métro, B. Alonso and D. Laurencin, *Inorg. Chem.*, 2020, **59**, 13050–13066.

(38) C.-H. Chen, F. Mentink-Vigier, J. Trébosc, I. Goldberga, P. Gaveau, E. Thomassot, D. Iuga, M. E. Smith, K. Chen, Z. Gan, N. Fabregue, T.-X. Métro, B. Alonso and D. Laurencin, *Chem. – A Eur. J.*, 2021, **27**, 12574–12588.

(39) J. Špačková, C. Fabra, S. Mittelette, E. Gaillard, C.-H. Chen, G. Cazals, A. Lebrun, S. Sene, D. Berthomieu, K. Chen, Z. Gan, C. Gervais, T.-X. Métro and D. Laurencin, *J. Am. Chem. Soc.*, 2020, **142**, 21068–21081.

(40) E. L. Hahn, *Phys. Rev.*, 1950, **80**, 580–594.

(41) U.-T. Pingel, J.-P. Amoureux, T. Anupold, F. Bauer, H. Ernst, C. Fernandez, D. Freude and A. Samoson, *Chem. Phys. Lett.*, 1998, **294**, 345–350.

(42) Z. Xu and J. Stebbins, *Solid State Nucl. Magn. Reson.*, 1998, **11**, 243–251.

(43) D. Freude, T. Loeser, D. Michel, U. Pingel and D. Prochnow, *Solid State Nucl. Magn. Reson.*, 2001, **20**, 46–60.

(44) R. Hussin, R. Dupree and D. Holland, *J. Non. Cryst. Solids*, 1999, **246**, 159–168.

(45) G. P. M. Bignami, Z. H. Davis, D. M. Dawson, S. A. Morris, S. E. Russell, D. McKay, R. E. Parke, D. Iuga, R. E. Morris and S. E. Ashbrook, *Chem. Sci.*, 2018, **9**, 850–859.

(46) C. J. Heard, L. Grajciar, C. M. Rice, S. M. Pugh, P. Nachtigall, S. E. Ashbrook and R. E. Morris, *Nat. Commun.*, 2019, **10**, 4690.

(47) S. M. Pugh, P. A. Wright, D. J. Law, N. Thompson and S. E. Ashbrook, *J. Am. Chem. Soc.*, 2020, **142**, 900–906.

(48) A. Fernandes, R. F. Moran, S. Sneddon, D. M. Dawson, D. McKay, G. P. M. Bignami, F. Blanc, K. R. Whittle and S. E. Ashbrook, *RSC Adv.*, 2018, **8**, 7089–7101.

(49) V. Kasneryk, M. Shamzhy, J. Zhou, Q. Yue, M. Mazur, A. Mayoral, Z. Luo, R. E. Morris, J. Čejka and M. Opanasenko, *Nat. Commun.*, 2019, **10**, 5129.

(50) M. De Prins, E. Verheyen, G. Vanbutsele, S. P. Sree, K. Thomas, J.-P. Gilson, J. Vleugels, C. E. Kirschhock and J. A. Martens, *Catal. Today*, 2019, **334**, 3–12.

(51) M. G. Marino and K. D. Kreuer, *ChemSusChem*, 2015, **8**, 513–523.

(52) J.-P. Amoureux, C. Fernandez and S. Steuernagel, *J. Magn. Reson. Ser. A*, 1996, **123**, 116–118.

(53) K. J. Pike, R. P. Malde, S. E. Ashbrook, J. McManus and S. Wimperis, *Solid State Nucl. Magn. Reson.*, 2000, **16**, 203–215.

Chapter 5

Solvent-free synthesis of germanosilicate zeolites

5.1 Introduction

One of the most important classes of inorganic materials are zeolites. These microporous silicate-based framework materials play a crucial role in the chemical industry for example as catalysts.[1,2] Despite the over 250 different known framework types reported to date,[3] only a handful are being used in such large-scale applications. One of the reasons is that despite materials with more complex structures potentially outperforming currently used zeolites such as ZSM-5 (**MFI**), the associated production cost due to more expensive reagents, especially the organic structure-directing agent (OSDA), often restricts large-scale syntheses. This is especially true since these OSDAs are often quaternary ammonium based salts, where the as made halide form needs to be anion exchanged to its hydroxide analogue for successful hydrothermal synthesis.[4,5] This way, a basic solution capable of dissolving silicon containing reagents, such as fumed silica (SiO_2), can be fashioned and the addition of bases like alkali hydroxides (e.g. NaOH) avoided. The presence of the alkali cations often has a disadvantageous effect on structure direction as it competes with the organic cation, and thus can lead to unwanted by-products or even the sole the formation of an entirely different, unwanted zeolite phase.

5.1.1 Shortcomings of hydrothermal synthesis and a solvent-free solution

Several of these more complex structures are attractive options for separation or catalytic applications due to larger pores.[6,7] This would enable targeting a wider range of applications since transformations of bulkier reagents would be possible, as well as lifting some of the diffusion limitations present in zeolites with narrower pore channels. However, many of the materials exhibiting these more open frameworks are only obtainable as heteroelement containing silicates, most notably germanosilicates.[8] The considerably higher price of germanium containing reagents, compared to silica, is a severe drawback and does not allow for economically feasible syntheses of germanosilicates in an industrial setting. Additionally, germanosilicates suffer from poor thermal stability, especially in the presence of water. Only in some cases, a change to the synthesis conditions, for example by using a different molecule as OSDA, has led to more stable materials with increased Si/Ge ratios or even as pure silica variants. Alternatively, post-synthetic stabilisation by replacing germanium atoms in the structure with silicon can improve

the lifetime of such materials and therefore their performance. Of course this additional step is a suboptimal solution and ideally, the more stable material would be synthesised directly.

Turning the inherent instability of germanosilicates into an advantage is realised in the ADOR methodology, where knowledge about the specific location of the Ge atoms in the structure of some of these frameworks, for example **UTL**, can be exploited (see also section 1.2.3.8 and chapter 4).[9] Germanium is removed in a controlled fashion and the remaining pure silica zeolitic intermediate structures can be re-connected to form materials with novel frameworks which are more stable due to their chemical composition. Thus obtained frameworks are inaccessible by direct hydrothermal synthesis, increasing the value of germanosilicate zeolites, acting as the parent material for subsequently derived ADOR daughter zeolites.

With all this said, one issue that is also frequently encountered in hydrothermal zeolite synthesis is the low yield of zeolite product, where a significant amount of the reagents remain as dissolved species in solution. This is problematic in conventional aluminosilicates but an even greater obstacle keeping in mind the price of germanium. These mother liquors and wash solutions can in principle be recycled and reused for subsequent syntheses and a recent report even demonstrates the possibility of recovery of germania.[10] Although such measures are certainly an opportunity for feasible zeolite production, a more efficient synthesis in the first place would be beneficial.

Addressing some of the inefficiency issues in traditional hydrothermal synthesis, the group of F.-S. Xiao has developed a solvent-free methodology for the synthesis of zeolites.[11–13] The seminal paper by Ren et al. introduced this synthesis technique reporting the successful preparation of zeolites such as the well-known ZSM-5 with (**MFI**) framework.[14] Over the last decade, various research groups have adopted this strategy and there are now materials exhibiting many different zeolite framework types (**MOR**, ***BEA**, **LTA**, ...) that can be synthesised using this method.[12,13] It revolves around the activation of the raw materials by mechanical forces and a subsequent heat treatment under conditions comparable to the conventionally performed reactions, utilising temperatures typically in the range of 150–220 °C. Often, the crystallisation progresses faster compared to solution-based syntheses, a significant advantage of the method. Additionally, the autoclaves used for the crystallisation can be utilised much more efficiently compared to reactions in solution, where most of the available volume is occupied by the solvent.

Using this methodology, several of the most important zeolites have been produced in a more economical and sustainable fashion, for example, ZSM-5, beta, or mordenite. Purely siliceous but also catalytically active aluminosilicate zeolites can be synthesised and several other heteroatoms, such as titanium, could be incorporated into the framework of theses materials.[15] Extension of the methodology to related aluminophosphate (AlPO) and silicoaluminophosphate (SAPO) frameworks has also been achieved.[16,17]

5.1.2 Mechanism of solvent-free synthesis of zeolites

The initial study on solvent-free synthesis towards zeolite frameworks used hydrated sodium silicate ($Na_2SiO_3 \cdot 9\,H_2O$) and fumed silica as silicon sources.[14] The commonly used OSDA tetrapropylammonium (TPA) was included in its bromide salt form and heteroatoms such as aluminium can be added to produce catalytically active materials. NH_4Cl was added to aid the reaction, ascribed to introduction of basicity due to the formation and liberation of ammonia (NH_3) during the mechanical treatment. However, this additive was later found not to be vital. In contrast, the crucial part of this reagent mix is the presence of a small amount of water. As is the case in the initial study, water can be introduce in the form of crystal water in sodium silicate (or other reagents) or also added separately. In either case it facilitates the depolymerisation of silica and thus enabling the ensuing crystallisation. As indicated in Equation 11, these reactions are the forward and back reactions of polymeric silicon oxide with water, which may be interpreted as water playing the role of a catalyst. This process can also be enabled by use of ammonium fluoride NH_4F, in analogy to the fluoride route in solution-based reactions.[17] Evidence for the intermediate shown in Equation 12 and Equation 13 was provided by solid-state NMR investigation of a material at different crystallisation times. The use of NH_4F opens up protocols with reagents nominally not containing water, but comes with the drawback of using a toxic reagent.

$$Si(OSi)_4 + nH_2O \rightleftharpoons Si(OSi)_{4-n}(OH)_n \quad [11]$$

$$SiO_2 + 6\,NH_4F \longrightarrow SiF_6^{2-} + 2\,NH_4^+ + 4\,NH_3 + H_2O \quad [12]$$

$$SiF_6^{2-} + 4\,NH_3 + 2\,H_2O \longrightarrow SiO_2 + 2\,NH_4^+ + 6\,F^- \quad [13]$$

A dedicated study of the mechanism in the formation of zeolites with **MFI** framework was conducted by Nada et al. who confirmed previous interpretations by Xiao and co-workers.[18–20] An interesting observation was made when the authors investigated

the solvent-free synthesis of **MOR** zeolites, where they could establish that a certain minimal mechanical energy was required in the pre-treatment, otherwise no zeolite product was formed. In some cases this means that only after a longer duration of manual grinding (mortar and pestle) the crystallisation of the desired zeolite phase was successful. However, as found by Pashkova et al., in the synthesis of zeolite SSZ-13 (**CHA**), a higher energy is required and a transition to use ball mills for the mechanical pre-treatment was necessary.[21] Use of such automated equipment with the accompanying higher energies can shorten the treatment time compared to manual operation and has the additional benefit of rendering the process more reproducible.[22]

5.1.3 Potential of the solvent-free method for germanosilicate zeolites

The synthesis of zeolites in absence of a solvent appears to be a well suited method for some of the most common framework types. However, so far more complex structures are rarely found in publications. Arguably the most sophisticated reported frameworks are **ITW** and **ITH** from a study by Wu et al.[23] Naturally, first investigations into a novel synthetic method target comparatively simple products, especially in light of their industrial relevance. At this point in time, however, testing the limits is an important step towards establishing its general applicability. The structure-directing and framework-building germanium has so far only been mentioned once in the published literature, in the synthesis of **ITH**, a framework that is also obtainable as a pure silica variant.[24] Several known zeolite frameworks are only known as germanosilicates and the question poses itself whether these can be produced using the solvent-free method as well. Additionally, the prospect of this limitation regarding elemental composition encountered in hydrothermal syntheses not being present in this solid-state transformations is quite intriguing.

The aforementioned benefits for zeolite synthesis would be even more advantageous with respect to germanosilicates. Improvements in synthesis conditions and a more effective production of such materials could mean that their potentially superior structural properties can be utilised without being hindered too drastically by the associated monetary cost.

5.2 Solvent-free synthesis of germanosilicate zeolites

5.2.1 Syntheses towards zeolites with ITH topology

The only reported solvent-free synthesis of a germanosilicate zeolite to date is by Liu et al., who investigated material ITQ-13 (**ITH**), in particular its *d4r* units using ^{19}F solid-state NMR.[24] This zeolite can be prepared as pure silica material but also as germanosilicate in various Si/Ge ratios. Based on an earlier publication by Wu et al. who synthesised pure silica **ITH** using the solvent-free method,[23] the authors were successful in obtaining the germanosilicate variant, albeit only with comparatively low amounts of germanium. Synthesis mixtures with Si/Ge ratios < 5 resulted only in formation of another, denser ammonium hydrogen germanate phase ($((NH_4)_3H(Ge_7O_{16}) \cdot n(H_2O))$.[25] In all cases, hexamethonium dibromide (HM-Br, hexane-1,6-bis(trimethylammonium) dibromide) was used as the OSDA. In traditional hydrothermal syntheses, this compound needs to be anion exchanged to its hydroxide form. However, due to the two quaternary nitrogen atoms, this is often a long, tedious, and even somewhat expensive procedure. Being able to use the OSDA as bromide, which is the form it is synthesised in (compare section 5.4.2) is an important advantage of the solvent-free methodology.

5.2.1.1 Si-ITH

Using the published procedures as a starting point, attempts to synthesise pure silica **ITH** were started. The dry, solid reagents silica gel (SiO_2), ammonium fluoride (NH_4F), and hexamethonium dibromide (HM-Br, $(N(CH_3)_3)C_6H_{12}Br_2$) were ground using mortar and pestle for 15 min. After heat treating the resulting paste at 180 °C for 6 d, the resulting material does not exhibit the structure of the expected zeolite phase, as seen in collected PXRD patterns shown in Figure 5.1a. This phase was identified as ammonium hexafluorosilicate ($(NH_4)_2SiF_6$) phase,[26] which is water-soluble.

Upon adding a small amount of **ITH** seed crystals (obtained through conventional hydrothermal synthesis) to the mixture, the targeted zeolite phase can be obtained, shown in Figure 5.1b. The remaining minor ammonium fluorosilicate phase can be removed by washing the synthesised material with water. Although the presence of a secondary phase means that not all of the reagents are transformed into the desired product, this synthesis works very well and the by-product is easily removed. The produced zeolite is also stable after removal of the OSDA by calcination. The efficacy of the method is also demonstrated by employing the crystals of the solvent-free obtained zeolite as seed

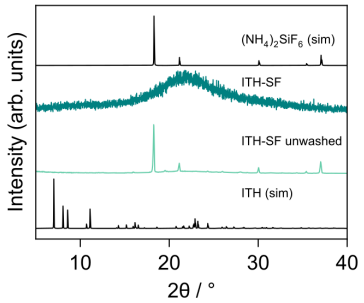

a) Samples obtained from grinding raw materials and subsequent heat treatment.

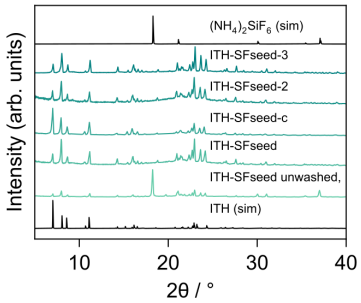

b) Samples obtained from grinding raw materials and **ITH** seed crystals and subsequent heat treatment. The calcined sample is suffixed by "-c". The samples suffixed with numbers have been obtained using crystals from the previous solvent-free synthesis.

Figure 5.1. PXRD patterns of products from solvent-free syntheses towards pure silica zeolites with **ITH** framework.

for two consecutive syntheses. The so produced zeolites are of the same quality as the original, solvent-free produced sample, judged from PXRD analysis. In both of these cases, the as synthesised material was washed with water to remove the ammonium fluorosilicate by-product.

SEM images of the seed crystals as well as the solvent-free obtained samples with **ITH** framework are shown in Figure 5.2. Both the original seeds as well as all consecutively obtained samples consist of rod-shaped crystallites. The solvent-free obtained samples also show ill-defined particles, most likely amorphous by-product. Nonetheless, crystals with sharp edges are predominant in all samples. Notably, the hydrothermal synthesis results in somewhat more separated rods, which only aggregate sparingly in a star shape as shown in Figure 5.2a. In absence of solvent, individual crystallites are rarely found and larger agglomerates and intergrowths are more common.

5.2.1.2 Ge-ITH

In the next iteration of syntheses, GeO_2 was added as germanium source to the reaction mixture. Experiments were conducted both with and without seed crystals and in both cases an **ITH** zeolite phase could be produced. Several Si/Ge ratios were used and PXRD patterns of all samples are shown in Figure 5.3a. In the synthesis with the lowest amount of germanium (Si/Ge=7.2), the previously seen ammonium fluorosilicate phase is also formed as by-product. The structure of the related germanate analogue is isomorphous and the two PXRD patterns are almost identical. Therefore it is uncertain whether the sample contains only the fluorosilicate, or also the germanate, or potentially even a mixed metal compound of this structure. This phase can be successfully removed by washing with water. Additionally, a minor phase with its main peak at 11.4° 2θ was noticed. It

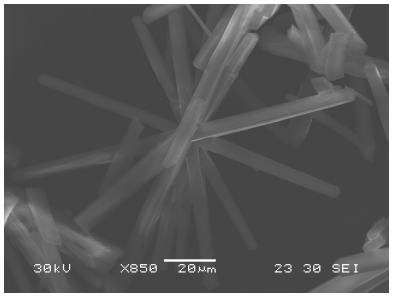

a) SEM image of hydrothermally synthesised zeolite **ITH** used as seed crystals for solvent-free syntheses.

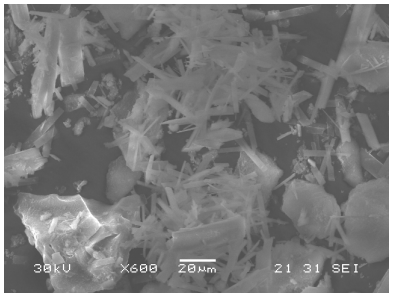

b) SEM image of solvent-free synthesised pure silica **ITH** using hydrothermally synthesised seed crystals shown in Figure 5.2a.

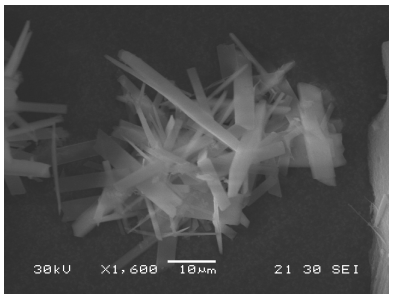

c) SEM image of solvent-free synthesised pure silica **ITH** using hydrothermally synthesised seed crystals shown in Figure 5.2b.

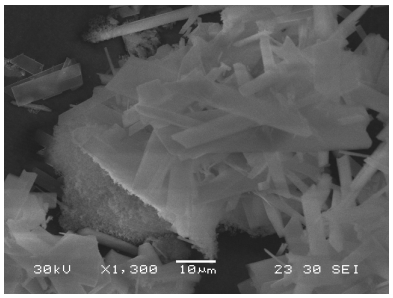

d) SEM image of solvent-free synthesised pure silica **ITH** using solvent-free synthesised seed crystals shown in Figure 5.2c.

Figure 5.2. SEM images of solvent-free synthesised pure silica samples targeting the **ITH** framework.

could be assigned to hydrated ammonium hydrogen germanate,[25] possibly the same phase which had been observed by Liu et al. in their studies. However, after calcination of this material at 575 °C peaks associated with this phase have disappeared. At this point it is unclear what the decomposition products are. It can be assumed that ammonia is released and it may also be likely that water is formed, leaving a germanium oxide phase as the sole solid product. The PXRD pattern of the calcined material does indeed show a peak at 26.0° 2θ which could indicate quartz-type GeO_2. However, this overlaps with reflections present in the **ITH** framework itself, so unambiguous assignment is not possible.

SEM analysis of this sample ("Ge-ITH-SF" in Figure 5.3a) shows a crystalline phase of similar morphology as solvent-free obtained Si-ITH samples (compare Figure 5.2 above). The rod or plank-shaped crystallites are typically agglomerated and possibly intergrown. Compared to the pure silica analogue, the crystals are roughly the same size with an average length of approximately 10 µm, however, considerably larger crystals, for example around 30–40 µm are also present.

Increasing the germanium content to Si/Ge ratios of 5.0 and 3.3, only a greater amount of the ammonium hydrogen germanate phase is observed. Still, both samples also show PXRD peaks corresponding to the **ITH** framework (Figure 5.3c). This is in

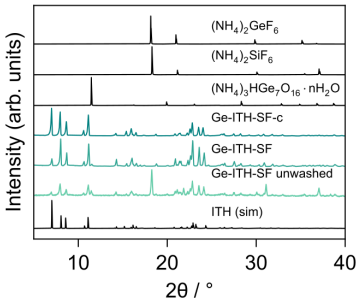

a) PXRD pattern of a sample obtained from a synthesis with ratios Si/Ge = 7.2, F/(Si+Ge) = 1.0, heated at 175 °C for 4 d. The calcined sample is suffixed by "-c".

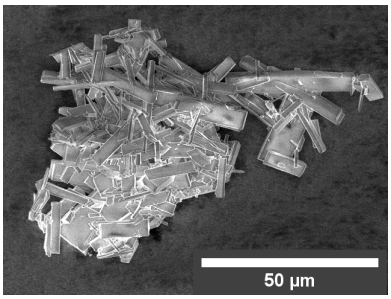

b) SEM image of solvent-free synthesised germanosilicate ("Ge-ITH-SF" in Figure 5.3a) sample targeting the **ITH** framework.

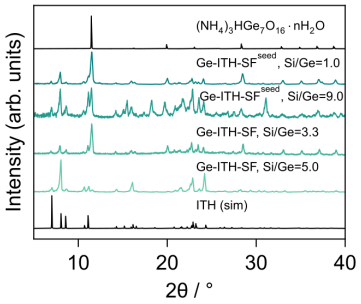

c) PXRD patterns of sample obtained from a synthesis with varying Si/Ge ratios and both with and without using **ITH** seeds.

Figure 5.3. PXRD patterns and SEM image of products from solvent-free syntheses towards germanosilicate zeolites with **ITH** framework.

contrast to the earlier report, where only the undesired germanate phase was obtained using Si/Ge ratios below 5.0. Testing whether seed crystals would have a beneficial effect on the synthesis by suppressing the formation of the unwanted germanate by-products, two experiments were conducted including previously synthesised **ITH** crystals in the reagent mix. Unfortunately, this adaption did not result in the desired effect and PXRD patterns of obtained materials still show their multi-phase nature.

5.2.1.3 Ball milled ITH

In addition to experiments involving manual grinding, several syntheses were attempted where the mechanochemical treatment of reagents was performed using a shaker ball mill. PTFE milling vessels and YSZ milling balls were chosen to avoid side-reactions that may occur with materials like steel. Looking at the PXRD patterns of the subsequently produced materials in Figure 5.4a, the pure silica experiment only lead to the previously seen ammonium fluorosilicate phase. Moving to higher germanium content (Si/Ge = 1.0), no reaction of note has taken place as the PXRD pattern only shows peaks corresponding to the starting material GeO_2 as an argutite phase (rutile-type). Lowering the Si/Ge ratio to 2.0, zeolite **ITH** is formed alongside the ammoniumhydrogen germanate phase as

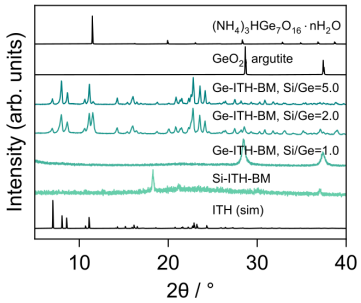

a) PXRD patterns of samples obtained from syntheses in varying Si/Ge ratios.

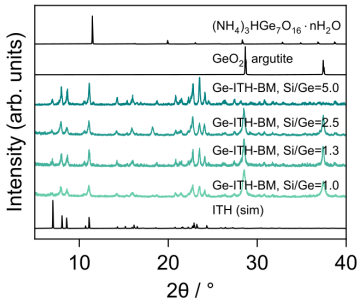

b) PXRD patterns of samples obtained from syntheses with additional water in varying Si/Ge ratios.

Figure 5.4. PXRD patterns of products from solvent-free syntheses towards zeolites with **ITH** framework using a ball mill for the mechanochemical treatment of reagents prior to synthesis.

well as some unreacted GeO_2. Evidence for the argutite phase is not observed anymore when decreasing the germanium content further.

A potential cause for the reagent GeO_2 to not participate in the reaction with low Si/Ge ratios could be a lack of mobility of the particles. Addition of a small amount of water to the milling reaction could help in this regard and a few experiments were carried out in this way. It is worth noting that that the used volumes of water are still low and should not be considered as a solvent but rather an additional reagent. Unfortunately, PXRD patterns of obtained materials show virtually no difference to the previously conducted syntheses as shown in Figure 5.4b. Both **ITH** and argutite are present in all cases except the experiment with the highest Si/Ge ratio of 5.0. Although this intended effect did not occur, the addition of water seems to have a beneficial effect in terms of decreasing the relative amount of the germanate phase (PXRD peak at 11.4° 2θ), but it could not be avoided altogether.

5.2.2 Syntheses towards zeolites with UTL topology

Parallel to experiments targeting zeolites with **ITH** framework, syntheses were conducted with the hope of producing materials with **UTL** topology. Although this zeolite phase can be obtained with a range of different OSDAs,[27] the piperidine-based 6,10-dimethyl-5-azoniaspiro[4.5]decane hydroxide (DMASD-OH) has been a tried and proven compound in hydrothermal experiments owing to its comparatively straight-forward synthesis and efficacy in the synthesis of zeolites with **UTL** framework. Analogously to above described experiments towards **ITH** materials, DMASD was used in its bromide form in the conducted solvent-free experiments. Ammonium halides, mostly fluoride, are used as mineralising agents and should compensate the lack of basicity otherwise ensured by a hydroxide OSDA. Fluoride anions further assist the depolymerisation due to reactive

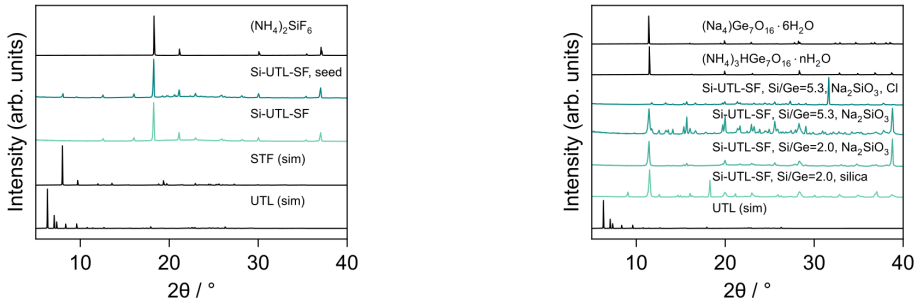

a) PXRD patterns of samples obtained from syntheses using only silica as T-atom source.

b) PXRD patterns of samples obtained from various syntheses in the presence of germanium. All syntheses were conducted using silica SiO_2 as source, in several $Na_2SiO_3 \cdot {}_9H_2O$ was used additionally.

Figure 5.5. PXRD patterns of products from solvent-free syntheses towards zeolites with **UTL** framework.

fluorosilicate intermediates.

Several experiments were conducted both in absence and presence of germanium in the synthesis mixture. No direct hydrothermal synthesis of a pure silica **UTL** has been discovered yet and this is also the case for the here presented attempts in a solvent-free manner. Using only silica, DMASD-Br, and NH_4F as reagents, with and without **UTL** seed crystals, the main product is an ammonium fluorosilicate phase (Figure 5.5a). Unfortunately, no trace of a **UTL** material is observed. Some other, minor phases are also present, one of which can be assigned to another zeolite phase **STF**, a known competing phase in syntheses towards **UTL**.[28]

Changing the reaction system to also include germanium in the mixture results once more in a mix of different phases (see Figure 5.5b,) with the most dominant the ammonium hydrogen germanate, previously also seen in experiments towards zeolite **ITH**. Additionally employing sodium silicate, which has been successfully used in solvent-free synthesis of other zeolite phases,[14] does not alter the product selectivity. This is also caused by the facile formation of a sodium germanate[29] or sodium ammonium germanate[29] phase which are isostructural to the ammonium analogue[25] and a mixture of these is most likely present. An additionally formed phase is sodium fluoride with its main peak at roughly 39° 2θ. In agreement with what has been found in the literature previously,[24] ammonium chloride proved to be less effective than the fluoride in activating the reagents. The dominant phase of this experiment is sodium chloride with other phases only showing minor contributions.

Investigating whether the addition of water or seed crystals would have an influence on the outcome of the reaction, several experiments were conducted. PXRD patterns of these products are shown in Figure 5.6. Even with the aid of water, the use of ammonium chloride does not result in any desired reaction and only quartz-type GeO_2 is obtained.

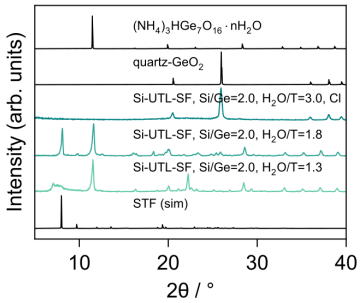

a) PXRD patterns of samples obtained from germanosilicate syntheses with water added as reagent.

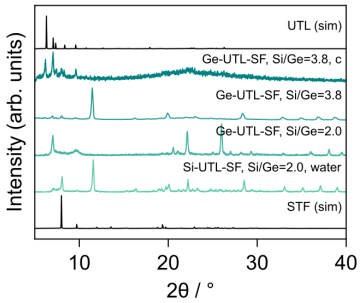

b) PXRD patterns of samples obtained from germanosilicate syntheses in the presence of **UTL** seed crystals.

Figure 5.6. PXRD patterns of products from solvent-free syntheses towards zeolites with **UTL** framework.

Using the more reactive fluoride leads to the previously seen ammonium germanate phase as well as the zeolite **STF**.

Employing seed crystals in syntheses with a Si/Ge ratio of 2.0 shows little difference to previously discussed products. However, decreasing the germanium content slightly to Si/Ge = 3.8 shows not only the familiar ammonium germanate phase but also some peaks at low 2θ angles. Calcination of this material reveals a PXRD pattern with high similarity to **UTL** as well as a considerable amount of amorphous material as a broad feature from around 15° to 25° 2θ. This is most likely the decomposition product of the germanate phase. This increase in background makes it difficult to accurately assess the structural integrity of the zeolitic phase, but judging from the distinguishable peaks, a **UTL** phase has been formed.

Interesting to note is also the significantly changed morphology of the obtained crystalline phase, determined by SEM imaging and shown in Figure 5.7. The hydrothermally synthesised seed crystals are plate-like as is common for zeolites with **UTL** topology. In contrast, the solvent-free obtained phase is rod-shaped with two dimensions considerably shorter than the third one. This is similar to the observation for solvent-free obtained samples with **ITH** framework which also crystallised in such a morphology. Visible in the image are also some large particles of irregular shape, most likely of amorphous nature in agreement with PXRD results. Calcination of this sample does not alter the morphology of individual crystals, but leads to agglomeration into larger, secondary particles. The Si/Ge ratio of these crystals is roughly 4.2±1.4, in line with the employed ratio in the synthesis. This is rather promising in terms of atom efficiency, compared to hydrothermal syntheses, where a Si/Ge=2 in the mixture usually leads to zeolite samples with a lower germanium content of Si/Ge = 3–4. Since germanium reagents are far more expensive than silicon sources the solvent-free synthesis methodology could help in reducing cost for germanosilicates by avoiding loss of the more precious metal due to

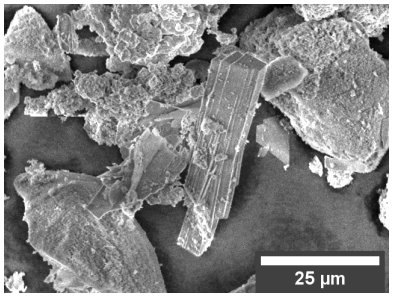

a) SEM image of the solvent-free synthesised sample using seed crystals and Si/Ge = 3.8.

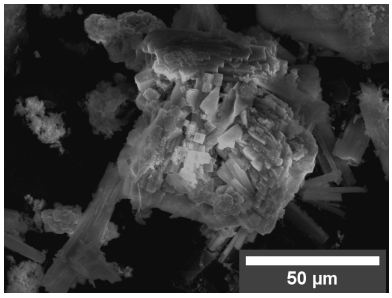

b) SEM image of the calcined sample shown in Figure 5.7a.

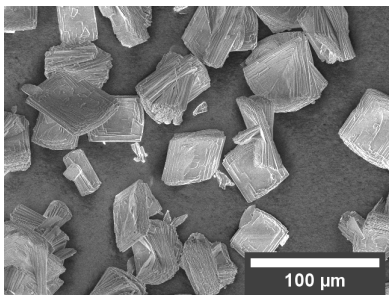

c) SEM image of the hydrothermally synthesised zeolite **UTL** sample used as seed crystals for solvent-free syntheses.

Figure 5.7. SEM images of solvent-free synthesised samples targeting the **UTL** framework.

inefficient synthesis. With these preliminary results, more work is required to establish a robust protocol targeting this so far only minor phase.

5.2.3 Syntheses towards zeolites with UOV topology

Another zeolite framework of interest is **UOV**, which is similar to **UTL** in that its framework can be described as stacked layers, connected by *d4r* units. A second similarity is that the **UOV** framework has so far only been found in germanosilicate materials. This is reflected in syntheses conducted with the solvent-free method when only silica is used as T atom source. Decamethonium (DM, decane-1,10-bis(trimethylammonium)) as hydroxide salt was used as OSDA in the original, hydrothermal synthesis of IM-17, the type material of the **UOV** framework.[30] In analogy to other solvent-free syntheses, the bromide salt (DM-Br) was used in this project. The PXRD patterns of the obtained material is displayed in Figure 5.8a. No crystalline phase is observed and only amorphous material is produced.

A similarly unsuccessful attempt is observed when using NH_4Cl as mineralising agent, despite an added germanium source to the solid mixture (Figure 5.8a). This is once more experimental evidence for the expected lower reactivity of the chloride anion compared to fluoride as shown below. The only crystalline phase of this experiment is unreacted quartz-type GeO_2.

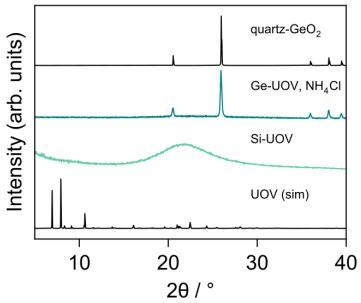

a) PXRD patterns of samples obtained from a pure silica synthesis and an experiment including a germanium source and using NH_4Cl as mineralising agent.

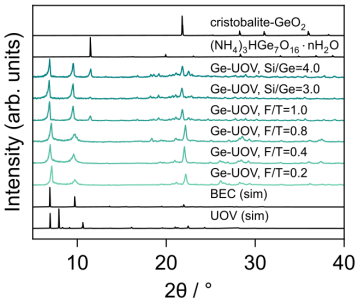

b) PXRD patterns of samples obtained from germanosilicate syntheses with varying Si/Ge and F/T (T=Si+Ge) ratios. Unless otherwise labelled, the synthesis was conducted with Si/Ge = 2.0 and F/T = 1.0.

Figure 5.8. PXRD patterns of products from solvent-free syntheses towards zeolites with **UOV** framework.

Transitioning to germanium containing reaction mixtures, a zeolite product was indeed formed, albeit not with the intended structure. The obtained phase was identified as **BEC**, a known competing phase in hydrothermal syntheses with the used OSDA DM-Br in the presence of fluoride.[30] Attempting to direct the reaction towards **UOV**, several different Si/Ge ratios as well as lowering the amount of fluoride compared to T atoms (F/T ratio) were tried, albeit with only negligible effect. The main difference is the presence of an additional ammonium germanate phase at higher F/T ratios. A third phase with its main diffraction peak at roughly 22° 2θ may be a cristobalite-type phase, commonly found as side-product in zeolite syntheses. Cristobalite-type structures are known with both SiO_2 and GeO_2 compositions so the found material may be either of these or potentially also a mixed metal oxide. The exact peak position is shifted for the individual samples, seemingly dependant on the fluoride concentration. Lower F/T ratios lead to the peak observed at slightly higher 2θ angles, indicative of a smaller unit cell.

Investigating materials obtained from germanium containing reactions with SEM

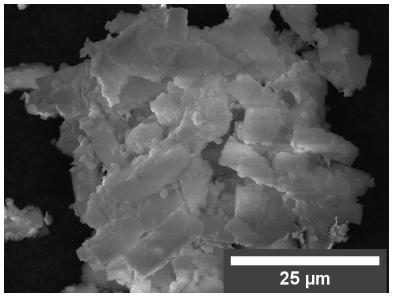

a) SEM image showing agglomerated block-shaped crystals mixed with smaller spherical particles possibly of a different crystalline phase.

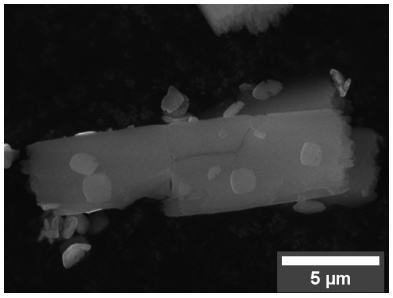

b) Single crystal potentially of the **BEC** zeolite phase with smaller spherical particles most likely cristobalite-type.

Figure 5.9. SEM images of solvent-free synthesised germanosilicate samples targeting the **UOV** framework with Si/Ge = 2.0 and F/T = 0.8.

supports the analysis of PXRD with at least two phases present. Shown in Figure 5.9 are images of the synthesis with Si/Ge = 2.0 and F/T = 0.8. The larger, block-shaped crystals are most likely the zeolite material with **BEC** framework, whereas the smaller, spherical particles are possibly the cristobalite phase.

5.2.4 Syntheses towards zeolites with ISV topology

As a final targeted structure for this project, the zeolite framework **ISV** was chosen. This framework type has been identified as the structure for both germanosilicates and also pure silica materials, similar to described **ITH**, discussed at the beginning of this section. The comparatively large TMATD-Br (1,3,3-trimethyl-6-azoniumtricyclo-[3.2.1.$4^{6,6}$]dodecane bromide) is used as OSDA, which has been used to hydrothermally synthesise the type material ITQ-7.[31] In contrast to syntheses towards other zeolite frameworks all of the experiments designed to lead to **ISV** materials were conducted by using a ball mill for the mechanochemical treatment. Obtained materials were also washed with water and dried before analysis using PXRD.

In the absence of germanium, only amorphous material is produced with the investigated conditions, shown in Figure 5.10a. However, the addition of GeO_2 to the mixture results in the crystalline material. Comparison with the simulated PXRD pattern for **ISV** shows good agreement and the synthesis can be considered a success. Some residual amorphous material is still visible, as well as peaks most likely corresponding to a cristobalite-type phase, which was also seen in syntheses towards zeolite with **UOV** framework (see section 5.2.3). The relative amount of amorphous material appears to be decreased when using a greater amount of fluoride in the reaction, ascribed to a higher degree of activation of the respective starting materials.

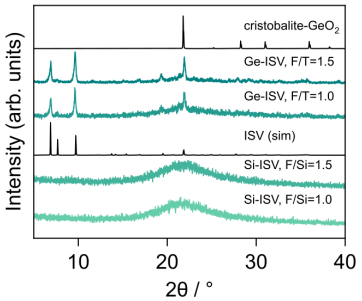

a) PXRD patterns of samples obtained from pure silica and germanosilicate (Si/Ge = 10.0) syntheses after washing.

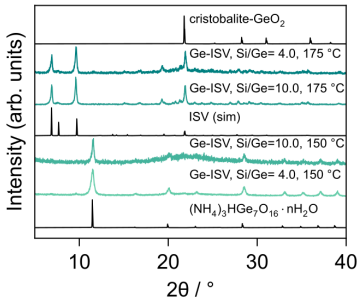

b) PXRD patterns of samples obtained from germanosilicate syntheses with F/T = 1.5 (T=Si+Ge).

Figure 5.10. PXRD patterns of products from solvent-free syntheses towards zeolites with **ISV** framework. All samples were washed and dried prior to the analysis.

The influence of both a lower temperature of 150 °C, as well as a variation in Si/Ge

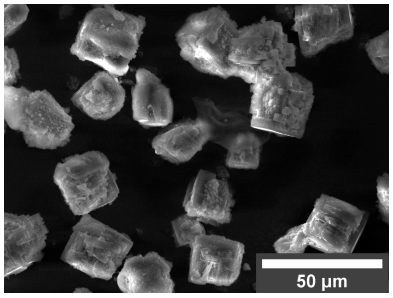

a) SEM image of the sample obtained from a synthesis using Si/Ge = 10.0.

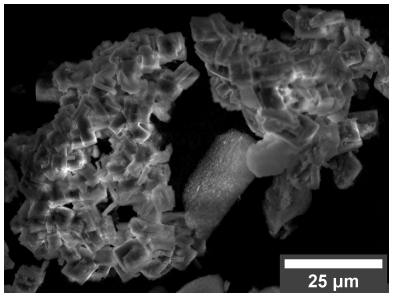

b) SEM image of the sample obtained from a synthesis using Si/Ge = 4.0.

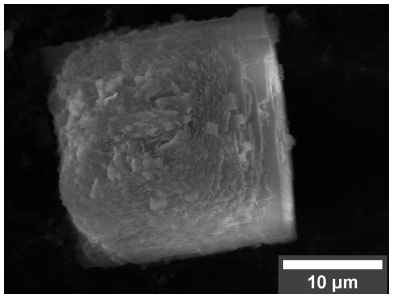

c) Single particle of the sample obtained from a synthesis using Si/Ge = 10.0.

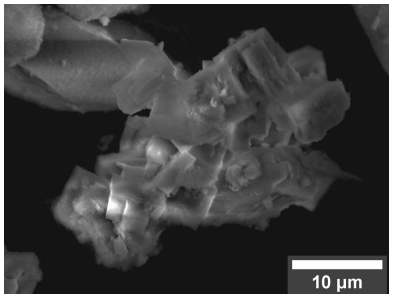

d) SEM image of the sample obtained from a synthesis using Si/Ge = 4.0 in higher magnification.

Figure 5.11. SEM images of solvent-free synthesised germanosilicate samples targeting the **ISV** framework with different Si/Ge ratios and F/T = 1.5.

ratio, were briefly investigated. The corresponding PXRD patterns are shown in Figure 5.10b. The formation of **ISV** seems to be favoured at higher temperatures as the materials obtained from 150 °C reactions show mainly peaks of the undesired ammonium germanate phase. The PXRD pattern of the sample with Si/Ge = 4.0 shows barely distinguishable features aligning with the expected peaks for the **ISV** framework. Besides this, the difference in tested Si/Ge ratio does not seem to impact the product formation as the desired zeolite phase is also observed with the higher germanium content without evidence for any additional by-product.

Investigating the crystal morphology of the obtained germanosilicate samples, SEM was performed and representative images are shown in Figure 5.11. For the sample obtained from the reaction with Si/Ge = 10.0, almost cubic blocks of intergrown crystals, with a length of 20–25 µm are observed. It is unclear whether the individual crystallites, also exhibiting a cubic shape with about 1 µm in length, are all of the zeolite phase or whether some of the smaller crystals (compare the higher magnification in Figure 5.11c) are the cristobalite phase. Some ill-formed particles are also visible, indicating amorphous material.

The samples obtained from syntheses with higher germanium content (Si/Ge = 4.0) showed agglomerated and intergrown large clusters of individual, block shaped

crystallites. The primary particles span roughly 6–7 μm in length and for non-cubic particles, the short side is about 2 μm. The greater amount of germanium in the reaction mixture seems to be beneficial in terms of crystal growth, an observation that is often also made in hydrothermal syntheses.

5.3 Conclusion and perspective

Although this project only scratches the surface of what may be possible for solvent-free synthesis of germanosilicate zeolites, several indications of its potential could be observed. In agreement with published works on more conventional aluminosilicate and purely siliceous zeolite materials, the streamlined methodology enables facile preparation of germanosilicate samples.

Reproducing literature reports,[24] samples exhibiting the **ITH** framework were obtained both as pure silica and germanosilicate variants. Products can be obtained directly, but the syntheses work especially well using seed crystals. These can be produced from conventional hydrothermal syntheses but crystals obtained through the solvent-free method are just as suitable.

In contrast to this success, the targeted framework **UOV** could not be obtained and instead another zeolite phase with **BEC** structure was formed. This is thought to be caused by the interplay between the OSDA used (decamethonium bromide) and the presence of fluoride, a combination which also in hydrothermal syntheses leads to the undesired framework. Unfortunately, it appears that for successful formation of any low density silicate based material ammonium halide sources are unavoidable and under the investigated conditions, the chloride salt did not achieve appreciable activation of the starting materials. One of the potential reasons why the formation of the **BEC** framework is favoured over **UOV** is due to its higher T atom density.

An analogous behaviour was observed for syntheses aiming to produce materials with **UTL** framework. The competing phase commonly found in reactions containing the OSDA DMASD-Br is zeolite **STF**, once more a framework with a higher density compared to the targeted structure. The most promising product was obtained when hydrothermally synthesised **UTL** crystals were used as seed crystals. Its PXRD pattern shows peaks that may correspond to the desired framework. This is not unequivocal evidence for the successful synthesis of **UTL** from the solvent-free route and further investigations are required. Additionally, this is only a minor phase of the material, which mainly consists of ammonium hydrogen germanate. Thus, optimisation of synthesis parameters

are required before this finding can be considered a complete success. These would include further adjustments to Si/Ge ratios and potentially using higher temperatures for the crystallisation, both of which could also aid in suppressing the formation of the undesired **STF** zeolite.

The most successful results of the project so far are the syntheses aiming to produce zeolites with **ISV** framework. Materials exhibiting this structure have so far not been reported using the solvent-free methodology. Expanding the pool of available frameworks with this novel synthesis method only cements its widespread usability and is another important step towards establishing a potential generalisability. Likewise, this is only the second time a germanosilicate zeolite has been synthesised without solvent, besides the reported zeolite **ITH**.[24] Since the performed syntheses does not yet lead to a single phase product, reaction conditions need to be adjusted before the claim can be made that this type of synthesis can be chosen reliably as an alternative to the traditional hydrothermal route. Judging from PXRD and SEM analysis, higher synthesis temperatures may be beneficial also in this case. Likewise, prolonging the heat treatment may aid the formation of the zeolite phase.

Although solvent-free synthesis towards germanosilicate zeolites has not yet been established satisfactorily, preliminary success has been achieved. It is important to note that the use of ammonium fluoride as reagent may still be considered a disadvantage due to its toxicity. As mentioned, the presence of other phases is so far still a major obstacle and requires further investigations. Such studies would aim to not only find the correct conditions for the synthesis of a specific framework type, but more generally obtain knowledge about the underlying mechanism leading to the formation of undesired phases, for example ammonium germanate, and how to avoid them.

5.4 Experimental section

5.4.1 Reagents

All chemicals (see Table 5.1) were used without purification prior to synthesis.

Table 5.1. Chemicals and their suppliers.

Chemical	Abbreviation	Supplier
Silica gel "Davisil"	SiO_2	Fluorochem
Germanium dioxide	GeO_2	Sigma-Aldrich
Germanium dioxide	GeO_2	Alfa Aesar
Ammonium fluoride	NH_4F	BDH
Hexamethonium dibromide	HM-Br	Aldrich
Decamethonium dibromide	DM-Br	Aldrich
N,N,N′,N′-tetramethyl-1,6-diaminohexane	TMDAH	TCI Chemicals
1,6-Dibromohexane	–	Aldrich
1,6-Dibromodecane	–	Aldrich
Diethyl ether	DE	Honeywell
Ethanol	EtOH	VWR
Trimethylamine, 33 wt% solution in EtOH	$N(CH_3)_3$	Aldrich

5.4.2 Synthesis details

5.4.2.1 Hexamethonium dibromide (HM-Br)

Syntheses of HM-Br were conducted by alkylation of trimethylamine with dibromohexane on various scales, keeping the reagent ratios constant as described in the example below. 1,6-dibromohexane (6.11 g, 25 mmol, 1 eq) was added to a commercial ethanolic solution of trimethylamine (33 wt%, 13.42 g, 75 mmol, 3 eq). The mixture was heated at 60 °C for 48 h. After the mixture had cooled down to room temperature, some white solid had formed and the precipitation was completed using 100 mL diethyl ether (DE). The white solid was washed with a further 200 mL DE and dried in a fume cupboard and later in an oven at 80 °C.

yield: 8.20 g white crystals (23 mmol, 90 %)

^{1}H NMR (400 MHz, MeOD): δ (ppm) = 3.44–3.39 (m, 4 H), 3.18 (s, 18 H), 1.94–1.79 (m, 4 H), 1.55–1.45 (m, 4 H).

^{13}C NMR (126 MHz, MeOD): δ (ppm) = 66.17, 52.26, 25.22, 22.22.

5.4.2.2 Decamethonium dibromide (DM-Br)

Syntheses of DM-Br were conducted by alkylation of trimethylamine with dibromodecane, adapting the procedure described for HM-Br. They were carried out on various scales, keeping the reagent ratios constant as described in the example below. 1,10-dibromodecane (3.02 g, 10 mmol, 1 eq) was added to a commercial ethanolic solution of trimethylamine (33 wt%, 5.37 g, 30 mmol, 3 eq). The mixture was heated at 60 °C for 48 h. After the mixture had cooled down to room temperature, some white solid precipitate was visible and the precipitation was completed using 50 mL diethyl ether (DE). The white solid was washed with a further 100 mL DE and dried in a fume cupboard and later in an oven at 80 °C.

yield: 3.64 g white crystals (9 mmol, 86 %)
^{1}H NMR (400 MHz, MeOD): δ (ppm) = 3.40–3.34 (m, 4 H), 3.15 (s, 18 H), 1.80 (dq, 4 H, J = 14.7, 7.4 Hz), 1.47–1.32 (m, 14 H).
^{13}C NMR (126 MHz, MeOD): δ (ppm) = 66.44, 52.16, 28.96, 28.74, 25.92, 22.55.

5.4.2.3 1,3,3-Trimethyl-6-azoniumtricyclo[3.2.1.4^{6,6}]dodecane bromide (TMATD-Br)

The synthesis of TMATD-Br was conducted by alkylation and cyclisation of the amine with the dibromoalkane, analogously to the synthesis of DMASD-Br described in chapter 4, section 4.4.2. 2,4,4-Trimethyl-6-azabicyclo[3.2.1]octane (26.75 g, 175 mmol 1 eq) was dissolved in 150 mL acetonitrile and added to a round-bottom flask with potassium carbonate (28.90 g, 209 mmol, 1.2 eq). 1,4-dibromobutane (37.69 g, 175 mmol, 1 eq) was dissolved in 50 mL acetonitrile and the mixture added dropwise under stirring and while cooling the flask in an ice bath. After the completed addition, the mixture was heated to 90 °C (reflux conditions) for 24 h. After letting the mixture cool down to room temperature, the carbonate was filtered off and washed with 300 mL acetonitrile. The solvent was then removed under reduced pressure and the residual solid redissolved in 100 mL ethanol. The so purified compound was precipitated by addition of diethyl ether (DE, 200 mL), filtered and washed with more DE.

yield: 37.943 g white crystals (132 mmol, 75 %)
^{1}H NMR (400 MHz, MeOD): δ (ppm) = 3.94 (td, 1 H, J = 4.8, 2.2 Hz), 3.82–3.73 (m, 1 H),3.72–3.64 (m, 3 H),3.64–3.54 (m, 1 H),3.38 (d, 1 H, J = 1.3 Hz),3.35 (d, 1 H, J = 1.6 Hz),2.33–2.24 (m, 1 H),2.21 (h, 6 H, J = 3.3, 2.8 Hz),1.79–1.63 (m, 2 H),1.27 (s,

3 H),1.22 (s, 3 H),1.12 (s, 3 H).

^{13}C NMR (126 MHz, MeOD): δ (ppm) = 74.08, 72.02, 69.55, 61.30, 53.21, 41.36, 38.63, 34.35, 28.30, 26.00, 22.83, 21.70.

5.4.2.4 Hydrothermal synthesis of zeolite JLG-18 (ITH)

The synthesis of **ITH** was conducted similar to reported procedures in the literature.[32] N,N,N′,N′-tetramethyl-1,6-diaminohexane (TMDAH) was was employed as OSDA. A gel was prepared with a composition of 1 SiO_2 : 0.67 GeO_2 : 14 TMDAH : 2.85 NH_4F 90 H_2O, using 0.09 g SiO_2, 0.11 g GeO_2, 4.5 mL TMDAH, 0.16 g NH_4F, and 2.5 mL H_2O. The mixture was stirred in a PTFE liner for 60 min and subsequently transferred in the corresponding stainless steel autoclave. The autoclave was place in an oven and heated at 175 °C for 7 d. After cooling to room temperature, the obtained solid was thoroughly washed with water and dried at 80 °C overnight.

yield: 0.20 g transparent-white powder of polycrystalline rods (light microscopy)

5.4.2.5 Solvent-free syntheses towards zeolite ITH

Reactions were conducted by grinding the solid raw materials by hand for 15 min using mortar and pestle. The employed OSDA is hexamethonium dibromide (HM-Br), either used from a commercial source or prepared as described above. **ITH** seed crystals were synthesised hydrothermally as material JLG-18 as described above. The formed paste was scooped into a PTFE liner of a stainless steel autoclave and the autoclave heated in an oven at the stated temperature. After the desired amount of time, the autoclave was left to cool to room temperature and the obtained solid either characterised directly or washed with water and thereafter dried at 80 °C overnight.

Table 5.2. Experimental details of solvent-free syntheses towards pure silica zeolite **ITH**. Seed crystals obtained by hydrothermal synthesis are denoted with superscript “ht” and those obtained from previous solvent-free syntheses with “sf”.

SiO_2 [g]	NH_4F [g]	HM-Br [g]	seed [g]	F/T [-]	temperature [°C]	time d
1.599	1.005	0.302		1.0	180	6
1.600	0.999	0.299	0.050^{ht}	1.0	175	1
1.599	1.004	0.300	0.051^{sf}	1.0	175	1
1.603	0.999	0.299	0.050^{sf}	1.0	175	2

Several experiments were carried out using a ball mill for the pre-synthetic, mechanochemical treatment of reagents. In these experiments, PTFE milling vessels (inner

Table 5.3. Experimental details of solvent-free syntheses towards germanosilicate zeolite **ITH**. Seed crystals obtained by hydrothermal synthesis are denoted with superscript "ht" and those obtained from previous solvent-free syntheses with "sf".

SiO_2 [g]	GeO_2 [g]	NH_4F [g]	HM-Br [g]	H_2O [g]	seed [g]	Si/Ge [-]	F/T [-]	temperature [°C]	time d
1.46	0.35	1.01	0.30			7.2	1.0	175	4
0.60	0.31	0.90	0.60	0.16		3.3	1.2	175	7
1.20	0.42	1.19	1.81	2.50		5.0	1.3	175	7
0.60	0.12	0.41	0.12		0.02^{sf}	1.0	9.0	175	1
0.60	1.05	0.59	0.97	0.90	0.02^{ht}	1.0	0.8	175	2

volume of 14 mL) were used due to avoid chemical reactions. Two YSZ (yttrium stabilised zirconia) milling balls of 10 mm, 3.4 g each were chosen as milling media. The reactants and milling balls were added to the milling vessel and milled for 30 min using a frequency of 25 Hz. Thereafter, the produced paste was scooped into a PTFE lined stainless steel autoclave. The autoclave was placed in an oven for the desired amount of time at 175 °C and afterwards left to cool down to room temperature. All products were filtered, washed with water and then dried at 80 °C overnight.

Table 5.4. Experimental details of solvent-free syntheses towards zeolite **ITH** using a ball mill for the mechanochemical treatment.

SiO_2 [g]	GeO_2 [g]	NH_4F [g]	HM-Br [g]	H_2O [g]	Si/Ge [-]	F/T [-]	temp. [°C]	time d
0.08		0.08	0.12			1.6	175	7
0.06	0.11	0.06	0.10		1.0	1.0	175	7
0.26	0.09	0.26	0.39		2.0	1.1	175	7
0.23	0.12	0.22	0.35		5.0	1.3	175	7
0.15	0.26	0.15	0.45	0.62	1.0	0.8	175	7
0.17	0.22	0.17	0.45	0.46	1.3	0.9	175	7
0.24	0.17	0.24	0.50	0.64	2.5	1.3	175	7
0.26	0.09	0.26	0.49	0.70	5.0	1.3	175	7

5.4.2.6 Solvent-free syntheses towards zeolite UTL

Reactions were conducted by grinding the solid raw materials by hand for 15 min using mortar and pestle. The employed OSDA is dimethylazoniaspirodecane bromide (DMASD-Br), synthesised as described in section 4.4.2. **UTL** seed crystals were synthesised hydrothermally as material IM-12 as described in the same section. The formed paste was scooped into a PTFE liner of a stainless steel autoclave and the autoclave heated

in an oven at the stated temperature. After the desired amount of time, the autoclave was left to cool to room temperature and the obtained solid either characterised directly or washed with water and thereafter dried at 80 °C overnight.

Table 5.5. Experimental details of solvent-free syntheses towards pure silica zeolites with **UTL** framework.

SiO_2 [g]	NH_4F [g]	DMASD-Br [g]	seed [g]	F/T [-]	temperature [°C]	time d
1.60	1.00	0.85		1.0	175	9
1.60	1.02	0.50	0.05	1.0	175	9

Table 5.6. Experimental details of solvent-free syntheses towards germanosilicate zeolites with **UTL** framework.

$Na_2SiO_3 \cdot 9\,H_2O$ [g]	SiO_2 [g]	GeO_2 [g]	NH_4F [g]	DMASD-Br [g]	Si/Ge [-]	F/T [-]	temp. [°C]	time d
1.31	0.33	0.20	0.42^{Cl}	0.22	5.3	0.6	180	1
1.31	0.33	0.20	0.30	0.23	5.3	0.7	180	2
1.30	0.30	0.50	0.25	0.25	2.0	0.5	180	2
	1.07	0.93	1.00	0.85	2.0	1.0	175	9

Table 5.7. Experimental details of solvent-free syntheses towards germanosilicate zeolites with **UTL** framework with additional water and seed crystals. Experiments where NH_4Cl was used instead of NH_4F are indicated by a superscript "Cl".

SiO_2 [g]	GeO_2 [g]	NH_4F [g]	DMASD-Br [g]	H_2O [g]	seed [g]	Si/Ge [-]	F/T [-]	H_2O/T [-]	temp. [°C]	time d
0.60	0.53	0.45	1.24	0.36		2.0	0.8	1.3	175	14
0.60	0.53	0.60	1.24	0.81		2.0	1.1		175	7
0.60	0.53	0.86^{Cl}	1.24	0.81		2.0	1.1	3.0	175	14
0.60	0.52	0.45	1.24		0.06	2.0	0.8		175	14
1.10	0.50	1.04	0.86		0.05	3.8	1.2		175	14
0.60	0.52	0.44	1.24	0.45	0.06	2.0	0.8	1.7	175	14

5.4.2.7 Solvent-free syntheses towards zeolite UOV

Reactions were conducted by grinding the solid raw materials by hand for 15 min using mortar and pestle. The employed OSDA is decamethonium dibromide (DM-Br), used from a commercial source or prepared as described above. The formed paste was scooped into a PTFE liner of a stainless steel autoclave and the autoclave heated in an oven at the stated temperature. After the desired amount of time, the autoclave was left to cool to

room temperature and the obtained solid either characterised directly or washed with water and thereafter dried at 80 °C overnight.

Table 5.8. Experimental details of solvent-free syntheses towards zeolites with **UOV** framework. Experiments where NH_4Cl was used instead of NH_4F are indicated by a superscript "Cl".

SiO_2 [g]	GeO_2 [g]	NH_4F [g]	DM-Br [g]	H_2O [g]	Si/Ge [-]	F/T [-]	H_2O/T [-]	temperature [°C]	time d
0.80		0.51	0.50			1.0		175	7
0.60	0.52	0.60	1.05	0.81	2.0	1.1	4.5	175	7
0.15	0.13	0.03	0.32	0.30	2.0	0.2	4.5	175	7
0.15	0.13	0.06	0.31	0.30	2.0	0.4	4.5	175	7
0.15	0.13	0.11	0.34	0.30	2.0	0.8	4.5	175	7
0.15	0.13	0.14	0.34	0.30	2.0	1.0	4.5	175	7
0.15	0.09	0.12	0.28	0.27	3.0	1.0	4.5	175	7
0.15	0.07	0.12	0.26	0.25	4.0	1.0	4.5	175	7
0.12	0.11	0.03^{Cl}	0.25	0.24	2.0	0.2	4.5	175	7
0.12	0.11	0.07^{Cl}	0.25	0.24	2.0	0.4	4.5	175	7

5.4.2.8 Solvent-free syntheses towards zeolite ISV

All experiments targeting zeolites with **ISV** framework were performed using a ball mill for the the mechanochemical treatment of the reagents. The milling was carried out in a Retsch MM 400 shaker mill, using bespoke PTFE milling vessels (inner volume of 14 mL) and two YSZ milling balls (10 mm, 3.4 g each). The mill was operated at 25 Hz for 30 min after which the paste was scooped into PTFE liner for stainless steel autoclaves. For the consecutive heat treatment, the autoclaves were placed in an oven and after the desired reaction time left to cool down to room temperature. The resulting solid was washed with water and dried in an oven at 80 °C overnight.

Table 5.9. Experimental details of solvent-free syntheses towards zeolites with **ISV** framework.

SiO_2 [g]	GeO_2 [g]	NH_4F [g]	TMATD-Br [g]	H_2O [g]	Si/Ge [-]	F/T [-]	H_2O/T [-]	temperature [°C]	time d
0.25		0.15	0.60	0.23		1.0	3.1	175	7
0.17		0.16	0.42	0.16		1.5	3.0	175	7
0.20	0.08	0.21	0.54	0.20	4.0	1.5	3.0	150	7
0.21	0.04	0.21	0.55	0.21	10.0	1.5	3.0	150	7
0.22	0.04	0.15	0.59	0.22	10.0	1.0	3.0	175	7
0.20	0.08	0.21	0.54	0.20	4.0	1.5	3.0	175	7
0.21	0.04	0.21	0.55	0.21	10.0	1.5	3.0	175	7

5.4.3 Physicochemical characterisation

Powder X-ray diffraction (PXRD)

Experiments were carried out on a PANalytical Empyrean disc diffractometer, operated in Bragg Brentano geometry in θ–2θ mode or a STOE STADI/P capillary diffractometer, operated in Debye-Scherrer geometry. Both diffractometers are equipped with a primary beam monochromator resulting in Cu $K\alpha_1$ radiation. Patterns were typically collected from 3–40° 2θ.

Scanning electron microscopy (SEM)

Images were acquired on a JEOL JSM-5600 or a JEOL JSM-IT200. Samples were placed on sticky carbon tape and gold coated at 10 mA for 30 s using a Quorum Q150R ES sputter coater. Both microscopes are equipped with an EDS system for elemental analysis.

Solution-state nuclear magnetic resonance spectroscopy (NMR) Solution-state NMR spectra were obtained on a Bruker AV III 500, with a CryoProbe Prodigy BBO probe.

5.5 References

(1) *Zeolites in Catalysis*, ed. J. Cejka, R. E. Morris and P. Nachtigall, Royal Society of Chemistry, Cambridge, 2017.

(2) J. Čejka, R. Millini, M. Opanasenko, D. P. Serrano and W. J. Roth, *Catal. Today*, 2020, **345**, 2–13.

(3) C. Baerlocher and L. B. McCusker, *Database of Zeolite Structures*.

(4) R. F. Lobo, S. I. Zones and M. E. Davis, *J. Incl. Phenom. Mol. Recognit. Chem.*, 1995, **21**, 47–78.

(5) *Insights into the Chemistry of Organic Structure-Directing Agents in the Synthesis of Zeolitic Materials*, ed. L. Gómez-Hortigüela, Springer International Publishing, Cham, 2018, vol. 175.

(6) J. Jiang, J. Yu and A. Corma, *Angew. Chemie Int. Ed.*, 2010, **49**, 3120–3145.

(7) J. Li, A. Corma and J. Yu, *Chem. Soc. Rev.*, 2015, **44**, 7112–7127.

(8) M. Opanasenko, M. Shamzhy, Y. Wang, W. Yan, P. Nachtigall and J. Čejka, *Angew. Chemie Int. Ed.*, 2020, **59**, 19380–19389.

(9) P. Eliášová, M. Opanasenko, P. S. Wheatley, M. Shamzhy, M. Mazur, P. Nachtigall, W. J. Roth, R. E. Morris and J. Čejka, *Chem. Soc. Rev.*, 2015, **44**, 7177–7206.

(10) J. Zhang, Q. Yue, M. Mazur, M. Opanasenko, M. V. Shamzhy and J. Čejka, *ACS Sustain. Chem. Eng.*, 2020, **8**, 8235–8246.

(11) Q. Wu, X. Meng, X. Gao and F.-S. Xiao, *Acc. Chem. Res.*, 2018, **51**, 1396–1403.

(12) Y. Wang, H. Duan, Z. Tan, X. Meng and F.-S. Xiao, *Dalton Trans.*, 2020, **49**, 6939–6944.

(13) J. Mei, A. Duan and X. Wang, *Materials*, 2021, **14**, 788.

(14) L. Ren, Q. Wu, C. Yang, L. Zhu, C. Li, P. Zhang, H. Zhang, X. Meng and F.-S. Xiao, *J. Am. Chem. Soc.*, 2012, **134**, 15173–15176.

(15) L. Zhu, J. Zhang, L. Wang, Q. Wu, C. Bian, S. Pan, X. Meng and F. S. Xiao, *J. Mater. Chem. A*, 2015, **3**, 14093–14095.

(16) Y. Jin, Q. Sun, G. Qi, C. Yang, J. Xu, F. Chen, X. Meng, F. Deng and F.-S. Xiao, *Angew. Chemie Int. Ed.*, 2013, **52**, 9172–9175.

(17) Q. Wu, X. Liu, L. Zhu, L. Ding, P. Gao, X. Wang, S. Pan, C. Bian, X. Meng, J. Xu, F. Deng, S. Maurer, U. Müller and F.-S. Xiao, *J. Am. Chem. Soc.*, 2015, **137**, 1052–1055.

(18) M. H. Nada, S. C. Larsen and E. G. Gillan, *Solid State Sci.*, 2019, **94**, 15–22.

(19) M. H. Nada, S. C. Larsen and E. G. Gillan, *Nanoscale Adv.*, 2019, **1**, 3918–3928.

(20) M. H. Nada, E. G. Gillan and S. C. Larsen, *Microporous Mesoporous Mater.*, 2019, **276**, 23–28.

(21) V. Pashkova, K. Mlekodaj, P. Klein, L. Brabec, R. Zouzelka, J. Rathousky, V. Tokarova and J. Dedecek, *Chem. – A Eur. J.*, 2019, **25**, 12068–12073.

(22) A. Kornas, J. E. Olszówka, P. Klein and V. Pashkova, *Catalysts*, 2021, **11**, 246.

(23) Q. Wu, X. Liu, L. Zhu, X. Meng, F. Deng, F. Fan, Z. Feng, C. Li, S. Maurer, M. Feyen, U. Müller and F.-S. Xiao, *Chinese J. Chem.*, 2017, **35**, 572–576.

(24) X. Liu, Y. Chu, Q. Wang, W. Wang, C. Wang, J. Xu and F. Deng, *Solid State Nucl. Magn. Reson.*, 2017, **87**, 1–9.

(25) M. Roberts, A. Fitch and A. Chadwick, *J. Phys. Chem. Solids*, 1995, **56**, 1353–1358.

(26) E. O. Schlemper, W. C. Hamilton and J. J. Rush, *J. Chem. Phys.*, 1966, **44**, 2499–2505.

(27) O. V. Shvets, N. Kasian, A. Zukal, J. Pinkas and J. Čejka, *Chem. Mater.*, 2010, **22**, 3482–3495.

(28) O. V. Shvets, A. Zukal, N. Kasian, N. Žilková and J. Čejka, *Chem. - A Eur. J.*, 2008, **14**, 10134–10140.

(29) M. A. Roberts and A. N. Fitch, *Zeitschrift für Krist. - Cryst. Mater.*, 2001, **216**, 225–229.

(30) Y. Lorgouilloux, M. Dodin, E. Mugnaioli, C. Marichal, P. Caullet, N. Bats, U. Kolb and J.-L. L. Paillaud, *RSC Adv.*, 2014, **4**, 19440–19449.

(31) J.-Q. Song, B. Marler and H. Gies, *Comptes Rendus Chim.*, 2005, **8**, 341–352.

(32) X. Ren, J. Liu, Y. Li, J. Yu and R. Xu, *J. Porous Mater.*, 2013, **20**, 975–981.

Chapter 6

Mechanosynthesis of sodium carboxylates

The contents of this chapter are based on data published in:

Daniel N. Rainer, Aamod V. Desai, A. Robert Armstrong, and Russell E. Morris, Mechanochemical synthesis of sodium carboxylates as anode materials in sodium ion batteries, *J. Mater. Chem. A*, 2021, **9**, 27 361–27 369.
DOI: 10.1039/D1TA07897F

Preparation of electrodes, electrochemical testing, and data processing was performed by Dr Aamod V. Desai. His help with assessment of these data is also acknowledged and greatly appreciated.

6.1 Introduction

One of the great challenges of today is the ever increasing global energy demand. Besides energy sources such as oil which can be used as fuels, electricity has one of the biggest shares of the total annual energy consumption.[1] Ensuring a sufficient supply of electrical energy can be addressed from many angles, one of which is to improve and expand the capabilities of current electrical energy storage (EES) technologies. The probably most widely known device in this respect is the rechargeable battery. Cars and transportable electronic devices, such as mobile phones and laptops, as well as large scale power stations, which need to be operable without connection to the general electricity grid, are entirely dependent on rechargeable batteries. This wide usage naturally requires a great quantity of active materials of high quality and performance, while keeping in mind concerns about resource availability, sustainable production of the components as well as end-of-life treatment.

The type of battery of particular interest is the alkali metal ion battery (AMIB). The most well-known member of this group, the lithium ion battery (LIB), powers almost every portable computing device.[2,3] Naturally, this means a heavy dependence on lithium deposits around the world in order to facilitate the great demand. Trying to avoid future problems of sourcing this one alkali metal, which occurs naturally only in a select few places,[4] renewed interest into sodium and potassium ion batteries (NIB and KIB, respectively) has developed.[5–8] Both of these elements are much more abundant in the earth's crust and also occur not only in small, spatially confined deposits, but are widely available. Such a shift away from lithium would mean greater freedom in terms of geographical availability of raw materials and should result in lower production cost overall.

At first glance one might expect that the accumulated knowledge and insight developed for lithium based battery materials and technologies may be easily translatable to other Group 1 elements. Unfortunately, the slight differences in electronic configuration between the alkali metals mean several adaptions are required in the materials' design. Most notably, widely used anode materials such as graphite or silicon are inapplicable for NIBs. Graphite relies on the insertion of metal ions into its interlayer space, which is unfavourable for sodium ions owing to a size mismatch with the interlayer spacing of the layers.[9,10] Silicon is able to insert sodium ions well, however, a low overall performance of this material has been reported, ascribed mainly to the low mobility of

Na^+.[11] Finding and developing alternatives are topics of current research, exploring options such as carbon-based materials, organic compounds, or metals and their oxides amongst others.[12–14] The benchmark for anode materials today is so called "hard carbon", which is mechanically durable and derived from high temperature treatment (> 1000 °C) of carbon containing matter.[15,16] Consisting of graphene sheets, interconnected in a non-ordered fashion, the resulting interlayer space is wide enough to accommodate sodium ions, contrasting to graphite where this distance is insufficient. This and several beneficial electrochemical properties make hard carbon a prime candidate as an anode material. However, for established commercialisation some improvements are still necessary. Fall-off in Coulombic efficiency after initial charge-discharge cycles and issues with long-term cyclability for example require further improvements in the design of this type of material. Furthermore, the porosity and typically extensive surface area require comparatively large amounts of electrolyte to ensure adequate coverage, reducing performance as well as increasing cost of the device overall. Thus, recent research has not only seen interest in optimising the properties of hard carbons, but also attempting to avoid such drawbacks by investigating organic-based compounds as viable substitute as the active anode material.

6.1.1 Organic compounds as sodium ion battery anode materials

Organic materials as active component in anodes have many advantages over other mentioned alternatives for several reasons.[17–19] Firstly, there are only few restrictions with respect to the structure of the molecule, besides the functional groups which provide the capability to undergo the redox reaction required for an active material in an electrode. For anodes, these functional groups are typically carboxylate, azo, or imine groups. These take up electrons during the reduction (discharge) thus carrying a negative charge, before oxidising back to the original, neutral state (charge). As such, compounds with this functionality are classified as *n-type*. The acquired negative charge during reduction is balanced by the sodium cation, which is inserted into the organic material. The reaction is shown in Figure 6.1 using the example of disodium benzenedicarboxylate Na_2BDC. The electrochemical potential required for the redox reaction to occur in these functional groups is comparatively low, again beneficial for anode materials. The potential can be fine tuned to the desired value by altering the backbone of the organic compound. This may be considered the most advantageous aspect, due to the vast number of possible combinations. Furthermore, the typically used organic molecules are obtainable through

biomass valorisation, an approach that has seen considerable interest in recent years.[20–22] Such a procedure would make the overall production of battery materials much more sustainable and increase the value of organic-based electrodes. Furthermore, synthesis conditions for organic molecules typically involve lower energy consumption compared to those required for inorganic materials. Since the main contribution to the overall cost of EES devices stems from electrode material production expenses, such improvements are considered one of the main goals of current research.[7]

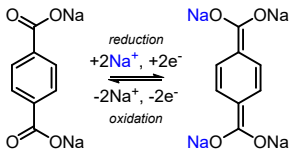

Figure 6.1. Mechanism of the redox reaction of organics with carboxylate groups using the example of disodium benzenedicarboxylate.

Despite all the listed beneficial properties of organics, there are some drawbacks which have hindered the use of organic-based electrodes so far. From a molecular point of view, most of the molecule is inactive in terms of electrochemistry, as only the functional group itself is the part involved in the reversible uptake of electrons. This results in a considerable amount of dead weight from a molar mass point of view, especially when compared to other types of materials. This is one of the reasons why electrodes based on organics typically show a comparatively lower specific capacity, one of the main areas with room for improvement in current research.[23]

Considering the practical aspects of assembling an electrode, commonly used electrolytes are polar organic solvents, and are thus unsuitable to be used with these types of active material due to eventual dissolution or even decomposition. In addition, the usually preferable low operating potential can also lead to the formation of a solid electrolyte interface (SEI) layer which leads to a decreased Coulombic efficiency at the start of battery cycling.[24,25] Keeping this drop in performance as low as possible is a major goal of designing a high quality anode material.

Another shortcoming of organic materials is their typically poor electrical conductivity. A well performing electrode, however, needs to facilitate not only high mobility of the metal ions, but also of electrons. As this is often intrinsically hindered in the organic compound itself, the situation can for example be remedied by fashioning composite materials consisting of the active organic and an electrically conductive carbon compound. This comes at a price though, as the share of inactive parts of the total mass of material is increased. It is important to aim for a sweet spot with just the right amount

of conductive carbon to facilitate reasonable movement of electrons, while keeping its mass percentage low. Ensuring all of the material is utilised requires homogeneous distribution of active compound and conductive carbon, which is enabled by using a binder. Traditional choices are for example PVDF (poly(vinylidene difluoride)), which is classified as mutagenic, raising concerns about safety. Suitable solvents for this and other binders are equally worrisome, especially chemicals such as the widely used N-methyl pyrrolidone (NMP) which is teratogenic and toxic. Here, a shift towards environmentally friendlier binder alternatives such as the water-soluble sodium alginate and CMC (carboxymethyl cellulose) is currently underway in many research labs.[26] Additionally, most organic-based electrode materials work well with these safer options, opening up possibilities to reduce hazards and safety issues related to fabrication of batteries.

6.1.2 Sustainable synthesis of sodium coordination polymers

One of the most important topics in current chemistry is the aim for sustainable and environmentally friendly processes, generally referred to as *green chemistry*.[27] The goal is to reduce accumulation of waste, increase atom efficiency of the reaction and decrease wasteful usage of energy, amongst others. Considering the grand scheme of things, many of these aspects have to be implemented at industrial scale, but even in laboratories, there is great potential for improvement. Likewise, new reaction pathways or conditions need to be evaluated on smaller scales first. With this in mind, the last couple of decades have seen the re-emergence of mechanochemistry as a tool to complement or potentially even replace commonly used solution-based reactions.[28–33]

The idea behind mechanochemical reactions is comparatively simple, whereas its mechanisms still prove rather elusive. The energy input into a given reaction system in traditional setups is by using heating plates or similar devices to increase the temperature of the solvent, thus enabling a chemical reaction by overcoming its activation barriers. In mechanochemistry, the required energy is mechanical in nature, exerted by manual grinding or milling media, for example, in ball mills. The continuous mechanical motion effectively mixes the reagents as well as generates heat by friction and shear forces. The efficacy of mechanosynthesis has been demonstrated in many areas of chemistry, notably organic chemistry[30,34] and metal-organic frameworks (MOFs).[35,36] The name of these latter materials originates from their structural motifs, where organic linking units connect metal(-oxide) nodes, forming a 3D connected framework. The bond between organic linker and inorganic node is typically a coordination bond, fa-

cilitated by functional groups such as carboxylates. When the metal is an alkali metal such as sodium, the bond is still coordinative but has a slightly more ionic character. These compounds are usually only referred to using the term coordination polymers due to their lack of potential voids.[37] All of these materials are typically synthesised in solution, requiring considerable amounts of solvent, especially in view of potential large scale production. Thus, a mechanochemical synthesis route was considered as possible alternative. Traditional, solution-based synthesis under solvothermal or reflux conditions suffer from poor resource management, safety concerns and drawbacks in terms of scalability. Mechanochemistry solves most if not all of these issues due to the low amount of required liquid, quantitative conversion of stoichiometric starting materials, and low energy consumption.[38] These and more benefits make mechanochemistry also an attractive prospect for industrial scale synthesis of materials.[39,40] This is especially relevant for the target application as active battery material, due the maturity of this field. A potential candidate material to replace the current state of the art needs to be available on appropriate scales. As such, the envisaged mechanochemical synthesis route for the targeted sodium carboxylates would qualify in this respect. Commercialisation of mechanochemical synthesis of some MOF materials by companies like MOF Technologies[40] is already established using twin screw extrusion for highly efficient production of these related materials at industrial scales.[41,42]

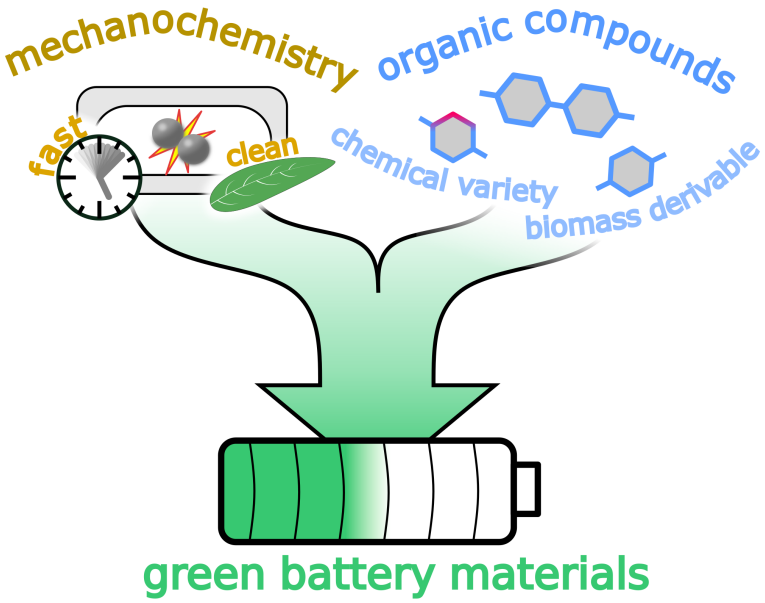

Figure 6.2. Schematic representation of the goal to produce green battery materials by mechanochemical synthesis of organic materials.[43]

The goal for this project was the development of a mechanochemical protocol for the production of sodium coordination polymers to be used as anode materials for sodium ion batteries.

6.2 Mechanochemical synthesis of sodium carboxylates

Experiments were conducted using several dicarboxylic acids as organic reagent and sodium acetate as the sodium source. There are several reasons to choose sodium acetate as reagent. Firstly, this sodium containing compound is readily available, has a low ecological impact and is considered a benign chemical by authorities such as the ECHA (European Chemicals Agency).[44] The choice for acetate as the counterion is that its conjugate base is a weak acid, making the salt overall slightly basic. Thus, deprotonation of carboxylic acid groups should be facilitated at least to some degree. Thirdly, the eventual by-product of the reaction is acetic acid, removable both by a washing step but also by drying itself, comparable to residual water due to the similar boiling point.

Other sodium sources that were considered but soon dismissed are sodium hydroxide and sodium carbonate. NaOH has been used for solution based synthesis of these sodium carboxylate compounds in the reported literature, due to its ability to serve both as a source of sodium ions as well as strong base for the deprotonation reaction. For the project at hand, however, this reagent was not used as sodium hydroxide is a corrosive reagent and may cause damage to humans such as skin burns. The goal was to develop an environmentally friendly and safe methodology and as such this strong base was not used.

Sodium carbonate on the other hand is a safer choice as reagent and would also provide the basicity required for the deprotonation reaction. The by-product of the reaction itself, however, is CO_2, once more an environmental and safety hazard. A carefully conducted test experiment using Na_2CO_3 confirmed this supposition as gas was released from the milling vessel upon opening.

These considerations led to sodium acetate as the sodium source of choice for the synthesis of sodium carboxylates in this project. Being the salt of a strong base and weak acid, there is still some, albeit potentially small capability to facilitate deprotonation, while of course still providing Na^+ ions.

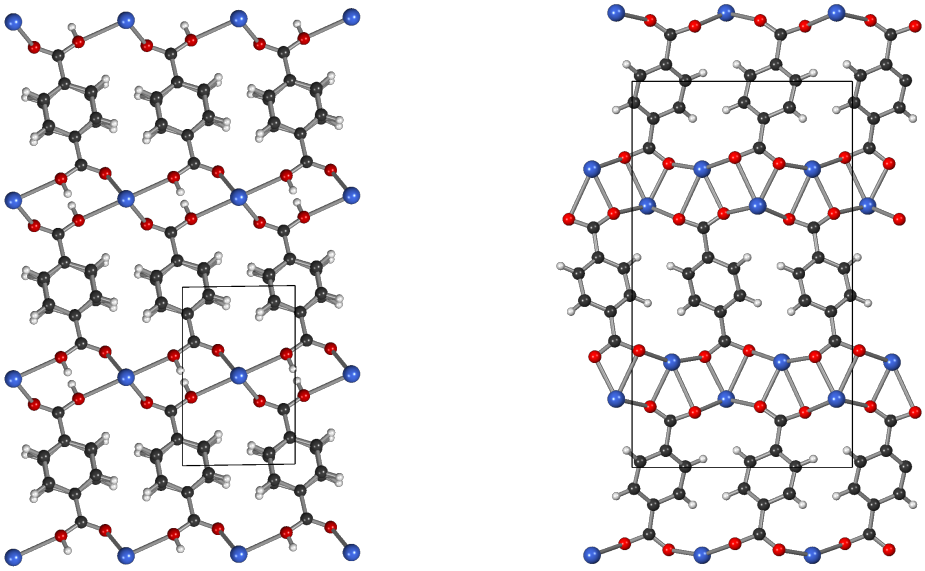

a) Crystal structure of NaHBDC, $C_6H_4(COO)_2HNa$ (CCDC code BEBFIY), viewed along the *a* direction.

b) Crystal structure of Na_2BDC, $C_6H_4(COO)_2Na_2$ (CCDC code QQQDHD01), viewed along the *a* direction.

Figure 6.3. Structures of NaHBDC[48] and Na_2BDC.[49] Carbon atoms are shown in black, hydrogen in white, oxygen in red, and sodium in blue.

6.2.1 Mechanochemical synthesis of sodium benzenedicarboxylate

The methodology was developed using 1,4-benzenedicarboxylic acid (BDC, also known as terephthalic acid) as organic reagent. Synthesis of disodium terephthalate (Na_2BDC, $C_6H_4(COO)_2Na_2$) for application in batteries has been reported previously by a solution based route from terephthalic acid and NaOH or sodium carbonate.[45–47] Using sodium ethoxide as Na source the monosodium salt (NaHBDC, $C_6H_4(COO)_2HNa$) is produced, owing to the lack of base in the reaction system resulting in a decreased likelihood for deprotonation.[47] As such, either or both of these two compounds were potential products for the mechanochemical approach. Figure 6.3 depicts the crystal structures for NaHBDC and Na_2BDC, clearly showing the close relation between them.

Availability and cost of resources is another important factor when deciding in favour of or against using a particular compound as functional material. A further reason to choose BDC as the main compound to investigate are recent reports about its accessibility from renewable resources[22] as well as by recycling the widely used polymer PET (polyethylene terephathalate) in an efficient manner.[50,51] Such sustainable pathways to source reagents are not only environmentally friendly but may even be cost-efficient. Similarly, a recent study by Crickmore et al. even showed how the synthesis of a calcium-BDC compound can be accomplished by using waste material (egg shells, plastic PET bottles) directly as reagent.[52]

Figure 6.4. Photos of the milling jar after the reaction and the pasty product after scooping it out of the jar.

First experiments were conducted varying the reagent ratio, further referred to as metal-to-linker ratio M/L, in analogy to the convention in the field of MOFs, where carboxylic acids act as linking units between nodes of metal atoms or clusters. The reactions were conducted similar to mechanochemical synthesis conditions that have been reported to successfully produce MOFs,[35,36,53] for details see section 6.5 below. In short, solid reagents were combined in a plastic milling jar (polycarbonate, PC) together with two stainless steel balls. Using sodium acetate trihydrate, water occluded in the salt is liberated during the milling process and acts in the same way as when added separately to the anhydrous reagents. Within the first minutes of grinding, the materials form a paste and the final product is shown in Figure 6.4. After the desired reaction duration of typically 60 min, the product is scraped out of the jars and dried in a oven overnight. The distinct smell of the by-product acetic acid can be made out, indicating successful conversion of the sodium salt.

PXRD patterns of products from these initial tests can be seen in Figure 6.5a. Comparison with simulated patterns indicates the formation of NaHBDC.[47,48] An increase in M/L only results in a greater amount of unreacted sodium acetate and concomitantly unreacted terephthalic acid. Important to note here is that these samples were not washed or otherwise purified. The intention behind this neglect of a usually performed treatment of crude product is that one of the main advantages of employing mechanochemical methods is the avoidance of bulk solvent. Hence, washing of products in this project was only conducted if unavoidable, for example to improve electrochemical performance. Additionally, Abouimrane et al. have shown that NaHBDC is transformed into a Na_2BDC phase during the first cycle of a galvanostatic cycling experiment due to insertion of sodium ions into the material.[47] Looking at Figure 6.3b incorporation of an additional Na^+ into NaHBDC seems plausible by insertion into the the existing sodium chains. Although this may not induce a phase transformation towards the crystal structure of Na_2BDC (Figure 6.3a), such a potentially disordered material can still be capable of excellent ion conduction.

Due to these outcomes, the product obtained from the reaction with M/L = 1 was

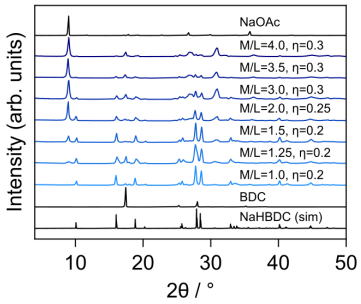

a) PXRD patterns of mechanochemically synthesised Na-BDC samples with varying metal-to-linker ratios M/L and liquid-to-solid ratio η in $\mu L\,mg^{-1}$.

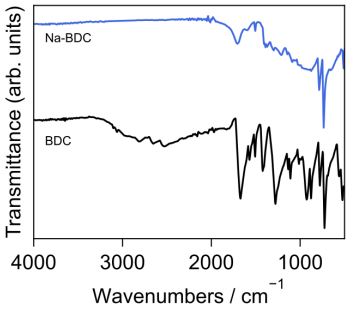

b) FTIR of Na-BDC and reagent BDC for comparison.

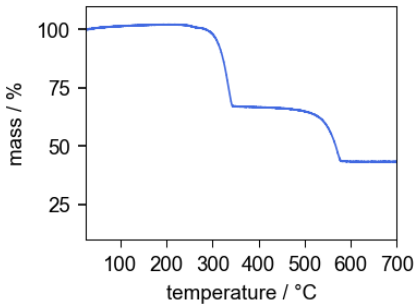

c) TGA of Na-BDC.

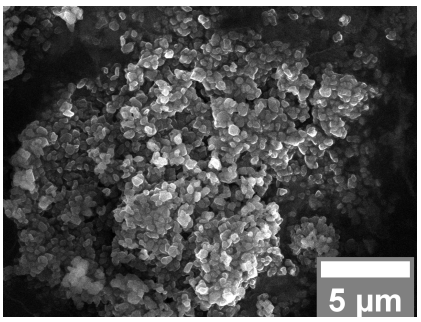

d) SEM image of Na-BDC, showing agglomerated primary particles of roughly 500 nm in size.

Figure 6.5. Characterisation of mechanochemically synthesised Na-BDC samples.

used for further analysis and is labelled *Na-BDC* from here on. The absence of bands at wavenumbers around 3000 cm^{-1} in the FTIR spectrum indicates no residual free carboxylic acid groups. The band at 1700 cm^{-1} can be assigned to a C=O bond of a carboxylic acid, supporting the notion of NaHBDC as the product, where one acid group remains protonated. Thermogravimetric analysis (TGA) adds further support for this interpretation as the main mass loss occurs well below 500 °C, representative of the thermally less stable monosodium salt. Finally, elemental analysis (C, H) agrees well with the expected mass for the chemical formula NaHBDC. Probing the morphology of the produced material, SEM analysis was conducted showing agglomerates of small primary particles with dimensions below 1 µm. This is a typical observation for a mechanochemically synthesised material using ball milling techniques, since the continued exerted mechanical force also results in particle size reduction.[54–57]

In order to assess whether the presence of a liquid is necessary for the reaction, reactions were carried out using only the solid reagents anhydrous NaOAc and BDC. The progress of the reaction was followed over time, showing product formation even after only 15 min and appreciably low amount of starting materials (see Figure 6.6a). The same trend is observed even when increasing the scale of the reaction, using jars with a volume of 25 mL and larger milling balls, shown in Figure 6.6a. This is a good

demonstration of the capability for facile upscaling of this mechanochemical reaction. Conducting the reaction under these dry conditions, however, is accompanied by a severe safety concern as the product of the reaction is a very fine powder which should not be handled without proper PPE (personal protective equipment) such as masks, preventing inhalation of fine dust. A photograph showing the powder product and comparing it with the paste obtained from liquid-containing reactions is shown in Figure 6.6d. With this in mind, following experiments towards sodium carboxylates were performed with at least a small amount of liquid present in the reaction system.

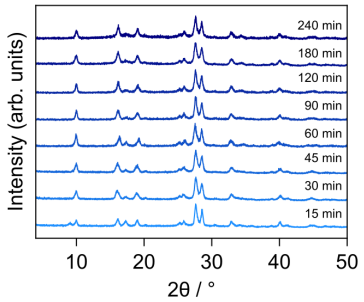

a) PXRD patterns of Na-BDC synthesised under dry conditions in 14 mL milling jars and its evolution over 240 min.

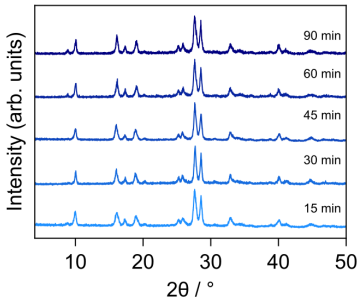

b) PXRD patterns of Na-BDC synthesised under dry conditions in 25 mL milling jars and its evolution over 90 min.

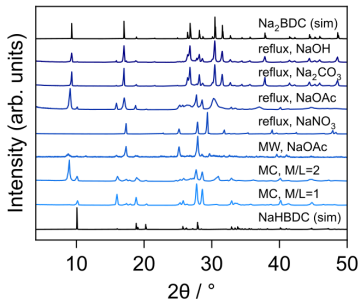

c) Comparison of mechanochemically synthesised Na-BDC with solution-based synthesis in ethanol under reflux conditions using several sodium sources as well employing microwave irradiation.

d) Photos of the milling jar after the reaction under dry conditions and the fine powder product after scooping it out of the jar in comparison to the paste obtained from reactions in the presence of a liquid additive, water in this case.

Figure 6.6. PXRD patterns of mechanochemically synthesised Na-BDC samples under dry conditions and comparison with solution-based syntheses.

Finally, Na-BDC of the mechanochemical synthesis is compared to materials obtained by solution methods. Figure 6.6c shows Na-BDC and samples from syntheses conducted in ethanol under reflux conditions. Additionally, a microwave synthesis was conducted using sodium acetate as Na source. These reactions were conducted using M/L = 2.1, attempting to drive the reaction towards Na_2BDC, as well as following the stoichiometry reported in similar protocols in the literature. The different sodium sources were chosen according to their basicity. As can be seen, using the neutral sodium nitrate, no product is formed. The slightly basic NaOAc results in formation of a small amount of the NaHBDC phase but a large amount of unreacted sodium acetate, similar to mechanochemical

reaction of higher M/L ratios. This observation is made for both the reflux synthesis as well as the microwave assisted reaction. The basic reagents Na_2CO_3 and NaOH yielded mainly Na_2BDC with some impurity of NaHBDC. These results show that although the complete reaction towards Na_2BDC appears to not be possible using the employed mechanochemical conditions, the reaction proceeds similarly to solution without need for solvent. Full conversion only succeeds when NaOH or Na_2CO_3 are used in solution-based synthesis. As discussed above, however, these chemicals are considered unsuitable in view of large scale processing due to safety concerns.

6.2.2 Electrochemical performance of Na-BDC as anode for NIBs

Testing the applicability of obtained Na-BDC as active component in anodes for sodium ion batteries was conducted using conventional galvanostatic cycling of coin half-cells. Electrodes were prepared by mixing the sodium carboxylate with a conductive carbon (Super C65) and sodium carboxymethyl cellulose (CMC) as binder material in a ratio of 60 : 30 : 10 by mass (see section 6.5.4 for further details). The carbon additive is necessary to facilitate electric conductivity of the resulting composite. PXRD patterns of the final electrode composite compare well with the pristine Na-BDC phase (see Figure 6.7a). As shown in Figure 6.7b, SEM imaging suggests a good distribution of the organic throughout the composite.

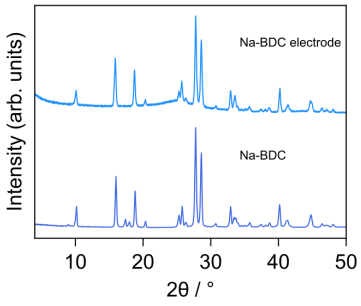

a) PXRD patterns of pristine Na-BDC and the electrode composite based on it.

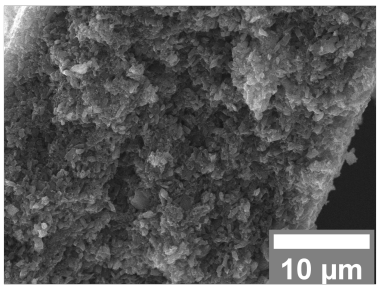

b) SEM image of the electrode composite material based on Na-BDC.

Figure 6.7. Characterisation of electrode composites based on Na-BDC.

A galvanostatic cycling experiment (Figure 6.8) was conducted using a moderate current density of 100 mA g^{-1}. Although the drop in capacity after the first cycle is unfavourable, it is a well-known phenomenon for organic-based anodes and is assigned to the formation of the solid-electrolyte interface (SEI) layer.[24,25] As alluded to earlier, the insertion of up to three Na^+ ions into the monosodium salt is thought to additionally

contribute to the observed difference between cycles one and two.[47] Following this initial decrease, the capacity stabilises at roughly 270 mA h g^{-1} and retains 86 % throughout 100 cycles. The Coulombic efficiency stays favourably high at more than 98 %, promising long lifetime of a battery based on this material.

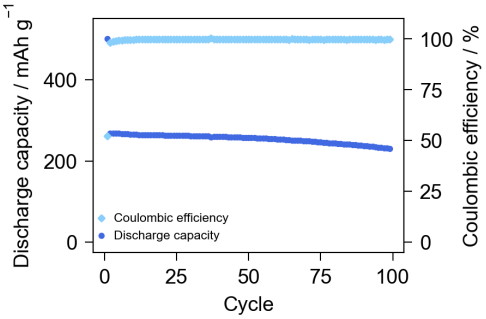

Figure 6.8. Discharge capacity and Coulombic efficiency for Na-BDC measured for 100 cycles at 100 mA g^{-1} in a voltage window of 0.01–2.5 V.

The observed value for the discharge capacity can be compared to the theoretically achievable capacities of 255 mA h g^{-1} and 285 mA h g^{-1} for Na_2BDC and NaHBDC, respectively. These values for the discharge capacity Q (in mA h g^{-1}) are calculated using Equation 6.1,

$$Q = \frac{nF}{3600M} \tag{6.1}$$

with Faraday's constant F (96 485.33 C mol^{-1}), the molecular mass of the compound M (g mol^{-1}), and number of involved electrons n. In both cases, the number of electrons was set to n = 2. Assuming that NaHBDC allows an insertion of three electrons for the initial cycle, Q = 427 mA h g^{-1}, supporting the explanation about the high irreversibility of the first cycle given above. As described above, the transformation into the disodium salt in this first cycle leads to only two electrons being involved in the redox reaction in all subsequent cycles.

Keeping used materials in the electrode composite in mind, the extent of the contribution of the added carbon C65 needed to be assessed. Thus, an electrode was prepared under the same conditions using only Super C65 as active material, adding 10 % CMC to allow direct comparison of the results to other electrode materials. The measurements done for this C65 electrode are applicable throughout this chapter as almost all electrodes were prepared using this type of carbon. During the first cycle, an irreversible capacity of 217 mA h g^{-1} is recorded, which stabilises afterwards around 112 mA h g^{-1}. For electrodes made with organic material, the carbon additive would only contribute a third of these values due to the composition of the composite, giving 37.3 mA h g^{-1} of stable discharge capacity. Additionally, a capacity drop after the initial cycle is also

observed for this pure C65 electrode which would translate to roughly 35 mA h g^{-1} in electrodes with sodium carboxylate as active material. Even with this contribution of the carbon additive to the measured capacity, the performance of the Na-BDC electrode is still competitive and only marginally below the theoretical limit.

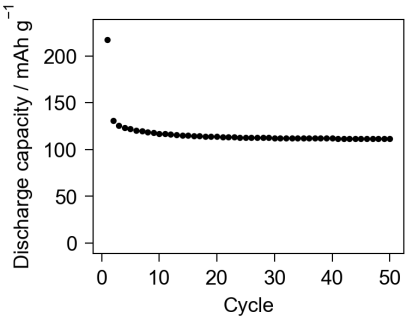

a) Discharge capacity for the pure C65 electrode. Cycling was performed at 100 mA g^{-1} in a voltage window of 0.01–2.5 V

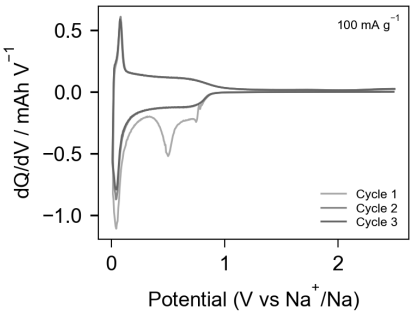

b) Differential dQ/dV plot for the pure C65 electrode of the initial three cycles.

Figure 6.9. Electrochemical characterisation of an electrode containing only conductive carbon Super C65 as active material.

Looking more closely at the underlying electrochemical reaction, two redox couples can be discerned in the cyclic voltammogram (CV, Figure 6.10a), conducted for five cycles. The small charge/discharge peaks at low potential stem from the conductive carbon (compare Figure 6.9b). The second, more prominent feature is assigned to the organic material and its peak positions at 0.35 V and 0.52 V are in line with previous reports. Visible is again the irreversibility of the initial cycle as seen in the cycling plots. Further assessing the material under varying current conditions, five cycles were recorded at different current densities ranging from 25–1000 mA g^{-1} and a final five cycles again at 25 mA g^{-1}. As seen in Figure 6.10b, the capacity at low current density is retained even after cycling at higher ones. These observations prove that mechanochemically synthesised Na-BDC can compete with materials obtained from solution in terms of their electrochemical performance.

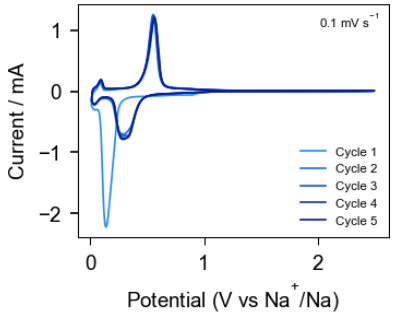

a) CV profile, conducted at a scan rate of 0.1 mV s^{-1}.

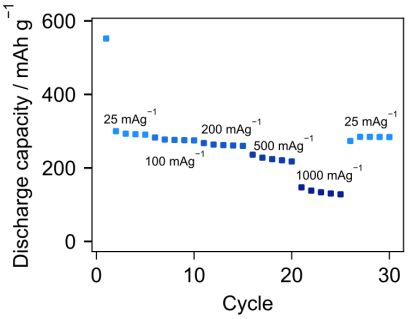

b) Rate performance from 25–1000 mA g^{-1}, cycled five times at each current rate.

Figure 6.10. Electrochemical performance of electrodes based on Na-BDC.

6.2.3 Synthesis of Na-BDC in the presence of carbon

The possibility to use Na-BDC directly after the mechanochemical synthesis, without the need for further purification such as washing suggests the possibility of conducting the synthesis in the presence of the carbon additive, reducing the number of required processing steps. In addition to the previously used conductive carbon Super C65, hard carbon (HC) was also employed. Comparison of PXRD patterns shows the successful synthesis of Na-BDC with added Super C65, hard carbon, and a mixture thereof (Figure 6.11a). The mixtures were prepared in ratios to be suitable to achieve the same final ratios of the electrode composites as used above, except for the C65/HC mixture which was prepared in a set ratio which showed success in a previous, unrelated study. In order to facilitate free movement of the starting materials in the milling jars, a slightly higher amount of water was added. These materials were used in the preparation of electrodes in the same manner as above.

Evaluation of the electrochemical performance of the three materials is based on their cyclability shown in Figure 6.11b. The Na-BDC sample prepared with C65 shows comparable discharge capacity to the conventionally obtained material, whereas in the hard carbon based sample this property is severely reduced and barely above what is expected for this type of carbon intrinsically. The electrode prepared with both types of conductive carbon performs slightly worse than “Na-BDC + C65” which could be an issue of finding a more optimal electrode composition. Despite this slight decrease in discharge capacity, the stability of the circa 150 mA h g^{-1} over 75 cycles is still competitive, keeping in mind, no optimisation has been attempted yet.

Although the electrode prepared from the Na-BDC/HC synthesis did not show the desired results, both other compositions performed very well. The aim of simplifying the overall process by combining two steps into a single procedure was successful. This is,

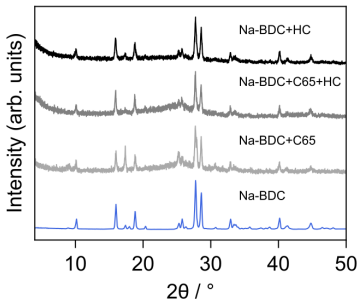

a) PXRD patterns of Na-BDC synthesised in the presence of electrically conductive carbon.

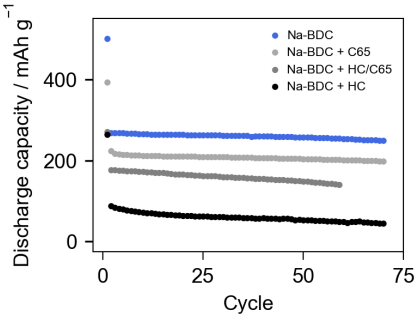

b) Electrochemical cycling performance of electrodes based on Na-BDC synthesised in the presence of electrically conductive carbon.

Figure 6.11. Mechanochemically synthesised Na-BDC in the presence of electrically conductive carbon. Materials "Na-BDC + C65" and "Na-BDC + HC" (hard carbon) were synthesised with a target electrode composition of 60 % Na-BDC, 30 % carbon, and 10 % binder. The electrode "Na-BDC + C65/HC" was prepared with a target composition of 29 % Na-BDC, 50 % HC, 11 % C65, and 10 % binder.

however, only a proof of concept and no optimisation has been performed yet. Adjusting the ratios in the synthesis as well as investigating other parameters such as water content, time, and many others may lead to even better performances and shall be subject of future studies. Furthermore, this is a promising step towards a complete one-pot process combining the synthesis of the sodium carboxylate with the preparation of the electrode composite. The possible easiest adaption would be to simply add the binder solution (CMC or sodium alginate in water) to the milling vessel after the reaction has concluded. This may still be considered a multi-step procedure, however, when considering large-scale mechanochemical processing typically occurs with technology like twin screw extrusion, feeding a certain reagent into the mixture at a later point during the extrusion is definitely a possibility that would not drastically impact the overall process. Additionally, a recent report by Zhang et al. has shown the possibility to grow crystalline ZIF-8 (zeolitic imidazolate framework) in a sodium alginate solution.[58] Although not using the same building blocks, ZIFs are still related to the here studied sodium carboxylate materials and as such, these published results indicate the potential for a similar procedure for the future of this project.

6.2.4 Extension of the organic backbone: Sodium biphenyl- and stilbene-dicarboxylates

After this first success, the question posed itself how extendable this synthesis method is to the wide variety of dicarboxylic acids, some of which have great potential as organic-based anodes for NIBs. One of the properties the organic molecule needs to possess for such an application is the capability to take up an extra electron and stabilise the resulting

radical so that insertion of sodium ions can occur. When taking BDC as the basis, the stabilisation can be improved by extending the π-system of the organic backbone. Two examples of this are 4,4′-biphenyldicarboxylic acid (BPDC) and 4,4′-stilbenedicarboxylic acid (SDC), shown in Figure 6.12. The introduction of a second aromatic ring in BPDC and a further double bond in SDC are helpful in this respect, without altering the basic shape of the molecule. Both of these compounds have shown excellent electrochemical performance and were thus chosen as candidate materials for the following syntheses.[59,60]

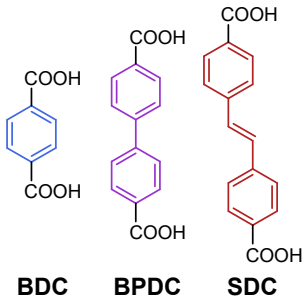

Figure 6.12. Structures of BDC, BPDC, and SDC.

Figure 6.13 shows characterisation of mechanochemical reaction products of sodium acetate and BPDC in different M/L ratios and water or ethanol as liquid additive. The PXRD patterns show the formation of a mixture of NaHBPDC as well as Na_2BPDC assigned by evaluation against published structures of both compounds.[59] Using an M/L ratio of 2, residual unreacted acid was observed in FTIR spectra. The sample prepare at M/L = 3 showed no evidence of unreacted acid and this sample was investigated further. The crude product showed comparatively low electrochemical performance, suggesting a considerable amount of inactive material (see Figure 6.15b below). This is assumed to be unreacted sodium salt and possibly some minor amounts of organic acid, which unfortunately required purification of the product by washing with ethanol. The TGA trace of this final, washed product shows a first mass loss of roughly 9% at 200 °C and a second loss of ca. 48% at 400 °C. This indicates that most of the material had been transformed into Na_2BPDC, accompanied by a small amount of the monosodium salt, which degrades at a lower temperature. Finally, SEM analysis shows irregularly shaped particles roughly 1 µm in size, which is in the same domain as seen for the Na-BDC example.

In stilbene containing reactions (Figure 6.14), M/L = 2 yields a product exhibiting a similar pattern to the reported literature.[60] The observed double peak at low 2θ angle might be an indication for the formation of both mono- and disodiated carboxylates.

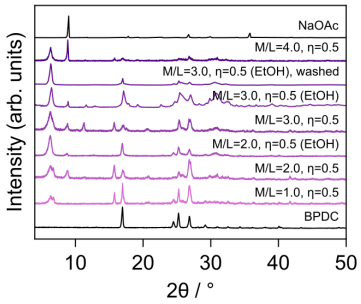

a) PXRD patterns of mechanochemically synthesised Na-BPDC samples with varying metal-to-linker ratios M/L and liquid-to-solid ratio η in $\mu L\,mg^{-1}$.

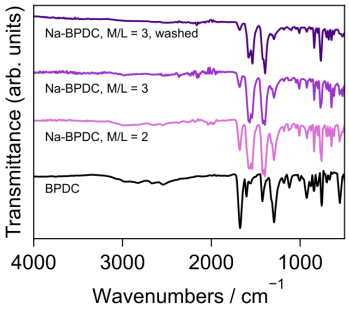

b) FTIR spectrum for Na-BPDC.

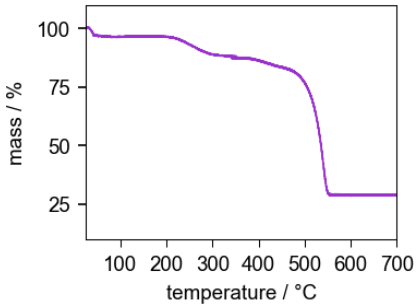

c) TGA profile for Na-BPDC.

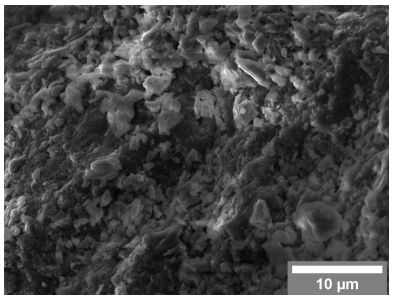

d) SEM image of the Na-BPDC sample.

Figure 6.13. Characterisation of mechanochemically synthesised Na-BPDC samples.

Unfortunately, there are no known crystal structures for NaHSDC or Na_2SDC, however, visual comparison of the pattern of this synthesis product with a published PXRD pattern of a solution-based synthesis suggests the product is of comparable nature. Similar to the Na-BPDC sample, a washing step was necessary due to low electrochemical performance in initial test runs (seeFigure 6.16b). The TGA trace of the washed product looks similar to that of Na-BPDC, with an even lower proportion of mass loss at earlier stages of the experiment, indicating a high conversion towards Na_2SDC. Na-SDC crystals exhibit a rod or plank-like like shape, up to 1 µm in length and below 250 nm in width.

Galvanostatic cycling experiments for Na-BPDC and Na-SDC containing electrodes based on products obtained directly from the mechanochemical synthesis indicated the presence of inactive material based on capacity and its retention during cycling being lower than expected (Figure 6.15b and Figure 6.16b below). This led to the decision to include a brief washing step at the end of the synthesis and these washed materials were used for further electrochemical testing.

Comparing the PXRD pattern of the electrode based on Na-BPDC with its parent compound confirm good retention of crystallinity and SEM analysis shows well distributed particles (Figure 6.15a. A loss of capacity is observed after the initial cycle, similar to the behaviour of Na-BDC. Thereafter, the discharge capacity is retained well throughout

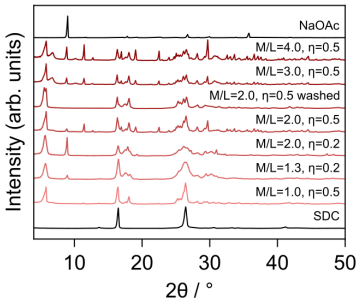

a) PXRD patterns of mechanochemically synthesised Na-SDC samples with varying metal-to-linker ratios M/L and liquid-to-solid ratio η in μL mg^{-1}.

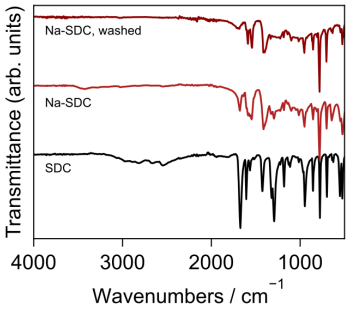

b) FTIR spectrum for Na-SDC.

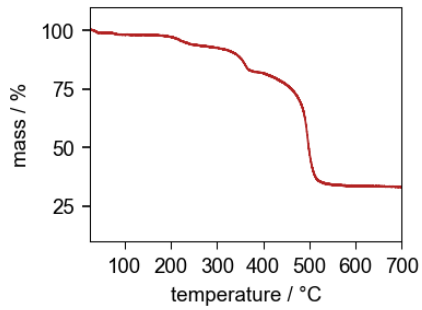

c) TGA profile for Na-SDC.

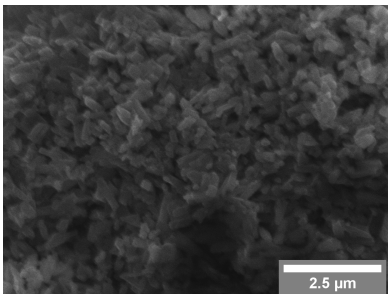

d) SEM image of the Na-SDC sample.

Figure 6.14. Characterisation of mechanochemically synthesised Na-SDC samples.

the tested 100 cycles. Cyclic voltammetry of Na-BPDC shows two oxidation peaks, most likely originating from the presence of both NaHBPDC and Na_2BPDC. Nonetheless, the capacity of circa 184 mA h g^{-1} and its stability over the measured 100 cycles is appreciably high. The ability to recover this high capacity even after cycling at high current rates of 1000 mA g^{-1} is also very promising.

Similar to the biphenyl compound, the Na-SDC electrode shows the presence of the organic compound in a recorded PXRD pattern and SEM images do not indicate any agglomeration of particles but rather well dispersed organic compound, shown in Figure 6.16a. The measured capacity of 146 mA h g^{-1} was well retained over the investigated 100 cycles. Once more, the capacity at 25 mA g^{-1} is recoverable even after cycling at high current rates. The discharge shows a slight shift in the peak during the first two cycles, settling at 0.49 V, which had been reported previously.[60] The charge peak remained at its initial value of 0.62 V, an improvement over the earlier report where a small secondary peak was observed, which may be assigned to a potentially amorphous by-product of the synthesis.

These good results for Na-BPDC and Na-SDC emphasise the potential for the presented mechanochemical methodology as the electrochemical performance is evidently retained compared to earlier reports, while the synthesis conditions have arguably been im-

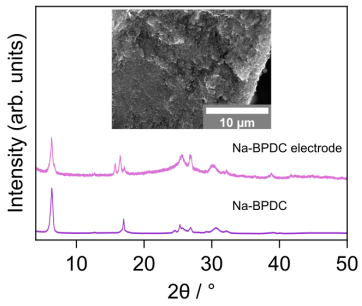

a) PXRD and SEM image (insert) of electrodes based on Na-BPDC.

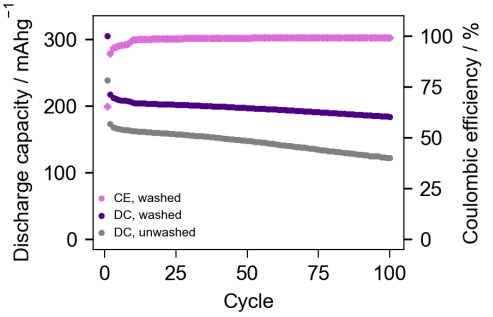

b) Discharge capacity (DC) for *unwashed* Na-BPDC and DC and Coulombic efficiency for washed Na-BDPC measured for 100 cycles at 100 mA g^{-1} in a voltage window of 0.01–2.5 V.

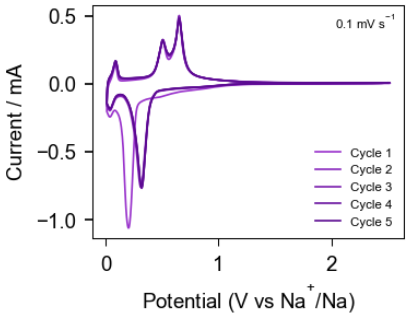

c) CV profile for Na-BPDC, conducted at a scan rate of 0.1 mV s^{-1}.

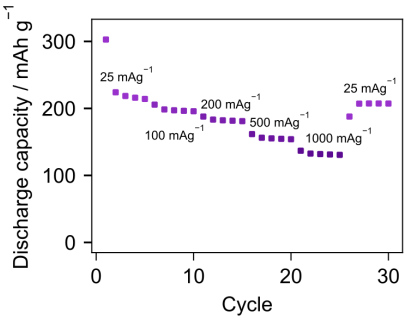

d) Rate performance for Na-BPDC from 25–1000 mA g^{-1}, cycled five times at each current rate.

Figure 6.15. Electrochemical performance of electrodes based on Na-BPDC.

proved. The demonstration of successful applicability of the mechanochemical method to include larger organic molecules is very promising. It hints at the possibility to target more complex compounds without the explicit need to overhaul the developed methodology, but suggesting a rather straight forward adaption.

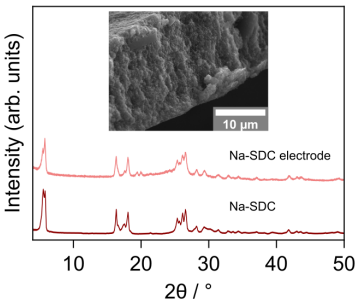

a) PXRD and SEM image (insert) of electrodes based on Na-SDC.

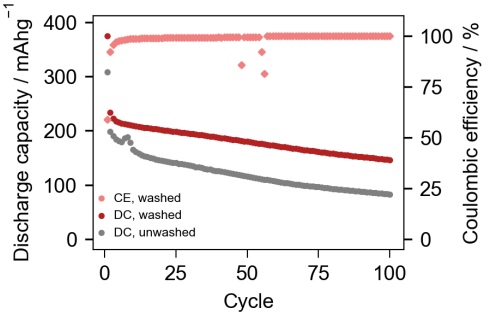

b) Discharge capacity (DC) for *unwashed* Na-SDC and DC and Coulombic efficiency for washed Na-SPC measured for 100 cycles at 100 mA g^{-1} in a voltage window of 0.01–2.5 V.

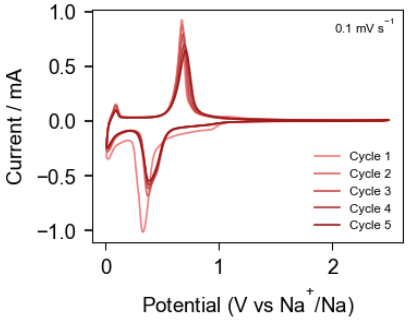

c) CV profile for Na-SDC, conducted at a scan rate of 0.1 mV s^{-1}.

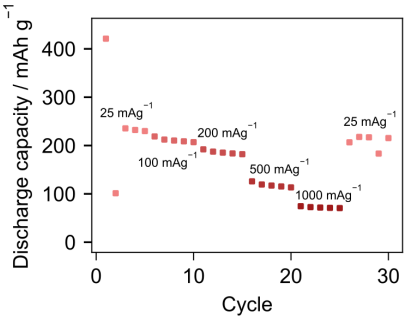

d) Rate performance for Na-SDC from 25–1000 mA g^{-1}, cycled five times at each current rate.

Figure 6.16. Electrochemical performance of electrodes based on Na-BPDC and Na-SDC.

6.2.5 Heteroatom containing aromatic sodium carboxylates

Another option to tailor the electrochemical properties of the organic compound compared to simple Na-BDC is the introduction of a heteroatom into the system. Once more, literature known compounds based on 2,5-pyridinedicarboxylic acid (PDC)[61] and 2,5-thiophenedicarboxylic acid (TDC)[62] were targeted.

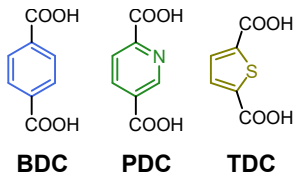

Figure 6.17. Structures of BDC, PDC, and TDC.

Figure 6.18a shows the PXRD patterns of a range of syntheses for Na-PDC, where the product of the synthesis with M/L = 2 and ethanol as liquid additive was chosen as most promising material. FTIR analysis does not indicate residual free carboxylic acid (OH bands) and only a minor peak at 1724 cm^{-1} is present suggesting a high degree of conversion towards Na_2PDC. It is assumed that the presence of nitrogen aids in the deprotonation due to its basic properties, thus shifting the equilibrium towards complete

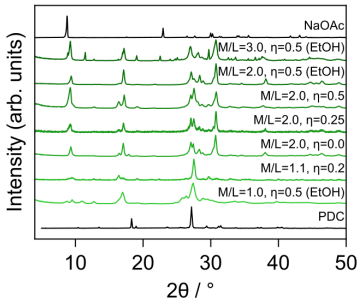

a) PXRD patterns of mechanochemically synthesised Na-PDC samples with varying metal-to-linker ratios M/L and liquid-to-solid ratio η in $\mu L\,mg^{-1}$.

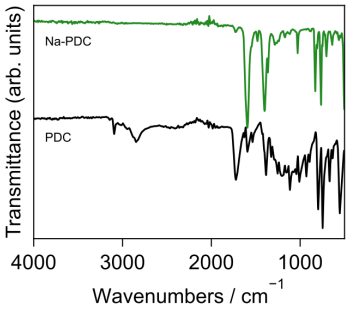

b) FTIR spectrum for Na-PDC.

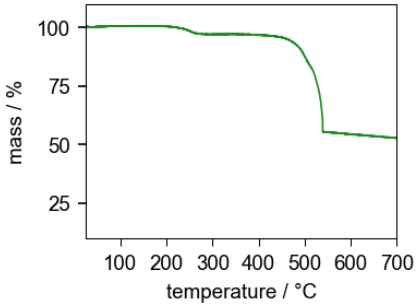

c) TGA profile for Na-PDC.

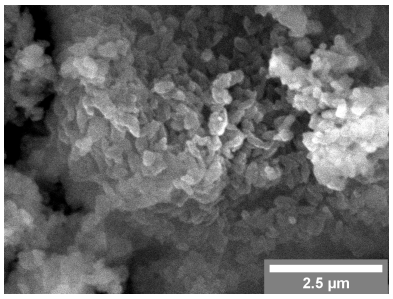

d) SEM image of the Na-PDC sample.

Figure 6.18. Characterisation of mechanochemically synthesised Na-PDC samples.

deprotonation of the dicarboxylic acid. TGA analysis is consistent with the identification of the product as the disodium salt as the main mass loss occurs at the relatively high temperature of 500 °C.

The synthesis towards Na-TDC was conducted analogously to other carboxylates. PXRD patterns show unreacted TDC up until M/L = 2 (see Figure 6.19a). Using larger amounts of the sodium reagent remedied this situation, while the now residual sodium acetate was removed by washing with ethanol. The FTIR spectrum of this washed sample shows bands consistent with what is expected for Na-TDC and no sign of free carboxylic acid O−H bonds at high wavenumbers (see Figure 6.19b). The band assigned to the COO functional group in the starting material TDC is clearly shifted to lower wavenumbers for the product phases.

Despite the similarity of these analyses with above described Na-xDCs (x being a placeholder for the various types dicarboxylic acids), Na-TDC did not perform as well as other compounds in galvanostatic cycling (see also Figure 6.21 below). This may be related to an observation that was made during and after the synthesis of the material itself. In contrast to other experiments TDC seemingly reacted with the stainless steel milling balls, leading to discolouration of the product as well as visible deterioration of the steel balls on the surface as shown in Figure 6.20. At this point it is unclear which

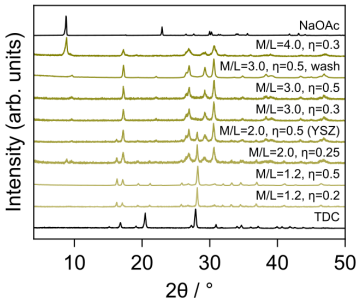

a) PXRD patterns of mechanochemically synthesised Na-TDC samples with varying metal-to-linker ratios M/L and liquid-to-solid ratio η in $\mu L\,mg^{-1}$.

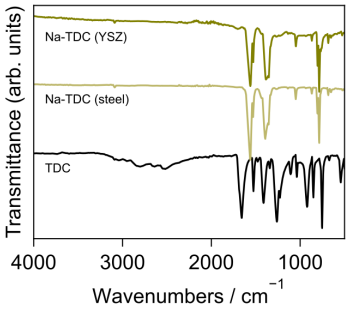

b) FTIR spectrum for Na-TDC milled with steel balls (M/L=3, η=0.5, washed) and the sample obtained with YSZ milling media.

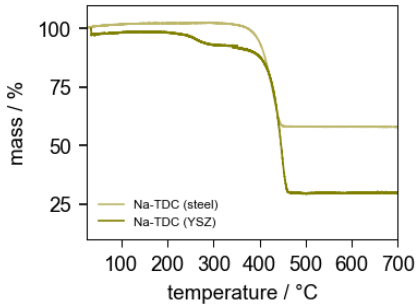

c) TGA profile for Na-TDC milled with steel balls (M/L=3, η=0.5, washed) and the sample obtained with YSZ milling media.

Figure 6.19. Characterisation of mechanochemically synthesised Na-TDC samples.

exact reaction might have occurred and how this led to diminished electrochemical properties. A plausible explanation is a reaction of the sulfur atom with iron in steel towards iron sulfide and the decomposition product of the organic. This would lead to the observed corrosion of the surface of the milling media and explain the slight darkening of the otherwise off-white Na-TDC. A change to milling media of a different material such as zirconia could resolve this issue. Indeed, using a single yttrium stabilised

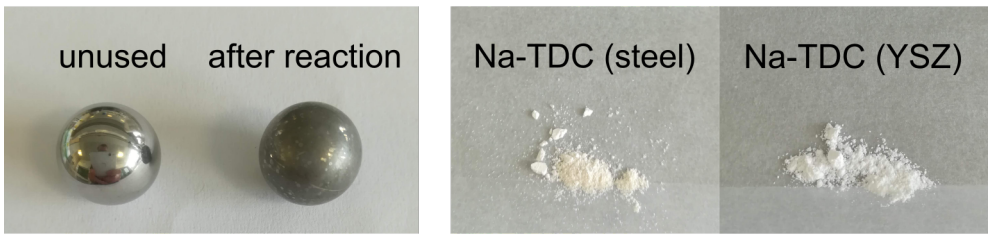

Figure 6.20. Photos of an unused stainless steel milling ball and the observable deterioration after a milling reaction towards Na-TDC (left). Discolouration of the Na-TDC material obtained using stain-less steel milling balls, compared to synthesis with YSZ (yttrium stabilised zirconia) balls (right).

zirconia (YSZ) milling ball with a diameter of 10 mm, the obtained sample did not show discolouration, indicating a potentially a pure compound with the promise of improved electrochemical properties compared to the previously prepared material. Thermal analysis (Figure 6.19c) reveals a clear difference of 29 % in final residual mass after

heating to 700 °C. This observation is in line with the previous hypothesis of a large amount of electrochemically inactive by-product, for example a decomposition product of the organic or residue from the steel balls. Unfortunately, PXRD patterns and FTIR (Figure 6.19) spectra of the two samples are essentially identical, making it difficult to assess what kind of impurity may have impeded the electrochemical performance in the material studied prior.

As is evident from the cycling studies, the Na-TDC sample synthesised with steel milling media has very low discharge capacities, using both the pristine phase and after washing with ethanol. Na-TDC prepared using a YSZ ball shows a more promising initial performance, however, fades rather rapidly. The essentially non-existing capacity of the first cycle stems from an issue regarding the open circuit voltage of the assembled half-cell, which is not indicative of the electrode performance. A value of 180 mA h g^{-1} is recorded for the second cycle, but over the course of the experiment, the discharge capacity drops significantly and levels off around 74 mA h g^{-1}, a similar performance as seen for Na-TDC produced using steel balls. The observed capacity profile have several causes. There could be a practical, compatibility issue with the chosen elements of the electrode composite, both with respect to the respective ratios as well as even the materials themselves. Likewise, the employed electrolyte may gradually dissolve the active Na-TDC compound, which would result in such a gradual decline. Lastly, there may be an issue with the reversibility of sodium ion insertion itself. Given that the compound Na-TDC has been reportedly used successfully as active anode material,[62] this would indicate an issue with the synthesis rather than the targeted compound itself. As these results clearly show, this project is a work in progress,, but initial obstacles regarding synthesis conditions have been overcome. The focus can now be set at improving the quality of the produced compounds as well as optimising electrode composition and fabrication.

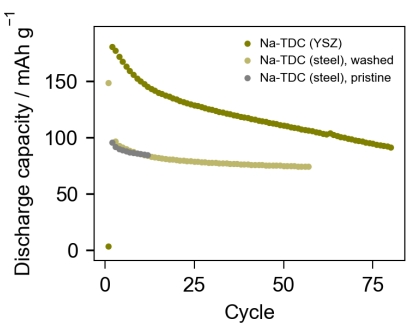

Figure 6.21. Discharge capacity for Na-TDC measured for 50 cycles at 100 mA h g^{-1} in a voltage window of 0.01–2.5 V.

In contrast to Na-TDC, the pyridine-based sample did not require any deviation from the standard synthesis protocol and the sample showed great potential in terms of cyclability, capacity and its retention, and recovery upon current rate changes. The CV shows a two-step profile, which is caused by the insertion of sodium ions not only into the carboxylate group but also onto the nitrogen. This is expected behaviour of such a compound and has also been described in the literature for Na-PDC obtained through solution-based synthesis.[61] The irreversible capacity of the first cycle is comparatively low and the corresponding Coulombic efficiency favourably high at 75 %. 258 mA h g^{-1} were measured for the 2nd cycle, which compares nicely to the theoretical limit of 254 mA h g^{-1} and the value retained reasonably well over the measured 100 cycles. These values also agree well with published data, which is considered a satisfying result as in this current study the water soluble binder CMC was used, as opposed to environmentally more concerning PVDF. Furthermore, a lower amount of conductive carbon (30% Super C65 instead of 35% Super P) was used, again favouring this work over earlier reports.

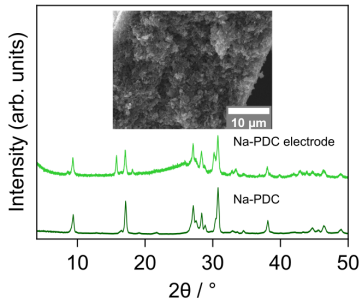

a) PXRD and SEM image (insert) of electrodes based on Na-PDC.

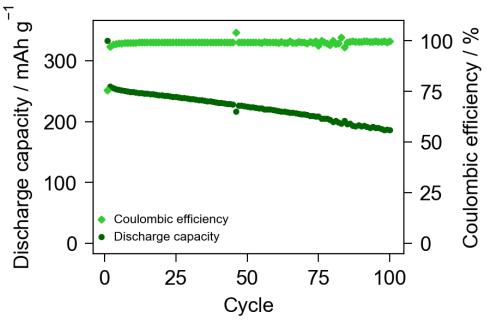

b) Discharge capacity and Coulombic efficiency for Na-PDC measured for 100 cycles at 100 mA g^{-1} in a voltage window of 0.01–2.5 V.

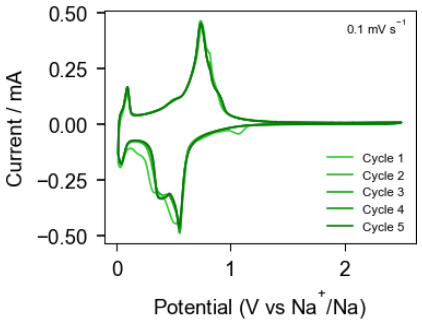

c) CV profile for Na-PDC, conducted at a scan rate of 0.1 mV s^{-1}.

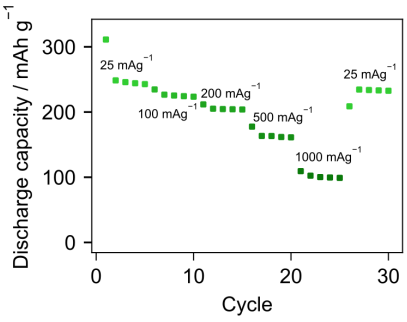

d) Rate performance for Na-PDC from 25–1000 mA g^{-1}, cycled five times at each current rate.

Figure 6.22. Electrochemical performance of electrodes based on Na-PDC.

When discovering and developing a new synthesis route for sodium carboxylate materials, such as the here presented mechanochemical method, it is important to test and evaluate its limitations with respect to reagents. The possibility to use heteroatom

containing organic starting materials broadens the scope for this promising synthesis protocol. Besides the aforementioned issue of using steel as material for milling media with the sulfur containing TDC, no further issues were encountered. Although only two compounds were tested so far, there doesn't seem to be an inherent obstacle expanding the pool of mechanochemically available products.

6.3 The curious case of Na-1,4-NDC

Extending the conjugated π-system of BDC not along its axis but rather in-plane leads to the molecule 1,4-naphthalenedicarboxylic acid. Although a sodium 1,4-dinaphthalate has been obtained previously from a solvothermal synthesis method,[63] these were considerably harsher conditions than reported for other sodium salt of carboxylic acids. This synthesis was carried out in autoclaves, which means that autogenous pressure was exerted onto the system. Furthermore, a solvent mix including the hazardous DMF (dimethylformamide) had to be used to produce the desired product. With this in mind, expectations were rather low that a mechanochemical synthesis aiming to exclusively use benign reagents could be successful.

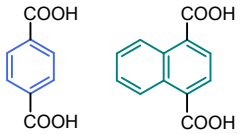

Figure 6.23. Structures of BDC and NDC.

6.3.1 Mechanochemical synthesis towards Na-NDC

A series of experiments was conducted in different M/L ratios and some variation in η, which is caused by the different amounts of hydrated sodium acetate. Figure 6.24a shows samples in the presence of water as non-solid reagent, whereas the influence of using additional methanol or DMF can be seen in Figure 6.24b. For M/L = 1 and M/L = 2, residual starting materials can be seen, however, for the two tested ratios in-between (1.33 and 1.5) peaks associated with sodium acetate and NDC are absent. Important to note is that none of these materials were purified post-synthetically, but are only dried at 80 °C in an oven overnight after the mechanochemical reaction had finished.

The nature of the mechanochemically synthesised sample is still unclear. It is conceivable that a different polymorph of sodium naphthalenedicarboxylate had formed,

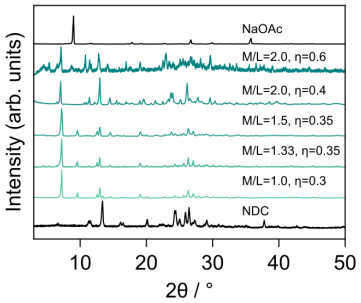

a) PXRD patterns of mechanochemically synthesised Na-NDC with varying metal-to-linker ratios M/L and liquid-to-solid ratio η in $\mu L\,mg^{-1}$.

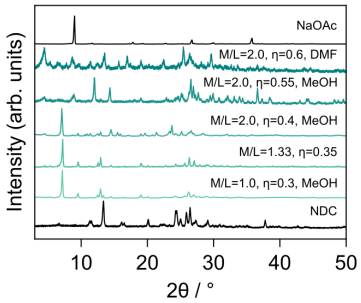

b) PXRD patterns of mechanochemically synthesised Na-NDC samples using additional methanol (MeOH) or dimethylformamide (DMF).

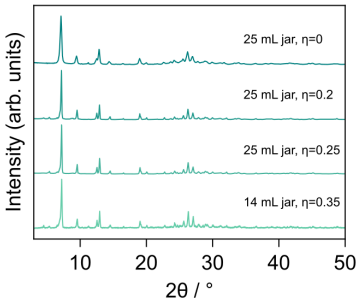

c) PXRD patterns of mechanochemically synthesised Na-NDC samples at different scales.

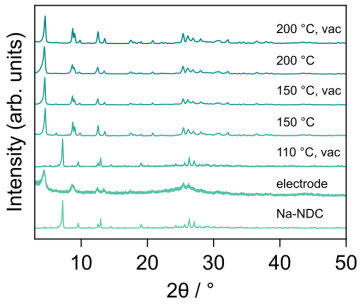

d) PXRD patterns of the mechanochemically synthesised Na-NDC sample used for electrochemical testing, the resulting electrode composite, as well as heat-treated Na-NDC samples.

Figure 6.24. PXRD characterisation of mechanochemically synthesised Na-NDC samples.

but it is also possible that a mixed acetate/naphthalate product was obtained. Given the conditions of the reported synthesis,[63] the effect of adding DMF to the reaction was tested. The obtained material exhibited broad peaks in PXRD, as well as a low angle peak at ca. 4.5° 2θ. A peak at this position is present in other samples as well, albeit barely distinguishable from the background. Experiments were also conducted using methanol as liquid additive. However, products are very similar to the ones obtained using water. Judging from this initial set of syntheses, the sample using M/L = 1.33 was the focus of further investigations and analysis. The difference between methanol and water containing syntheses seems negligible, thus choosing water over the comparatively less benign methanol is reasonable albeit both may be considered for future studies. Furthermore, it is not necessary to add water additionally when using the hydrated sodium reagents. These environmental and safety concerns are also the main reason to avoid hazardous chemicals like DMF. Thus, further characterisation was focused on syntheses only containing water.

Looking at scalability of this synthesis, larger milling jars (25 mL instead of 14 mL) were used to produce Na-NDC on a gram scale. In order to ensure sufficient energy input employed milling balls were similarly larger in size and mass, using two balls with

a diameter of 12 mm (7 g). PXRD patterns of the chosen Na-NDC small scale synthesis compare well with the scaled up analogues, demonstrating that obtained larger quantities of material is easily achieved. One of the reactions was conducted using anhydrous sodium acetate, proving that the presence of a liquid is not required for the reaction itself. On first glance, a dry milling experiment may seem to be an improvement over reactions in which a liquid is added. As discussed above, however, the product of such a neat milling operation is a fine powder accompanied by severe safety concerns, for example inhaling the material during handling. Thus, only products of syntheses with at least some water content were used further.

The aim to synthesise Na-NDC in the first place was its potential application as active material in negative electrodes for sodium ion batteries. The preparation of such an electrode requires mixing of the carboxylate material with electrically conductive carbon and combining this with a binder material using a water slurry (for details see section 6.5.4). After evaporation of the water at room temperature, a drying step at 110 °C under vacuum is required. This procedure induced a profound change in the structure of the sample, evidenced in its PXRD pattern (see Figure 6.24d). Further investigating this curious change, the pristine sample was also exposed to these conditions but this did not result in the same second phase as seen before. Increasing the temperature to 150 °C or 200 °C, however, yields the new product, both in air as well as under vacuum. The PXRD pattern also matches reasonably well with several of the peaks in the pattern obtained from the product of the DMF synthesis, indicating that this phase is potentially obtainable directly through synthesis. Presence of DMF may have a two-fold effect on driving the reaction to a different product. On the one hand, the increased basicity of such a reaction system helps to deprotonate carboxylic acids. On the other hand, the decomposition products of DMF and potentially the intact molecule itself can act as a template for the formation of a specific material.[64] Although it is at this point unclear how DMF acts in this synthesis, the fact that this phase can also be obtained without the use of this chemical is favourable. It is worth noting that all the samples may contain more than one phase, for example a mixture of the fully converted disodium naphthalate and a monosodium variant.

Comparing the PXRD pattern of the obtained Na-NDC phase with the previously published [Na_2(NDC)(DMF)] (Figure 6.25), it is clear that neither of the obtained materials is the previously reported one. The crystal structure of this published phase shows sodium chains of NaO_6 and NaO_5 polyhedra (one each per asymmetric unit, shown in

Figure 6.25c), interconnected by bridging naphthalene units, which are stacked along the *c* axis. This structure also shows circular pore channels along this axis upon removal of the solvent molecule DMF, which coordinates with its oxygen atom to sodium, extending into this void space. Given that this structure has so far only been reported as obtainable using this type of synthesis, DMF itself may play vital role in the formation of this crystal structure. The structure of the Na-NDC material synthesised in this project may at least in principle exhibit a similar structure, where sodium chains are connected to each other by NDC linking units. The as synthesised phase could still include acetate units, acting like capping agents in a similar fashion to DMF in the shown crystal structure. After the heat treatment these would be removed, and a somewhat altered framework results. These are still speculative notions, and further structural work is required.

Looking at further characterisation of this intriguing two-phase Na-NDC system, elemental analysis (CHN), TGA and FTIR spectroscopy were performed. For the as made sample, the measured elemental content for carbon and hydrogen does not match with any of the pure compounds. Through a simple minimisation equation, a possible composition for the material was found to be a mixture of sodium acetate CH_3COONa and sodiumhydrogen naphthalate $C_{10}H_6(COONa)(COOH)$ with a ratio of 0.2788. Thus, calculated theoretical values of 51.81 % carbon and 3.16 % hydrogen would agree well with the found content of 51.81 % and 3.44 %. Thermal analysis of this sample shows an endothermic mass loss of 17 % with its onset around 140 °C (see Figure 6.26a), suggesting a phase transition as seen in PXRD. The temperature would roughly agree with the boiling point for acetic acid (118 °C) or hydrated sodium acetate (122 °C). The second mass loss at 310 °C accounting for roughly 15 % has both endothermic and exothermic contributions, with the latter one being dominant. Thereafter, decomposition commences at about 400 °C. It may be possible that the initial phase contains acetate in its structure, which is then released upon heating and the remaining naphthalate recrystallises into the pure sodium naphthalate compound.

TGA data measured for the previously heated sample shows two clear mass losses at 310 °C and 460 °C, with 22 % and 26 %, respectively. Comparing this with materials described in section 6.2, the relatively low temperature for the first mass loss may originate from monosodium naphthalate, whereas the second one corresponds to the more stable disodium salt. Elemental analysis, however, would suggest only the presence of Na_2NDC with the difference between calculated and found percentage of 0.445 % and 0.245 % for carbon and hydrogen, respectively. Unfortunately, even this information

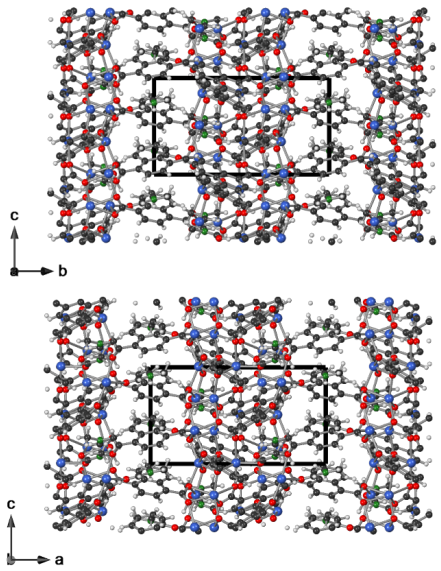

a) Crystal structure of [Na_2(NDC)(DMF)] (CCDC code KIYMIQ) viewed along the *a* (top) and *b* (bottom) direction.

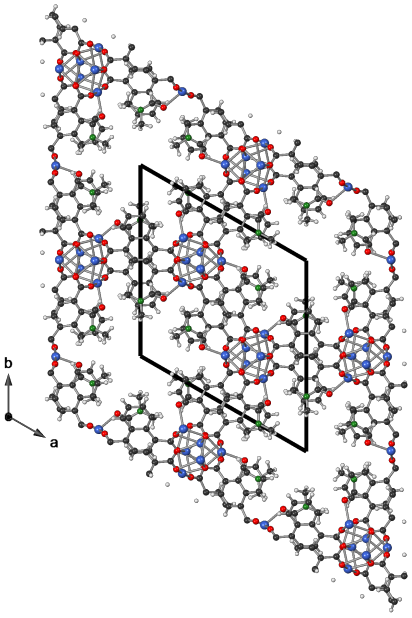

b) Crystal structure of [Na_2(NDC)(DMF)] (CCDC code KIYMIQ) viewed along the *c* direction.

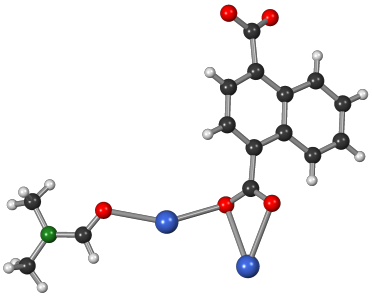

c) Asymmetric unit of [Na_2(NDC)(DMF)].

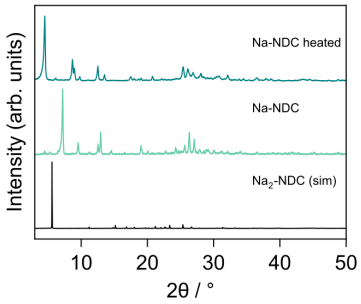

d) Simulated PXRD pattern for [Na_2(NDC)(DMF)] and comparison to mechanochemically synthesised Na-NDC and the phase obtained after heat treatment.

Figure 6.25. Crystal structure for the known [Na_2(NDC)(DMF)] (CCDC code KIYMIQ) compound[63] and comparison with PXRD patterns of Na-NDC obtained in this project. Carbon atoms are shown in black, hydrogen in white, oxygen in red, sodium in blue, and nitrogen in green.

does not fully resolve the encountered discrepancies. Assuming the sample consists only of Na_2NDC and the final, residual material is Na_2CO_3, the corresponding mass loss should account for 59 %, whereas only 54 % are observed. Additionally, it is also unclear why there are two distinct mass losses. The DTA profile shows a negative curvature coinciding with the first event, which may indicate another structural transformation accompanying the release of some part of the compound. It is conceivable, that if there are two binding modes of the naphthalene component in the structure such as one forming layers and the other pillars in between, that these would cause two separate decomposition temperatures.

The findings of FTIR spectroscopy of these two Na-NDC samples, shown in Fig-

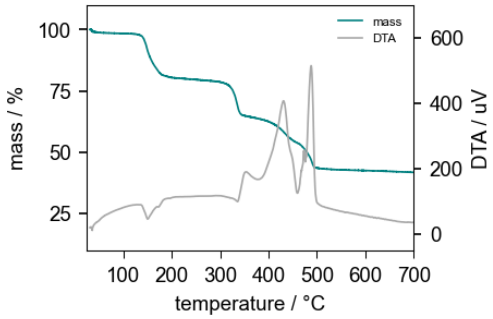

a) TGA and DTA profile for pristine Na-NDC.

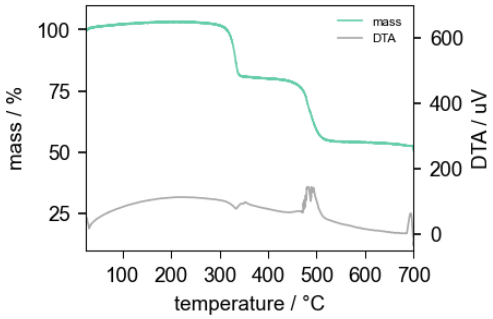

b) TGA and DTA profile for Na-NDC after heat treatment.

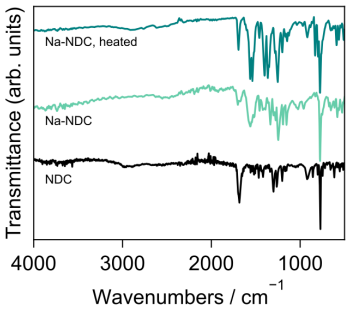

c) FTIR spectra of pristine Na-NDC and the phase obtained after heat treatment, compared with the free acid NDC.

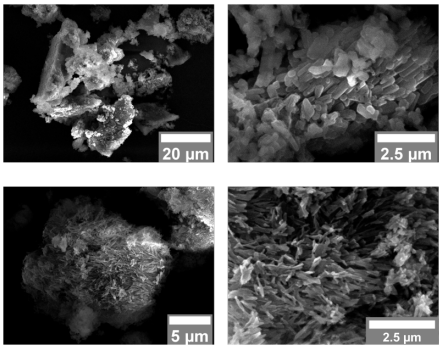

d) SEM images of mechanochemically synthesised Na-NDC (top row) and the heat-treated sample (bottom row).

Figure 6.26. Thermal analysis, FTIR spectra and SEM characterisation of the mechanochemically synthesised Na-NDC sample.

ure 6.26c, agree well with other characterisation methods. The strong sharp band corresponding to a carboxylic acid is observed at 1683 cm^{-1} for NDC. For pristine Na-NDC, this is reduced to a broad band. This indicates some residual free acids groups, for example due to incomplete deprotonation of both acid groups on a single NDC molecule as observed for other mechanochemically synthesised Na-xDC materials. In addition to aromatic C=C vibrations, the broad feature at 1600–1500 cm^{-1} may also include asymmetric stretch vibrations of a COO^- group. The symmetric stretch of this functional group is assigned to a band at 1334 cm^{-1}. The spectrum of the heat treated sample is fairly similar to the as synthesised one, with the same features only resolved better. These findings indicate that both samples contain some amount of protonated COOH groups, but at the same time the presence of carboxylate groups is evident.

SEM images of Na-NDC in Figure 6.26d show large agglomerates, approximately 10 µm in size. Individual primary particles are rod-like, extending up to 1.5 µm and appear to have grown together throughout the material. Heat treatment leads to particles with more pronounced shape, retaining the elongated crystal habit of the pristine sample. These images also clearly show why single crystal X-ray diffraction, still by far the most common method for structure determination, is not available for these samples. The

intergrowth of crystallites as well as the small size render them inapplicable for this characterisation technique.

6.3.2 Electrochemical testing of Na-NDC

Building on what has been learned from other mechanochemically synthesised sodium carboxylate materials, the potential presence of both mono- and disodiated Na-NDC material may not have a drastic effect on the electrochemical properties of obtained samples. Performing a cycling experiment using a current rate of $50\,\mathrm{mA\,g^{-1}}$ shows an initial drop in capacity of about $200\,\mathrm{mA\,h\,g^{-1}}$. As with previous materials, this irreversible capacity is attributed to the formation of the SEI layer as well as the presence of the monosodium species and some contribution from the conductive carbon additive. After the second cycle, the capacity stabilises at $180\,\mathrm{mA\,h\,g^{-1}}$ and gradually fades to $112\,\mathrm{mA\,h\,g^{-1}}$ over the investigated 100 cycles. Comparing these values to the theoretical capacity for Na_2NDC of $206\,\mathrm{mA\,h\,g^{-1}}$, this can still be considered a decent result. The Coulombic efficiency is also appreciably high, with values above 98 % after stabilisation. Cycling experiments at $100\,\mathrm{mA\,g^{-1}}$ and $200\,\mathrm{mA\,g^{-1}}$ showed the expected drop in capacity at these higher applied current densities, but in both cases the measured values are still well above the expected contributions of the carbon additive (compare Figure 6.9 above). The differential plot dQ/dV shows a minor shift of the discharge peak from 0.5 mA h in the first cycle to roughly 0.6 mA h for subsequent ones. The reduction peak is observed at 0.7 mA h, showing appreciably low polarisability of the material. The fact that only one distinct discharge peak is recorded suggests only one insertion mechanism, indicative of a single material with only one type of redox active moiety. If two phases such as mono- and disodiated naphthalate were present, one would expect a second peak, as seen in the Na-BPDC example (section 6.2.4).

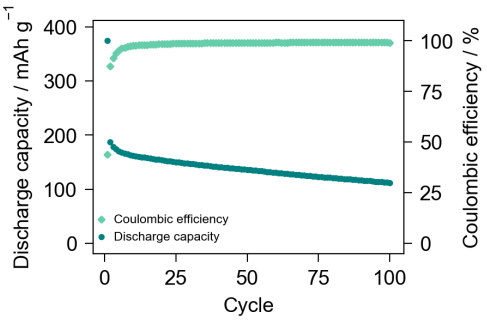

a) Discharge capacity and Coulombic efficiency for Na-NDC measured for 100 cycles at 50 mA g^{-1} in a voltage window of 0.01–2.5 V.

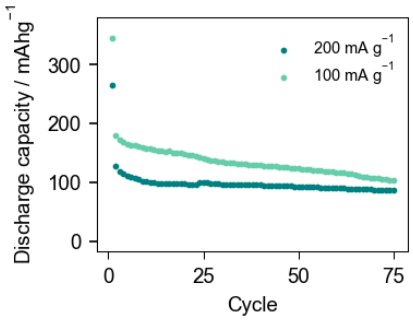

b) Discharge capacity and Coulombic efficiency for Na-NDC measured for 75 cycles at 100 mA g^{-1} in a voltage window of 0.01–2.5 V.

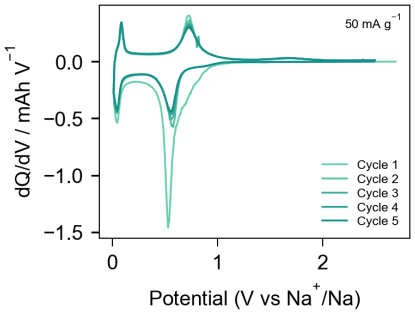

c) dQ/dV plot for the initial five cycles of Na-NDC at 50 mA g^{-1}.

Figure 6.27. Electrochemical performance of electrodes based on Na-NDC.

6.4 Conclusion and perspective

Employing a mechanochemical synthesis method, several known sodium carboxylate compounds were produced in a sustainable and environmentally friendly manner. Thus prepared Na-BDC was investigated for its application as anode materials for NIBs, exhibiting good performance, competitive with materials synthesised from solution. Using the related organic acids BPDC and SDC showed that extension of the backbone of the used organic compound is not an issue for this methodology either. Again, the products performed well in comparison with published results by other groups. The two examples of Na-TDC and Na-PDC demonstrate the applicability of the employed mechanochemical synthesis to heteroatom containing sodium carboxylates. Na-PDC showed competitive electrochemical performance, which is a promising result considering the use of environmentally friendlier binder in the electrode preparation contrasting to previous studies. Initially obtained Na-TDC showed reduced electrochemical performance, ascribed to side-reaction with the steel-based milling media. Optimisation of the synthesis by means of changing the milling media to chemically more inert zirconia balls resulted in a material displaying improved performance as NIB anode material, although adaptions are

still necessary for this compound to be competitive.

In addition to reproducing published compounds in a more sustainable manner, a potentially new sodium coordination polymer built from 1,4-naphthalenedicarboxylic acid has been obtained using this mechanochemical methodology. Other attempts to produce a compound based on this organic acid through synthesis from solution had to rely on the hazardous solvent DMF and harsh conditions, both of which are avoided in this protocol. The product recovered directly from the milling process is unstable with respect to heat, however, forms a stable material if such conditions are applied in a controlled and intended manner. Unfortunately, so far neither the structure of the as made as nor the phase obtained after heat treatment could be solved. A possible solution to this problem could be three-dimensional electron diffraction techniques (3DED) which are capable of obtaining data of high quality from crystals well below 1 μm. Given the small crystal size of products obtained through ball milling, such methods may help to elucidate the structure of the obtained Na-NDC materials and progress this project. Despite the lack of a structure model for this material, its synthesis is still considered a success, especially in light of this material being seemingly unavailable through other synthetic methods.

The developed protocols for the mechanochemical production of sodium carboxylate materials are considered a robust synthesis approach. Although the reaction conditions may still be optimised, in view of their application as anode materials, however, the methodology may already be at a stage where upscaling to larger quantities may be worthwhile. The transformation of a process from lab-scale to (pilot) plant scale requires careful adjustments of synthesis conditions and parameters. Even after optimising a protocol for a bench top ball mill does not necessarily mean that such a transition can occur without a series of tests and implementation adjustment when using larger equipment.

Likewise, the variety of the used carboxylic acids gives a glimpse into what may be possible using mechanochemistry especially in the field of organic electrode materials. The simplicity of the method means that besides the initial acquisition cost of the milling device, a very cheap, streamlined synthesis of a plethora of materials can be accomplished. Another promising finding is the combination of the synthesis with the preparation of the electrode composite, as demonstrated on the example with Na-BDC. This result hints at the quite real possibility for an all-in-one approach to

synthesise the electrochemical active material and combine it with the required electrically conductive carbon in one step. The combination with the binder material to ensure sufficient contact between the two materials may also occur in the same reaction vessel either as an in situ synthesis or as an addition of the binder solution at a later stage.

With all mentioned advantages, the presented mechanochemical synthesis of organic-based sodium carboxylates is thought to be setting a great precedent in the field of organic electrode materials. The methodology promises to work similarly well for other alkali metal carboxylates and may even be applicable in the to compounds containing other redox active groups such as imine and azo. The potential for this environmentally friendly synthesis of such compounds adds to the advantages of organic-based electrode materials and gives hope for sustainable production of batteries in the future.

6.5 Experimental section

6.5.1 Reagents

All chemicals (see Table 6.1) were used without purification prior to synthesis.

Table 6.1. Chemicals and their suppliers.

Chemical	Abbreviation	Supplier
Sodium acetate (anhydrous)	NaOAc	Sigma
Sodium acetate trihydrate	NaOAc-h	Alfa Aesar
1,4-benzenedicarboxylic acid	BDC	Aldrich
4,4′-biphenyldicarboxylic acid	BDPC	Acros Organics
4,4′-stilbenedicarboxylic acid	SDC	TCI Chemicals
2,5-pyridinedicarboxylic acid	PDC	Aldrich
2,5-thiophenedicarboxylic acid	TDC	TCI Chemicals
1,4-naphthalenedicarboxylic acid	NDC	Alfa Aesar
1,4,5,8-naphthalenetetracarboxylic acid	NTC	Fluorochem
Ethanol	EtOH	VWR
Dimethylformamide	DMF	Acros Organics
Conductive carbon Super C65	C65	Imerys – Graphite & Carbon
Hard carbon	HC	Deregallera
Sdoium carboxymethyl cellulose	CMC	Sigma-Aldrich
Sodium alginate	–	Sigma-Aldrich
Sodium (metallic)	–	Sigma-Aldrich
Sodium hexafluorophosphate in ethylene carbonate and diethyl carbonate (1:1)	$NaPF_6$ in EC/DEC	Kishida

6.5.2 Synthesis details

Mechanochemical syntheses were carried out in a Retsch MM 400 Shaker Mill. Milling jars were home-made from polycarbonate at the university's workshop and based on technical drawings in reference [53]. All reactions were carried out using a frequency of 30 Hz. Further details for individual experiments can be found in the tables below.

Table 6.2. Experimental details of mechanochemical syntheses towards Na-BDC. [h] denotes sodium acetate trihydrate NaOAc · 3 H_2O, otherwise the anhydrous salt was used. The highlighted row indicates the sample used for further analysis and electrochemical testing.

BDC [g]	NaOAc [g]	M/L [-]	liquid [µL]	η [µL/mg]	jar size [mL]	balls [mm]	time [min]	workup	yield [g]
0.27	0.23[h]	1	0	0.2	14	2 × 7	60		0.29
0.25	0.26[h]	1.25	0	0.2	14	2 × 7	60		0.27
0.25	0.28[h]	1.5	0	0.2	14	2 × 7	60		0.24
0.19	0.31[h]	2	0	0.25	14	2 × 7	90		0.20
0.15	0.36[h]	3	0	0.3	14	2 × 7	60		0.17
0.13	0.37[h]	3.5	0	0.3	14	2 × 7	90		0.21
0.12	0.38[h]	4	0	0.3	14	2 × 7	60		0.18
0.34	0.17	1	0	0	25	2 × 12	240		n.d.
1.01	0.50	1	0	0	14	2 × 7	90		n.d.

Table 6.3. Experimental details of mechanochemical syntheses towards Na-BDC in the presence of electrically conductive carbon. All experiments were conducted in 14 mL milling jars, using two stainless steel milling balls with a diameter of 7 mm.

BDC [g]	NaOAc [g]	M/L [-]	liquid [µL]	η [µL/mg]	C65 [g]	HC [g]	time [min]	workup	yield [g]
0.27	0.13	1	200[H_2O]	0.5	0.20		60		0.50
0.27	0.13	1	200[H_2O]	0.5		0.20	60		0.44
0.13	0.06	1	200[H_2O]	0.5	0.07	0.25	60		0.48

Table 6.4. Experimental details of solution-based syntheses towards Na-BDC. All syntheses were conducted using ethanol as solvent and stirred under reflux conditions for 24 h. The microwave based synthesis is marked with an asterisk and was performed at 150 °C for 15 min. The crude products were filtered and washed with ethanol.

BDC [g]	Na source [g]		M/L	synthesis	yield [g]
0.67	0.34	NaOH	2.1	reflux	0.81
0.67	0.47	Na_2CO_3	2.1	reflux	0.91
0.67	0.69	NaOAc	2.1	reflux	1.13
0.67	0.71	$NaNO_3$	2.1	reflux	0.86
0.17	0.17	NaOAc	2.1	microwave	0.19

Table 6.5. Experimental details of mechanochemical syntheses towards Na-BPDC. ^{h} denotes sodium acetate trihydrate NaOAc · 3 H_2O, otherwise the anhydrous salt was used. Added liquid is denoted in superscript, where ^{H_2O} means water and ^{EtOH} means ethanol. The highlighted row indicates the sample used for further analysis and electrochemical testing.

BPDC [g]	NaOAc [g]	M/L [-]	liquid [µL]	η [µL/mg]	jar size [mL]	balls [mm]	time [min]	workup	yield [g]
0.37	0.13	1	250^{H_2O}	0.5	14	2 × 7	60		0.35
0.30	0.20	2	250^{H_2O}	0.5	14	2 × 7	60		0.28
0.30	0.20	2	250^{EtOH}	0.5	14	2 × 7	60		0.42
0.25	0.25	3	250^{H_2O}	0.5	14	2 × 7	60		0.39
0.25	0.25	3	250^{EtOH}	0.5	14	2 × 7	60	EtOH	0.42
0.21	0.29	4	250^{EtOH}	0.5	14	2 × 7	60		0.35

Table 6.6. Experimental details of mechanochemical syntheses towards Na-SDC. ^{h} denotes sodium acetate trihydrate NaOAc · 3 H_2O, otherwise the anhydrous salt was used. Added liquid is denoted in superscript, where ^{H_2O} means water and ^{EtOH} means ethanol. The highlighted row indicates the sample used for further analysis and electrochemical testing.

SDC [g]	NaOAc [g]	M/L [-]	liquid [µL]	η [µL/mg]	jar size [mL]	balls [mm]	time [min]	workup	yield [g]
0.38	0.12	1	250^{H_2O}	0.5	14	2 × 7	60		0.36
0.24	0.16^{h}	1.3	0	0.2	14	2 × 7	15		0.24
0.20	0.20^{h}	2	0	0.2	14	2 × 7	15		0.21
0.25	0.25^{h}	2	120^{H_2O}	0.5	14	2 × 7	60	EtOH	0.20
0.26	0.24	3	250^{H_2O}	0.5	14	2 × 7	60		0.34
0.23	0.28	4	250^{EtOH}	0.5	14	2 × 7	60		0.35

Table 6.7. Experimental details of mechanochemical syntheses towards Na-PDC. ^{h} denotes sodium acetate trihydrate NaOAc · 3 H_2O, otherwise the anhydrous salt was used. Added liquid is denoted in superscript, where ^{H_2O} means water and ^{EtOH} means ethanol. The highlighted row indicates the sample used for further analysis and electrochemical testing.

PDC [g]	NaOAc [g]	M/L [-]	liquid [µL]	η [µL/mg]	jar size [mL]	balls [mm]	time [min]	workup	yield [g]
0.34	0.17	1	250^{EtOH}	0.5	14	2 × 7	60		0.35
0.21	0.19^{h}	1.1	0	0.2	14	2 × 7	60		0.19
0.20	0.20	2	0	0	14	2 × 7	15		0.25
0.15	0.25^{h}	2	0	0.25	14	2 × 7	60		0.14
0.15	0.25^{h}	2	103^{H_2O}	0.5	14	2 × 7	60		0.17
0.15	0.25^{h}	2	103^{EtOH}	0.5	14	2 × 7	60		0.14
0.20	0.30	3	250^{EtOH}	0.5	14	2 × 7	60		0.31

Table 6.8. Experimental details of mechanochemical syntheses towards Na-TDC. ^{h} denotes sodium acetate trihydrate NaOAc · 3 H_2O, otherwise the anhydrous salt was used. Added liquid is denoted in superscript, where ^{H_2O} means water. The row highlighted in yellow indicates the sample used for further analysis and electrochemical testing. The row highlighted in green indicates the sample produced using a zirconia milling ball.

TDC [g]	NaOAc [g]	M/L [-]	liquid [µL]	η [µL/mg]	jar size [mL]	balls [mm]	time [min]	workup	yield [g]
0.21	0.12^{h}	1.2	0	0.2	14	2×7	60		17
0.21	0.12^{h}	1.2	122^{H_2O}	0.5	14	2×7	60		17
0.16	0.25^{h}	2	0	0.25	14	2×7	60		12
0.41	0.59	3	300^{H_2O}	0.3	25	2×12	15	EtOH	0.40
0.41	0.59	3	500^{H_2O}	0.5	25	2×12	15	EtOH	0.45
0.10	0.30^{h}	4	0	0.3	14	2×7	60		0.14
0.26	0.24	2	100^{H_2O}	0.2	14	1×10	60		0.23

Table 6.9. Experimental details of mechanochemical syntheses towards Na-NDC. ^{h} denotes sodium acetate trihydrate NaOAc · 3 H_2O, otherwise the anhydrous salt was used. Added liquid is denoted in superscript, where ^{H_2O} means water, ^{MeOH} methanol, and ^{DMF} dimethylformamide. The highlighted row indicates the sample used for further analysis and electrochemical testing.

NDC [mg]	NaOAc [mg]	M/L [-]	liquid [µL]	η [µL/mg]	jar size [mL]	balls [mm]	time [min]	workup	yield [mg]
0.38	0.24^{h}	1.0	100^{MeOH}	0.3	14	2×7	30		0.40
0.32	0.20^{h}	1.0	0	0.15	14	2×7	15		0.41
0.38	0.24^{h}	1.0	100^{H_2O}	0.3	14	2×7	60		0.41
0.33	0.17	1.33	0	0	14	1×10	60		0.37
1.00	0.51	1.33	0	0	25	2×12	90		n.d.
0.33	0.17	1.33	0	0	14	1×7	60		0.40
0.27	0.23^{h}	1.33	0	0.2	14	2×7	60		0.35
0.32	0.27^{h}	1.33	0	0.2	14	2×7	60		0.41
1.09	0.91^{h}	1.33	0	0.2	25	2×12	60		1.49
0.27	0.14	1.33	90^{H_2O}	0.2	14	2×7	60		0.34
0.32	0.27^{h}	1.33	100^{H_2O}	0.35	14	2×7	60		0.36
1.09	0.91^{h}	1.33	137^{H_2O}	0.25	25	2×12	60		1.53
0.32	0.31^{h}	1.5	100^{H_2O}	0.35	14	2×7	60		0.36
0.27	0.34^{h}	2.0	100^{H_2O}	0.4	14	2×7	30		0.40
0.29	0.22	2.0	0	0	14	2×7	60		0.38
0.27	0.34^{h}	2.0	200^{MeOH}	0.55	14	1×10	60	MeOH	0.18
0.27	0.34^{h}	2.0	100^{MeOH}	0.4	14	2×7	30		0.36
0.27	0.34^{h}	2.0	100^{H_2O}	0.4	14	2×7	60	MeOH	n.d.
0.22	0.28^{h}	2.0	200^{DMF}	0.6	14	2×7	60		0.07
0.22	0.28^{h}	2.0	200^{H_2O}	0.6	14	2×7	60		0.14

6.5.3 Physicochemical characterisation

Powder X-ray diffraction (PXRD)

Experiments were carried out on a PANalytical Empyrean disc diffractometer, operated in Bragg Brentano geometry in θ–2θ mode or a STOE STADI/P capillary diffractometer, operated in Debye-Scherrer geometry. Both diffractometers are equipped with a primary beam monochromator resulting in Cu $K\alpha_1$ radiation. Patterns were typically collected from 3–50° 2θ.

Scanning electron microscopy (SEM)

Images were acquired on a JEOL JSM-IT200 and a JEOL JSM-IT800. Samples were placed on sticky carbon tape and gold coated at 10 mA for 30 s using a Quorum Q150R ES sputter coater.

Fourier-transform infrared spectroscopy (FTIR)

Spectra were recorded on a Shimadzu Affinity-1 in a range of 500–4000 cm^{-1}.

Thermogravimetric analysis (TGA) and differential thermal analysis (DTA)

Thermal analysis data were acquired on a Stanton Redcroft STA-780 in air (25 mL min^{-1}) heating up to 700 °C with a ramp rate of 5 °C min^{-1}. On several samples part of the run was conducted at a slower rate of 1.5 °C min^{-1} to avoid artefacts due to highly exothermic decompositions.

6.5.4 Electrode preparation and electrochemical experiments

Preparation of electrodes was conducted by Dr Aamod V. Desai.
All electrode composites were prepared as a mixture of active materials Na-x (60 %, where x is a placeholder for the different carboxylates such as BDC), conductive carbon Super C65 (30 %) and a binder material (10 %). All percentages are given as mass percentage. The employed binder was CMC for all composites except Na-NDC and Na-NTC, where sodium alginate was used. The organic compound and carbon were manually ground using mortar and pestle and combined with an aqueous solution of the binder. This slurry was stirred for 4 h and subsequently cast onto aluminium foil using a doctor blade. Copper foil was used in the case of Na-TDC, following a published study.[62] After air drying for 2 h, electrodes with a diameter of roughly 13 mm were punched and dried at 110 °C

under vacuum. As prepared composite to be characterised prior to cycling was obtained from the remaining material on the foil and scraped off using a spatula. Assembly of batteries was conducted in a glove box (argon filled, oxygen and water content < 1 ppm), using sodium metal as counter electrode, separated by glass fibre, and employing $NaPF_6$ in a mix of EC/DEC (1:1 ratio) as electrolyte. The materials were pressed into coin cells (CR2325) using a standard lab press inside the glove box. All electrochemical tests were conducted on a Biologic BDC-805 modular battery testing system, using a potential window of 0.01–2.5 V vs Na/Na^+ and controlling the temperature at 30 °C. Obtained data were processed and analysed using BT-Lab software.

6.6 References

(1) IEA (2020), *Key World Energy Statistics 2020*, 2020.

(2) M. Li, J. Lu, Z. Chen and K. Amine, *Adv. Mater.*, 2018, **30**, 1800561.

(3) G. Zubi, R. Dufo-López, M. Carvalho and G. Pasaoglu, *Renew. Sustain. Energy Rev.*, 2018, **89**, 292–308.

(4) C. Grosjean, P. H. Miranda, M. Perrin and P. Poggi, *Renew. Sustain. Energy Rev.*, 2012, **16**, 1735–1744.

(5) M. D. Slater, D. Kim, E. Lee and C. S. Johnson, *Adv. Funct. Mater.*, 2013, **23**, 947–958.

(6) J.-Y. Hwang, S.-T. Myung and Y.-K. Sun, *Chem. Soc. Rev.*, 2017, **46**, 3529–3614.

(7) C. Vaalma, D. Buchholz, M. Weil and S. Passerini, *Nat. Rev. Mater.*, 2018, **3**, 18013.

(8) J. Xiang, L. Yang, L. Yuan, K. Yuan, Y. Zhang, Y. Huang, J. Lin, F. Pan and Y. Huang, *Joule*, 2019, **3**, 2334–2363.

(9) P. Ge and M. Fouletier, *Solid State Ionics*, 1988, **28-30, Par**, 1172–1175.

(10) Y. Li, Y. Lu, P. Adelhelm, M.-M. Titirici and Y.-S. Hu, *Chem. Soc. Rev.*, 2019, **48**, 4655–4687.

(11) U. Arrieta, N. A. Katcho, O. Arcelus and J. Carrasco, *Sci. Rep.*, 2017, **7**, 5350.

(12) H. Kim, H. Kim, Z. Ding, M. H. Lee, K. Lim, G. Yoon and K. Kang, *Adv. Energy Mater.*, 2016, **6**, 1600943.

(13) T. Perveen, M. Siddiq, N. Shahzad, R. Ihsan, A. Ahmad and M. I. Shahzad, *Renew. Sustain. Energy Rev.*, 2020, **119**, 109549.

(14) K. Holguin, M. Mohammadiroudbari, K. Qin and C. Luo, *J. Mater. Chem. A*, 2021, **9**, 19083–19115.

(15) B. Xiao, T. Rojo and X. Li, *ChemSusChem*, 2019, **12**, 133–144.

(16) D. Chen, W. Zhang, K. Luo, Y. Song, Y. Zhong, Y. Liu, G. Wang, B. Zhong, Z. Wu and X. Guo, *Energy Environ. Sci.*, 2021, **14**, 2244–2262.

(17) J. J. Shea and C. Luo, *ACS Appl. Mater. Interfaces*, 2020, **12**, 5361–5380.

(18) A. V. Desai, R. E. Morris and A. R. Armstrong, *ChemSusChem*, 2020, **13**, 4866–4884.

(19) A. E. Lakraychi, F. Dolhem, A. Vlad and M. Becuwe, *Adv. Energy Mater.*, 2021, 2101562.

(20) R. A. Sheldon, *Green Chem.*, 2014, **16**, 950–963.

(21) L. Wu, T. Moteki, A. A. Gokhale, D. W. Flaherty and F. D. Toste, *Chem*, 2016, **1**, 32–58.

(22) M. Volanti, D. Cespi, F. Passarini, E. Neri, F. Cavani, P. Mizsey and D. Fozer, *Green Chem.*, 2019, **21**, 885–896.

(23) H. Kang, Y. Liu, K. Cao, Y. Zhao, L. Jiao, Y. Wang and H. Yuan, *J. Mater. Chem. A*, 2015, **3**, 17899–17913.

(24) E. Peled and S. Menkin, *J. Electrochem. Soc.*, 2017, **164**, A1703–A1719.

(25) C. Bommier and X. Ji, *Small*, 2018, **14**, 1703576.

(26) D. Bresser, D. Buchholz, A. Moretti, A. Varzi and S. Passerini, *Energy Environ. Sci.*, 2018, **11**, 3096–3127.

(27) P. T. Anastas and J. C. Warner, *Green Chemistry: Theory and Practice*, Oxford University Press, 2000, p. 135.

(28) S. L. James, C. J. Adams, C. Bolm, D. Braga, P. Collier, T. Friščić, F. Grepioni, K. D. M. Harris, G. Hyett, W. Jones, A. Krebs, J. Mack, L. Maini, A. G. Orpen, I. P. Parkin, W. C. Shearouse, J. W. Steed and D. C. Waddell, *Chem. Soc. Rev.*, 2012, **41**, 413–447.

(29) W. Jones and M. D. Eddleston, *Faraday Discuss.*, 2014, **170**, 9–34.

(30) J. Andersen and J. Mack, *Green Chem.*, 2018, **20**, 1435–1443.

(31) D. Tan and F. García, *Chem. Soc. Rev.*, 2019, **48**, 2274–2292.

(32) T. Friščić, C. Mottillo and H. M. Titi, *Angew. Chemie Int. Ed.*, 2020, **59**, 1018–1029.

(33) S. Mateti, M. Mathesh, Z. Liu, T. Tao, T. Ramireddy, A. M. Glushenkov, W. Yang and Y. I. Chen, *Chem. Commun.*, 2021, **57**, 1080–1092.

(34) D. Tan and T. Friščić, *European J. Org. Chem.*, 2018, **2018**, 18–33.

(35) T. Friščić, in *Encyclopedia of Inorganic and Bioinorganic Chemistry*, John Wiley & Sons, Ltd, Chichester, UK, 2014, pp. 1–19.

(36) T. Stolar and K. Užarević, *CrystEngComm*, 2020, **22**, 4511–4525.

(37) S. R. Batten, N. R. Champness, X.-M. Chen, J. Garcia-Martinez, S. Kitagawa, L. Öhrström, M. O'Keeffe, M. Paik Suh and J. Reedijk, *Pure Appl. Chem.*, 2013, **85**, 1715–1724.

(38) K. J. Ardila-Fierro and J. G. Hernández, *ChemSusChem*, 2021, **14**, 2145–2162.

(39) E. Colacino, V. Isoni, D. Crawford and F. García, *Trends Chem.*, 2021, **3**, 335–339.

(40) J. Casaban, Y. Zhang, R. Pacheco, C. Coney, C. Holmes, E. Sutherland, C. Hamill, J. Breen, S. L. James, D. Tufano, D. Wong, E. Stavrakakis, H. Annath and A. Moore, *Faraday Discuss.*, 2021, **231**, 312–325.

(41) D. E. Crawford and J. Casaban, *Adv. Mater.*, 2016, **28**, 5747–5754.

(42) D. E. Crawford, C. K. G. Miskimmin, A. B. Albadarin, G. Walker and S. L. James, *Green Chem.*, 2017, **19**, 1507–1518.

(43) D. N. Rainer, A. V. Desai, A. R. Armstrong and R. E. Morris, *J. Mater. Chem. A*, 2021.

(44) *Sodium acetate - Substance Information - ECHA*.

(45) Y. Park, D.-S. S. Shin, S. H. Woo, N. S. Choi, K. H. Shin, S. M. Oh, K. T. Lee and S. Y. Hong, *Adv. Mater.*, 2012, **24**, 3562–3567.

(46) L. Zhao, J. Zhao, Y.-S. S. Hu, H. Li, Z. Zhou, M. Armand and L. Chen, *Adv. Energy Mater.*, 2012, **2**, 962–965.

(47) A. Abouimrane, W. Weng, H. Eltayeb, Y. Cui, J. Niklas, O. Poluektov and K. Amine, *Energy Environ. Sci.*, 2012, **5**, 9632.

(48) S. H. Dale and M. R. J. Elsegood, *Acta Crystallogr. Sect. C Cryst. Struct. Commun.*, 2003, **59**, m475–m477.

(49) J. A. Kaduk, *Acta Crystallogr. Sect. B Struct. Sci.*, 2000, **56**, 474–485.

(50) S. Ghosh, M. A. Makeev, Z. Qi, H. Wang, N. N. Rajput, S. K. Martha and V. G. Pol, *ACS Sustain. Chem. Eng.*, 2020, **8**, 6252–6262.

(51) S. Kaabel, J. P. D. Therien, C. E. Deschênes, D. Duncan, T. Friščić and K. Auclair, *Proc. Natl. Acad. Sci.*, 2021, **118**, e2026452118.

(52) T. S. Crickmore, H. B. Sana, H. Mitchell, M. Clark and D. Bradshaw, *Chem. Commun.*, 2021, **57**, 10592–10595.

(53) I. Halasz, S. A. J. Kimber, P. J. Beldon, A. M. Belenguer, F. Adams, V. Honkimäki, R. C. Nightingale, R. E. Dinnebier and T. Friščić, *Nat. Protoc.*, 2013, **8**, 1718–1729.

(54) W. Yuan, A. L. Garay, A. Pichon, R. Clowes, C. D. Wood, A. I. Cooper and S. L. James, *CrystEngComm*, 2010, **12**, 4063.

(55) M. Klimakow, P. Klobes, A. F. Thünemann, K. Rademann and F. Emmerling, *Chem. Mater.*, 2010, **22**, 5216–5221.

(56) B. Karadeniz, A. J. Howarth, T. Stolar, T. Islamoglu, I. Dejanović, M. Tireli, M. C. Wasson, S.-Y. Moon, O. K. Farha, T. Friščić and K. Užarević, *ACS Sustain. Chem. Eng.*, 2018, **6**, 15841–15849.

(57) T. Stolar, A. Prašnikar, V. Martinez, B. Karadeniz, A. Bjelić, G. Mali, T. Friščić, B. Likozar and K. Užarević, *ACS Appl. Mater. Interfaces*, 2021, **13**, 3070–3077.

(58) Q. Zhang and F. Saito, *Adv. Powder Technol.*, 2012, **23**, 523–531.

(59) A. Choi, Y. K. Kim, T. K. Kim, M.-S. Kwon, K. T. Lee and H. R. Moon, *J. Mater. Chem. A*, 2014, **2**, 14986–14993.

(60) C. Wang, Y. Xu, Y. Fang, M. Zhou, L. Liang, S. Singh, H. Zhao, A. Schober and Y. Lei, *J. Am. Chem. Soc.*, 2015, **137**, 3124–3130.

(61) H. Padhy, Y. Chen, J. Lüder, S. R. Gajella, S. Manzhos and P. Balaya, *Adv. Energy Mater.*, 2018, **8**, 1701572.

(62) C. Ma, L. Wu, Z. Jin, X.-Y. Zhao, Y.-S. Liu, Y.-L. Bai, H. Sun, K.-X. Wang and J.-S. Chen, *Chem. Mater.*, 2018, **30**, 8426–8430.

(63) D. S. Raja, J.-H. Luo, C.-T. Yeh, Y.-C. Jiang, K.-F. Hsu and C.-H. Lin, *CrystEng-Comm*, 2014, **16**, 1985–1994.

(64) A. D. Burrows, K. Cassar, R. M. W. Friend, M. F. Mahon, S. P. Rigby and J. E. Warren, *CrystEngComm*, 2005, **7**, 548.

Chapter 7

Summary and outlook

Mechanochemistry is still a recent addition to the synthetic chemists' toolbox and as such its possibilities and potential applications are yet to be explored to their full extent. This work has investigated several new avenues on how this easily implementable and advantageous experimental technique may aid in the synthesis of framework materials, in particular zeolites and sodium coordination polymers.

Improvement of reaction conditions during hydrolysis within the ADOR process for the synthesis of zeolites has been realised through a mechanochemically assisted procedure using low energy ball milling. In this way, reduction of solvent amount and decrease of reaction temperature and time have been achieved, beneficial in light of possible large scale synthesis and from an economical point of view.

Starting from zeolite **UTL** as parent material, several known ADOR daughter zeolites exhibiting **OKO**, ***PCS**, and **PCR** frameworks can be targeted by varying the concentration of hydrochloric acid as hydrolysis reagent. A similar behaviour has been demonstrated previously using the traditional solution based route. However, the mechanochemically adapted method follows a subtly different path and the most dense material IPC-4 (**PCR**) can be obtained from the arguably harshest conditions using undiluted HCl. The reaction can also be conducted using water which leads to IPC-2 **OKO** zeolites. It was demonstrated that this reaction still occurs under almost dry conditions using low liquid to solid ratios of $0.2\,\mu L\,mg^{-1}$. Such low volumes are immensely important for cost-efficient reactions where the monetary cost of used reagents is of concern, for example in isotopic enrichment procedures aiming to introduce the NMR active oxygen isotope ^{17}O into materials. The developed mechanochemical protocol is well suited for this purpose, offering a rapid and cost-efficient route towards isotopically enriched products.

Expanding on the current knowledge of solvent-free synthesis of zeolites, germanosilicates of several topologies were targeted aiming to find novel synthetic routes which are able to alleviate concerns regarding cost and efficiency of such materials caused by many factors including the financial burden of germanium containing reagents. Reproducing literature reports, zeolites with **ITH** framework were obtained using this economical method to establish working principles for the mechanical pre-treatment of solid starting materials and their subsequent crystallisation at elevated temperatures.

Experiments towards structurally more complex frameworks were not yet successful. Syntheses aimed towards materials showing the **UOV** framework led to the related, but denser **BEC** structure. Attempts to produce **UTL**-type zeolites were equally ineffective,

although a seed-assisted experiment showed promise, yielding a mixed sample possibly including a minor phase of the desired structure. The combination of the solvent-free method with seed-assisted protocols may be the way forward in producing more open frameworks which are more demanding and stringent in terms of synthesis conditions.

Finally, germanosilicate zeolites with **ISV** topology could be obtained for the first time utilising this mechanochemically aided synthetic route. Producing zeolites in this manner enables cheaper synthesis by avoiding the costly anion exchange of the structure-directing agent and remove the requirement for a solvent. Produced samples were not yet phase pure, which leaves some room for future optimisation of reaction conditions. Nonetheless, expanding the pool of zeolite frameworks available under such experimental conditions is helpful to determine how general this methodology can be and where its limitations lie.

In contrast to zeolites which seemingly necessitate a second heating procedure, metal coordination compounds such as MOFs are directly obtainable through mechanosynthesis. Exploiting this efficient route, five sodium carboxylate coordination polymers have been synthesised in a rapid manner, preventing production of large amounts of waste solvent, and utilising a safe and benign sodium source in the synthesis. The chemical variety in used organic dicarboxylic acids, ranging from the simple benzenedicarboxylic acid to heteroatom containing pyridinedicarboxylic acid, demonstrates the robustness of the developed protocol. Obtained materials are utilised as active anode material in sodium ion batteries and show competitive electrochemical performance compared to compounds produced using common synthesis routes in solution. These results have the potential to elevate the development of organic-based sodium ion batteries to the next level towards large scale production, a hindrance of currently used syntheses. This is especially true as preliminary experiments hint at the possibility for all-in-one preparation of the electrode composite. So far the active coordination polymer can be synthesised in the presence of electrically conductive carbon, necessary for a fully functional electrode material. Further steps in this regard should involve integration of the binder material, for a streamlined, direct fabrication of the electrode composite.

The investigations of mechanochemical synthesis methods for sodium carboxylates have also led to the formation of a potentially novel compound based on 1,4-napthalenedicarboxylic acid (NDC). A sodium-NDC compound has so far only been reported from a hydrothermal method using the toxic DMF as solvent. The compound synthesised in the present work is structurally distinct from the published material and its so far

elusive solution may shed more light onto the underlying formation mechanism of this compound class.

All parts of the work carried out during this PhD showcase the advantages of mechanochemical methods for the synthesis of solids, in particular framework materials. Industrially relevant compounds such as the widely used silicate-based zeolites and sodium coordination polymers with applications in sodium ion batteries profit from the economical and ecological improvements of these synthesis routes.

Future efforts may be directed towards possibilities for materials so far unexplored in regard to mechanochemistry as well as diving deeper and investigating the principles governing these solid-state transformations. A lot of work has been dedicated into in situ investigations of the synthesis of the related class of metal-organic frameworks, which are deemed to be a worthwhile effort for compounds described in this work.